L-Tyrosine Based Polymer Brushes for Drug Delivery In-vitro and In-vivo

विद्या वाचस्पति की
उपाधि की अपेक्षाओं की आंशिक पूर्ति में प्रस्तुत शोध प्रबंध

A thesis submitted in partial fulfillment of the requirements of the degree of Doctor of Philosophy

द्वारा / By

उत्रेश्वर अर्जुन गव्हाणे /

Utreshwar Arjun Gavhane

पंजीकरण सं. / Registration No.:

20183577

शोध प्रबंध पर्यवेक्षक / Thesis Supervisor:

प्रो. एम. जयकन्नन/ Prof. M. Jayakannan

IISER PUNE

भारतीय विज्ञान शिक्षा एवं अनुसंधान संस्थान पुणे

INDIAN INSTITUTE OF SCIENCE EDUCATION AND RESEARCH PUNE

2025

भारतीय विज्ञान शिक्षा एवं अनुसंधान संस्थान पुणे
IISER PUNE INDIAN INSTITUTE OF SCIENCE EDUCATION AND RESEARCH PUNE

CERTIFICATE

Certified that the work incorporated in the thesis entitled ***"L-Tyrosine Based Polymer Brushes for Drug Delivery In-vitro and In-vivo"*** Submitted by **Mr. Utreshwar Arjun Gavhane** was carried out by the candidate, under my supervision. The work presented here or any part of it has not been included in any other thesis submitted previously for the award of any degree or diploma from any other University or institution.

Date: **15/01/2025**

Place: **Pune**

Prof. M. Jayakannan
(Supervisor)
15/1/2025

Declaration by Student

Name of Student: **Utreshwar Arjun Gavhane**

Reg. No.: **20183577**
Thesis Supervisor(s): **Prof. M. Jayakannan**

Department: Chemistry
Date of joining program: **01/01/2018**

Date of Pre-Synopsis Seminar: **02/08/2024**

Title of Thesis: **L-Tyrosine Based Polymer Brushes for Drug Delivery in-vitro and in-vivo.**

I declare that this written submission represents my idea in my own words and where others' ideas have been included; I have adequately cited and referenced the original sources. I declare that I have acknowledged collaborative work and discussions wherever such work has been included. I also declare that I have adhered to all principles of academic honesty and integrity and have not misrepresented or fabricated or falsified any idea/data/fact/source in my submission. I understand that violation of the above will be cause for disciplinary action by the Institute and can also evoke penal action from the sources which have thus not been properly cited or from whom proper permission has not been taken when needed. The work reported in this thesis is the original work done by me under the guidance of Prof. M. Jayakannan.

Date: 16/01/2025

Signature of the student

Dedicated to

My

Parents

Shri. Arjun Maroti Gavhane (Father)

Smt. Panchafula Arjun Gavhane (Mother)

For their endless love, support, and encouragement

Acknowledgements

First and foremost, I express my deepest gratitude and sincere appreciation to my supervisor, Prof. M. Jayakannan. I am truly fortunate to have had him as my mentor during this journey. His insightful scientific guidance, constructive feedback, and consistent encouragement pushed me to exceed my limits and deliver my best in research. His open-door policy, accessibility, and unwavering support created a nurturing and productive environment, enabling me to think creatively and solve research challenges innovatively. His mentorship has been invaluable, and I will carry the lessons I have learned under his guidance throughout my career. I am also profoundly thankful to Dr. S. K. Asha (NCL Pune) for her invaluable scientific advice, insightful discussions, and the many contributions he made to my research. My sincere gratitude extends to my Research Advisory Committee (RAC) members, Dr. Kadhiravan Shanmuganathan and Dr. S. Sandanaraj Britto, for their insightful feedback and constructive suggestions during RAC meetings, which greatly enhanced the quality of my research. I am immensely grateful to Prof. Sunil Bhagwat (Director, IISER-PUNE) and Prof. Jayant B. Udgaonkar (Former Director, IISER-PUNE) for providing access to excellent infrastructure and advanced instrumentation, which greatly facilitated my research work. I would like to acknowledge the faculty members of the Department of Chemistry at IISER Pune for their interactive discussions and for teaching me foundational chemistry courses, which enriched my understanding and knowledge in the field. I would also like to express my gratitude to the technical staff at IISER Pune for their invaluable assistance with instrumentation and analysis: Dr. Sandeep and Nitin (NMR), Prajapati (MALDI), Dr. Sandeep (HRMS), Megha (AFM), Mahesh Jadhav, and Yatish (FE-SEM). My thanks also go to the National Chemical Laboratory (NCL) Pune for providing access to HR-TEM facilities. I would also like to express Animal house staff Suraj Sir, Krishna Veni Madam and Anubha Madam, Chetan sir, I would like to express my gratitude to Microscopy facility especially Vijay Vithal Sir, and Santosh Sir. This acknowledgement would be incomplete without expressing my heartfelt thanks to everyone who contributed directly or indirectly to my research journey. Thank you for your support, guidance, and encouragement. I am deeply thankful to my past and present IISER and NCL lab mates for their camaraderie and support and for creating a stimulating and memorable environment at IISER Pune. Special thanks go to Dr. Dheeraj, Dr. Nilesh, Dr. Bhagyashree, Dr. Sonashree, Dr. Rahul, Dr. Ruma, Dr. Khuddus, Dr. Mishika Virmani, Shahid Pathan, and Parshuram Kamble, Aditi Gujare, Keertana, Anu Pradeep, Sharafudheen P C, Saradha Sarjane,

Rashika Daware, Akash. A, Bhatta Chandrashekar, Pooja Patil, Bhushan Pawar, Akshay Nagrikar, Sunidhi Singh, Sayali Jadhav, Jewel, Ridham Oberai. A special acknowledgement is due to Dr Dheeraj, whose critical academic insights and unwavering support have had a profound influence on my work. He has been an exceptional colleague, and I have learned invaluable lessons from his about tackling challenges in research and conducting impactful studies. I would like to extend my heartfelt thanks to the Resonance team because, without their support and encouragement, I would not have been able to achieve this. My gratitude also extends to the University Grants Commission (UGC), New Delhi, for awarding me the prestigious UGC-JRF and SRF fellowships, as well as for their financial support. I am profoundly thankful to my family for their unwavering support and encouragement throughout this journey. To my parents, my brother, and my sister, your constant belief in me and your unwavering assistance have been my pillars of strength. To my brother, balasaheb, your boundless support and unwavering faith in my abilities have been a source of immense motivation, for which I am forever grateful. My heartfelt thanks also go to my sister-in-law, Sonali, and my adorable nephews, kajal and komal, for their love and encouragement.

To my wife, Swati, words cannot fully express my gratitude for your love, patience, and unwavering support throughout this journey. Your faith in me has been a guiding light, and I am forever indebted to you for being my anchor. To our son, utkarsh, you are the joy and inspiration of my life, making every moment worthwhile. Your presence has filled our lives with boundless happiness and has been a driving force for my accomplishments. Lastly, I extend my gratitude to my extended family the Gavhane and Kolhe families for their constant encouragement and support throughout this thesis journey. Your unwavering belief in me has been invaluable, and I am deeply indebted to you all for your presence in my life.

Utreshwar Arjun Gavhane

Synopsis

Polymer-based drug delivery systems are innovative platforms designed to enhance the effectiveness and safety of therapeutic agents. These systems utilize biocompatible and biodegradable polymers to control drug release, improve stability, and target specific sites within the body. By tailoring polymer properties, they offer precise drug delivery, reducing side effects and improving patient outcomes. Nanoparticles offer significant potential for improving drug delivery by enhancing therapeutic efficacy and targeting drugs to specific sites of action. Among various nanoparticle types, polymeric, inorganic, and lipid-based polymeric nanoparticles stand out due to their versatility and advanced designs. These nanoparticles, constructed from polymer building blocks, allow for control over size, shape, and surface charge, along with the incorporation of diverse chemical and biological functionalities. Such attributes enable targeted delivery, intracellular compartment specificity, and stimuli-responsive drug release, making polymeric nanoparticles a key focus in smart drug delivery systems. Synthetic polymers derived from L-amino acids have obtained significant interest due to their excellent biocompatibility and functional diversity, which enhance their hydrophilicity and allow for modifications with bioactive molecules. These features open up substantial opportunities for developing amino acid-based polymer brushes for biomedical applications. In this research, a propargyl-functionalized poly(ester-urethane)s platform based on L-tyrosine; further, this propargyl functionalized poly(ester-urethane)s was clicked with a PEGylated chain to develop ultra-high molecular weight polymers. This amphiphilic polymer brushes self-assembles to tune their size and shape by varying the chain length. The study focused on investigating the lysosomal enzymatic degradation of these polymers to facilitate the targeted delivery of anticancer drugs into cancer cells. and bio-derived pendant units were synthesized and polymerized using a solvent-free melt polycondensation method. The resulting high molecular weight poly(ester-urethane)s exhibited tunable thermal properties and was Further; this methodology was explored to make new classes of amino acid and sugar-based fully biodegradable hybrid polymer brushes as next-generation green polymers for thermoplastic and exploited for various biomedical applications, including drug delivery, bioimaging, and biodistribution.

The thesis is divided into four chapters:

Chapter 1: Literature Review

This chapter provides a comprehensive review of polymer-based brush systems for drug delivery to cancer cells. It highlights the key aspects of polymer-based drug delivery systems and explores the potential of natural resource-derived polymers for various biomedical applications.

Chapter 2: Development of size and shape-controlled polymer brushes based on L-amino acid bioresource and study of the role of polymer topology on the enzymatic-biodegradation and deep-tissue penetration under in-vitro and in-vivo.

Chapter 3: To Design and Development of L-Tyrosine Sugar Hybrid Biodegradable Polymer Brushes for fine-tuning their Thermoplastic application as well as to encapsulate various cargos to deliver into cancer cells and in-vivo biodistribution.

Chapter 4: Development of CUM Fluorophore-Tagged Polymer Brushes for Cellular FRET-Based theragnostic Application in cancer cells. The loaded cargo nanoparticle brushes interact with a fluorophore-tagged polymer to monitor the FRET phenomena in the nanocarrier.

In Chapter 2, We developed polymer brushes with controlled size and shape using L-amino acid-based materials and studied how their shape affects enzymatic breakdown and deep-tissue penetration in both in-vitro and in-vivo. A designed monomer made from L-tyrosine was polymerized using a solvent-free process to produce hydrophobic, biodegradable poly(ester-urethane)s that can be further modified through click chemistry by changing the lengths of PEG-azides in the reaction, we designed two types of polymer brushes: one-dimensional rod-like and three-dimensional spherical structures. These polymer brushes are non-toxic to cancerous cell MCF-7 as well as wild type MEF cell line; it was found that these polymer brushes were highly compatible, polymer brushes are non-hemolytic in nature, the RBcs pallet are intact, polymer brushes can transport the anticancer drug doxorubicin (DOX) and a near-infrared biomarker, IR-780, for imaging. In-vitro studies showed that rod-like

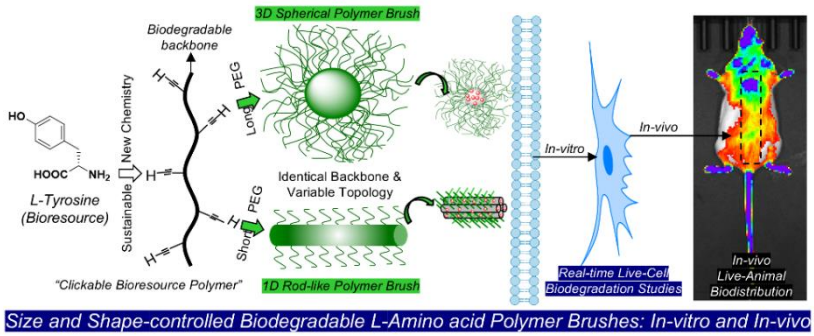

brushes work better than spherical ones, as they are absorbed by cells more quickly, break down efficiently in endo-lysosomal compartments, and deliver DOX to the cell nucleus. Animal studies using IVIS imaging confirmed that rod-like brushes penetrate deep into tissues more effectively and highlighted the importance of polymer brush shapes for biological applications. The brushes remained stable in blood for over 72 hours and mostly accumulated in organs like the liver, kidneys, and spleen, with minimal effects on the heart and brain. Imaging of tissue slices confirmed their ability to penetrate deeply. This study emphasizes the potential of bio-derived, biodegradable polymer brushes as next-generation smart drug delivery platforms.

In this chapter 3, we developed the synthesis of biodegradable poly(ester-urethane) by solvent-free melt polymerization. Further, these propargyl functionalized polymers were clicked with another biobased partner, like sugar (Glucose and Mannose), to get amphiphilic hybrid sugar polymer brushes. It is confirmed by 1H NMR and FT-IR. These sugar polymer brushes showed higher glass transition temperature ($T_g \geq 107$ °C) as compared to their homopolymer, and they can used for thermoplastic application. The sugar polymer brushes were synthesized by introducing propargyl-functionalized groups into the poly(ester-urethane) backbone, which were later converted into Sugar-functionalized polymer brushes. These polymer brushes exhibited thermal properties and were self-assembled into nanoparticles with sizes below 100 nm in aqueous environments. The nanoparticles were capable of encapsulating fluorescent dyes such as HPTS, and therapeutic agents like CPT, TPT, CUR. The photophysical properties were analyzed using absorbance and emission spectroscopy and retained their photophysical properties. These sugar polymer brushes were performed on their biocompatibility and cytotoxicity assay. We found that these sugar polymer brushes are non-toxic to the cancerous as well as normal cell lines at higher concentrations of 100 µg/mL. Further, the drug-loaded polymer brushes showed comparable cytotoxicity as a free drug in the cancerous cell line MCF-7 as well as the HEK-293 cell line. The nanoparticles exhibited excellent biocompatibility with both normal and cancer cell lines and showed non hemolytic in nature. Drug-loaded polymer bioimaging studies using confocal laser scanning microscopy (CLSM) confirmed the interaction between the polymer and its cargo at the cellular level. In

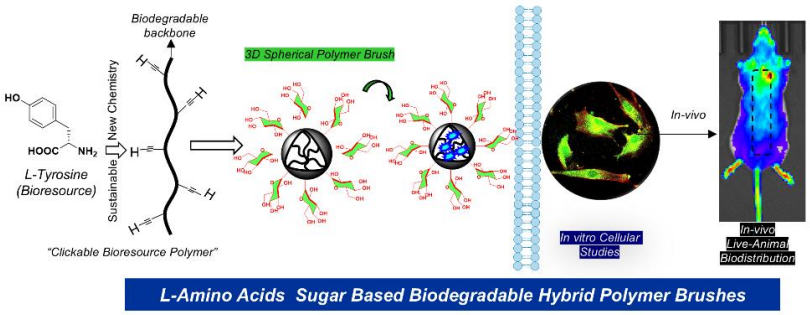

vivo, biodistribution studies showed that ICG-loaded nanoparticles demonstrated prolonged nanoparticle retention compared to free ICG.

Chapter 4, explore the design and development of a biodegradable poly(ester-urethane)s derived from L-tyrosine, clicked with PEG-750, 5000 and coumarin (CUM) fluorescence, for the creation of polymer self-assemblies with theragnostic applications in cancer cells. The synthesis began for that CUM azide was prepared, followed by PEG-750, 5000 azides also prepared and characterized by ^{1}H NMR and FT-IR spectroscopy. Further, it was clicked with poly(ester-urethane) to form a fluorescent-tagged polymer brush.

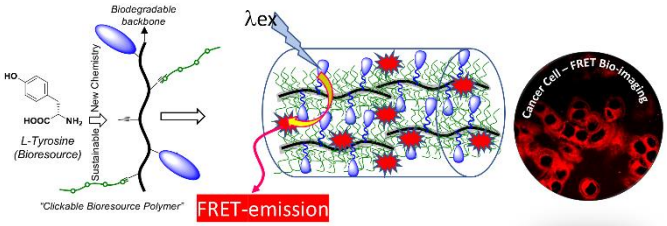

Fluorophore-Tagged Theranostic FRET Polymer Brushes for Real-time Cellular Monitoring

These polymer brushes were self-assembled into nanorods with sizes below 220 nm in aqueous environments. The nanorods polymer brushes were capable of encapsulating fluorescent dyes such as Nile Red (NR). The photophysical properties were analyzed using absorbance and emission spectroscopy, and we found that these polymer lifetime measurements revealed energy transfer via Förster resonance energy transfer (FRET). The CUM Donar molecule transfers its excitation energy to acceptor molecules confirming the FRET. The fixed cell imaging only CUM polymer brushes were excited at 405 nm using confocal laser scanning microscopy (CLSM), and we found out that the indeed rod-like polymer brushes showed better uptake as compared to Sphere-like polymer brushes. The polymer brush nanoparticles exhibited excellent biocompatibility with both normal HEK-293 and cancer cell MCF-7 lines, and the hemolysis assay showed no RBcs rupture. The live cell experiment demonstrated that the FRET pair remained stable and functional within cells for a prolonged period This study highlights the potential of these fluorescent polymer brushes for bioimaging and drug delivery applications. The overall importance of biodegradable polymer brushes in this field exists in their ability to enhance the biocompatibility, functionality, and degradability of materials, which is particularly significant in both in vitro and in vivo studies involving L-tyrosine poly(ester-urethane)s, as these materials offer promising applications in biomedical application, such as targeted drug delivery, theragnostic, bioimaging, and biodistribution. The findings demonstrate the versatility and efficacy of these polymers, creating the way for future research in the field of biodegradable polymers for healthcare applications.

Table of Contents

Chapter 1: Introduction

1.1 Introduction to Cancer……..13-15
1.2 Chemotherapy using nanocarrier……..16-18
1.3 Enhance Permeability and Retention (EPR) Effect……..19-21
1.4 Polymeric nanoparticles for cancer therapy…….21-22
1.5 Polymeric Nanoparticles for Drug Encapsulation……23-24
1.6 Polymeric Nanocarriers for Drug Delivery…….....24-24
1.7 Polymer brushes…….....24-26
1.8 Stimuli Responsive polymer brushes……...26-28
1.9 Sustainable Polymers in Drug Delivery…….....29-29
1.10 Polymer from Natural resources L-Amino acid…….30-42
1.11 Aim of the thesis…….43-44
1.12 References……..45-53

Chapter 2: Size and Shape-controlled Biodegradable Polymer Brushes Based on L-Tyrosine for Intracellular Drug Delivery and Deep-Tissue Penetration.

2.1 Introduction……...56-59
2.2 Experimental Section……59-71
2.3 Result and discussion……72-112
2.4 Conclusion……112-113
2.5 References……114-118

Chapter 3: Design and Development of L-Tyrosine–Sugar Hybrid Biodegradable Polymer Brushes

3.1 Introduction……...121-123
3.2 Experimental Section……123-132
3.3 Result and discussion……132-158
3.4 Conclusion……159-159
3.5 References……160-164

Chapter 4: Development of Fluorophore-Tagged Polymer Brushes for Cellular FRET-Based Real-time Monitoring.

4.1 Introduction……..167-170
4.2 Experimental Section……170-173
4.3 Result and discussion……174-191
4.4 Conclusion……192-192
4.5 References……193-198

5 Overall Conclusion……..199-200
6 **Future Directions**……...201-201
7 **List of publications**……203-203
8 **Appendix**……210-224

Chapter 1

Introduction

1.1 Introduction to Cancer

Cancer is a significant global health issue and one of the leading causes of death worldwide, as highlighted by the World Health Organization in 2020.[1,2] The prevalence and impact of cancer are shaped by various factors,[3,4] such as the type of cancer, an individual's age, and their geographical region. For example, lung cancer ranks as a primary cause of cancer-related deaths globally, whereas breast cancer is particularly common among women in high-income countries. Cancer can develop in many forms, affecting various parts of the body. Some of the most frequently diagnosed cancers include breast cancer, lung cancer, prostate cancer, colorectal cancer, skin cancer (including melanoma), leukemia (blood cancers), lymphoma, ovarian cancer, pancreatic cancer, and bladder cancer.[5–8] There are also numerous rare types of cancer, as illustrated in Figure 1.1

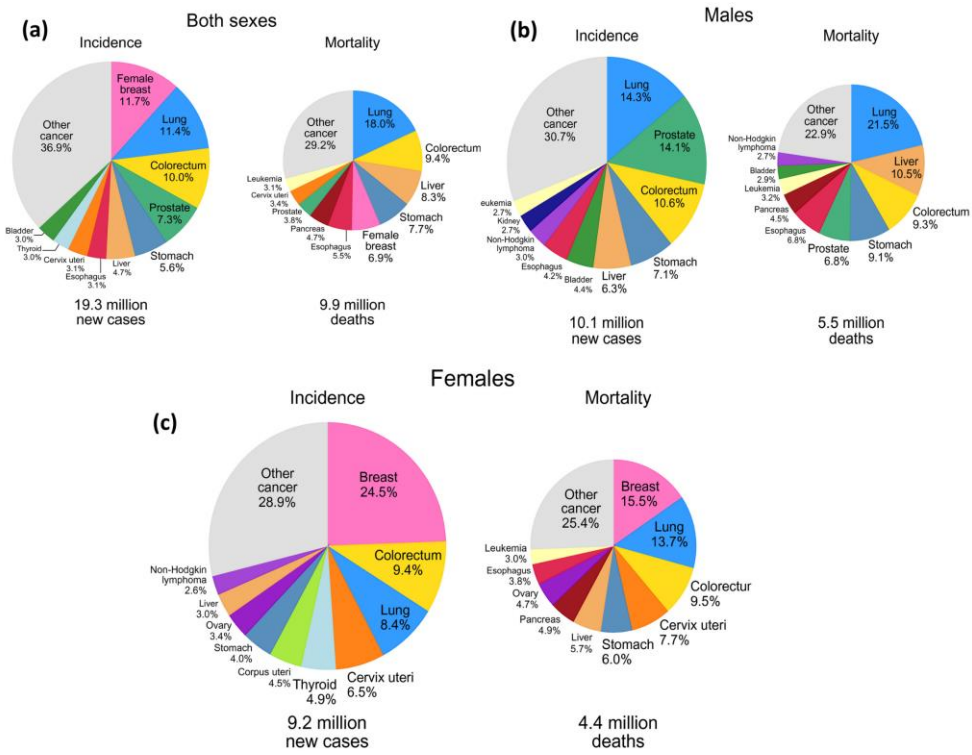

Figure 1.1 *Different Types of cancer and their ratio (Adapted from CA CANCER J CLIN 2021;71:209–249)*

The specific type of cancer a person has influences the progression of their disease, available treatment options, and overall prognosis. Improvements in cancer prevention, early detection, and treatment methods have contributed to a decline in cancer-related deaths in some parts of the world. However, other regions continue to face challenges with high mortality rates from cancer.[9] Cancer treatment encompasses a range of approaches designed to address the

disease based on its type, stage, and the overall health of the patient. Common treatment methods include radiotherapy,[10,11] chemotherapy,[12,13] immunotherapy,[14] surgical removal of tumors,[15] and hormone therapy,[16] as depicted in Figure 1.2.

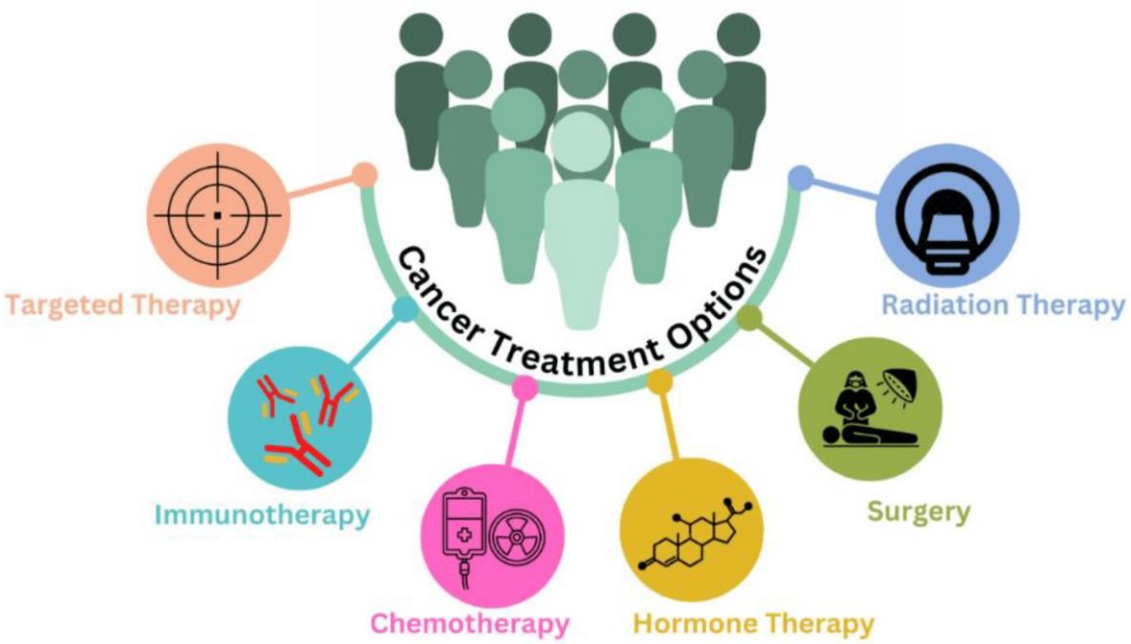

***Figure 1.2**: Different types of cancer treatment (adapted from Polymers **2023,** 23, 2928).*

Treatment strategies are often complex and tailored to individual needs. Surgery is typically used for localized cancers, while chemotherapy works to inhibit the growth and spread of cancer cells. Radiation therapy specifically targets and destroys cancerous cells. Immunotherapy boosts the immune system's ability to recognize and fight cancer, while targeted therapy focuses on specific molecular pathways involved in cancer development. Hormone therapy is employed for cancers sensitive to hormonal changes, such as breast or prostate cancer. Additionally, advancements in precision medicine enable treatments to be customized based on genetic analysis of the tumor. Stem cell transplants are used to regenerate damaged bone marrow, and palliative care is provided to enhance the quality of life for patients with advanced stages of cancer. The selection of treatments often involves combining these approaches to achieve the most effective outcomes. Determining the most suitable treatment for cancer is not a straightforward process, as it depends on numerous factors, including the type and stage of cancer, the patient's overall health,[4] and their personal preferences. Chemotherapy is one of the key treatment options available, but its effectiveness and suitability

vary based on individual circumstances. Chemotherapy works by administering drugs that circulate throughout the body,[17] allowing them to target cancer cells that have spread to different areas. This makes it particularly effective for treating metastatic cancers. Commonly used chemotherapy drugs include doxorubicin, cisplatin, camptothecin, and topotecan. These drugs act at the cellular level, either by intercalating into the DNA helix or by inhibiting the action of enzymes like topoisomerase,[18] ultimately leading to cancer cell death. Chemotherapy is often used alongside other treatments, such as surgery or radiation therapy, to enhance overall treatment outcomes. It is versatile and can treat a wide range of cancers, including solid tumors and blood cancers.[19] However, despite its advantages, chemotherapy has notable limitations due to its side effects. Side effects of chemotherapy, are shown in Figure 1.3. include nausea, vomiting, fatigue, hair loss, immune suppression, and more, significantly impacting the patient's quality of life. Because chemotherapy drugs are not highly specific, they can harm healthy cells alongside cancer cells, potentially damaging normal tissues and organs. Over time, some cancer cells may develop resistance to chemotherapy, such as multidrug resistance caused by the activation of efflux pumps like P-glycoprotein. Additionally, chemotherapy can be toxic, and its dosing and scheduling must be carefully managed to minimize harm while maintaining effectiveness.

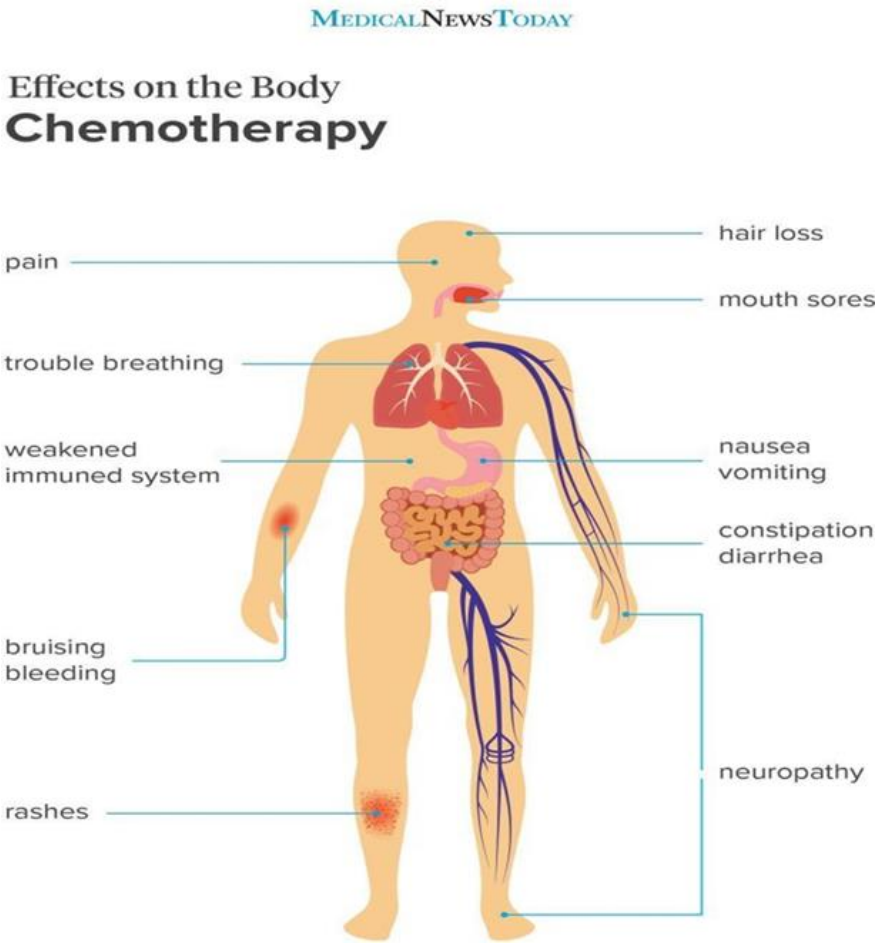

Figure 1.3 *Side effects of chemotherapy (Adapted from https://www.medicalnewstoday.com/articles/323485).*

1.2 Chemotherapy Using Nanocarriers

The advent of precision medicine has ushered in a new era in cancer treatment, with nanotechnology playing a pivotal role. Through nanotechnology-based platforms, drug molecules can be conjugated or encapsulated within nanoparticles, enabling targeted delivery directly to cancerous tissues.[20] This approach utilizes nanocarriers, such as nanoparticles or liposomes, to encapsulate chemotherapy drugs.[21–23] These carriers improve drug solubility, enhance stability, and allow for precise delivery to tumor sites, thereby reducing unintended effects on healthy tissues. Nanocarriers are often designed to exploit the enhanced permeability and retention (EPR) effect,[24–26] which enables them to preferentially accumulate in tumor tissues. This targeted accumulation increases drug concentration at the tumor site while

minimizing exposure to normal tissues, improving the therapeutic efficacy of chemotherapy agents and potentially reducing the side effects of conventional chemotherapy.[13] The use of nanocarriers offers additional advantages, including targeted delivery and controlled drug release,[1] which further minimize damage to healthy cells. Their enhanced specificity and efficient delivery allow for lower drug dosages while maintaining therapeutic effectiveness, thereby reducing toxicity. Furthermore, nanotechnology can modify drug biodistribution, addressing challenges like poor solubility and rapid clearance associated with traditional chemotherapy. Nanocarriers can also be engineered to carry multiple drugs simultaneously, facilitating combination therapy by delivering different agents to the same tumor site. This capability enhances treatment effectiveness and may help overcome drug resistance. However, developing nanocarriers with optimal drug loading, stability, and precise targeting requires complex engineering and advanced formulation techniques. Additionally, ensuring the safe clearance of nanocarriers and understanding their long-term safety remain active areas of research.[27,28] Nanotechnology-based chemotherapy holds significant promise for improving cancer treatment. By enhancing drug specificity, reducing off-target effects, and enabling combination therapies, it offers a potential path toward more effective and less toxic cancer therapies. An example of this innovative platform is illustrated in Figure 1.4.

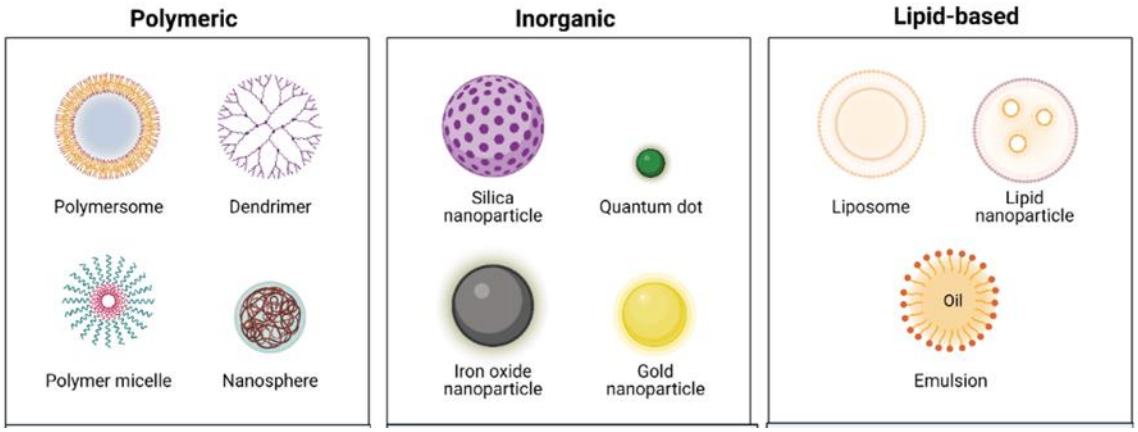

Figure 1.4 *Role of Nanoparticles for Cancer, Biomedical Properties, and Therapeutic (Adapted from AAPS PharmSciTech* ***25****, 23 (2024).*

When nano-formulations are administered intravenously, they follow a complex process known as the CAPIR mechanism,[29–31] which comprises five interconnected steps. Each step plays a vital role in determining the efficiency of drug delivery. These steps circulation, accumulation, permeation, internalization, and release are illustrated in Figure 1.5.

Circulation: In the first stage, nano-formulations circulate through the bloodstream. For effective drug delivery, these nanomedicines must remain stable and intact as they navigate the circulatory system. Maintaining their structural integrity during this phase is critical to ensuring successful delivery to the target site.[30]

Accumulation: Following circulation, nano-formulations accumulate at the tumor site. This step leverages the unique properties of tumor vasculature, such as its leaky and rapidly formed blood vessels, to localize therapeutic agents in the tumor tissue. Sufficient accumulation is essential for delivering a concentrated dose to the target.[31]

Permeation: After accumulation, the nano-formulations must penetrate deep into the tumor tissue to reach cancer cells. Effective permeation is necessary for ensuring that the therapeutic agents can access the target cells within the tumor microenvironment.[31]

Internalization: Once the nano-formulations have permeated the tumor, they must be internalized by the cancer cells. This step is critical for enabling the therapeutic agents to exert their intended effects directly within the cells.[31]

Release: The final step involves the release of the drug within the target cell. At this stage, the therapeutic agents are delivered in their active, unbound form, ready to act on the cancer cells.[31]

Efficiency Considerations: The ultimate goal of the CAPIR process is to maximize the proportion of drug molecules delivered to cancer cells in their active form. This requires optimizing each of the five steps: circulation efficiency (QC), accumulation efficiency (QA), permeation efficiency (QP), internalization efficiency (QI), and release efficiency (QR). The overall delivery efficiency (Q) is determined by the percentage of active drug molecules successfully delivered to the target cells relative to the total amount administered. Importantly, the success of the CAPIR mechanism depends on achieving high efficiency in all five steps, as a failure in any one step can significantly reduce overall effectiveness.[30,31]

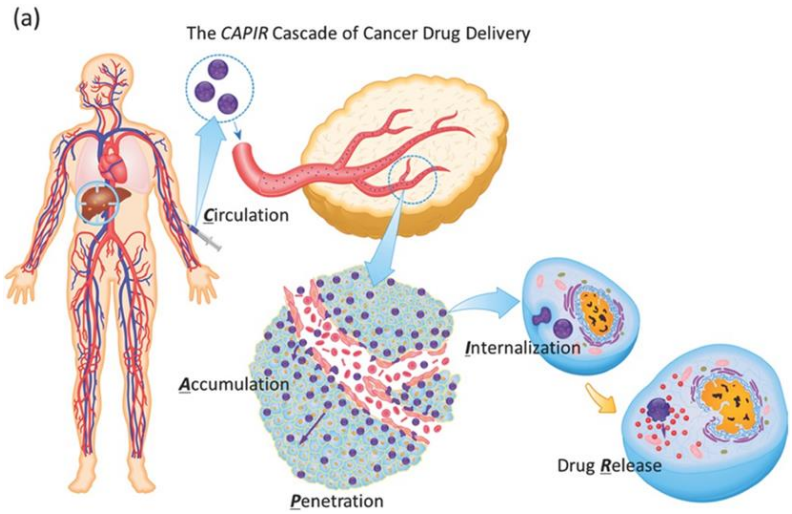

Figure 1.5 *CAPIR cascades for targeted drug delivery (Adapted from small 2016, 12, No. 37, 5108–5119).*

1.3 Enhanced Permeability and Retention (EPR) effect

describes the unique ability of nanoparticles to preferentially penetrate and accumulate in tumor tissues compared to normal tissues.[32–35] This phenomenon was first demonstrated by Maeda et al., who found that nanoparticles smaller than 500 nm could enter tumor tissues and remain retained at the intercellular level. Tumor cells, due to their rapid and unregulated growth, exhibit abnormal cellular arrangements and large intercellular spaces.[36,37] Additionally, tumors often develop poor vasculature and lack an efficient lymphatic drainage system, further supporting nanoparticle retention in the tumor microenvironment. When nanoparticles encapsulating therapeutic drugs are introduced into the bloodstream, they can passively accumulate at tumor sites due to the EPR effect. This occurs because the leaky vasculature of tumors allows nanoparticles to penetrate, while poor lymphatic drainage prevents their clearance. Once within the tumor, nanoparticles are internalized by cancer cells through endocytosis, as depicted in Figure 1.6.

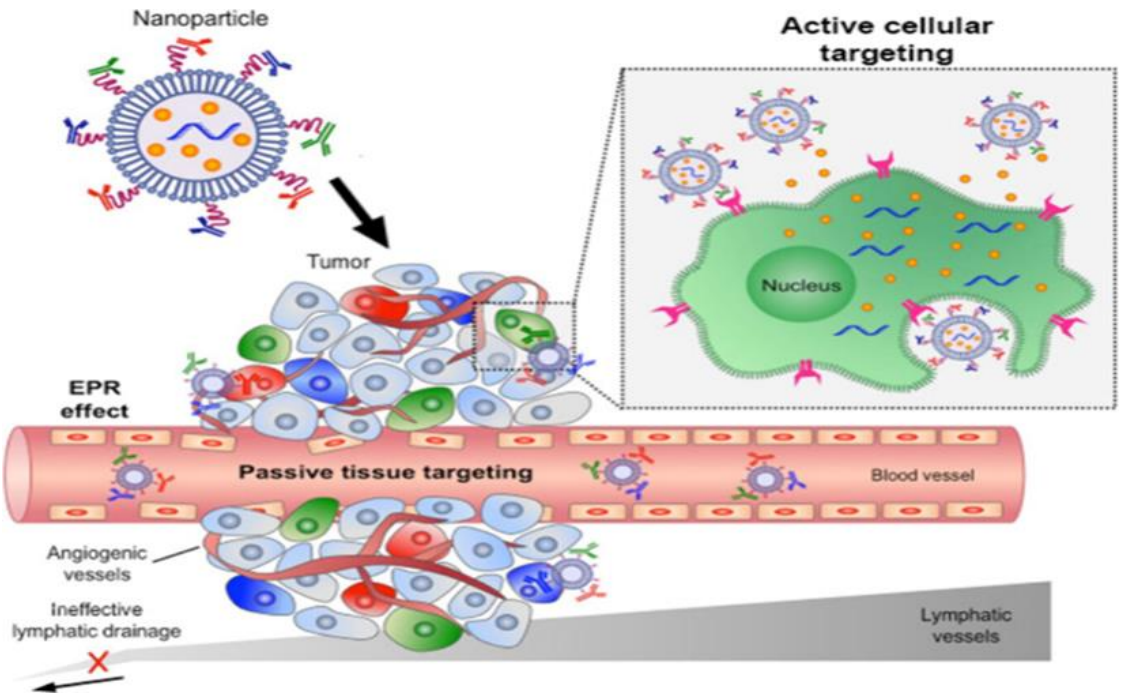

Figure 1.6 *Comparison of the Enhanced Permeability and Retention (EPR) Effect in Normal vs. Cancerous Tissue for Nanoparticle-Based Chemotherapy Treatment. (Adapted from Bioconjugate Chem. 2019, 30, 9, 2300–2311).*

Drug delivery via nanocarriers can be categorized into passive targeting and active targeting, based on how the nanoparticles reach the tumor site: Passive Targeting: This approach relies solely on the EPR effect. Nanoparticles accumulate in tumor tissues without requiring any specific targeting ligands. They exploit the unique characteristics of the tumor microenvironment, such as leaky blood vessels and impaired lymphatic drainage, to deliver drugs selectively to cancer tissues over normal tissues.[37]Active Targeting In this method, nanoparticles are engineered with specific ligands or stimuli-responsive features to enhance their targeting precision. Active targeting involves decorating nanoparticles with ligands that bind to receptors or molecules overexpressed on cancer cells,[38,39] improving the delivery specificity and therapeutic efficacy. Examples of Active Targeting Systems[38,39] Christine E. Wang et al. Developed sunflower-type polymers with an outer layer decorated with folate ligands for targeted drug delivery. The polymer's inner core contained doxorubicin (DOX), linked via a pH-sensitive hydrazone bond, enabling controlled drug release in acidic tumor environments.[40] Mingyang Li et al.: Engineered silicon nanoparticles (Si NPs) designed to target HER2-positive breast cancer cells. By adjusting the density of Fab fragments, the nanoparticles' targeting efficiency and cytotoxic effects were enhanced, showing a strong correlation between Fab density, HER2 expression, and therapeutic response.[41] Arpan Satsangi

et al.: Synthesized a paclitaxel (PTX) conjugate using a PAMAM dendrimer linked with a cathepsin B-cleavable GFLG peptide spacer (PGD). This conjugate demonstrated improved cytotoxicity and metabolic activity reduction in cancer cells, particularly those with moderate-to-high cathepsin B expression levels.[42] Simon A. Costa et al. Introduced a novel biopolymer-based nanoparticle system with genetic encoding for a drug conjugation site and a structured bioactive domain. By using an unnatural amino acid for drug attachment and incorporating a nanobody targeting element stabilized by a disulfide bond, this approach enabled precise cellular-level active targeting[43] (Figure 1.7). These advancements in passive and active targeting systems demonstrate the potential of nanotechnology in improving the specificity, efficacy, and safety of cancer therapies.

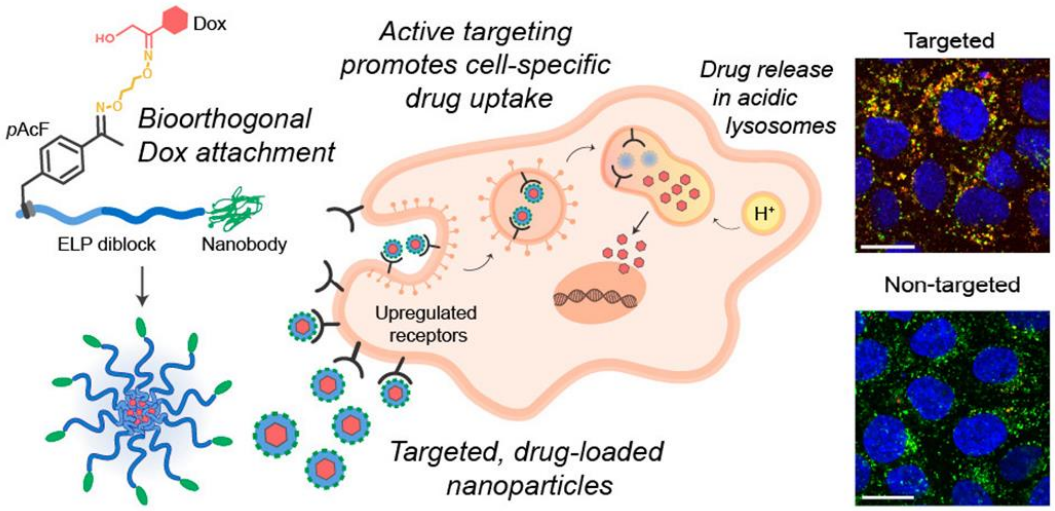

Figure 1.7 *Active targeting nanoparticles drug release in lysosomal. (Adapted from Nano Lett.* ***2019,*** *19, 247−254).*

1.4 Polymeric nanoparticles for cancer therapy

Various types of nanoparticles have been developed for chemotherapy applications, classified based on the materials used, such as lipid-based nanoparticles,[44] polymeric nanoparticles,[45,46] and inorganic nanoparticles.[47,48] This section focuses specifically on polymeric materials employed for drug delivery. Ringsdorf's Contribution to Polymeric Drug Delivery Systems: Helmut Ringsdorf, a German chemist, was a pioneer in the field of polymers and materials science. His work laid the foundation for polymer-based drug delivery systems,

particularly the development of water-soluble polymer-drug conjugates. Ringsdorf proposed a model (Figure 1.8) in which hydrophobic drug molecules could be covalently linked to water-soluble polymers. This approach improved the solubility, stability, and bioavailability of the drugs, while also enabling the attachment of targeting ligands to enhance site-specific delivery and minimize off-target effects. Building upon Ringsdorf's model,[49–51] numerous successful polymeric drug delivery systems have been developed. These systems include drug molecules conjugated to polymer backbones using either covalent or non-covalent interactions. Polymer-drug conjugates, for instance, involve linking pharmacologically active compounds to polymers via cleavable bonds such as ester, hydrazone, or imine bonds. A. P. Mansur et al This study developed carboxymethyl cellulose-doxorubicin (CMC-DOX) conjugates functionalized with RGD peptides and arginine for targeted drug delivery. DOX was covalently attached to the polymer via cleavable amide bonds. Cellular uptake was facilitated by RGD peptides, and upon internalization, DOX was released within lysosomes, effectively killing cancer cells.[52] Pedro R. Figueiredo et al This research evaluated 30 polymer-drug conjugates that undergo enzymatic degradation using human carboxylesterase 2 (hCE2). By employing docking and simulation methods, the study demonstrated the importance of certain drug features, such as a flat core and small size, for optimal binding and enzymatic hydrolysis.[53]

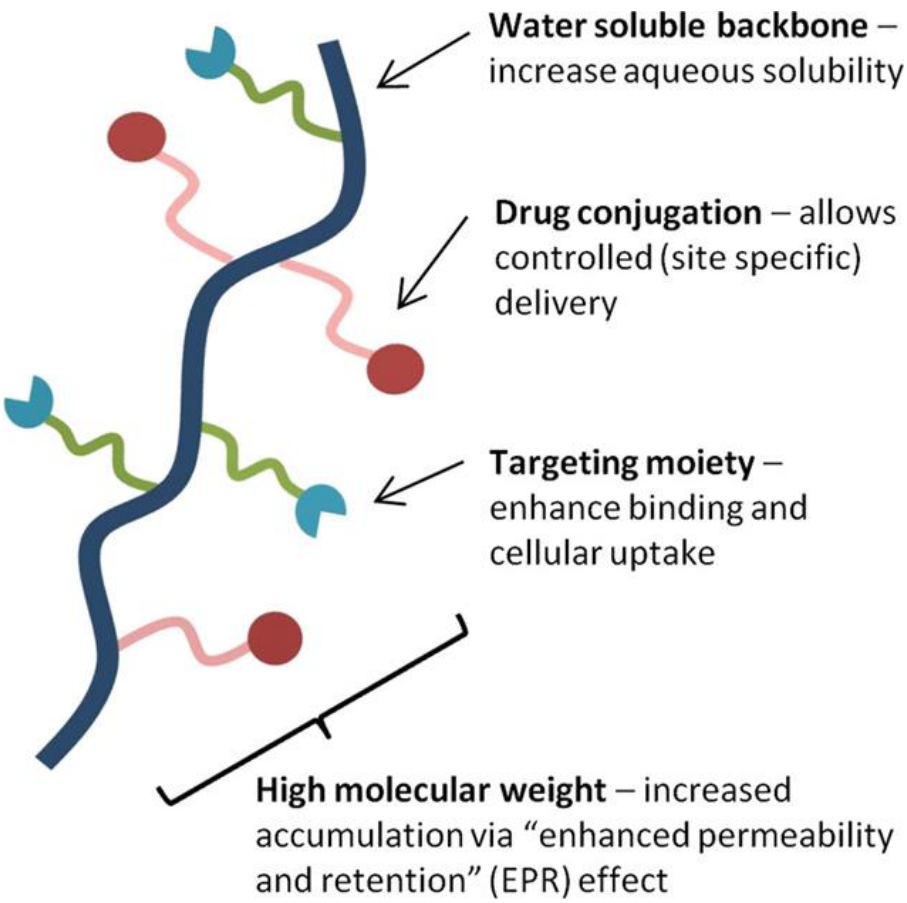

Figure 1.8 *Helmut Ringsdorf's Model for Drug Delivery (Adapted from Chem. Mater.* ***2012,*** *24, 840−853)*

1.5 Polymeric Nanoparticles for Drug Encapsulation

Another approach involves encapsulating drugs within polymeric nanoparticles via non-covalent interactions, such as Van der Waals forces, hydrogen bonding, and ionic interactions. These methods enable high drug-loading capacity while maintaining nanoparticle stability.[54,55] Ahmadi et al. This team developed a one-step method to synthesize urethane-activated monomers, creating block-polypeptides such as P(Glu-b-NADA) with varying hydrophilic/hydrophobic ratios. Among the synthesized polymers, a moderately hydrophobic variant demonstrated excellent stability and high drug-loading efficiency (4 wt%). These polymers formed 200 nm spherical nanoparticles and exhibited controlled drug release in skin-like pH conditions (5.5–6.5). Cytotoxicity studies showed the nanoparticles were biocompatible, causing no harm to HaCaT and HeLa cells at concentrations up to 1 mg/mL. This makes them a promising candidate for safe and effective drug delivery, particularly in

dermal applications.[56] These advances in polymeric materials illustrate the versatility and potential of these systems to improve drug delivery by enhancing therapeutic efficacy, reducing side effects, and enabling targeted or controlled release of drugs. Min Qiu and colleagues developed a nanoplatform utilizing PEG-b-poly(α-amino palmitic acid) block copolymers for precise anticancer drug delivery. Synthesized from α-amino palmitic acid N-carboxyanhydride (APA-NCA), these block copolymers self-assembled into stable polylipopeptide micelles (Lipep-Ms). The micelles demonstrated high efficiency in loading and releasing potent anticancer drugs such as docetaxel (DTX) within cancer cells, underscoring their potential as advanced drug delivery vehicles.[57]

1.6 Polymeric Nanocarriers for Drug Delivery

Polymeric nanocarriers are innovative systems designed to encapsulate and deliver therapeutic agents, such as small-molecule drugs, proteins, or nucleic acids, in a controlled and efficient manner. These nanoscale platforms enhance drug solubility, improve bioavailability, extend circulation times, and enable targeted delivery, reducing side effects while improving therapeutic outcomes. Common types of polymeric nanocarriers These nanoparticles, typically ranging in size from 10 to 500 nm, are composed of polymers like PLGA, PEG, or chitosan. They provide versatile options for encapsulating both hydrophobic and hydrophilic drugs, ensuring controlled release and drug protection. Polymeric Micelle Formed by the self-assembly of amphiphilic polymers in aqueous solutions, polymeric micelles feature a hydrophobic core and a hydrophilic shell. The hydrophobic core encapsulates poorly water-soluble drugs, while the hydrophilic shell provides stability in biological environments.

1.7 Polymer brushes

Polymer brushes grom Polymer brushes are assemblies of polymer chains that are tethered by one end to a surface, interface, or nanoparticle. These chains extend away from the surface into the surrounding medium, forming a brush-like structure. The unique arrangement of polymer brushes allows them to exhibit diverse properties, such as tunable wettability, lubricity, biocompatibility, and resistance to fouling. Polymer brushes can be synthesized using various techniques, including "grafting to" and "grafting from" methods as shown in Figure 1.9. The "grafting to" approach involves attaching pre-synthesized polymer chains to a surface,

while the "grafting from" method grows polymer chains directly from initiator sites on the substrate. Advances in polymerization techniques, such as atom transfer radical polymerization (ATRP)[58–60] and reversible addition–fragmentation chain-transfer (RAFT)[61] polymerization, have significantly improved the precision and functionality of polymer brushes. Applications of polymer brushes span numerous fields, including biomedical devices, drug delivery,[62–65] antifouling coatings,[66] attenuating cellular oxidative stress,[67,68] sensors, and nanotechnology.[69] Their ability to modify surface properties without altering the bulk material makes them an invaluable tool in modern material science and engineering.[70] Chun Feng et.al developed One-dimensional polymer brushes are promising templates for creating precise nanostructures, as their composition, backbone, side chain length, grafting density, and distribution can be finely tuned. Unlike linear copolymers, 1D polymer brushes enable versatile self-assembly, supporting the development of hierarchical nano- and microstructures for various applications. Furthermore, 2D and 3D polymer brushes integrate the functional properties of inorganic matrices, such as magnetic and electronic characteristics, with polymer attributes like responsiveness and antifouling as shown in Figure 1.10. These unique features make polymer brushes a highly versatile and innovative area of study with broad application potential.[71]

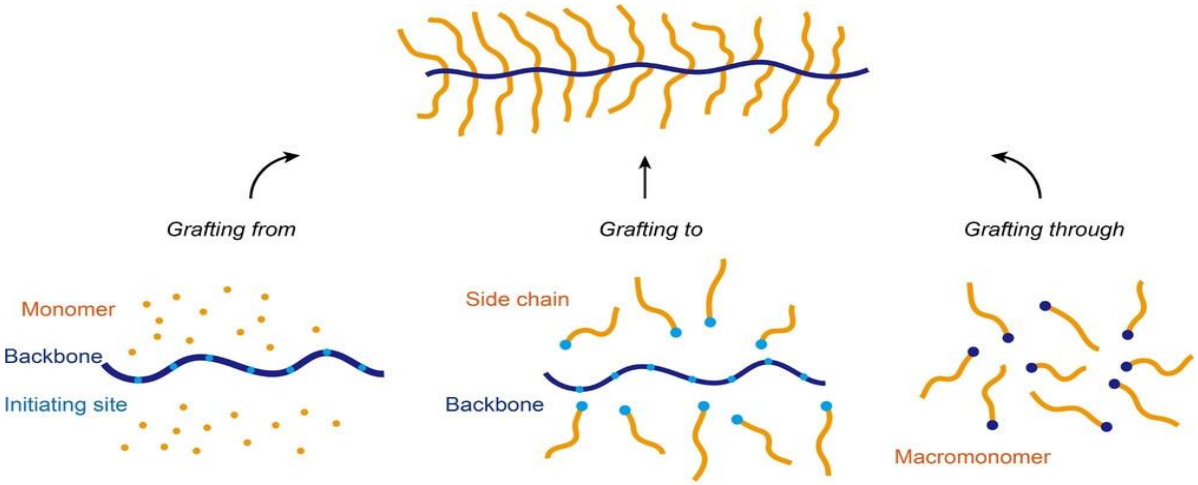

Figure 1.9 *Polymer brushes strategy like grafting from, grafting to, and grafting through.*

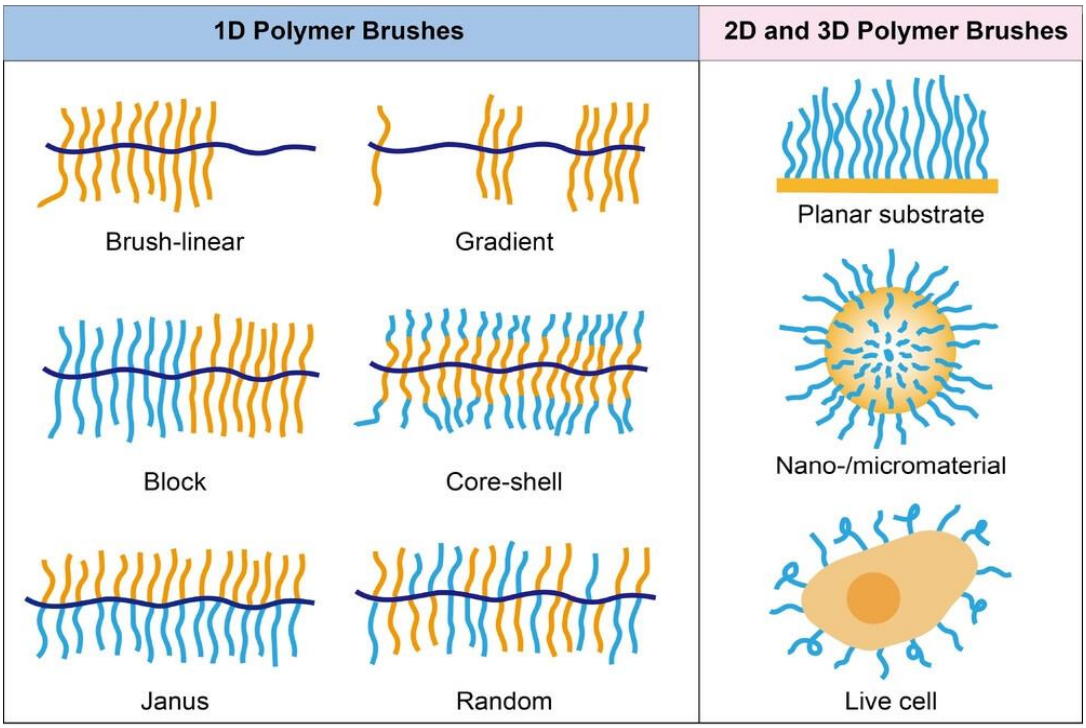

Figure 1.10 *polymer brushes different structure like linear 1D brush and with different molecular structures. (adapted from Acc. Chem. Res.* ***2018****, 51, 2314−2323)*

1.8 Stimuli responsive polymer brushes

Quing Yao et.al In this study, amphiphilic bottlebrush block copolymers were synthesized using ROMP of a hydrophilic macromonomer (NB-PEG16) and a post polymerization thio-bromo "click" reaction to incorporate a hydrophobic thiocresol (TC) moiety. The resulting PEG-PNB-TC copolymers self-assembled into micelles capable of encapsulating hydrophobic drugs like paclitaxel (PTX) and curcumin (CUR) see Figure 1.11. The copolymers and micelles were characterized for chemical structure, particle size, zeta potential, critical micelle concentration, stability, drug-polymer interactions, drug loading, and release profiles. Cellular uptake and cytotoxicity were evaluated in drug-sensitive cancer cells, and the codelivery potential was further assessed in multidrug-resistant cancer cells.[72] Here Yun Yu et.al developed a novel brush polymer-drug conjugate (BPDC), PLA-g-DOX/PEG, featuring a pH-sensitive Schiff base linkage for DOX delivery.[63,65,73] Unlike PLA-g-DOX nanoparticles, the water-soluble BPDC, with its brush-like architecture, functions directly as pegylated nanotherapeutics, offering improved clinical potential for sustained DOX delivery. This study covers synthesis, characterization, drug release, and in vitro evaluation of the BPDC.

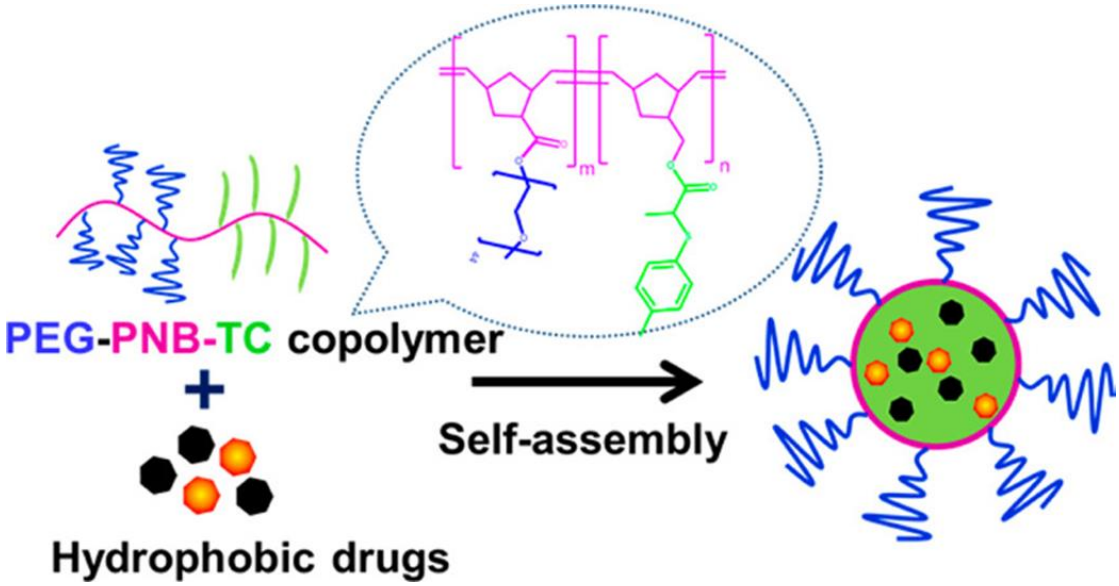

Figure 1.11 *Efficient Co-Delivery of Paclitaxel and Curcumin Using Novel Bottlebrush Copolymer-Based Micelles. (adapted from Quing Yao et.al Mol. Pharmaceutics* ***2017****, 14, 2378−2389).*

This study presents a straightforward method to synthesize bottlebrush polymers (PBs) with high grafting densities and evaluates their antifouling properties. PBs were prepared by grafting PEG modified with benzaldehyde (PEG-BA) or o-phthalaldehyde (PEG-OPA) onto polymer backbones to compare functional group effects on grafting efficiency. Results showed that PEG-OPA exhibited higher reactivity with amine groups, leading to improved grafting density and antifouling performance. To assess backbone rigidity, PBs with stiff backbones were synthesized using norbornenyl PEG methyl ether (NB-PEG) via ROMP. PB-OPA demonstrated reduced cell association and prolonged circulation time compared to PB-NB, highlighting backbone rigidity's influence on antifouling behavior see Figure 1.12. Additionally, PB-OPA showed excellent biocompatibility, effective tumor accumulation, and potential as a contrast agent for MRI applications.[74]

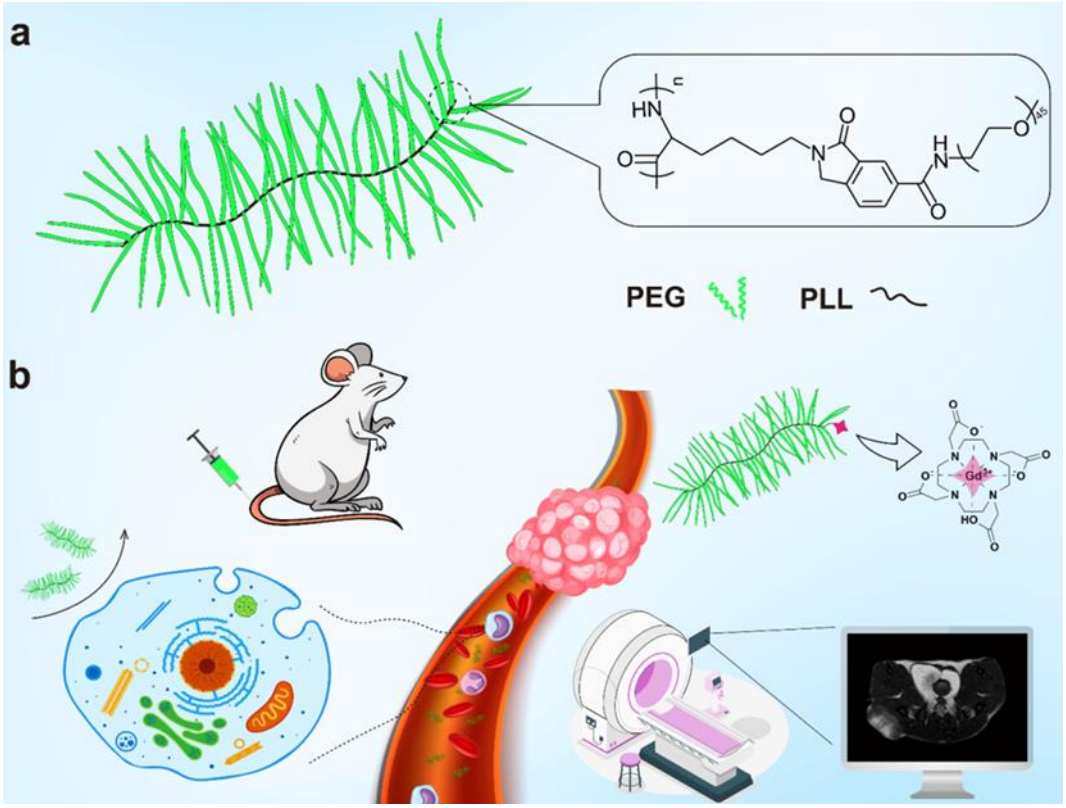

Figure 1.12 *PEG-OPA effective tumor accumulation, and potential as a contrast agent for MRI applications (adapted from Biomacromolecules* ***2024****, 25, 10, 6727–6736).*

Another study explored the shape-dependent aqueous assembly of nonionic bottlebrush block copolymer surfactants composed of hydrophilic poly(ethylene oxide) (PEO) and hydrophobic polylactide (PLA) branches. By varying the bottlebrush asymmetry through a modular synthetic approach, we investigated molecular shape-morphology relationships, resulting in highly uniform spherical and long cylindrical micelles, visualized by cryogenic transmission electron microscopy (cryo-TEM). These findings pave the way for designing tunable nanostructures see Figure 1.13. Additionally, PLA-PEO bottlebrush block copolymers are promising for biomedical applications due to the biodegradability of PLA and the biocompatibility of PEO, as shown in their linear copolymer counterparts.[75]

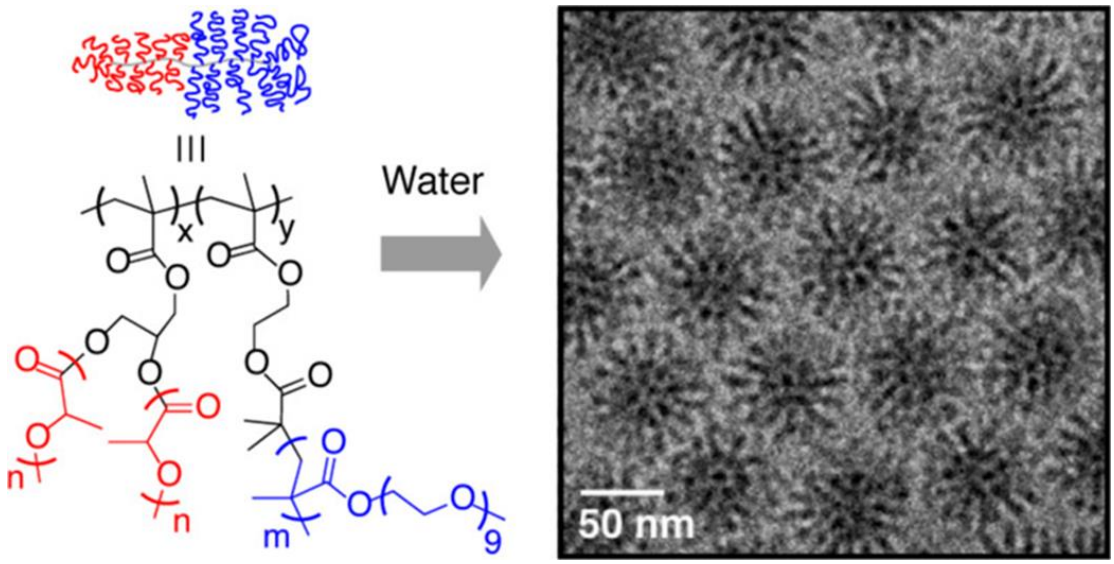

Figure 1.13 *Aqueous self-assembly of block copolymer brushes and tunable shape and size. (adapted from J. Am. Chem. Soc.* ***2014,*** *136, 21, 7762–7770).*

1.9 Sustainable Polymers in Drug Delivery

The use of sustainable polymers in drug delivery systems has gained significant attention due to their potential to enhance therapeutic outcomes while minimizing environmental impact. These polymers, derived from renewable or biocompatible resources,[76,77] offer unique properties such as biodegradability, biocompatibility, and tunable functionalities, making them ideal candidates for advanced drug delivery applications. Natural polymers like chitosan, alginate, and cellulose, as well as synthetic biobased polymers derived from renewable sources,[78,79] are increasingly being explored for designing drug carriers. These materials enable controlled and targeted drug release, reducing side effects and improving efficacy. Additionally, their ability to degrade into non-toxic byproducts aligns with the growing emphasis on sustainability in healthcare materials. Recent advances in polymer chemistry have facilitated the development of innovative drug delivery systems, including nanoparticles, hydrogels, and micelles, using sustainable polymers. These systems are designed to respond to physiological triggers, such as pH or temperature changes, ensuring precise drug release at the desired site. The integration of sustainable polymers in drug delivery is a promising step toward achieving environmentally responsible and patient-centered therapeutic solutions.

1.10 Polymer from Natural resources L-Amino acid:

L-amino acid-based polymers are a fascinating category of materials with significant potential in biomedical applications, particularly drug delivery. These polymers are derived from natural L-amino acids, the fundamental components of proteins, offering inherent biocompatibility and biodegradability. Additionally, they can be chemically tailored to meet specific drug delivery needs. Synthetic Peptides and Polypeptides L-amino acids are first transformed into polymerizable monomer units known as NCAs (N-carboxyanhydrides), which are subsequently subjected to ring-opening polymerization (ROP) using appropriate initiators to generate polypeptides as shown in Figure 1.14.

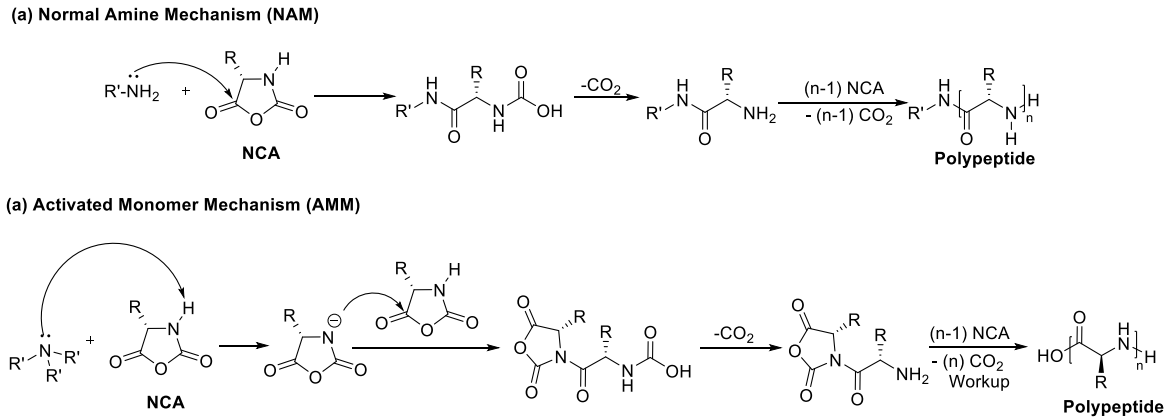

Figure 1.14 *NCA ring-opening polymerization (adapted from Polymers* ***2017****, 9(11), 551).*

This process enables the production of precisely defined di- and triblock synthetic polypeptides. These polypeptides exhibit a strong tendency to self-assemble into diverse nanostructures, such as micelles, vesicles, and fibrillar networks, which have attracted significant interest in biomedical and material science fields. Ifat Cohen Erez and team developed a nanoparticle platform using oppositely charged γ-PGA and cationic PFK peptides. These particles, referred to as PoP-NPs, are capable of delivering charged molecules, such as LND. Studies demonstrated core-shell assembly, cellular uptake via endocytosis, and localization near mitochondria, facilitating effective drug release. LND-loaded mPoP-NPs showed enhanced toxicity. Despite their favorable biocompatibility, challenges such as intracellular enzymatic degradation of high-molecular-weight polypeptides remain, potentially limiting their long-term applications in biomedical contexts.[80,81]

Nonpeptide Polymers from Amino Acids

To address some limitations, researchers have explored alternative polymers derived from amino acids, including poly(α-hydroxy acids),[82,83] poly(ester amides),[64,84] polyurethanes,[85] and poly(disulfide-urea-urethanes).[86,87] These materials exhibit excellent mechanical properties, biocompatibility, and biodegradability, making them highly suitable for a variety of medical and engineering applications. Poly(α-Hydroxy Acids) This class of polymers includes poly(lactide), poly(glycolide), and poly(lactide-co-glycolide), which are extensively used in biomedical applications such as resorbable sutures, implantable devices, and drug delivery systems. Functional polyesters can be synthesized from α-amino acids through methods such as polycondensation or ring-opening polymerization. For instance, Jianjun Cheng and colleagues synthesized polyesters using hydroxy acids derived from amino acids like leucine, phenylalanine, and methionine, employing p-toluenesulfonic acid as a catalyst. Alternative approaches, such as cyclic dimerization followed by ring-opening polymerization, allow for the creation of poly(α-hydroxy acids) with controlled molecular weights and precise chain structures. Poly(ester amides) Poly(ester amides) are a promising polymer class known for their exceptional mechanical strength, biocompatibility, and biodegradability. They are synthesized through ring-opening polymerization or polycondensation methods.[88] For example, Helder and colleagues synthesized poly(depsipeptides) (PDPs), alternating copolymers of α-amino acids and α-hydroxy acids, through ring-opening polymerization of morpholine-2,5-dione derivatives. These PDPs exhibit acid-catalyzed degradation into monomers. Chang-Xia Shi's research group developed PDPs from amino acids like glycine and leucine, using lipase-catalyzed ring-opening polymerization. Solution polycondensation remains another effective method for synthesizing poly(ester amides). Katasarawa et al pioneered this approach, which involves reacting di-toluenesulfonic acid salts of bis-α-(L-amino acid)-α,ω-alkylene diesters with activated carboxylic acids. More recently, Sun et al synthesized amino acid-based poly(ester-amides) via solution polycondensation, producing materials that degrade enzymatically and under reductive conditions. Their nanoparticles, loaded with doxorubicin, demonstrated high cytotoxicity in drug-resistant cancer cells, underscoring their potential for drug delivery.[89] Poly(disulfide-urethanes) Polymers like poly(disulfide-urethanes) incorporate both acetal and polyurethane units, exhibiting dual degradability in response to enzymatic and acidic conditions as shown in Figure 1.15. Zhiyuan Zhong and colleagues developed this class of polymers using lysine-

based isocyanate monomers and redox-responsive diols. These polymers form nano micelles suitable for drug delivery applications,[87] offering redox stimuli responsiveness.

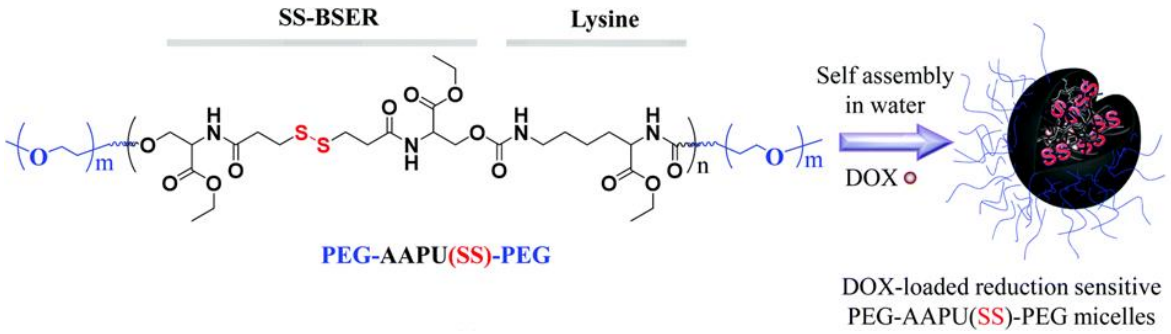

Figure 1.15 *Poly-disulphide urethane from lysine (Adapted from Polym. Chem., **2015**, 6, 6001–6010).*

L-amino acid-based polymers, both peptide-based and nonpeptide, represent a versatile platform for the development of advanced biomaterials. They combine tunable chemical properties with biocompatibility and degradability, making them valuable in drug delivery systems, tissue engineering, and biomedical devices. Continued research into polymerization techniques and material characterization will enable the design of innovative polymers with enhanced functionality and clinical relevance. Among stimuli-responsive polymers, a notable class involves amide-based repeating units synthesized from cystine, an amino acid. The synthesis begins with the conversion of cystine into its dimethyl ester, followed by coupling the amine and acid groups to produce polyamides containing disulfide bonds derived from the amino acid precursor. Tyrosine-Based Polycarbonates Tyrosine-based polycarbonates have also gained significant attention,[90] with Mathew L. Becker and colleagues reporting their application in biomaterial research. They investigated the effects of iodinated surfaces on osteoblast cell morphology using 2D thin films of poly(desaminotyrosyl tyrosine ethyl ester carbonate) (poly-DTE carbonate), its iodinated variant (poly(I2-DTE carbonate)), and several distinct blends. Their findings highlight the potential of these materials in biomedical applications, particularly in bone tissue engineering. In related research,[91] Chih-Chang Chu and collaborators demonstrated that tyrosine-based polycarbonates are not only biocompatible but also hold promise for drug delivery, including in cancer treatment. These polymers offer a unique combination of properties suitable for controlled therapeutic delivery. Enzyme-Catalyzed Synthesis of Polyesters Enzyme-catalyzed methods for synthesizing polyesters have

also been explored extensively. Recent advancements in this field have enabled the production of high molecular weight polyesters with helical chiral structures.[92] This improved enzymatic strategy provides a greener and more efficient approach to synthesizing complex polyesters for various biomedical and industrial applications as shown in Figure 1.16.

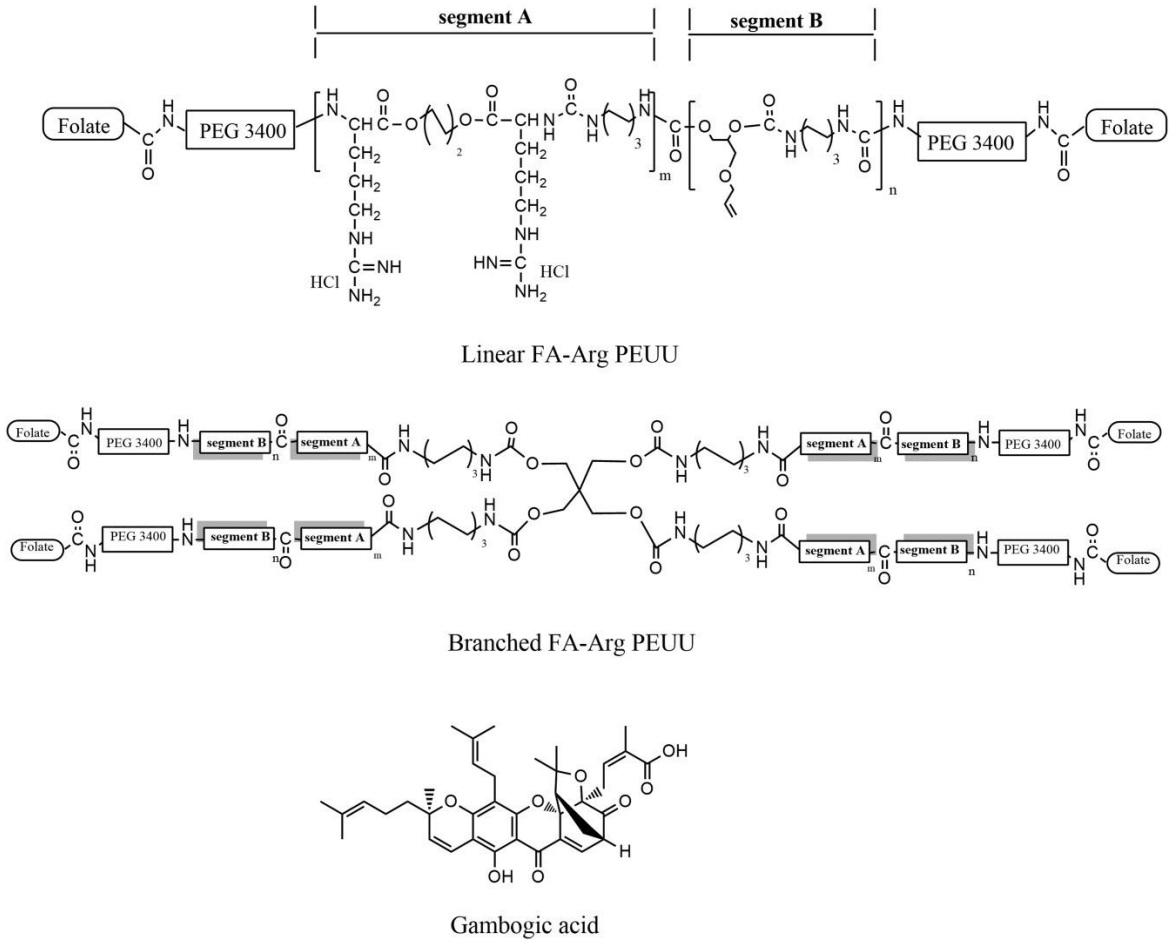

Figure 1.16 *Structure of linear and branched poly(ester-urethane)s (adapted from J Biomed Mater Res Part A: 105A: 475–490, 2017).*

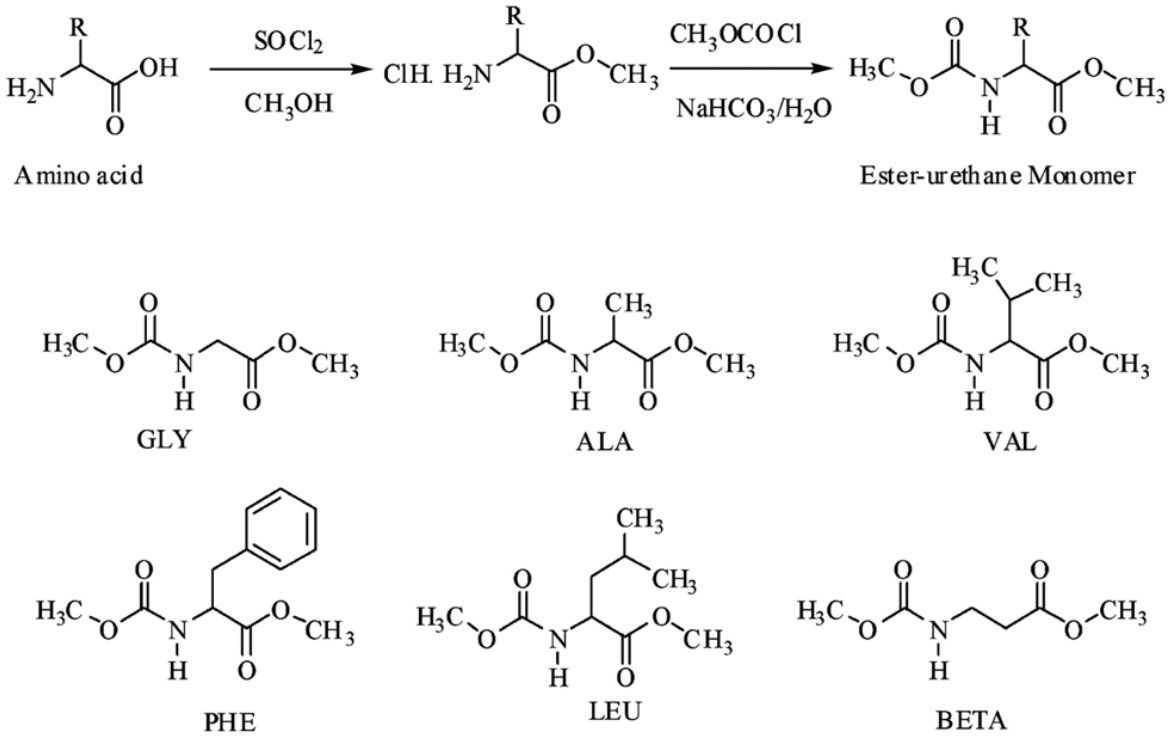

Figure 1.17 *Synthesis of dual ester-urethane monomers from L-amino acids via the melt polycondensation route. (Adapted from Biomacromolecules* ***2012****, 13, 2446−2455).*

Melt Polycondensation from Our lab

A novel solvent-free, non-isocyanate melt trans-urethane polycondensation approach for synthesizing aliphatic polyurethanes was pioneered by Deepa and collaborators. This method involves converting diamines into di-carbamate monomers, followed by melt polymerization with various diols in the presence of a titanium-based catalyst. The result is high molecular weight polyurethanes.[93–95] Building on this, Ananthraj et al. adapted the method to amino acids, enabling the synthesis of poly(ester urethane)s. This process begins with amino acids reacting with thionyl chloride and methanol to form amino acid methyl ester hydrochloride salts. These salts then react with methyl chloroformate to yield dual ester urethane monomers as shown in Figure 1.17. Melt polymerization of these monomers with equimolar amounts of diols occurs in a two-step process: initial reaction at 150 °C under nitrogen with 1 mol% catalyst, followed by high-vacuum treatment to form poly(ester urethane)s, which are purified through methanol precipitation to yield fibrous polymers.[96]The success of the polycondensation reaction is verified via NMR, which confirms the formation of ester and urethane linkages by comparing the polymer chain end groups. Reactivity studies

of the amino acid monomers show that steric hindrance at the carbonyl carbon reduces reactivity, leading to lower molecular weight polymers.

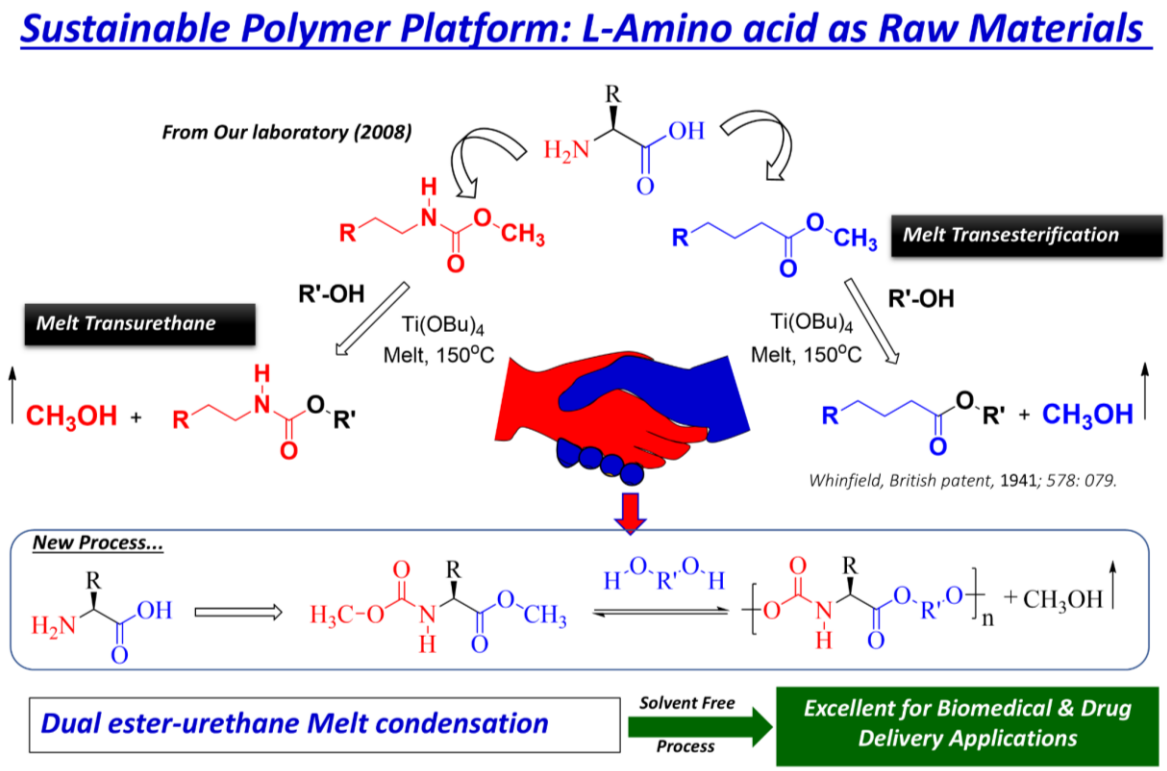

Figure 1.18 *Synthesis of poly(ester-urethane)s from L-amino acids via melt polycondensation.(adapted from Ananthraj et.al Adapted from Biomacromolecules* ***2012****, 13, 2446−2455).*

Experimental results further demonstrate temperature-dependent selectivity: at 120 °C, the ester groups undergo exchange reactions while urethane groups remain unreactive; at 150 °C, both groups exhibit exchange reactions see Figure 1.18. Mechanistic studies indicate that in the molten state, the hydroxyl group forms an active complex with [$Ti(OBu)_4$], which facilitates the carbonyl attack through a four-membered transition state. Density functional theory (DFT) calculations reveal that the lone pair on the urethane nitrogen interacts with the carbonyl carbon, increasing its electron density and reducing electrophilicity as shown in Figure 1.19. At higher temperatures, increased rotation disrupts this interaction, enabling reactivity.[97]

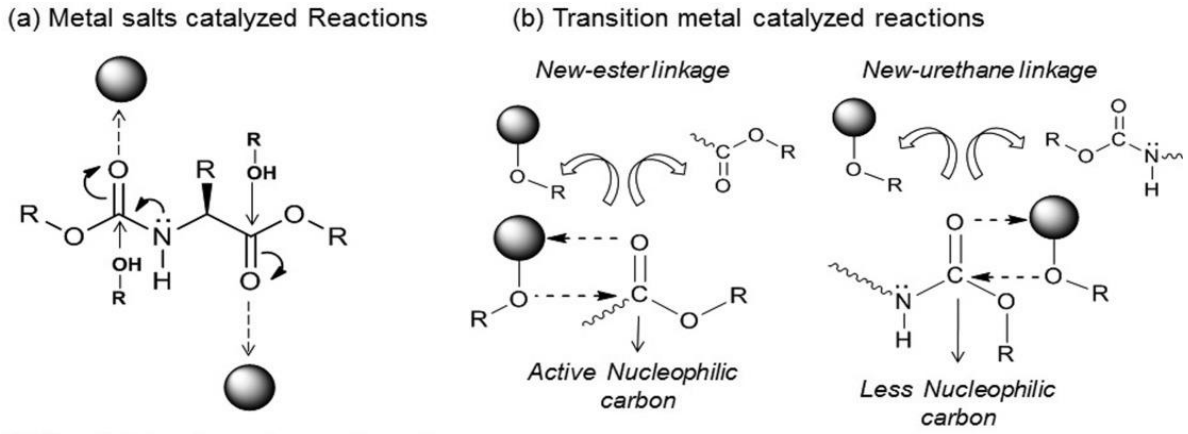

1.19 *Mechanism of melt polycondensation facilitated by a transition metal catalyst. (Adapted from J. Polym. Sci., Part A: Polym. Chem.* ***2016****, 54, 1065–1077).*

Catalyst efficiency was investigated across a range of metal, alkali-earth metal, transition metal, and lanthanide compounds.[98] Expanding this chemistry, L-cystine was employed as a precursor for redox-responsive polyesters. In this process, cystine's acid groups were converted into methyl esters, and the amine group was protected as Boc urethane. At 120°C, selective ester exchange reactions occurred, forming polyesters with disulfide linkages. Post-polymerization deprotection of the Boc group produced cationic polymers that self-assembled in aqueous solutions into charged nanoparticles. Degradation studies with dithiothreitol (DTT) confirmed the cleavage of disulfide bonds, resulting in monomer formation as verified by GPC and NMR.[99]

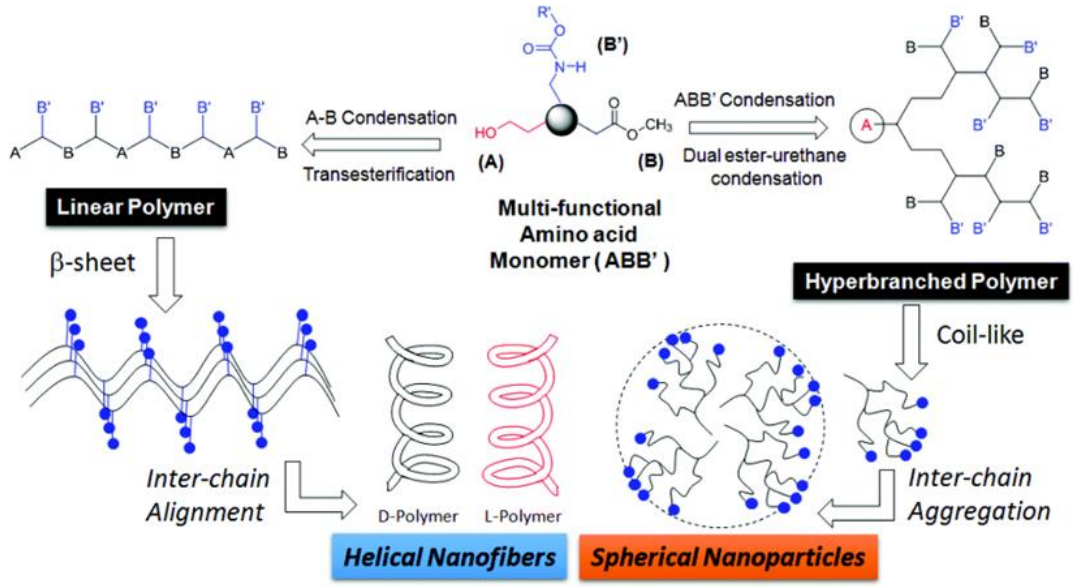

Figure 1.20 *The novel L-serine containing liner and hyperbranched polycondensation approach and their self-assembly. (Adapted from Rajendra et.al Polym. Chem.,* ***2015****, 6, 4641-4649).*

Rajendra extended melt polycondensation to multifunctional amino acids like D- and L-serine, L-threonine, and L-tyrosine, enabling the synthesis of linear and hyperbranched poly(ester urethane)s. A unique strategy leveraging the selective reactivity of ester and urethane groups facilitated the formation of ABB'-type monomers. At 120 °C, only the ester group reacted with hydroxyl groups, producing linear polymers as shown in Figure 1.20. At higher temperatures, both ester and urethane groups reacted, forming hyperbranched structures.[100] Tyrosine-based poly(ester urethane)s were further developed for drug delivery. Phenolic hydroxyl groups in tyrosine-derived monomers were modified with alkyl halides of varying chain lengths.

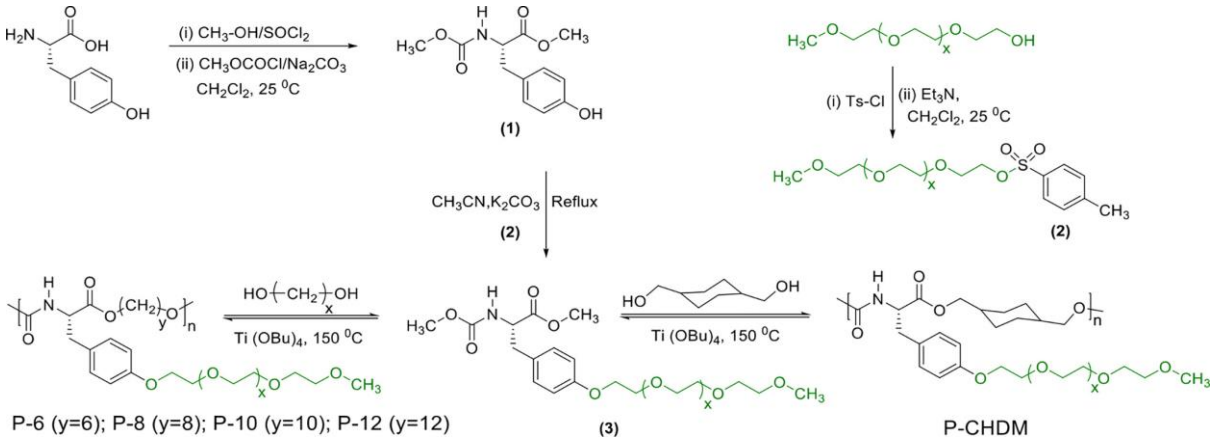

Figure 1.21 *Synthetic scheme of the poly(ester-urethane) s from L Tyrosine by melt condensation approach (Adapted from Biomacromolecules* ***2018****, 19, 2166−2181).*

Polymerization with polyethylene glycol (PEG) diols produced amphiphilic polymers with aliphatic side chains as hydrophobic components and PEG as the hydrophilic segment. These polymers self-assembled into nanoparticles (~200 nm) in aqueous solutions, demonstrating drug encapsulation capabilities. In one system, polymers with C16 alkyl chains and PEG 400 exhibited well-defined amphiphilicity.[101] Another system utilized multifunctional amphiphilic assemblies for cancer drug delivery, incorporating diols like 1,4-cyclohexanedimethanol, 1,6-hexanediol, and 1,12-dodecanediol, with thermoresponsive behavior (LCST 32–50°C) dependent on diol length.[102] as shown in Figure 1.21. Further advancements by Sonashree et al. involved enzyme and pH-responsive nanocarriers synthesized from L-aspartic acid via melt polycondensation. L-aspartic acid was transformed into multifunctional monomers with methyl ester and Boc urethane groups. These monomers underwent thermoselective copolymerization with triethylene glycol and dodecanediol, yielding amphiphilic copolymers with diverse

applications in drug delivery. These amphiphilic polymers have a notable ability to self-assemble into core-shell nanoparticles when dispersed in aqueous solutions. These nanoparticles are highly effective at encapsulating multiple anticancer drugs, including Topotecan, Doxorubicin, and Curcumin. Their biodegradability, which is influenced by enzymatic and pH conditions, is attributed to the polyester backbone and the presence of Boc urethane side groups. Comprehensive studies on their cellular uptake and cytotoxicity have been conducted using cervical (HeLa) and breast (MCF-7) cancer cell lines. The results highlight the nanoparticles' efficiency in intracellular drug delivery, leading to a significant cytotoxic effect.

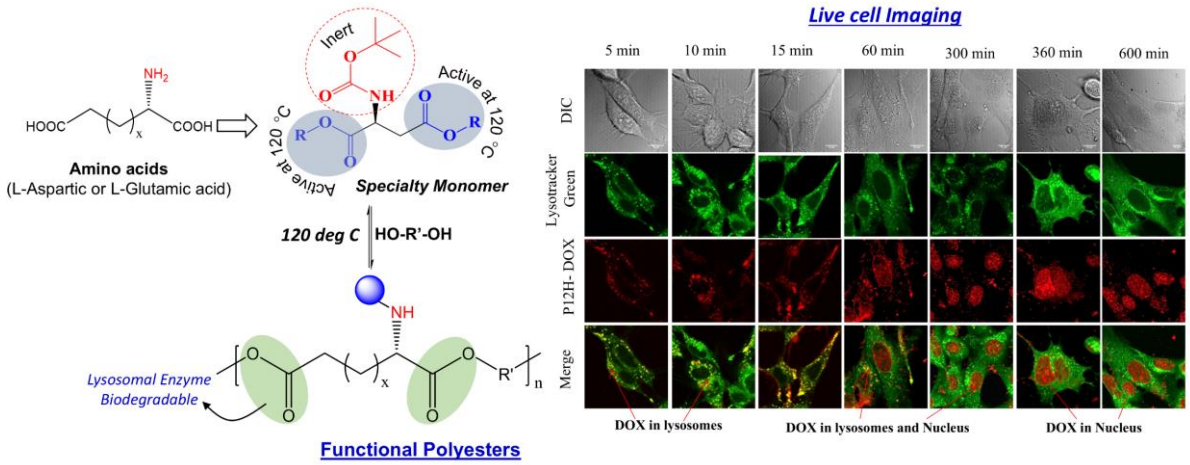

Figure 1.22 *PH responsive polymer for anticancer doxorubicin drug delivery in cancer cell real-time monitoring (adapted from Sonashree et al. J. Polym. Sci., Part A: Polym. Chem.* ***2016****, 54, 3279–3293).*

pH-responsive polymers are widely utilized in drug delivery and anticancer applications due to their ability to release therapeutic agents in response to specific pH changes in the target environment.[103] see Figure 1.22. Additionally, L-aspartic acid-based monomers were copolymerized with triethylene glycol, dodecanediol, and oligo-phenylenevinylene (OPV) diols via melt polymerization, yielding amphiphilic polymers functionalized with fluorophores. These polymers demonstrate self-assembly in aqueous environments driven by π-π stacking, forming blue luminescent nanoparticles approximately 200 nm in size. The fluorescent nanoparticles encapsulate Nile red as a model drug, as shown in Figure 1.23. establishing a fluorescence resonance energy transfer (FRET) system, where OPV fluorophores act as donors and Nile red as the acceptor.[104]

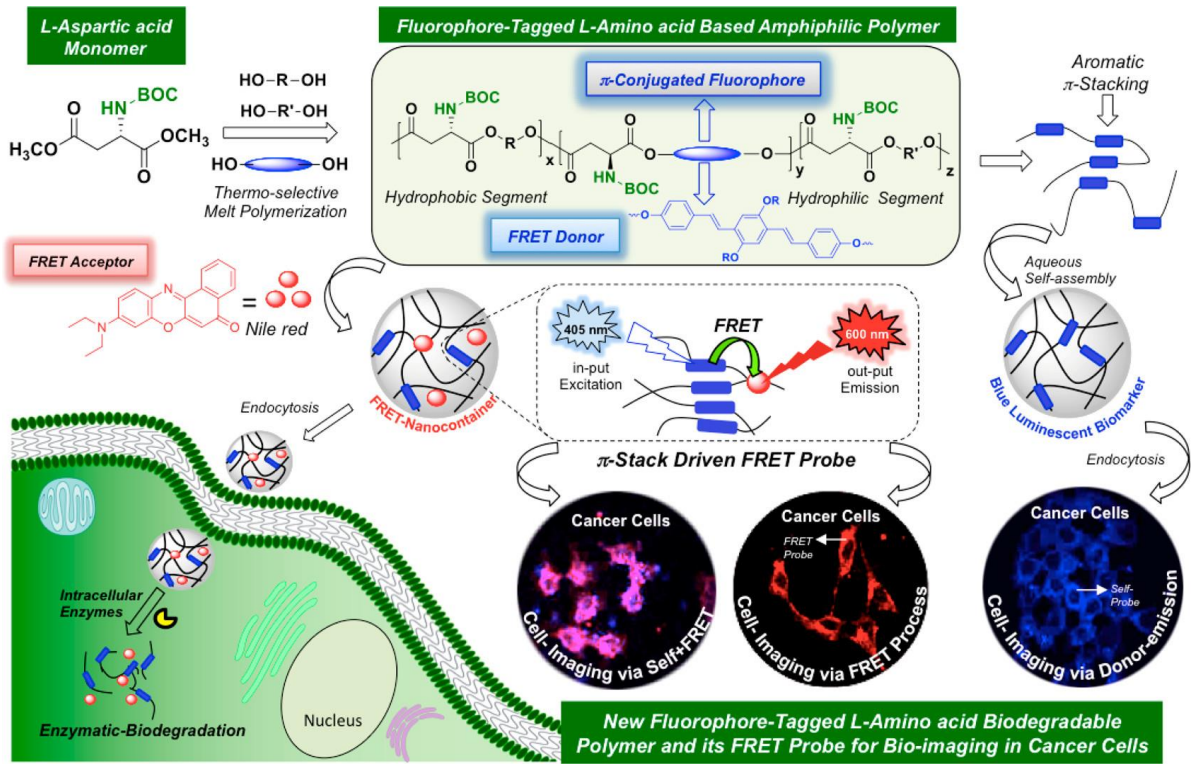

Figure 1.23 *An enzyme-responsive π-conjugated fluorophore-tagged L-aspartic acid polyester and its FRET probe have been developed for bioimaging at the intracellular level. (adapted from Biomacromolecules* ***2017****, 18, 2594–2609).*

Hydroxyl-functionalized polyesters were synthesized using L-aspartic acid as a precursor. A multifunctional monomer was designed by incorporating acetal-protected groups and dicarboxylic esters. Transesterification of this monomer with various commercially available diols under melt conditions produced acetal-functionalized polyesters. Acid-catalyzed deprotection yielded hydroxyl-functionalized polymers with two hydroxyl groups per repeat unit. These hydroxyl-functionalized polyesters were utilized to create nanoassemblies for drug delivery applications targeting cancer cells[105] as shown in Figure 1.24. Dheeraj et al. further advanced melt polycondensation strategies to develop polyurethanes from L-lysine. In this approach, a di-urethane monomer was designed by converting the two amino groups of L-lysine into urethanes and the acid group into an amide. Polymerization at 150 °C produced a new class of amphiphilic polyurethanes capable of forming nanoparticles in aqueous solutions. These nanoparticles successfully encapsulated Doxorubicin (DOX).

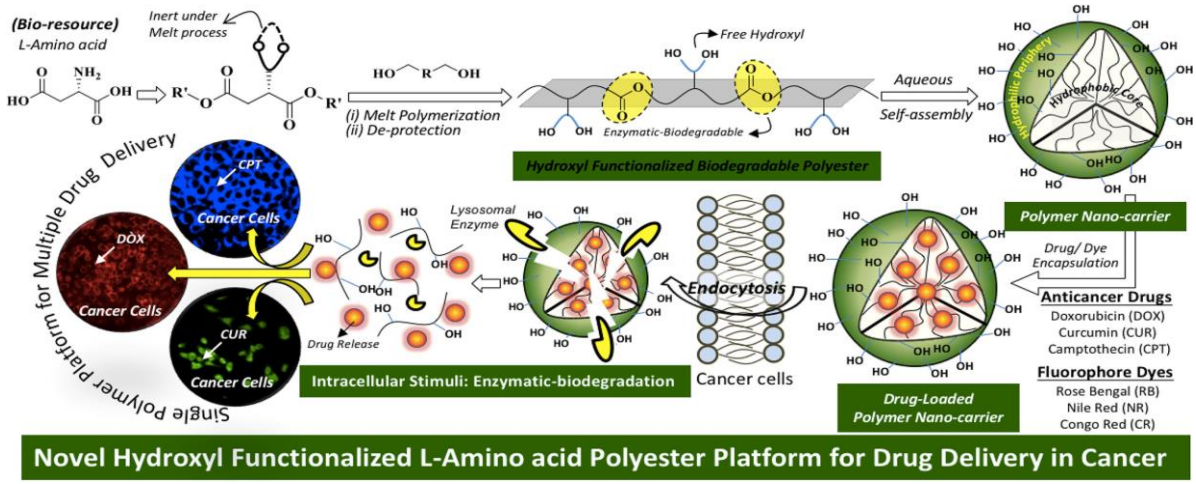

Figure 1.24 *Novel hydroxyl functionalized L-amino acid-based polyester for anticancer drug delivery. (adapted from Sonashree et al. Biomacromolecules* ***2020****, 21, 171−187).*

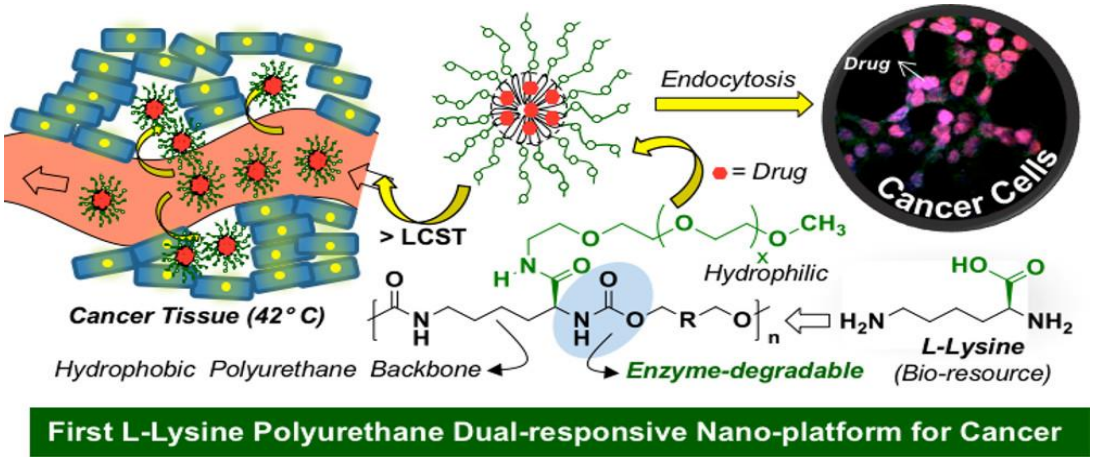

Figure 1.25 *L-Lysine-based dual responsive drug delivery for cancer research. (Adapted from Dheeraj et.al ACS Appl. Polym. Mater.* ***2019,*** *1, 7, 1866–1880).*

The polymers exhibited thermoresponsive behavior, transitioning from transparent to turbid solutions at a specific lower critical solution temperature (LCST) of 40–42 °C, as determined through variable-temperature transmittance studies. Biocompatibility assessments confirmed that the nanoparticles were suitable for use with both normal and cancerous cell lines, effectively delivering drugs to cancer cells. Drug release kinetics from DOX-loaded nanoparticles were analyzed at or above the LCST using dialysis, revealing controlled release profiles[85] see Figure 1.25. In another study, Dheeraj et al. developed poly(ester urethane)s functionalized with phenol and catechol groups using Tyrosine and L-Dopa amino acids as building blocks. This work demonstrated the significance of π-π stacking and hydrogen bonding in stabilizing drug molecules within the polymeric nanoparticles. These interactions

enhanced the stability and drug-loading efficiency of the nanoparticles, providing an effective platform for targeted drug delivery systems.

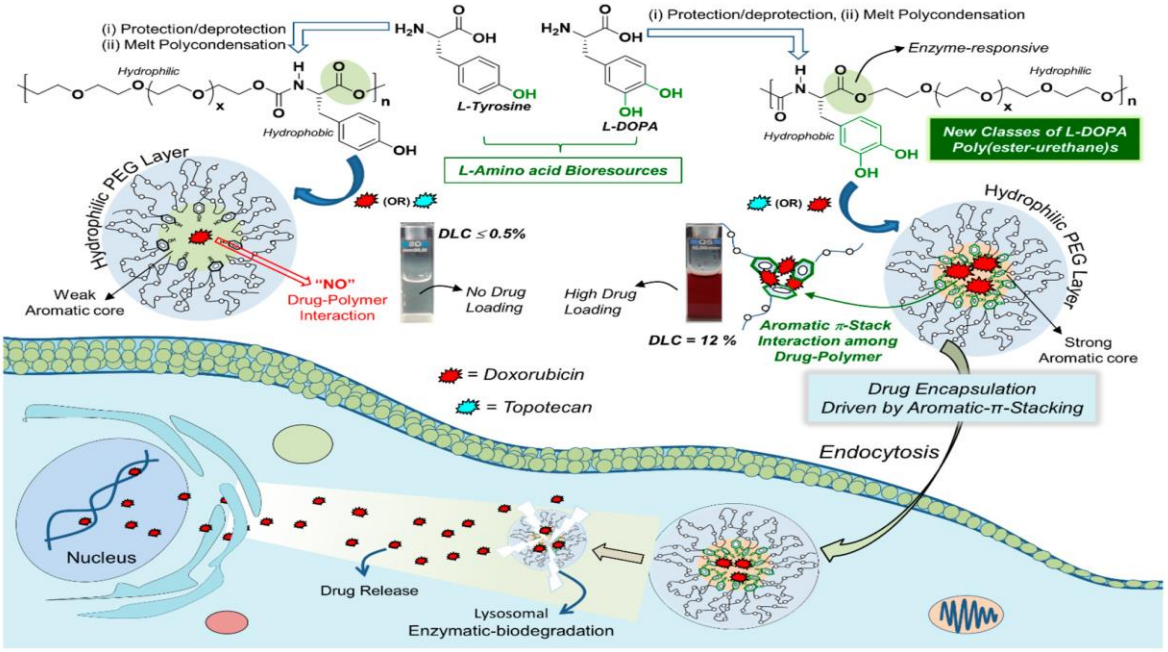

Figure 1.26 *aromatic-II stacking drug delivery from the amino acid-based platform (adapted from Dheeraj et.al ACS Appl. Bio Mater.* ***2022,*** *5, 11, 5432–5444).*

After the formation of an L-dopa-based polymer, it self-assembles in an aqueous medium to form spherical nanoparticles. These polymers were capable of encapsulating the anticancer drug Dox in its larger number of drugs. This dopa catechol unit is crucial. This work demonstrated the significance of π-π stacking and hydrogen bonding in stabilizing drug molecules within the polymeric nanoparticle cavity. These interactions enhanced the stability and drug-loading efficiency of the nanoparticles, providing an effective platform for targeted drug-delivery systems[106] see Figure 1.26. In another example is that Khuddus et al. developed an innovative polyester platform functionalized with amides, utilizing L-amino acids, particularly L-aspartic acid, as key building blocks to achieve this, diester monomers with diverse amide-functionalized side chains, including aromatic, aliphatic, and bio-derived pendant units, was meticulously designed and synthesized. This aspartic acid monomer incorporated PEG as a side chain. Further; these custom-designed monomers underwent

solvent-free melt polycondensation, resulting in high molecular weight polyesters with adjustable thermal properties.

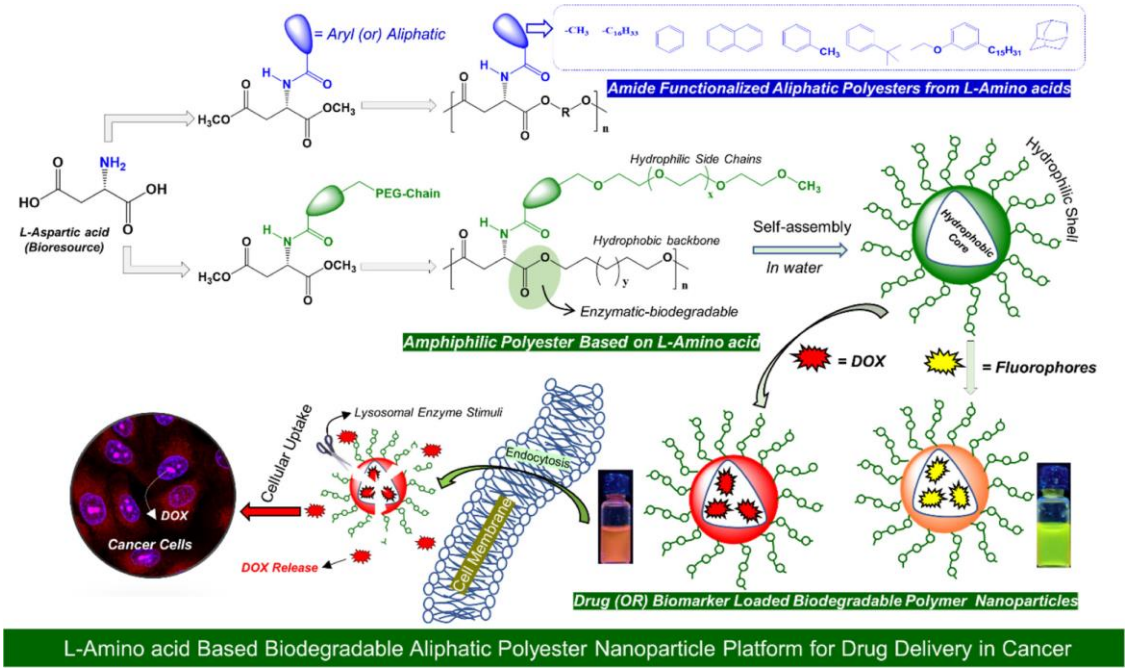

Figure 1.27 *L-amino acid-based aliphatic polyester platform for drug delivery in cancer (adapted from Khuddus et.al Biomacromolecules* ***2023****, 24, 6, 2643–2660).*

The synthesized amphiphilic polyesters exhibited self-assembly behavior in aqueous environments, forming spherical nanoparticles with an average size of 140 ± 10 nm. These nanoparticles demonstrated a lower critical solution temperature (LCST) in the range of 40–42°C. Their versatility was evident in their ability to encapsulate various therapeutic and diagnostic agents, such as the anticancer drug doxorubicin (DOX), the anti-inflammatory compound curcumin (CUR), and biomarkers like Rose Bengal (RB) and 8-hydroxypyrene-1,3,6-trisulfonic acid trisodium salt (HPTS). While the nanoparticles remained stable under extracellular conditions, they underwent enzymatic degradation when exposed to horse liver esterase in phosphate-buffered saline (PBS). cellular uptake of DOX-loaded nanoparticles, revealing their successful internalization and subsequent enzymatic degradation inside cells. It is used for drug delivery applications[107] as shown in Figure 1.27.

1.11 Aim of my thesis

With the aforementioned literature review, it was comprehended that polymeric nanocarriers are one of the most suitable choices for the drug delivery and theranostic application. However, most of the nanocarrier systems reported in the literature are composed of non-biodegradable polymeric systems; therefore, their degradation and toxicities are of major concern. To overcome these limitations, nanocarriers composed of fully biodegradable materials are urgently needed to be developed and investigated in preclinical trials. For that purpose, one of the best choices is to use bioresource-based substrates such as amino acids. Therefore, we have developed a strategy to use the amino acid-based monomer for condensation polymerization to yield poly(ester-urethane)s which are fully biodegradable polymers. The main aim of my thesis work is to design and validate amino acid-based polymers for drug delivery applications. Figure 1.28 shows the diagrammatic representation of my overall work. My thesis divided into three working chapter and brief outline is given below.

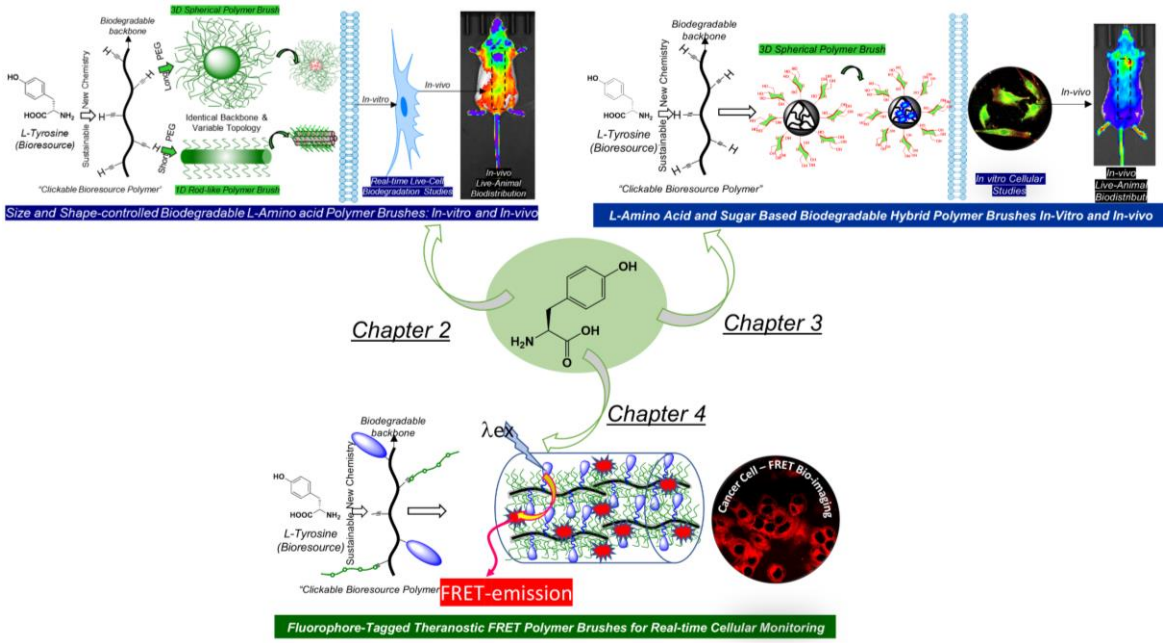

Figure 1.28 *Consolidated work of my thesis in schematic representation.*

Chapter 2: Development of size and shape-controlled polymer brushes based on L-amino acid bioresource and study of the role of polymer topology on the enzymatic-biodegradation and deep-tissue penetration under in-vitro and in-vivo. A designed monomer made from L-tyrosine was polymerized using a solvent-free process to produce hydrophobic, biodegradable poly(ester-urethane)s that can be further modified through click chemistry by changing the

lengths of PEG-azides in the reaction, we designed two types of polymer brushes: one-dimensional rod-like and three-dimensional spherical structures. In-vitro studies showed that rod-like brushes work better than spherical ones, as they are absorbed by cells more quickly, break down efficiently in endo-lysosomal compartments, and deliver DOX to the cell nucleus. In vivo bioimaging of tissue slices confirmed their ability to penetrate deeply.

Chapter 3: To Design and Development of L-Tyrosine Sugar Hybrid Biodegradable Polymer Brushes for fine-tuning their Thermoplastic application as well as to encapsulate various cargos to deliver into cancer cells and in-vivo biodistribution. These sugar polymer brushes showed higher glass transition temperature ($T_g \geq 107$ °C) as compared to their homopolymer, and they can used for thermoplastic application. Further, the drug-loaded polymer brushes showed comparable cytotoxicity as a free drug in the cancerous cell line MCF-7 as well as the HEK-293 cell line. In vivo, biodistribution studies showed that ICG-loaded nanoparticles demonstrated prolonged nanoparticle retention compared to free ICG.

Chapter 4: Development of CUM Fluorophore-Tagged Polymer Brushes for Cellular FRET-Based theragnostic Application in cancer cells. The cargo (Nile red) loaded nanoparticle brushes interact with a fluorophore-tagged polymer to monitor the FRET phenomena in the nanocarrier. The CUM Donar molecule transfers its excitation energy to acceptor molecules confirming the FRET. The fixed cell imaging only CUM polymer brushes were excited at 405 nm using confocal laser scanning microscopy (CLSM), and we found out that the indeed rod-like polymer brushes showed better uptake as compared to Sphere-like polymer brushes.

All the polymers based on L-tyrosine poly(ester-urethane)s, depicted excellent applications as drug delivery carriers in vitro and in vivo through detailed investigation. And these materials offer promising applications in biomedical applications, such as targeted drug delivery, theranostic, bioimaging, and biodistribution.

1.12 References

(1) Kamaly, N.; Yameen, B.; Wu, J.; Farokhzad, O. C. Degradable Controlled-Release Polymers and Polymeric Nanoparticles: Mechanisms of Controlling Drug Release. *Chemical Reviews*. American Chemical Society February 24, 2016, pp 2602–2663.

(2) Sung, H.; Ferlay, J.; Siegel, R. L.; Laversanne, M.; Soerjomataram, I.; Jemal, A.; Bray, F. Global Cancer Statistics 2020: GLOBOCAN Estimates of Incidence and Mortality Worldwide for 36 Cancers in 185 Countries. *CA Cancer J Clin* **2021**, *71* (3), 209–249.

(3) Silberschmidt, G. The World Health Organization and Global Health. In *Handbook of Global Health*; Springer International Publishing: Cham, 2021; pp 1–47.

(4) White, M. C.; Holman, D. M.; Boehm, J. E.; Peipins, L. A.; Grossman, M.; Jane Henley, S. Age and Cancer Risk. *Am J Prev Med* **2014**, *46* (3), S7–S15.

(5) Gill, E.; Perks, C. M. Mini-Review: Current Bladder Cancer Treatment—The Need for Improvement. *Int J Mol Sci* **2024**, *25* (3), 1557.

(6) Bray, F.; McCarron, P.; Parkin, D. M. The Changing Global Patterns of Female Breast Cancer Incidence and Mortality. *Breast Cancer Research*. November 2004, pp 229–239.

(7) Hassanpour, S. H.; Dehghani, M. Review of Cancer from Perspective of Molecular. *Journal of Cancer Research and Practice* **2017**, *4* (4), 127–129.

(8) Bray, F.; Laversanne, M.; Sung, H.; Ferlay, J.; Siegel, R. L.; Soerjomataram, I.; Jemal, A. Global Cancer Statistics 2022: GLOBOCAN Estimates of Incidence and Mortality Worldwide for 36 Cancers in 185 Countries. *CA Cancer J Clin* **2024**, *74* (3), 229–263.

(9) Ahmad, M. F.; Ahmad, F. A.; Alsayegh, A. A.; Zeyaullah, Md.; AlShahrani, A. M.; Muzammil, K.; Saati, A. A.; Wahab, S.; Elbendary, E. Y.; Kambal, N.; Abdelrahman, M. H.; Hussain, S. Pesticides Impacts on Human Health and the Environment with Their Mechanisms of Action and Possible Countermeasures. *Heliyon* **2024**, *10* (7), e29128.

(10) Song, M.; Liu, N.; He, L.; Liu, G.; Ling, D.; Su, X.; Sun, X. Porous Hollow Palladium Nanoplatform for Imaging-Guided Trimodal Chemo-, Photothermal-, and Radiotherapy. *Nano Res* **2018**, *11* (5), 2796–2808.

(11) Virmani, T.; Kumar, G.; Sharma, A.; Pathak, K.; Akhtar, M. S.; Afzal, O.; Altamimi, A. S. A. Amelioration of Cancer Employing Chitosan, Its Derivatives, and Chitosan-Based Nanoparticles: Recent Updates. *Polymers*. Multidisciplinary Digital Publishing Institute (MDPI) July 1, 2023.

(12) Tang, S.; Chen, M.; Zheng, N. Multifunctional Ultrasmall Pd Nanosheets for Enhanced Near-Infrared Photothermal Therapy and Chemotherapy of Cancer. *Nano Res* **2015**, *8* (1), 165–174.

(13) Kawish, S. M.; Sharma, S.; Gupta, P.; Ahmad, F. J.; Iqbal, M.; Alshabrmi, F. M.; Anwer, M. K.; Fathi-karkan, S.; Rahdar, A.; Aboudzadeh, M. A. Nanoparticle-Based Drug Delivery Platform for Simultaneous Administration of Phytochemicals and

Chemotherapeutics: Emerging Trends in Cancer Management. *Particle and Particle Systems Characterization*. John Wiley and Sons Inc December 1, 2024.

(14) Poilil Surendran, S.; Moon, M. J.; Park, R.; Jeong, Y. Y. Bioactive Nanoparticles for Cancer Immunotherapy. *Int J Mol Sci* **2018**, *19* (12), 3877.

(15) Zugazagoitia, J.; Guedes, C.; Ponce, S.; Ferrer, I.; Molina-Pinelo, S.; Paz-Ares, L. Current Challenges in Cancer Treatment. *Clinical Therapeutics*. Excerpta Medica Inc. July 1, 2016, pp 1551–1566.

(16) Baker, K. E.; Wilson, L. M.; Sharma, R.; Dukhanin, V.; McArthur, K.; Robinson, K. A. Hormone Therapy, Mental Health, and Quality of Life Among Transgender People: A Systematic Review. *J Endocr Soc* **2021**, *5* (4).

(17) Wang, K.; Tepper, J. E. Radiation Therapy-associated Toxicity: Etiology, Management, and Prevention. *CA Cancer J Clin* **2021**, *71* (5), 437–454.

(18) Nitiss, J. L. Targeting DNA Topoisomerase II in Cancer Chemotherapy. *Nat Rev Cancer* **2009**, *9* (5), 338–350.

(19) Dana, H.; Chalbatani, G. M.; Jalali, S. A.; Mirzaei, H. R.; Grupp, S. A.; Suarez, E. R.; Rapôso, C.; Webster, T. J. CAR-T Cells: Early Successes in Blood Cancer and Challenges in Solid Tumors. *Acta Pharm Sin B* **2021**, *11* (5), 1129–1147.

(20) Abdellatif, A. A. H.; Alshubrumi, A. S.; Younis, M. A. Targeted Nanoparticles: The Smart Way for the Treatment of Colorectal Cancer. *AAPS PharmSciTech*. Springer Science and Business Media Deutschland GmbH January 1, 2024.

(21) WONG, H.; BENDAYAN, R.; RAUTH, A.; LI, Y.; WU, X. Chemotherapy with Anticancer Drugs Encapsulated in Solid Lipid Nanoparticles☆. *Adv Drug Deliv Rev* **2007**, *59* (6), 491–504.

(22) Mohajer, F.; Mirhosseini-Eshkevari, B.; Ahmadi, S.; Ghasemzadeh, M. A.; Mohammadi Ziarani, G.; Badiei, A.; Farshidfar, N.; Varma, R. S.; Rabiee, N.; Iravani, S. Advanced Nanosystems for Cancer Therapeutics: A Review. *ACS Appl Nano Mater* **2023**, *6* (9), 7123–7149.

(23) Yin, P. T.; Pongkulapa, T.; Cho, H.-Y.; Han, J.; Pasquale, N. J.; Rabie, H.; Kim, J.-H.; Choi, J.-W.; Lee, K.-B. Overcoming Chemoresistance in Cancer via Combined MicroRNA Therapeutics with Anticancer Drugs Using Multifunctional Magnetic Core–Shell Nanoparticles. *ACS Appl Mater Interfaces* **2018**, *10* (32), 26954–26963.

(24) Pelaz, B.; Alexiou, C.; Alvarez-Puebla, R. A.; Alves, F.; Andrews, A. M.; Ashraf, Wolfgang J. Parak. Diverse application of nanomedicine. *ACS Nano* **2017**, *11* (3), 2313–2381.

(25) Riehemann, K.; Schneider, S. W.; Luger, T. A.; Godin, B.; Ferrari, M.; Fuchs, H. Nanomedicine - Challenge and Perspectives. *Angewandte Chemie - International Edition*. January 19, 2009, pp 872–897.

(26) Lang, J.; Zhao, X.; Wang, X.; Zhao, Y.; Li, Y.; Zhao, R.; Cheng, K.; Li, Y.; Han, X.; Zheng, X.; Qin, M.; Shi, J.; Anderson, G. J.; Hao, J.; Ren, H.; Nie, G. Targeted Co-Delivery of the Iron Chelator Deferoxamine and a HIF1α Inhibitor Impairs Pancreatic Tumor Growth. *ACS Nano* **2019**, *13* (2), 2176–2189.

(27) Tang, S.; Hang, Y.; Ding, L.; Tang, W.; Yu, A.; Zhang, C.; Sil, D.; Xie, Y.; Oupický, D. Intraperitoneal SiRNA Nanoparticles for Augmentation of Gemcitabine Efficacy in the Treatment of Pancreatic Cancer. *Mol Pharm* **2021**, *18* (12), 4448–4458.

(28) Wang, L.-C.; Chang, L.-C.; Su, G.-L.; Chang, P.-Y.; Hsu, H.-F.; Lee, C.-L.; Li, J.-R.; Liao, Yeh, C.-S. Chemical Structure and Shape Enhance MR Imaging-Guided X-Ray Therapy Following Marginative Delivery. *ACS Appl Mater Interfaces* **2022**, *14* (11), 13056–13069.

(29) Xu, C.; Sun, Y.; Yu, Y.; Hu, M.; Yang, C.; Zhang, Z. A Sequentially Responsive and Structure-Transformable Nanoparticle with a Comprehensively Improved 'CAPIR Cascade' for Enhanced Antitumor Effect. *Nanoscale* **2019**, *11* (3), 1177–1194.

(30) Si, J.; Shao, S.; Shen, Y.; Wang, K. Macrophages as Active Nanocarriers for Targeted Early and Adjuvant Cancer Chemotherapy. *Small* **2016**, *12* (37), 5108–5119.

(31) Sun, Q.; Zhou, Z.; Qiu, N.; Shen, Y. Rational Design of Cancer Nanomedicine: Nanoproperty Integration and Synchronization. *Advanced Materials*. Wiley-VCH Verlag April 11, 2017.

(32) Pearce, A. K.; O'Reilly, R. K. Insights into Active Targeting of Nanoparticles in Drug Delivery: Advances in Clinical Studies and Design Considerations for Cancer Nanomedicine. *Bioconjug Chem* **2019**, *30* (9), 2300–2311.

(33) Beach, M. A.; Nayanathara, U.; Gao, Y.; Zhang, C.; Xiong, Y.; Wang, Y.; Such, G. K. Polymeric Nanoparticles for Drug Delivery. *Chemical Reviews*. American Chemical Society May 8, 2024, pp 5505–5616.

(34) Peer, D. Harnessing RNAi Nanomedicine for Precision Therapy. *Mol Cell Ther* **2014**, *2* (1), 5. https://doi.org/10.1186/2052-8426-2-5.

(35) Peer, D.; KarP, J. M.; Hong, S.; faroKHzaD, oMiD C.; Margalit, riMona; langer, robert. *Nanocarriers as an Emerging Platform for Cancer Therapy*; 2007.

(36) Cheng, L.; Yu, J.; Hao, T.; Wang, W.; Wei, M.; Li, G. Advances in Polymeric Micelles: Responsive and Targeting Approaches for Cancer Immunotherapy in the Tumor Microenvironment. *Pharmaceutics* **2023**, *15* (11), 2622.

(37) Wan, D.; Li, C.; Pan, J. Polymeric Micelles with Reduction-Responsive Function for Targeted Cancer Chemotherapy. *ACS Appl Bio Mater* **2020**, *3* (2), 1139–1146.

(38) Miller, T.; Hill, A.; Uezguen, S.; Weigandt, M.; Goepferich, A. Analysis of Immediate Stress Mechanisms upon Injection of Polymeric Micelles and Related Colloidal Drug Carriers: Implications on Drug Targeting. *Biomacromolecules*. June 11, 2012, pp 1707–1718.

(39) Cabral, H.; Kataoka, K. Progress of Drug-Loaded Polymeric Micelles into Clinical Studies. *Journal of Controlled Release* **2014**, *190*, 465–476.

(40) Wang, C. E.; Wei, H.; Tan, N.; Boydston, A. J.; Pun, S. H. Sunflower Polymers for Folate-Mediated Drug Delivery. *Biomacromolecules* **2016**, *17* (1), 69–75.

(41) Li, M.; Dong, J.; Cheng, F.; Li, C.; Wang, H.; Sun, T.; He, W.; Wang, Q. Controlling Conjugated Antibodies at the Molecular Level for Active Targeting Nanoparticles toward HER2-Positive Cancer Cells. *Mol Pharm* **2021**, *18* (3), 1196–1207.

(42) Satsangi, A.; Roy, S. S.; Satsangi, R. K.; Vadlamudi, R. K.; Ong, J. L. Design of a Paclitaxel Prodrug Conjugate for Active Targeting of an Enzyme Upregulated in Breast Cancer Cells. *Mol Pharm* **2014**, *11* (6), 1906–1918.

(43) Costa, S. A.; Mozhdehi, D.; Dzuricky, M. J.; Isaacs, F. J.; Brustad, E. M.; Chilkoti, A. Active Targeting of Cancer Cells by Nanobody Decorated Polypeptide Micelle with Bio-Orthogonally Conjugated Drug. *Nano Lett* **2019**, *19* (1), 247–254.

(44) Mitchell, M. J.; Billingsley, M. M.; Haley, R. M.; Wechsler, M. E.; Peppas, N. A.; Langer, R. Engineering Precision Nanoparticles for Drug Delivery. *Nature Reviews Drug Discovery*. Nature Research February 1, 2021, pp 101–124.

(45) Davis, M. E.; Chen, Z.; Shin, D. M. Nanoparticle Therapeutics: An Emerging Treatment Modality for Cancer. *Nature Reviews Drug Discovery*. Nature Publishing Group September 1, 2008, pp 771–782.

(46) Xu, M.; Zhang, C.; Zeng, Z.; Pu, K. Semiconducting Polymer Nanoparticles as Activatable Nanomedicines for Combinational Phototherapy. *ACS Appl Polym Mater* **2021**, *3* (9), 4375–4389.

(47) Vines, J. B.; Yoon, J. H.; Ryu, N. E.; Lim, D. J.; Park, H. Gold Nanoparticles for Photothermal Cancer Therapy. *Frontiers in Chemistry*. Frontiers Media S.A. 2019.

(48) Wang, J.; Potocny, A. M.; Rosenthal, J.; Day, E. S. Gold Nanoshell-Linear Tetrapyrrole Conjugates for near Infrared-Activated Dual Photodynamic and Photothermal Therapies. *ACS Omega* **2020**, *5* (1), 926–940.

(49) Larson, N.; Ghandehari, H. Polymeric Conjugates for Drug Delivery. *Chemistry of Materials*. March 13, 2012, pp 840–853.

(50) Ringsdorf, H. *STRUCTURE AND PROPERTIES OF PHARMACOLOGICALLY ACTIVE POLYMERS*; 1975.

(51) Duncan, R. *Designing Polymer Conjugates as Lysosomotropic Nanomedicines*; 2007; Vol. 35. http://www.esf.org/.

(52) Mansur, A. A. P.; Carvalho, S. M.; Lobato, Z. I. P.; Leite, M. D. F.; Cunha, A. D. S.; Mansur, H. S. Design and Development of Polysaccharide-Doxorubicin-Peptide Bioconjugates for Dual Synergistic Effects of Integrin-Targeted and Cell-Penetrating Peptides for Cancer Chemotherapy. *Bioconjug Chem* **2018**, *29* (6), 1973–2000.

(53) Figueiredo, P. R.; González, R. D.; Carvalho, A. T. P. Insights into the Degradation of Polymer-Drug Conjugates by an Overexpressed Enzyme in Cancer Cells. *J Med Chem* **2023**, *66* (4), 2761–2772.

(54) Liu, Y.; Yang, G.; Zou, D.; Hui, Y.; Nigam, K.; Middelberg, A. P. J.; Zhao, C. X. Formulation of Nanoparticles Using Mixing-Induced Nanoprecipitation for Drug Delivery. *Industrial and Engineering Chemistry Research*. American Chemical Society March 4, 2020, pp 4134–4149.

(55) Ediriwickrema, A.; Saltzman, W. M. Nanotherapy for Cancer: Targeting and Multifunctionality in the Future of Cancer Therapies. *ACS Biomaterials Science and Engineering*. American Chemical Society February 9, 2015, pp 64–78.

(56) Ahmadi, V.; Zabihi, F.; Rancan, F.; Staszak, A. A.; Nie, C.; Dimde, M.; Achazi, K.; Wiehe, A.; Vogt, A.; Haag, R. Amphiphilic Co-Polypeptides Self-Assembled into Spherical Nanoparticles for Dermal Drug Delivery. *ACS Appl Nano Mater* **2021**, *4* (7), 6709–6721.

(57) Qiu, M.; Ouyang, J.; Sun, H.; Meng, F.; Cheng, R.; Zhang, J.; Cheng, L.; Lan, Q.; Deng, C.; Zhong, Z. Biodegradable Micelles Based on Poly(Ethylene Glycol)-b-Polylipopeptide Copolymer: A Robust and Versatile Nanoplatform for Anticancer Drug Delivery. *ACS Appl Mater Interfaces* **2017**, *9* (33), 27587–27595.

(58) Zoppe, J. O.; Ataman, N. C.; Mocny, P.; Wang, J.; Moraes, J.; Klok, H. A. Surface-Initiated Controlled Radical Polymerization: State-of-the-Art, Opportunities, and Challenges in Surface and Interface Engineering with Polymer Brushes. *Chem Rev* **2017**, *117* (3), 1105–1318.

(59) Chen, C.; Wunderlich, K.; Mukherji, D.; Koynov, K.; Heck, A. J.; Raabe, M.; Barz, M.; Fytas, G.; Kremer, K.; Ng, D. Y. W.; Weil, T. Precision Anisotropic Brush Polymers by Sequence Controlled Chemistry. *J Am Chem Soc* **2020**, *142* (3), 1332–1340.

(60) Mazurowski, M.; Gallei, M.; Li, J.; Didzoleit, H.; Stühn, B.; Rehahn, M. Redox-Responsive Polymer Brushes Grafted from Polystyrene Nanoparticles by Means of Surface Initiated Atom Transfer Radical Polymerization. *Macromolecules* **2012**, *45* (22), 8970–8981.

(61) Riachi, C.; Schüwer, N.; Klok, H.-A. Degradable Polymer Brushes Prepared via Surface-Initiated Controlled Radical Polymerization. *Macromolecules* **2009**, *42* (21), 8076–8081.

(62) Wang, R.; Yin, C.; Liu, C.; Sun, Y.; Xiao, P.; Li, J.; Yang, S.; Wu, W.; Jiang, X. Phenylboronic Acid Modification Augments the Lysosome Escape and Antitumor Efficacy of a Cylindrical Polymer Brush-Based Prodrug. *J Am Chem Soc* **2021**, *143* (49), 20927–20938.

(63) Yu, Y.; Chen, C.-K.; Law, W.-C.; Sun, H.; Prasad, P. N.; Cheng, C. A Degradable Brush Polymer–Drug Conjugate for PH-Responsive Release of Doxorubicin. *Polym Chem* **2015**, *6* (6), 953–961.

(64) Winnacker, M.; Rieger, B. Poly(Ester Amide)s: Recent Insights into Synthesis, Stability and Biomedical Applications. *Polymer Chemistry*. Royal Society of Chemistry December 14, 2016, pp 7039–7046.

(65) Takano, S.; Islam, W.; Nakazawa, K.; Maeda, H.; Sakurai, K.; Fujii, S. Phosphorylcholine-Grafted Molecular Bottlebrush–Doxorubicin Conjugates: High Structural Stability, Long Circulation in Blood, and Efficient Anticancer Activity. *Biomacromolecules* **2021**, *22* (3), 1186–1196.

(66) Xu, X.; Huang, X.; Chang, Y.; Yu, Y.; Zhao, J.; Isahak, N.; Teng, J.; Qiao, R.; Peng, H.; Zhao, C.-X.; Davis, T. P.; Fu, C.; Whittaker, A. K. Antifouling Surfaces Enabled by Surface Grafting of Highly Hydrophilic Sulfoxide Polymer Brushes. *Biomacromolecules* **2021**, *22* (2), 330–339.

(67) Ercole, F.; Kim, C.-J.; Dao, N. V.; Tse, W. K. L.; Whittaker, M. R.; Caruso, F.; Quinn, J. F. Synthesis of Thermoresponsive, Catechol-Rich Poly(Ethylene Glycol) Brush Polymers for Attenuating Cellular Oxidative Stress. *Biomacromolecules* **2023**, *24* (1), 387–399.

(68) Ercole, F.; Kim, C.-J.; Dao, N. V.; Tse, W. K. L.; Whittaker, M. R.; Caruso, F.; Quinn, J. F. Synthesis of Thermoresponsive, Catechol-Rich Poly(Ethylene Glycol) Brush Polymers for Attenuating Cellular Oxidative Stress. *Biomacromolecules* **2023**, *24* (1), 387–399.

(69) Shi, J.; Votruba, A. R.; Farokhzad, O. C.; Langer, R. Nanotechnology in Drug Delivery and Tissue Engineering: From Discovery to Applications. *Nano Letters*. September 8, 2010, pp 3223–3230.

(70) Wang, R.; Wei, Q.; Sheng, W.; Yu, B.; Zhou, F.; Li, B. Driving Polymer Brushes from Synthesis to Functioning. *Angewandte Chemie International Edition* **2023**, *62* (27).

(71) Feng, C.; Huang, X. Polymer Brushes: Efficient Synthesis and Applications. *Acc Chem Res* **2018**, *51* (9), 2314–2323.

(72) Yao, Q.; Gutierrez, D. C.; Hoang, N. H.; Kim, D.; Wang, R.; Hobbs, C.; Zhu, L. Efficient Codelivery of Paclitaxel and Curcumin by Novel Bottlebrush Copolymer-Based Micelles. *Mol Pharm* **2017**, *14* (7), 2378–2389.

(73) Yu, Y.; Chen, C.-K.; Law, W.-C.; Weinheimer, E.; Sengupta, S.; Prasad, P. N.; Cheng, C. Polylactide- *Graft* -Doxorubicin Nanoparticles with Precisely Controlled Drug Loading for PH-Triggered Drug Delivery. *Biomacromolecules* **2014**, *15* (2), 524–532.

(74) Zhao, K.; Li, M.; Geng, H.; Gao, Z.; Zhang, X.; Sekhar, K. P. C.; Zhang, P.; Cui, J. Synthesis of Antifouling Poly(Ethylene Glycol) Brushes via "Grafting to" Approach for Improved Biodistribution. *Biomacromolecules* **2024**, *25* (10), 6727–6736.

(75) Fenyves, R.; Schmutz, M.; Horner, I. J.; Bright, F. V.; Rzayev, J. Aqueous Self-Assembly of Giant Bottlebrush Block Copolymer Surfactants as Shape-Tunable Building Blocks. *J Am Chem Soc* **2014**, *136* (21), 7762–7770.

(76) Wang, Z.; Ganewatta, M. S.; Tang, C. Sustainable Polymers from Biomass: Bridging Chemistry with Materials and Processing. *Progress in Polymer Science*. Elsevier Ltd February 1, 2020.

(77) Scholten, P. B. V.; Detrembleur, C.; Meier, M. A. R. Plant-Based Nonactivated Olefins: A New Class of Renewable Monomers for Controlled Radical Polymerization. *ACS Sustain Chem Eng* **2019**, *7* (2), 2751–2762.

(78) Zhu, Y.; Romain, C.; Williams, C. K. Sustainable Polymers from Renewable Resources. *Nature*. Nature Publishing Group December 14, 2016, pp 354–362.

(79) Zhang, X.; Fevre, M.; Jones, G. O.; Waymouth, R. M. Catalysis as an Enabling Science for Sustainable Polymers. *Chemical Reviews*. American Chemical Society January 24, 2018, pp 839–885.

(80) Cohen-Erez, I.; Rapaport, H. Coassemblies of the Anionic Polypeptide γ-PGA and Cationic β-Sheet Peptides for Drug Delivery to Mitochondria. *Biomacromolecules* **2015**, *16* (12), 3827–3835.

(81) Park, S. E.; Sajid, M. I.; Parang, K.; Tiwari, R. K. Cyclic Cell-Penetrating Peptides as Efficient Intracellular Drug Delivery Tools. *Molecular Pharmaceutics*. American Chemical Society September 3, 2019, pp 3727–3743.

(82) Basu, A.; Kunduru, K. R.; Katzhendler, J.; Domb, A. J. Poly(α-Hydroxy Acid)s and Poly(α-Hydroxy Acid-Co-α-Amino Acid)s Derived from Amino Acid. *Advanced Drug Delivery Reviews*. Elsevier B.V. December 15, 2016, pp 82–96.

(83) Yu, Y.; Zou, J.; Cheng, C. Synthesis and Biomedical Applications of Functional Poly(α-Hydroxyl Acid)s. *Polymer Chemistry*. Royal Society of Chemistry October 21, 2014, pp 5854–5872.

(84) Han, S.; Wu, J. Recent Advances of Poly(Ester Amide)s-Based Biomaterials. *Biomacromolecules*. American Chemical Society May 9, 2022, pp 1892–1919.

(85) Joshi, D. C.; Saxena, S.; Jayakannan, M. Development of L-Lysine Based Biodegradable Polyurethanes and Their Dual-Responsive Amphiphilic Nanocarriers for Drug Delivery to Cancer Cells. *ACS Appl Polym Mater* **2019**, *1* (7), 1866–1880.

(86) Levkovskyi, I. O.; Mochizuki, S.; Zheng, A.; Zhang, X.; Zhang, F. Lipoic Acid-Based Poly(Disulfide)s: Synthesis and Biomedical Applications. *Nano TransMed*. KeAi Publishing Communications Ltd. September 1, 2023.

(87) Lu, W.; Wang, X.; Cheng, R.; Deng, C.; Meng, F.; Zhong, Z. Biocompatible and Bioreducible Micelles Fabricated from Novel α-Amino Acid-Based Poly(Disulfide Urethane)s: Design, Synthesis and Triggered Doxorubicin Release. *Polym Chem* **2015**, *6* (33), 6001–6010.

(88) Yin, Q.; Yin, L.; Wang, H.; Cheng, J. Synthesis and Biomedical Applications of Functional Poly(α-Hydroxy Acids) via Ring-Opening Polymerization of O-Carboxyanhydrides. *Acc Chem Res* **2015**, *48* (7), 1777–1787.

(89) Sun, H.; Cheng, R.; Deng, C.; Meng, F.; Dias, A. A.; Hendriks, M.; Feijen, J.; Zhong, Z. Enzymatically and Reductively Degradable α-Amino Acid-Based Poly(Ester Amide)s: Synthesis, Cell Compatibility, and Intracellular Anticancer Drug Delivery. *Biomacromolecules* **2015**, *16* (2), 597–605.

(90) Jain, S.; John, A.; George, C. E.; Johnson, R. P. Tyrosine-Derived Polymers as Potential Biomaterials: Synthesis Strategies, Properties, and Applications. *Biomacromolecules*. American Chemical Society February 13, 2023, pp 531–565.

(91) Aamer, K. A.; Genson, K. L.; Kohn, J.; Becker, M. L. Impact of Polymer-Bound Iodine on Fibronectin Adsorption and Osteoblast Cell Morphology in Radiopaque Medical Polymers: Tyrosine-Derived Polycarbonate Blends as a Model System. *Biomacromolecules* **2009**, *10* (9), 2418–2426.

(92) He, M.; Ro, L.; Liu, J.; Chu, C. C. Folate-Decorated Arginine-Based Poly(Ester Urea Urethane) Nanoparticles as Carriers for Gambogic Acid and Effect on Cancer Cells. *J Biomed Mater Res A* **2017**, *105* (2), 475–490.

(93) Deepa, P.; Jayakannan, M. Solvent-Free and Nonisocyanate Melt Transurethane Reaction for Aliphatic Polyurethanes and Mechanistic Aspects. *J Polym Sci A Polym Chem* **2008**, *46* (7), 2445–2458.

(94) Deepa, P.; Jayakannan, M. Polyurethane-Oligo(Phenylenevinylene) Random Copolymers: π-Conjugated Pores, Vesicles, and Nanospheres via Solvent-Induced Self-Organization. *J Polym Sci A Polym Chem* **2008**, *46* (17), 5897–5915.

(95) Deepa, P.; Jayakannan, M. Solvent-Induced Self-Organization Approach for Polymeric Architectures of Micropores, Hexagons and Spheres Based on Polyurethanes Prepared via Novel Melt Transurethane Methodology. *J Polym Sci A Polym Chem* **2007**, *45* (12), 2351–2366.

(96) Anantharaj, S.; Jayakannan, M. Polymers from Amino Acids: Development of Dual Ester-Urethane Melt Condensation Approach and Mechanistic Aspects. *Biomacromolecules* **2012**, *13* (8), 2446–2455.

(97) Anantharaj, S.; Jayakannan, M. Amyloid-Like Hierarchical Helical Fibrils and Conformational Reversibility in Functional Polyesters Based on L-Amino Acids. *Biomacromolecules* **2015**, *16* (3), 1009–1020.

(98) Anantharaj, S.; Jayakannan, M. Catalysts and Temperature Driven Melt Polycondensation Reaction for Helical Poly(Ester-Urethane)s Based on Natural L-Amino Acids. *J Polym Sci A Polym Chem* **2016**, *54* (8), 1065–1077.

(99) Anantharaj, S.; Jayakannan, M. Melt Polycondensation Approach for Reduction Degradable Helical Polyester Based on L-cystine. *J Polym Sci A Polym Chem* **2016**, *54* (18), 2864–2875.

(100) Aluri, R.; Jayakannan, M. One-Pot Two Polymers: ABB′ Melt Polycondensation for Linear Polyesters and Hyperbranched Poly(Ester-Urethane)s Based on Natural L-Amino Acids. *Polym Chem* **2015**, *6* (25), 4641–4649.

(101) Aluri, R.; Jayakannan, M. Development of L-Tyrosine-Based Enzyme-Responsive Amphiphilic Poly(Ester-Urethane) Nanocarriers for Multiple Drug Delivery to Cancer Cells. *Biomacromolecules* **2017**, *18* (1), 189–200.

(102) Aluri, R.; Saxena, S.; Joshi, D. C.; Jayakannan, M. Multistimuli-Responsive Amphiphilic Poly(Ester-Urethane) Nanoassemblies Based on L-Tyrosine for Intracellular Drug Delivery to Cancer Cells. *Biomacromolecules* **2018**, *19* (6), 2166–2181.

(103) Saxena, S.; Jayakannan, M. Enzyme and PH Dual Responsive L-Amino Acid Based Biodegradable Polymer Nanocarrier for Multidrug Delivery to Cancer Cells. *J Polym Sci A Polym Chem* **2016**, *54* (20), 3279–3293.

(104) Saxena, S.; Jayakannan, M. π-Conjugate Fluorophore-Tagged and Enzyme-Responsive l -Amino Acid Polymer Nanocarrier and Their Color-Tunable Intracellular FRET Probe in Cancer Cells. *Biomacromolecules* **2017**, *18* (8), 2594–2609.

(105) Saxena, S.; Jayakannan, M. Development of L-Amino-Acid-Based Hydroxyl Functionalized Biodegradable Amphiphilic Polyesters and Their Drug Delivery Capabilities to Cancer Cells. *Biomacromolecules* **2020**, *21* (1), 171–187.

(106) Chandra Joshi, D.; Ashokan, A.; Jayakannan, M. L-Amino Acid Based Phenol- and Catechol-Functionalized Poly(Ester-Urethane)s for Aromatic π-Interaction Driven Drug Stabilization and Their Enzyme-Responsive Delivery in Cancer Cells. *ACS Appl Bio Mater* **2022**, *5* (11), 5432–5444.

(107) Khuddus, M.; Jayakannan, M. Melt Polycondensation Strategy for Amide-Functionalized L-Aspartic Acid Amphiphilic Polyester Nano-Assemblies and Enzyme-Responsive Drug Delivery in Cancer Cells. *Biomacromolecules* **2023**, *24* (6), 2643–2660.

Chapter 2

Size and Shape-controlled Biodegradable Polymer Brushes Based on L-Amino acid for Intracellular Drug Delivery and Deep-Tissue Penetration

Abstract

We report size and shape-controlled polymer brushes based on L-amino acid bioresource and study the role of polymer topology on the enzymatic-biodegradation and deep-tissue penetration under in-vitro and in-vivo. For this purpose, L-tyrosine based propargyl-functionalized monomer is tailor-made and polymerized via solvent free melt polycondensation strategy to yield hydrophobic and clickable biodegradable poly(ester-urethane)s. Post-polymerization click chemistry strategy is applied to make well-defined amphiphilic one-dimensional rod-like and three-dimensional spherical polymer brushes by merely varying the lengths of PEG-azides in the reaction. These core-shell polymer brushes are found to be non-toxic, non-hemolytic and capable of loading clinical anticancer drug doxorubicin and deep-tissue penetrable near infrared biomarker IR 780. In vitro enzymatic-drug release kinetics and lysotracker-assisted real-time live-cell confocal bioimaging revealed that the rod-like polymer brush is superior than its spherical counterparts for faster cellular uptake and enzymatic-biodegradation at the endo-lysosomal compartments to release DOX at the nucleus. Further, in-vivo live-animal bioimaging by IVIS technique established that the IR-780 loaded rod-like polymer brush exhibited efficient deep-tissue penetration ability and emphasized the importance of polymer brush topology-control for biological activity. Polymer brushes exhibit good stability in the blood plasma for more than 72 h and they predominately accumulated in the digestive organs like liver, kidney and spleen and they were less toxic to heart and brain tissues. IVIS imaging of cryotome tissue slices of organs confirmed that deep-penetrating ability of the polymer brushes. The present investigation opens opportunity for bio-derived and biodegradable polymer brushes as next generation smart drug delivery scaffolds.

2.1 Introduction

Polymer brushes are higher order synthetic macromolecules consisting discrete nano-compartmentalization and provide unique opportunities to precisely control one-and three-dimensional shapes, sub-nanometer size objects and surfaces, chemical functions, and they offer unlimited opportunity for application in material science and biomedical field.[1–4] Polymer brushes are typically synthesized by grafting-to and grafting-from strategies on the well-defined rigid polymer backbone with flexible side-chains for self-assembly in solution and solid state (in thin films).[5–7] Plug-and-play interfaces for guest-host interaction,[8] protein-conjugates,[9] hybrid molecular brushes,[10] cross-linkable block copolymer brushes,[11] NIR-probe tagged triblock micelles,[12] and bottlebrush adhesives[13] are some of the recent examples reported for multifaceted polymer brushes. Polymer brushes for biomedical field is typically achieved by incorporating hydrophilic-hydrophobic balance in combination with pH, redox or thermal stimuli-responsiveness to impart on-demand delivery of cargoes at the intracellular compartments and tumor-specific environments.[14,15] Among many choices to introduce amphiphilicity in the polymer system, polyethylene glycols (PEG) and their derivatives emerged as a primary choice due to their biocompatibility, non-immunogenicity, non-hemolytic properties, etc. PEG grafting-to strategy in polymer brush synthesis required nearly 99 % efficient organic reactions; thus, alkyne-azide, thiol-yne click chemistry and Diels-Alder reactions are commonly employed synthetic routes.[16–20] Further, size, rigidity and aspect ratio of the polymer brushes were found to influence on the pharmacokinetics, biodistribution, and rate of clearance in the *in vivo* models.[21] Polymer brushes were also reported for the release of proteins[22], attenuating cellular oxidative stress,[23] growth factor bearing functional surfaces, etc.[24] Astonishingly, majority of the above cited polymer brushes were primarily built on non-biodegradable polyacrylate platform; thus, the fate of polymer chains under physiological conditions and their clearance under biological systems still lacking clarity. Thus, new efforts are required to build next generation smart polymer brushes that are non-toxic, stable under blood circulation for in-vivo administration, and most importantly enzymatic-biodegradable at the intracellular compartments for minimal or no-side effects under physiological conditions.

Aliphatic polyesters are enzymatic-biodegradable at the intracellular compartments; thus, they contribute nearly 50 % of the pro-drug design in the market.[25] Commercial aliphatic polyesters such as polycaprolactone (PCL) is highly hydrophobic and render limited accessibility for enzyme adherence,[26,27] and therefore, many research groups including us have developed functional PCL having -COOH, -NH_2 or -OH functionalities to improve intracellular

biodegradation aspects.[28–32] PLLA is another excellent biodegradable polymer; however, it offers limited scope for drug delivery wherein the nanocarrier required to be stable at neutral pH for in-vitro and in-vivo analysis.[33–35] PLLA-containing oligo-ethylene glycols were designed with fluorescent molecules to study intracellular localization in Hela Cells.[36] Aliphatic polymer brushes were also built by polycondensation routes using propargyl-functionalized monomers and subject the resultant polymers for PEGylation in the post-polymerization step via click chemistry.[37,38] These PEGylated polyesters were predominately studied for crystallization phenomena, chain packing, mesophase-formation, and structural-property relationships;[39–42] however, they were rarely tested for biological applications. Our research group has developed solvent free melt polycondensation strategy to L-amino acid bioresources and this methodology enabled us to explore many inaccessible aliphatic polymers such as hydroxyl[43] and amine functionalized polyesters,[44] poly(ester-urethane)s[45–49] polyurethanes,[50] etc. Amphiphilicity in these non-peptides were optimized along with pH, enzyme and thermo-responsive for drug delivery in cancer research and bio-FRET probes were built to study their biodegradation aspects, etc.[51–56]

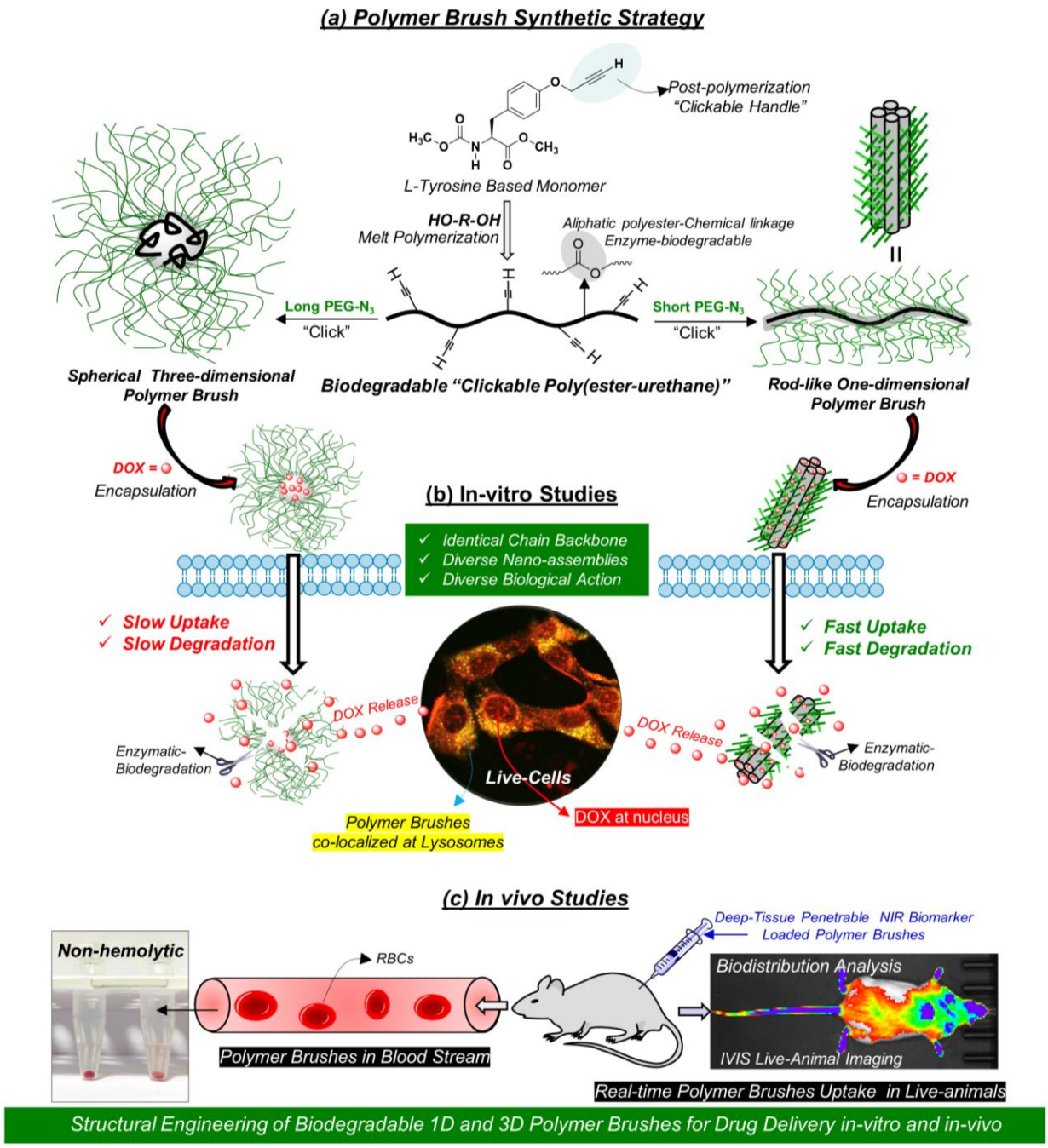

Figure 2.1. *(a) Design and development of L-amino acid based biodegradable polymer brushes with precise control in size and shape. (b) Probing the biodegradation of polymer brush topology by in-vitro real time live-cells bioimaging. (c) Deep-tissue penetrable near infrared biomarkers IR-780 assisted in-vivo live-animal bioimaging of the polymer brushes.*

The success of building new classes of biodegradable polymer brushes for biomedical application is highly depended on the following factors: (i) selection of the biodegradable polymer backbone, (ii) choice of the monomers, (iii) method of polymerization, (iv) polymer

brush topology-control (like size and shape), and (v) finally establishing the proof-of-concept in-vitro and in-vivo biological studies. For this purpose, here we have chosen aliphatic poly(ester-urethane) backbone and the monomer was chosen from L-tyrosine amino acid so that the resultant structures are potential candidates as sustainability polymers. The polymers were synthesized by solvent free melt polycondensation process and the polymer brush topology was fine-tuned as one-dimensional rod-like and three-dimensional sphere-like by carefully varying PEG chain length at the periphery as shown in Figure 1. The polymer brushes were found to be sub-nanometer in size, non-toxic and non-hemolytic, and enzymatically-biodegradable at the intracellular compartments to deliver clinical anticancer drug doxorubicin. The role of the polymer topology was studied on the endocytosis of the polymer brushes by real-time in-vitro cellular uptake, and the lysosomal-biodegradation was further probed in living-cell confocal bioimaging. Deep tissue penetrable near infra-red biomarker IR-780 was loaded in the polymer brushes which enabled the in-vivo live-animal bioimaging and biodistribution by IVIS bioimaging techniques. In a nut shell, the present investigation opened new avenue for the development of bio-resource based biodegradable polymer brushes and put forward the importance of polymer topology-control in polymer brushes for efficient cell and tissue penetration for their long-term impact in drug delivery applications.

2.2 Experimental Section

2.2.1 Materials and Methods:

L-Tyrosine, polyethylene glycol monomethyl ether (PEG-350, 750, 2000, 5000), and 1,12-dodecane diol, Titanium (IV) butoxide $Ti(OBu)_4$, paraformaldehyde, glycerol, HPLC Grade Dimethyl Sulphoxide (DMSO), methyl chloroformate, propargyl Bromide, thionyl chloride, and tosyl chloride, Copper sulphate pentahydrate $CuSO_4$. $5H_2O$, Sodium ascorbate, acetonitrile, PBS 1x, pyrene, NIR probe (IR-780) Iodide, Doxorubicin hydrochloride (DOX. HCl), horse liver esterase enzyme, 3-(4,5-dimethylthiazol-2-yl)-2,5-diphenyltetraazolium bromide (MTT), 4 % Paraformaldehyde, In DMEM media containing phenol red, 10% (v/v) fetal bovine serum (FBS), 4',6-diamido-2-phenylindole (DAPI), and 1% (v/v) penicillin-streptomycin, were purchased from Sigma-Aldrich and many other reagents, solvents, and salts were purchased from locally and used without any purification. the cancer cells of human breast (MCF-7), Wild type mouse embryonic (WT-MEF), and ovarian cancer cell line (SKOV3) were maintained at temp. of 37 ℃ under a 5% CO_2 atmosphere.

2.2.2 General Procedures:

400-MHz Bruker and 400-MHz JEOL NMR Spectrophotometers were used to record the ^{13}C NMR and ^{1}H spectra of Monomers and polymers. All NMR spectra were recorded in $CDCl_3$ with TMS as a standard. Biosystems 4800 PLUS MALDI TOF/TOF Analyzer was used to determine the monomer mass. Polystyrene was used as standard for size exclusion chromatographic (SEC) analysis in tetrahydrofuran (THF) using Viscotek VE 1122 pump and VE 3580 RI detector. For SEC analysis in DMF Agilent PLgel 10 μm MIXED-B, 7.5 × 300 mm columns are used at temperature of 70 °C. The absolute molecular weights were determined using triple detector setup (RALS, RI and LALS) using polystyrene standard (PolyCAL PS-99K, Mw = 99,209 from Viscotek) for the calibration. Five different concentrations of each polymer were made to accurately calculate the refractive index increment (dn/dc) values of the polymers in DMF at 70 °C. Each solution's differential refractive index (DRI) values were acquired, and Omnisec software was used to plot DRI data versus concentration to obtain the dn/dc values. The dn/dc values were found to be 0.0316 mL/g, 0.0518 mL/g, and 0.0111 mL/g for P-Tyr-PEG-750, P-Tyr-PEG-2000, and P-Tyr-PEG-5000, respectively. Perkin Elmer Thermal Analyzer STA 6000 model and TAQ20 Differential Scanning Calorimeter were used for thermal analysis at 10°/min heating rate. Bruker alphaT FT-IR, Malvern Instruments Nano ZS-90, Zeiss UltraPlus scanning electron microscope, by VeecoNanoscope IV device in tapping mode Atomic force microscopy (AFM), and Leica SP8 (zeiss LSM 710) Confocal microscopic were used.

2.2.3 Synthesis of methyl (methoxycarbonyl)-L-tyrosinate (compound 2):

L-Tyrosine (15.0 g, 0.082 mol) was immersed in 70.0 mL of dry methanol in a clean 250 mL two-neck round bottom flask. Thionyl chloride (10.7 g, 6.7 mL, 0.091 mol) was added dropwise under ice-cold conditions. After warming to room temperature, it was refluxed for 12 hours under a nitrogen atmosphere. The thionyl chloride and methanol were removed via vacuum distillation, leaving behind a white solid residue. The resulting L-tyrosine ester amine salt (compound **1**) was then neutralized by 15% sodium carbonate (90.0 mL) solution and kept in an ice-cold condition. Methyl chloroformate (7.1 mL, 0.0911 mol) in dichloromethane (90.0 mL) was added dropwise and the reaction mixture was stirred for 12 hours at room temperature. The solvent was evaporated using a rotary evaporator and the resulting mixture was diluted with dichloromethane and passed through anhydrous Na_2SO_4. The product was then purified

using column chromatography using chloroform-methanol eluent (9:1 v/v) to obtain a white solid product. Yield = 18.0 g (85 %). ^{1}H NMR (400 MHz, $CDCl_3$) δ ppm:3.01−3.05 (m, 2H, Ph-CH_2), 3.67 (s, 3H, -NH-$COOCH_3$), 3.73 (s,3H, -$COOCH_3$), 4.61 (s, 1H, Ph-CH_2CH), 5.19 (s, 1H, NH),6.73−6.75 (m, 2H, Ph), 6.96−6.98 (m, 2H, Ph). ^{13}C NMR (100 MHz, $CDCl_3$) δ ppm: 173, 157, 156, 131, 128, 116, 55, 53, 38. FT-IR: 3291, 2954, 1713, 1610, 1508, 1441, 1358, 1262, 1213, 1059, 1023, 700.

2.2.4 Synthesis of methyl (S)-2(methoxycarbonyl)amino)-3-(4-(prop-2-yn-1-yloxy) phenyl) propanoate, Compound-3 (Monomer):

Compound-**2** (5.0 g (0.019 mol) was dissolved in 70 mL of dry acetonitrile in a clean 100 ml two-neck round bottom flask. K_2CO_3 (3.26 g, 0.023 mol) was added, and refluxed for 30 minutes under nitrogen. Propargyl bromide (2.6 mL, 0.023 mol) was added and the reaction mixture was refluxed for 12 hours under nitrogen environment. Solvent was removed using a rotary evaporator, water was added, extracted three times with ethyl acetate. The product was then purified using column chromatography with a dichloromethane-methanol eluent (9:1 v/v) to obtain a white solid product. Yield = 5.2 g (91 %) ^{1}H NMR (400 MHz, $CDCl_3$) δ ppm:2.52 (t, 1H, - CH-Alkyne) 3.00−3.04 (m, 2H, -Ph-CH_2), 3.67 (s, 3H, -NH-$COOCH_3$), 3.73 (s,3H, -$COOCH_3$), 4.61 (s, 1H, Ph-CH_2CH), 4.66 (s, CH_2 Alkyne), 5.18 (s, 1H, NH),6.89−6.91 (m, 2H, Ph), 7.04−7.06 (m, 2H,). ^{13}C NMR (100 MHz, $CDCl_3$) δ ppm: 172, 156, 155, 130, 127, 115, 78, 75, 55, 54, 52, 37. FT-IR: 3291, 2954, 2120, 1713, 1610, 1508, 1441, 1358, 1262, 1213, 1059, 1023, 700. HR-MS (ESI): m/z calcd. For C_{15} H_{17} NO_5 $[M + H]^+$, 291.1107, found $[M + Na]^+$, 314.1002.

2.2.5 Synthesis of Polyethylene glycol 350 monomethyl ether Chloride:

Typical procedure for the chlorination was explained in detail for MeO-PEG-350. In a 30 mL clean U-shaped tube with adopter, PEG-350 monomethyl ether (5.00 g, 0.0142 mol) was added. Then 2.5 g of thionyl chloride, 0.0214 mol, was added dropwise at 4 °C, then the reaction mixture was brought to room temperature 15 minutes. The reaction mixture was maintained at 100 °C for 16 h. It was dissolved in dichloromethane (30 mL) and washed three times with fresh water, and dried over anhydrous Na_2SO_4. Solvent was removed to get pure product. Yield = 4.5 g (86 %). ^{1}H NMR (400 MHz, $CDCl_3$) δ ppm: 3.38 (s, 3H, -O-CH_3), 3.74-3.77 (t, 2H, -O-CH_2-CH_2-Cl), 3.55-3.67 (m, 28H, -O-CH2-CH2-O-). ^{13}C-NMR (100 MHz, $CDCl_3$) δ ppm: 42, 59, 70, 71.

2.2.6 Synthesis of Polyethylene glycol 750 monomethyl ether Chloride:

Typical procedure for the chlorination was explained in detail for MeO-PEG-750. In a 30 mL clean U-shaped tube with adopter, PEG-750 monomethyl ether (5.00 g, 0.0066 mol) was added. Then thionyl chloride (1.25 g, 0.010 mol) was added dropwise at 4 °C, then the reaction mixture was brought to room temperature 15 minutes. The reaction mixture was maintained at 100 °C for 16 h. It was dissolved in dichloromethane (30 mL) and washed three times with fresh water, and dried over anhydrous Na_2SO_4. The solvent was removed to get pure product. Yield = 4.5 g (88 %). ^{1}H NMR (400 MHz, $CDCl_3$) δ ppm: 3.38 (s, 3H, -O-CH_3), 3.74-3.77 (t, 2H, -O-CH_2-CH_2-Cl), 3.55-3.67 (m, 70H, -O-CH2-CH2-O-). ^{13}C-NMR (100 MHz, $CDCl_3$) δ ppm: 42, 59, 70, 71. FT-IR: 2868, 1453, 1290, 1094, 849 750.

2.2.7 Synthesis of Polyethylene glycol 2000 monomethyl ether Chloride:

Typical procedure for the chlorination was explained in detail for MeO-PEG-2000. In a 30 mL clean U-shaped tube with adopter, PEG-2000 monomethyl ether (10.00 g, 0.005 mol)) was added. Then 1.0 g of thionyl chloride, 0.008 mol, was added dropwise at 4 °C, then the reaction mixture was brought to room temperature 15 minutes. The reaction mixture was maintained at 100 °C for 16 h. It was dissolved in minimum amount of dichloromethane (2 mL) and precipitated in diethyl ether and residue was filtered by Whatman filter paper and washes with diethyl ether to get white solid powder pure product. Yield = 8.5 g (85 %). ^{1}H NMR (400 MHz, $CDCl_3$) δ ppm: 3.38 (s, 3H, -O-CH_3), 3.74-3.77 (t, 2H, -O-CH_2-CH_2-Cl), 3.55-3.67 (m, 194H, -O-CH2-CH2-O-). ^{13}C-NMR (100 MHz, $CDCl_3$) δ ppm: 42, 59, 70, 71.

2.2.8 Synthesis of Polyethylene glycol 5000 monomethyl ether Chloride:

Typical procedure for the chlorination was explained in detail for MeO-PEG-2000. In a 30 mL clean U-shaped tube with adopter, PEG-2000 monomethyl ether (10.00 g, 0.002 mol)) was added. Then 0.33 g of thionyl chloride, 0.0032 mol, was added dropwise at 4 °C, then the reaction mixture was brought to room temperature 15 minutes. The reaction mixture was maintained at 100 °C for 16 h. It was dissolved in minimum amount of dichloromethane (2 mL) and precipitated in diethyl ether and residue was filtered by Whatman filter paper and washes with diethyl ether to get white solid powder pure product. Yield = 8.4 g (84%). ^{1}H NMR (400 MHz, $CDCl_3$) δ ppm: 3.38 (s, 3H, -O-CH_3), 3.74-3.77 (t, 2H, -O-CH_2-CH_2-Cl), 3.55-3.67 (m, 440H, -O-CH2-CH2-O-). ^{13}C-NMR (100 MHz, $CDCl_3$) δ ppm: 42, 59, 70, 71.

2.2.9 Synthesis of Polyethylene glycol 350 monomethyl ether azide:

Typical procedure for the chlorination was explained in detail for MeO-PEG-350. Sodium azide (1.40 g, 0.0216 mol) was added in to PEG-350 monomethyl ether chloride (4.00 g, 0.0108 mol) in 30.00 mL of dry DMF in 100 mL two neck RB and the reaction mixture was refluxed under nitrogen for 24 h. Excess solvent was distilled out by vacuum distillation and residue It was dissolved in dichloromethane (30 mL) and washed three times with fresh water, and dried over anhydrous Na_2SO_4. The solvent was removed to get pure product. Yield = 3.5 g (87%). ^{1}H-NMR (400 MHz, $CDCl_3$) δ ppm: 3.37 (s, 3H, -O-CH_3), 4.38 (t, 2H, - O-CH_2-CH_2-N_3), 3.52-3.67 (m, 28H, -O-CH_2-CH_2-O-). ^{13}C-NMR (100 MHz, $CDCl_3$) δ ppm: 50, 59, 70, 71. FT-IR: 2868, 2100, 1453, 1290, 1094, 849.

2.2.10 Synthesis of Polyethylene glycol 750 monomethyl ether azide:

Typical procedure was explained in detail for MeO-PEG-750. Sodium azide (0.50 g, 0.0077 mol) was added into PEG-750 monomethyl ether chloride (3.00 g, 0.0038 mol) in 20.00 mL of dry DMF in 100 mL two neck RB and the reaction mixture was refluxed under nitrogen for 24 h. Excess solvent was distilled out by vacuum distillation and residue It was dissolved in dichloromethane (30 mL) and washed three times with fresh water, and dried over anhydrous Na_2SO_4. The solvent was removed to get pure product. Yield = 2.5 g (83 %). ^{1}H-NMR (400 MHz, $CDCl_3$) δ ppm: 3.37 (s, 3H, -O-CH_3), 4.38 (t, 2H, - O-CH_2-CH_2-N_3), 3.52-3.67 (m, 60H, -O-CH_2-CH_2-O-). ^{13}C-NMR (100 MHz, $CDCl_3$) δ ppm: 50, 59, 70, 71. FT-IR: 2868, 2100, 1453, 1290, 1094, 849.

2.2.11 Synthesis of Polyethylene glycol 2000 monomethyl ether 2000 azide:

Typical procedure for the chlorination was explained in detail for MeO-PEG-2000. Sodium azide (0.515 g, 0.0079 mol) was added in to PEG-2000 monomethyl ether chloride (8.00 g, 0.0039 mol) in 80.00 mL of dry DMF in 100 mL two neck RB and the reaction mixture was refluxed under nitrogen for 24 h. Excess solvent was distilled out by vacuum distillation and residue redispersed in the minimum amount of DCM and precipitated in diethyl ether then filtered by Whatman filter paper to get white powder. Yield = 7.0 g (87%). ^{1}H-NMR (400 MHz, $CDCl_3$) δ ppm: 3.37 (s, 3H, -O-CH_3), 4.38 (t, 2H, - O-CH_2-CH_2-N_3), 3.52-3.67 (m, 200H, -O-CH_2-CH_2-O-). ^{13}C-NMR (100 MHz, $CDCl_3$) δ ppm: 50, 59, 70, 71. FT-IR: 2868, 2100, 1453, 1290, 1094, 849.

2.2.12 Synthesis of Polyethylene glycol 5000 monomethyl ether 5000 azide:

Typical procedure for the chlorination was explained in detail for MeO-PEG-5000. Sodium azide (0.12 g, 0.0019 mol) was added in to PEG-2000 monomethyl ether chloride (5.00 g, 0.0009 mol) in 30.00 mL of dry DMF in 100 mL two neck RB and the reaction mixture was refluxed under nitrogen for 24 h. Excess solvent was distilled out by vacuum distillation and residue were redispersed in the minimum amount of DCM and precipitated in diethyl ether then filtered by Whatman filter paper to get white powder. Yield = 4.5 g (90%). ^{1}H-NMR (400 MHz, $CDCl_3$) δ ppm: 3.37 (s, 3H, -O-CH_3), 4.38 (t, 2H, - O-CH_2-CH_2-N_3), 3.52-3.67 (m, 446H, -O-CH_2-CH_2-O-. ^{13}C-NMR (100 MHz, $CDCl_3$) δ ppm: 50, 59, 70, 71. FT-IR: 2868, 2100, 1453, 1290, 1094, 849.

2.2.13 Synthesis of Propargyl-substituted L-Tyrosine poly(ester-urethane)s (P-Tyr):

L-Tyrosine monomer **3** (0.75 g, 0.0025 mol) and 1,12-dodecanediol (0.52 g, 0.0025mol) were taken in a polymerization tube and allowed to melt at 100 °C. The polymerization mixture was subjected to nitrogen purging and subsequent vacuum applied, and the degassing was performed at least thrice to make it oxygen and moisture free. Titanium (IV) butoxide [$Ti(OBu)_4$), 1 mol%] was added as catalyst, and the polymerization was continued by stirring under nitrogen purge for 4 h at 150 °C. The polymerization mixture was then placed in a high vacuum for two hours at 150 °C. In this process, the condensate methanol was removed along with nitrogen purge. The viscus melt was subjected to high vacuum 10^{-2} mbar for 2 hours at 150 °C. The polymer (**P-Tyr**) was produced as a viscous material and it was purified by dissolving in THF and precipitated into methanol. yield= 0.98 g, (89 %). ^{1}H-NMR (400 MHz, $CDCl_3$) δ ppm: = 7.11 - 7.00 (m, 2H), 6.96 - 6.84 (m, 2H), 5.15 (br. s., 1H), 4.66 (s, *J* = 2.4 Hz, 2H), 4.58 (br. s., 1H), 4.18 - 3.97 (m, 4H), 3.04-3.06 (m, 2H), 2.52 (s, 1H), 1.57-1.61 (m, 4H), 1.27-1.29 (m, 16H). ^{13}C-NMR (100 MHz, $CDCl_3$) δ ppm: = 171.8, 156.6, 156.0, 130.3, 128.8, 114.9, 78.5, 77.3, 76.7, 75.5, 65.6, 65.3, 55.7, 54.7, 37.5, 29.5, 29.5, 29.2, 29.2, 28.9, 28.4, 25.8. FT-IR: 3303, 2924, 2853, 1713, 1610, 1508, 1441, 1358, 1262, 1213, 1112, 1059, 1028.

2.2.14 Post-polymerization Click Chemistry: Post-polymerization was performed using click chemistry as follows.

2.2.15 P-Tyr coupled with PEG-350 Azide (P-Tyr-PEG-350):

Typical procedure for the click chemistry was explained in detail for MeO-PEG-350 azide reaction with P-Tyr. P-Tyr (100 mg, 0.234 mmol) and PEG_{350} azide (105.0 mg, 0.281 mmol) were taken into the polymerization tube and dissolve in 5 mL of DMSO. Once the solution become clear, Copper sulphate (29.0 mg, 0.117 mmol) and sodium ascorbate (46.0 mg, 0.234 mmol) were added. The reaction mixture stirred for 24 hours at 70 ℃. It was cooled and subjected to dialysis using 3.5 kDa semipermeable membrane for 48 h with continuous replenishing with fresh water. The reservoir is cheeked with the EDTA regularly and the dialysis is continued till the end of removal of Cu-residues completely. Yield = 175 mg (93 %). ^{1}H NMR (400 MHz ,$CDCl_3$) δ: 7.84 (br. °s., 1 H), 7.04 (d, *J* = 8.6 Hz, 2 H), 6.91 (d, *J* = 8.6 Hz, 2 H), 5.17 (br. s., 2 H), 5.17 (br.s NH), 4.64 - 4.47 (m, 3 H), 4.20 - 3.96 (m, 4 H), 3.88 (t, *J* = 5.3 Hz, 2 H), 3.79 - 3.68 (m, 1 H), 3.68 - 3.48 (m, 28 H), 3.38 (s, 3 H), 3.05 – 3.02 (m, 2 H), 1.61 - 1.57 (m, 4 H), 1.44 (s, 2 H), 1.30 - 1.27 (m, 16 H). ^{13}C NMR (100 MHz, $CDCl_3$) δ: = 171.8, 157.4, 156.0, 130.3, 114.8, 77.3, 76.7, 71.9, 70.5, 69.4, 65.6, 65.3, 59.0, 54.8, 29.7, 29.6, 29.4, 29.2, 28.9, 28.5, 25.8, 25.8 FT-IR: 2974, 1647, 1459, 1056, 897, 658.

2.2.16 P-Tyr coupled with PEG-750 Azide (P-Tyr-PEG-750):

Typical procedure for the click chemistry was explained in detail for MeO-PEG-750 azide reaction with P-Tyr. P-Tyr (100 mg, 0.234 mmol) and PEG_{750} azide (217.0 mg, 0.281 mmol) were taken into the polymerization tube and dissolve in 5 mL of DMSO. Once the solution become clear, Copper sulphate (29.0 mg, 0.117 mmol) and sodium ascorbate (46.0 mg, 0.234 mmol) were added. The reaction mixture stirred for 24 hours at 70 ℃. It was cooled and subjected to dialysis using 3.5 kDa semipermeable membrane for 48 h with continuous replenishing with fresh water. The reservoir is cheeked with the EDTA regularly and the dialysis is continued till the end of removal of Cu-residues completely. yield= 260 mg, 92 % ^{1}H NMR (400 MHz ,$CDCl_3$) δ: = 7.84 (br. °s., 1 H), 7.04 (d, *J* = 8.6 Hz, 2 H), 6.91 (d, *J* = 8.6 Hz, 2 H), 5.17 (br. s., 2 H), 5.17 (br.s NH), 4.64 - 4.47 (m, 3 H), 4.20 - 3.96 (m, 4 H), 3.88 (t, *J* = 5.3 Hz, 2 H), 3.79 - 3.68 (m, 1 H), 3.68 - 3.48 (m, 50 H), 3.38 (s, 3 H), 3.05 – 3.02 (m, 2 H), 1.61 - 1.57 (m, 4 H), 1.44 (s, 2 H), 1.30 - 1.27 (m, 16 H). ^{13}C NMR (100 MHz ,$CDCl_3$) δ: = 171.8, 157.4, 156.0, 130.3, 114.8, 77.3, 76.7, 71.9, 70.5, 69.4, 65.6, 65.3, 59.0, 54.8, 29.7, 29.6, 29.4, 29.2, 28.9, 28.5, 25.8, 25.8 FT-IR: 2974, 1647, 1459, 1056, 897, 658

2.2.17 P-Tyr coupled with PEG-2000 Azide (P-Tyr-PEG-2000):

Typical procedure for the click chemistry was explained in detail for MeO-PEG-2000 azide reaction with P-Tyr. P-Tyr (100 mg, 0.234 mmol) and PEG_{2000} azide (568.0 mg, 0.281 mmol) were taken into the polymerization tube and dissolve in 5 mL of DMSO. Once the solution become clear, Copper sulphate (29.0 mg, 0.117 mmol) and sodium ascorbate (46.0 mg, 0.234 mmol) were added. The reaction mixture stirred for 24 hours at 70 ℃. It was cooled and subjected to dialysis using 3.5 kDa semipermeable membrane for 48 h with continuous replenishing with fresh water. The reservoir is cheeked with the EDTA regularly and the dialysis is continued till the end of removal of Cu-residues completely. Yield = 0.5 g, 87 % ^{1}H NMR (400 MHz ,$CDCl_3$) δ: 7.84 (br. °s., 1 H), 7.04 (d, *J* = 8.6 Hz, 2 H), 6.91 (d, *J* = 8.6 Hz, 2 H), 5.17 (br. s., 2 H), 5.17 (br.s NH), 4.64 - 4.47 (m, 3 H), 4.20 - 3.96 (m, 4 H), 3.88 (t, *J* = 5.3 Hz, 2 H), 3.79 - 3.68 (m, 1 H), 3.68 - 3.48 (m, 172 H), 3.38 (s, 3 H), 3.05 – 3.02 (m, 2 H), 1.61 - 1.57 (m, 4 H), 1.44 (s, 2 H), 1.30 - 1.27 (m, 16 H) ^{13}C NMR (100 MHz , $CDCl_3$) δ: 171.8, 157.4, 156.0, 130.3, 114.8, 77.3, 76.7, 71.9, 70.5, 69.4, 65.6, 65.3, 59.0, 54.8, 29.7, 29.6, 29.4, 29.2, 28.9, 28.5, 25.8, 25.8 FT-IR: 2974, 1647, 1459, 1056, 897, 658.

2.2.18 P-Tyr coupled with PEG-5000 Azide (P-Tyr-PEG-5000):

Typical procedure for the click chemistry was explained in detail for MeO-PEG-5000 azide reaction with P-Tyr. P-Tyr (100 mg, 0.234 mmol) and PEG_{5000} azide (1.41 g, 0.281 mmol) were taken into the polymerization tube and dissolve in 5 mL of DMSO. Once the solution become clear, Copper sulphate (29.0 mg, 0.117 mmol) and sodium ascorbate (46.0 mg, 0.234 mmol) were added. The reaction mixture stirred for 24 hours at 70 ℃. It was cooled and subjected to dialysis using 10.0 kDa semipermeable membrane for 48 h with continuous replenishing with fresh water. The reservoir is cheeked with the EDTA regularly and the dialysis is continued till the end of removal of Cu-residues completely. Yield = 1.15 g, 90% ^{1}H NMR (400 MHz , ,$CDCl_3$) δ: 7.84 (br. °s., 1 H), 7.04 (d, *J* = 8.6 Hz, 2 H), 6.91 (d, *J* = 8.6 Hz, 2 H), 5.17 (br. s., 2 H), 5.17 (br.s NH), 4.64 - 4.47 (m, 3 H), 4.20 - 3.96 (m, 4 H), 3.88 (t, *J* = 5.3 Hz, 2 H), 3.79 - 3.68 (m, 1 H), 3.68 - 3.48 (m, 448 H), 3.38 (s, 3 H), 3.05 – 3.02 (m, 2 H), 1.61 - 1.57 (m, 4 H), 1.44 (s, 2 H), 1.30 - 1.27 (m, 16 H) ^{13}C NMR (100 MHz , ,$CDCl_3$) δ: 171.8, 157.4, 156.0, 130.3, 114.8, 77.3, 76.7, 71.9, 70.5, 69.4, 65.6, 65.3, 59.0, 54.8, 29.7, 29.6, 29.4, 29.2, 28.9, 28.5, 25.8, 25.8 FT-IR: 2974, 1647, 1459, 1056, 897, 658.

2.2.19 Self-assembly of Polymers:

5.0 mg of polymer and 0.5 mg of doxorubicin drug were added in 15 ml vials, and 2 ml HPLC grade dimethyl sulphoxide (DMSO) was added into the vial. Once the polymer as well as drug were dissolved completely, then 3 ml of milli Q water was added slowly. The solution was stirred for 4 hours at 25 ℃, and the solution was transferred into the dialysis membrane of 1 kDa and dialyzed against milli Q water for 48 h to remove the unencapsulated drug/dye and DMSO. The drug loading content and drug loading efficiency were measured by using UV absorbance spectroscopy as reported earlier.[43] A similar method was adopted to encapsulate NIR bio probe IR-780.

To encapsulate DOX in the nano-precipitation method, the 5.0 mg polymer and 0.5 mg drug/dye were added into the vial contains 5 mL water, and sonicated for 1 h in the milli Q water. The solution was centrifugation at 8000 rpm for 5 minutes, and then it was subjected to dialysis as described above to remove unencapsulated dye or drug.

To encapsulate the DOX by solvent evaporation method, 5.0 mg polymer was dissolved in the 0.5 ml THF it was mixed with 0.5 mg of DOX and dissolved in 0.25 mL of THF. 5.0 ml Milli Q water was taken in a 15 ml vial and kept stirring. The polymer+DOX solution was added dropwise into the vial and mixed with constant stirring for 30 minutes at ambient temperature. The vial was kept in a water bath at 70 ℃ for 20 minutes to remove the THF. Further, the solution was centrifugation at 8000 rpm for 5 minutes, and the unencapsulated drug or dye settled down to the falcon it was filtered and removed.

2.2.20 CAC Measurements:

The critical aggregation concentration of the polymer was determined by pyrene as a probe as reported earlier.[30] The pyrene concentration was fixed as 0.6 µM and the polymer concentration varied from 0.5 mg/mL to $1x10^{-6}$ mg/mL. The polymer solution containing pyrene was sonicated for 3 hours and then kept for equilibration up to 12 hours. Further nitrogen purging was done to remove the O_2 from the sample. The fluorescence spectra of the samples were recorded and the ratio of the vibronic levels I_1 and I_3 was plotted to determine the CAC. The pyrene was excited at 337 nm and collected at 347-500 nm.

2.2.21 Release kinetic studies:

1 ml DOX loaded sample and 10 U Esterase enzyme were taken in 1 kDa dialysis tube. 3 ml 1x PBS were taken in the reservoir and the incubation was done at 37 ℃ for 24h. Reservoir solution (2 ml) were taken frequently estimate the DOX release by absorbance spectroscopy and cumulative drug release profiles were estimated as reported earlier.[30] A similar experiment was performed without esterase enzyme as control.

2.2.22 Cell viability assay:

In the 3-(4,5-dimethylthiazol-2-yl)-2,5-diphenyltetraazolium bromide (MTT) assay in 96-well plate following earlier procedure.[43] The cell viability and biocompatibility of the polymer alone and the drug with nanoparticles were recorded using an MTT assay. For this experiment, the MCF 7 breast cancer cell and healthy wild-type MEF cell lines were used. 1000 cells per well were seeded in 100 µL of complete media and incubated for 16 hours. After 16 hours, the media were aspirated from a 96-well plate before the sample addition. Samples were dissolved in 300 µL complete media and added to each well. The complete media comprised of DMEM media with 1% penicillin-streptomycin solution and 10 % fetal bovine serum. The 96-well plate was incubated for 72 hours in an incubator under standard conditions of 5 % CO_2 and 70 % humidity at 37 ^oC. After completion of 72 hours, the media were aspirated and the MTT reagent dissolved in the complete media at a concentration of 0.5 mg/mL was added to each well and incubated for 4 hours. After 4 hours the media was carefully aspirated without disturbing the formed Formazan crystal. Then in each well 100 µL of HPLC-grade Dimethyl sulphoxide (DMSO) was added to dissolve formazan crystals, forming a purple color solution. The 96 well plate protected from light was additionally kept on a shaker for 10 minutes for homogeneous mixing. A Varioscan microplate reader was also used to record the absorbance at 570 nm from each well on the 96-well plate. These experiments were recorded in triplicate. The percentage of cell viability was calculated against the control cells.

2.2.23 Cellular uptake studies:

Fixed cell imaging was carried out the cellular uptake of drug or dye-loaded polymeric nanoparticles following our earlier report.[43] The cellular uptake for that cancerous cell MCF-7 were used. In 6 well plate coverslips were kept then 10^5 cells were added in each well and along with 2 ml complete media. the cells were incubated at 37 ℃ for 16 hours, under the incubator in the 5 % CO_2 and 1 % O_2 atmosphere. The lyophilized polymeric samples were redispersed

in the complete media. These polymeric samples were added into the 6 well plate containing 10^5 cells. These plates were incubated at various time points; however, the media were aspirated and cells were fixed on microscopic slides for following procedure as follows. The media from the 6-well plates was aspirated, and the cells were washed twice with 1 mL of 1x PBS in each well. Subsequently, 1 mL of 4 % paraformaldehyde was added to each well and left for 15 minutes at 4 ℃ to fix the cells. Afterward, the cells were washed twice with 1 mL of 1x PBS. Next, a solution of DAPI was added to the wells and allowed to incubate for 2 minutes. Excess DAPI was then washed with 1x PBS. For slide preparation, one drop of 70 % glycerol solution was added to each microscopic slide, and a coverslip was carefully placed on top, ensuring the stained cells were exposed to the glycerol solution. The fixed slides were left to dry for 12-18 hours and were then ready for confocal microscopy. Confocal microscopy imaging was performed using a Zeiss LSM 710 microscope. The scan settings involved using a laser with a wavelength of 488 nm for DOX excitation and a wavelength of 405 nm for DAPI dye excitation. The acquired images were analyzed using Fiji software.

2.2.24 Hemolysis Assay:

To assess the hemolytic activity of a polymer, a hemolysis assay was conducted as reported earlier.[31,32] The polymer samples were prepared by dissolving them in 1x PBS at a concentration of 100 µg/mL. Fresh blood was collected from C57BL/6 mice, and red blood cells (RBCs) were separated via centrifugation at 8000 rpm. Subsequently, a 5 % v/v RBCs solution was prepared in PBS. For the assay, 100 µL of the polymer solution in PBS was combined with 100 µL of the RBCs solution. The mixture was then incubated at 37 ℃ for 1 hour. To serve as controls, a 1 % solution of Triton-X was used as a positive control, while PBS was used as a negative control. The experiment was conducted in triplicates to ensure reliability. Following the incubation period, the samples were centrifuged at 8000 rpm for 5 minutes. The observation of RBCs pellet at the bottom of the Eppendorf tube indicated the biocompatibility of the polymer. The percentage of hemolysis was determined using a previously reported procedure[31]

2.2.25 IVIS-mediated Biodistribution studies:

For biodistribution studies using IVIS, 8 female Balb/c mice aged 8-12 weeks and weighing ~25g were randomly divided into 3 groups. The first group (n=3) received intraperitoneal injections of free IR-780 dye (0.5 mg/kg) in PBS (100 µL), the second group (n=3) received intraperitoneal injections of IR-780 loaded polymer nanoparticles (0.5 mg/kg) in PBS (100

µL), and the last group (n=2) received injections of PBS (100 µL). Retro-orbital plexus puncture was used to collect Blood samples at 24-, and 72-hours post-injection from alternate sides. In case of bleeding, an absorbable hemostatic gelatin sponge (AbGel) was used. Biodistribution was monitored in real time using IVIS spectrum (Perkin Elmer). The mice were anesthetized and imaged at 4, 24, 48 and 72 hours to capture both dorsal and ventral views using the emission and excitation filters of λexc = 745 nm and λem = 800 nm, respectively. At the end of 72 hours, the mice were euthanized using an overdose of anesthesia (isoflurane) and perfused with PBS prior to organ harvesting. The harvested organs were used for whole-organ imaging analysis commissioning the same excitation and emission filters. Plasma samples were isolated from the collected blood by centrifugation, and 10 µL was inoculated in each well of a 96-well plate. Samples were then diluted 10 times with PBS (n=3) and subjected to IVIS imaging using the same filters as mentioned above. The average radiance was calculated from the instrument software and used to quantify the amount of the IR-780 dye.

2.2.26 Enzyme Release and Inhibition Studies:

In order to conduct in vitro release studies, DOX-loaded P-Tyr-PEG-750 samples (1 mL) were subjected to incubation in PBS at a physiological temperature of 37 °C using a UV absorbance spectrophotometer. Combination of 10 U of Horse Liver Esterase Enzyme and 3 mg of the inhibitor (4-nitrophenyl-octyl-carbamate)[57] was used, and the samples were incubated at 37 °C. For enzymatic hydrolysis, 10 U of horse Liver Esterase enzymes were employed. Subsequently, UV absorbance readings were taken at three-hour intervals, and the data obtained were utilized to generate a plot illustrating cumulative release versus concentration.

$$\text{Drug or Dye Loading Content (\%)} = \frac{\text{weight of drug or dye in nanoparticle}}{\text{weight of polymer taken}} \times 100$$

$$\text{Drug or Dye Loading Efficiency (\%)} = \frac{\text{weight of drug or dye in nanoparticle}}{\text{weight of drug in feed}} \times 100$$

2.2.27 In Vivo Toxicity Studies:

All experiments were conducted under the approval of the Animal Ethics Committee, with the assigned approval number IISER Pune/ IAEC/2022_01/16. Healthy female Balb/c mice, aged 8–12 weeks, were utilized in the study. The experimental groups included a control injected with PBS, and samples loaded with IR-780 and P-Tyr-PEG-750+IR780, administered at a dose of 15 mg/kg via intraperitoneal injection. After a 72-hour interval, blood was collected from the mice through the retro-orbital sinus, and organs were harvested. Subsequently, Chaitanya Laboratories performed hematological and biochemical analyses to assess the toxicity of the administered samples.

2.2.28 Hematological analysis of organ:

Firstly, a hematological analysis was conducted by intraperitoneally injecting female Balb/c mice with samples of 15 mg/kg PBS, P-Tyr-PEG-750, IR-780 loaded, and free IR-780. The mice were then kept for 72 hours. Subsequently, deep anesthesia was administered, and perfusion was carried out using 1X PBS. Organs were harvested and fixed in 4% paraformaldehyde at 4 °C for 24 hours. The organs were later transferred to 30% sucrose for cryo-preservation over 24-48 hours. Organ sections of 3-4 µm thickness were obtained on gelatin-coated slides. For staining, a stock of Hematoxylin and Eosin was prepared and stored in a couplin jar at room temperature. The slides were processed stepwise: first, a 5-minute dip in hematoxylin, followed by two dips in tap water, a 1-minute immersion in Scott's tap water, and a 30-second exposure to Eosin. The slides then underwent a series of alcohol grades (95%, 100%, 50%, 50% xylene) and xylene (100%). Finally, the sections were mounted using DPX mountant from (Thermo Fisher Scientific). The prepared slides were stored at 4 °C and imaged using a bright-field microscope (Carl Zeiss).

2.3 Results and Discussion

2.3.1 Synthesis of monomer

L-Tyrosine is a bioresource contains trifunctional groups such as carboxylic acid, amine and phenolic OH units. The acid group was converted into methyl ester, the amine group was converted into urethane, and the phenolic OH functionality was anchored with propargyl unit as shown in Scheme 2.1.

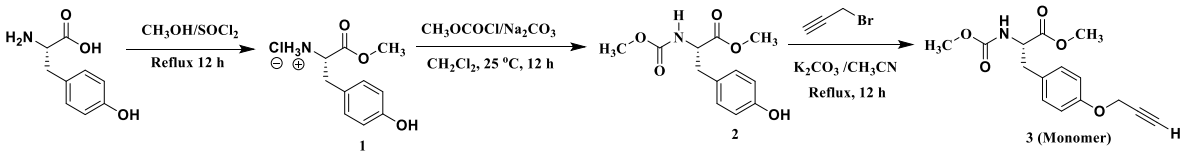

Scheme 2.1 *Synthesis of propargyl functionalized L-Tyrosine ester-urethane monomer.*

The structure of the multifunctional L-tyrosine monomer was confirmed by NMR and it was found to be thermally stable up to 250 ℃ and established their suitability for solvent-free melt polymerization (see Appendix Figure S1). The L-tyrosine monomer **3** and 1,12-dodecane diol were taken 1:1 mole ratio in melt polymerization tube and subjected to polymerization at 150 ℃ for 4 h under nitrogen purge in the presence of 1 mol % [$Ti(OBu)_4$] as catalyst. In this process, oligomers consisting of 2-6 repeating units were produced which was subjected to high vacuum (0.01mbar) to yield high molecular weight polymers and their chemical structure are shown in scheme 2.2.

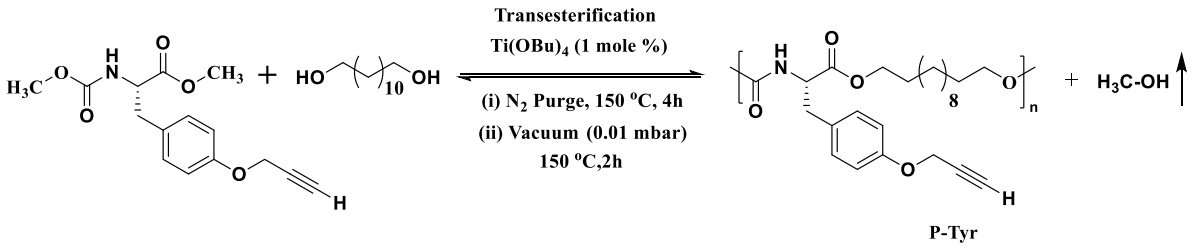

Scheme 2.2 *Melt transesterification process to formed new poly(ester-urethane)s.*

The chemical structures of the P-Tyr is confirmed by ^{1}H-NMR as shown in Figure 2.2. During the dual trans (ester-urethane) polycondensation, the methoxy proton of monomer at 3.71 ppm and 3.66 ppm (proton a and a,' in Figure 2.2a) vanished and new ester peaks appeared at 4.07 ppm and

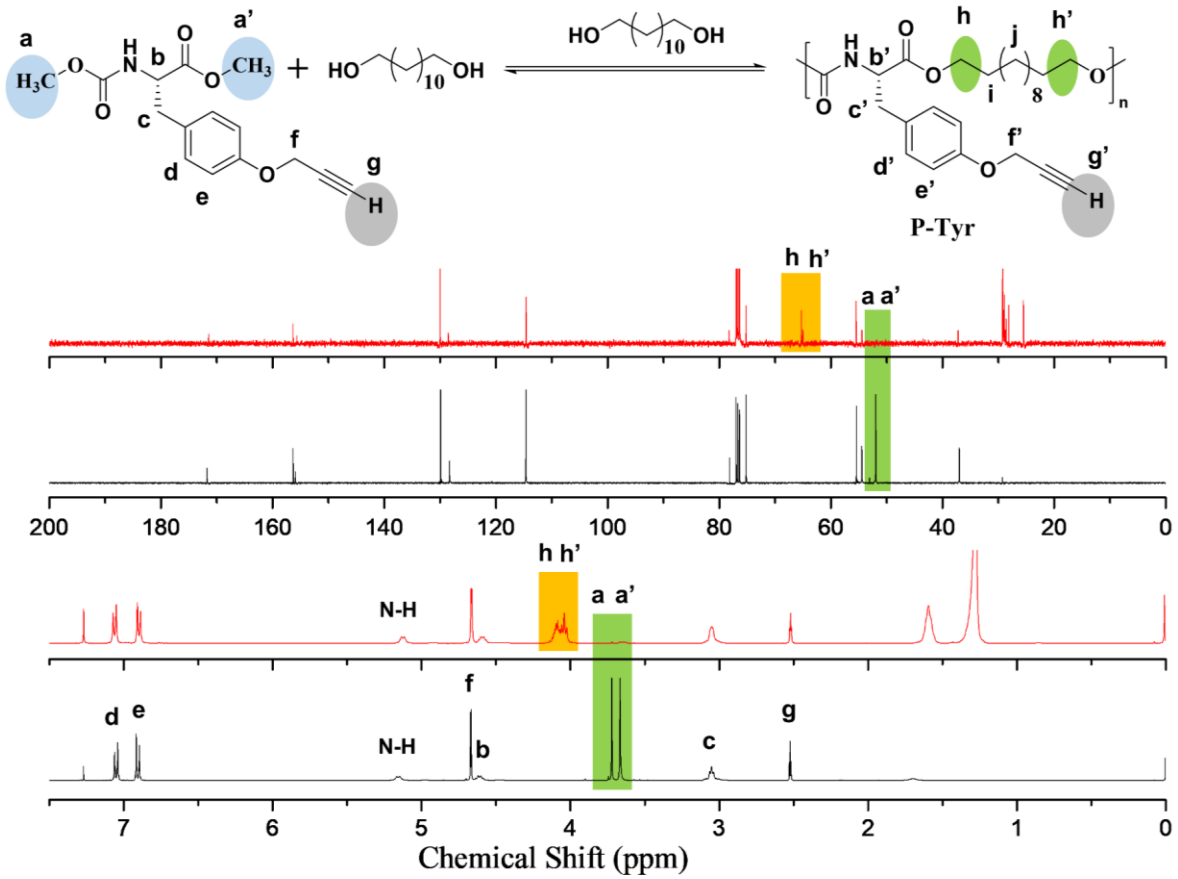

Figure 2.2 *(a) ^{1}H-NMR spectrum of monomer. (b) homo polymer P-Tyr, and (c) ^{13}C-NMR spectrum of monomer. (d) ^{13}C-NMR spectrum of polymer. All the spectra were recorded in $CDCl_3$.*

4.10 ppm (proton h and h' in Figure 2.2b) in the polymer. The peak corresponding to propargyl group at 2.5 ppm (peak-g') and its intensity matched very well with other protons indicating that it is completely inert during the polycondensation process. The two peaks corresponding to the -OCH_3 protons in monomer at a+a' (in Figure 2.2a) nearly vanished during the polymerization; thus, they appeared very small in intensities in Figure 2.2b. Since the chains contain both ester and urethane chain ends in the poly(ester-urethane)s the intensities of both methoxy protons were required to be considered for the estimation of DPn. By comparing the intensity of the methoxy end groups at 3.71 to 3.66 ppm with the new ester peaks at 4.07- 4.10 ppm in the polymer spectrum (Figure 2.2b), the degree of polymerization (n or X_n) was estimated. The degree of polymerization was found to be 40, which corresponds to the occurrence of 97 to 98 % of reaction as per the Carothers formula [X_n= (1/1-p), where p is the extent of reaction].

Based on NMR, the number average molecular weight was estimated to be M_n = 17,000 g/mol corresponding to the occurrence of 97.5 % reaction. In the present investigation, the lab-scale melt polycondensation chemistry showed the occurrence of ~ 98 % reaction and more than 99 % is only feasible in the industrial scale gallon reactor. ^{13}C-NMR of the monomer (3) showed methoxy carbon atoms at 52 to 53 ppm (see Figure 2.2c) which were completely vanished in the polymer P-Tyr spectrum and new carbon peaks for the ester chemical linkage in the backbone appeared at 62 to 63 ppm indication the formation of high molecular weight polymers (see Figure 2.2d). Molecular weight of the P-Tyr was determined by size exclusion chromatography (SEC) in a THF solvent using polystyrene as a standard (see Appendix Figure S1). The SEC chromatograms exhibited mono-model distribution with M_n = 18,200 g/mol and M_w = 46,800 g/mol with polydispersity Đ = 2.5. The M_n determined by ^{1}H-NMR and SEC are matching very well. Azide-functionalized polyethylene glycol monomethyl ether having various molecular weights ranging from 350 to 5000 g/mol (PEG-350, PEG-750, PEG-2000, and PEG-5000) were synthesized and their structures are shown in Scheme 1.3.

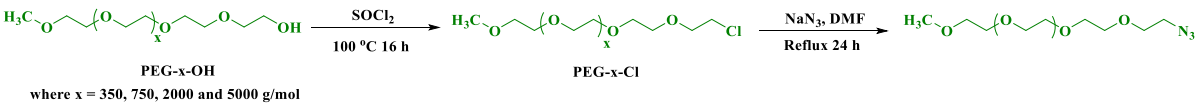

Scheme 2.3 *Synthesis of polyethylene glycol monomethyl ether azides.*

For this purpose, the hydroxyl group was converted into chloride by thionyl chloride which was subsequently reacted with sodium azide to yield corresponding PEG-azides. PEG-azides were completely characterized by ^{1}H-NMR, ^{13}C-NMR, in Proton NMR the polyethylene glycol monomethyl ether-OH (PEG-750-OH) -**CH$_2$**-OH peak at 3-72 ppm were completely vanish after formation polyethylene glycol monomethyl ether-Cl (PEG-750-Cl) -**CH$_2$**-Cl comes at 3.78 ppm and after formation of polyethylene glycol monomethyl ether-N_3 (PEG-750-N_3) the proton at 3.78 were completely vanished and new peak were appeared at -**CH$_2$**-N_3 3.38 ppm its merging with end group of methoxy proton. In ^{13}C-NMR the polyethylene glycol monomethyl ether-OH (PEG-750-OH) -**CH$_2$**-OH at 61 ppm are vanished completely and new peak were appeared at 42 ppm it confirms the formation polyethylene glycol monomethyl ether-Cl (PEG-750-Cl) -**CH$_2$**-Cl subsequently after formation of polyethylene glycol monomethyl ether-N_3 azide (PEG-750-N_3)-**CH$_2$**-N_3 the peak at 42 ppm were completely vanished and new peak were appeared at 50 ppm it confirms the formation of P-750-Azide the spectra are (see Appendix Figure S2) and other spectra of PEG-350-Azide, PEG-2000-Azide

and PEG-5000 (see Appendix Figure S3-S4) MALDI TOF, and FTIR these details are given in Figures 2.3a to 2.3b.

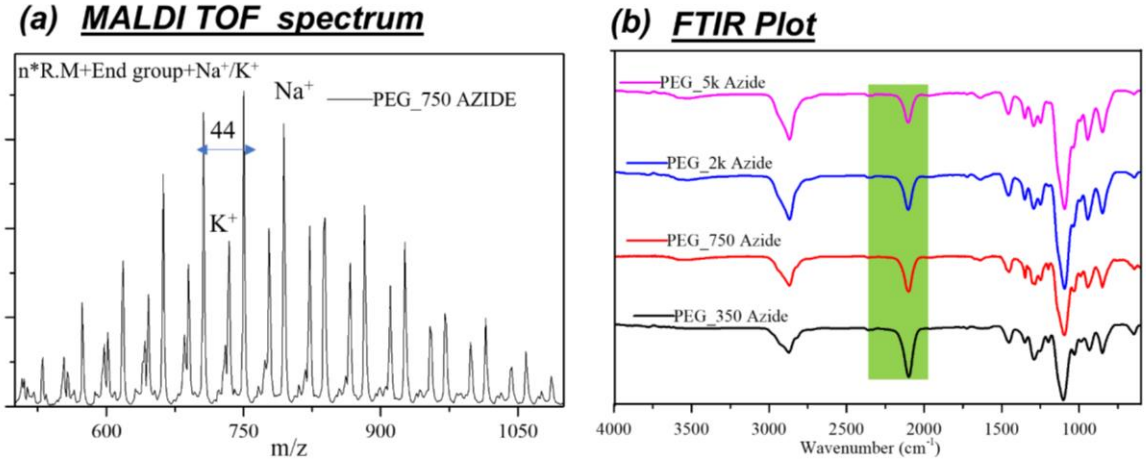

Figure 2.3 *(a) MALDI TOF spectra of PEG-750 Azide. (b) FT-IR spectra of All the PEG-azides. The peak corresponding to azide stretching frequency is shown in Figure 2.3b by arrow.*

The MALDI TOF spectrum of PEG-750 Azide were showing single distribution and the peak were matches with the PEG-750 Azide molecular weight and the spectra are shown in Figure 2.3a Further it confirms the formation of PEG-750 Azides and other PEG Azides MALDI are (see Appendix Figure S5). After that all PEG Azide were confirmed by FT-IR analysis and in FTIR the Azide stretching frequency 2100 cm^{-1} it confirms the formation of PEG Azides and the spectra are shown in Figure 2.3b. Propargyl functionalized P-Tyr polymer was subjected to click chemistry with PEG-azides in DMSO using sodium ascorbate and Copper (II) sulphate as a catalyst. The polymers were purified by continuous dialysis using 3.5 kDa dialysis membranes for PEG-350 to PEG-2000 and 10 kDa for PEG-5000 to remove the unreacted PEG chains and Cu-residues. The reservoir was checked with EDTA till all the cupper completely removed by the dialysis method, and the polymers were lyophilized and stored. These polymers were referred as P-Tyr-PEG-X, where x= 350, 750, 2000 and 5000, and the structure are shown in Scheme 2.4.

2.3.2 Post polymerization click reaction

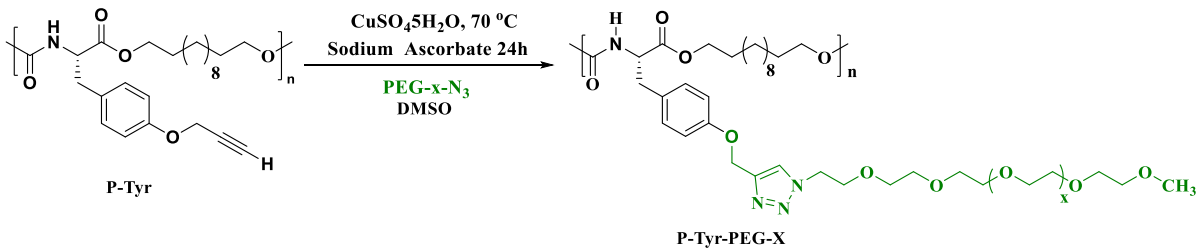

Scheme 2.4 *Synthesis of clickable L-tyrosine poly(ester-urethane) and its clicked PEGylated amphiphilic polymers.*

In Figure 2.4a, the ^{1}H-NMR spectrum of P-Tyr PEG-750-clicked polymer P-Tyr-PEG-750 showed completely vanishing of propargyl units at 2.5 ppm in the end product confirming the occurrence of > 99 % of the click reaction as shown in Figure 2.4c.

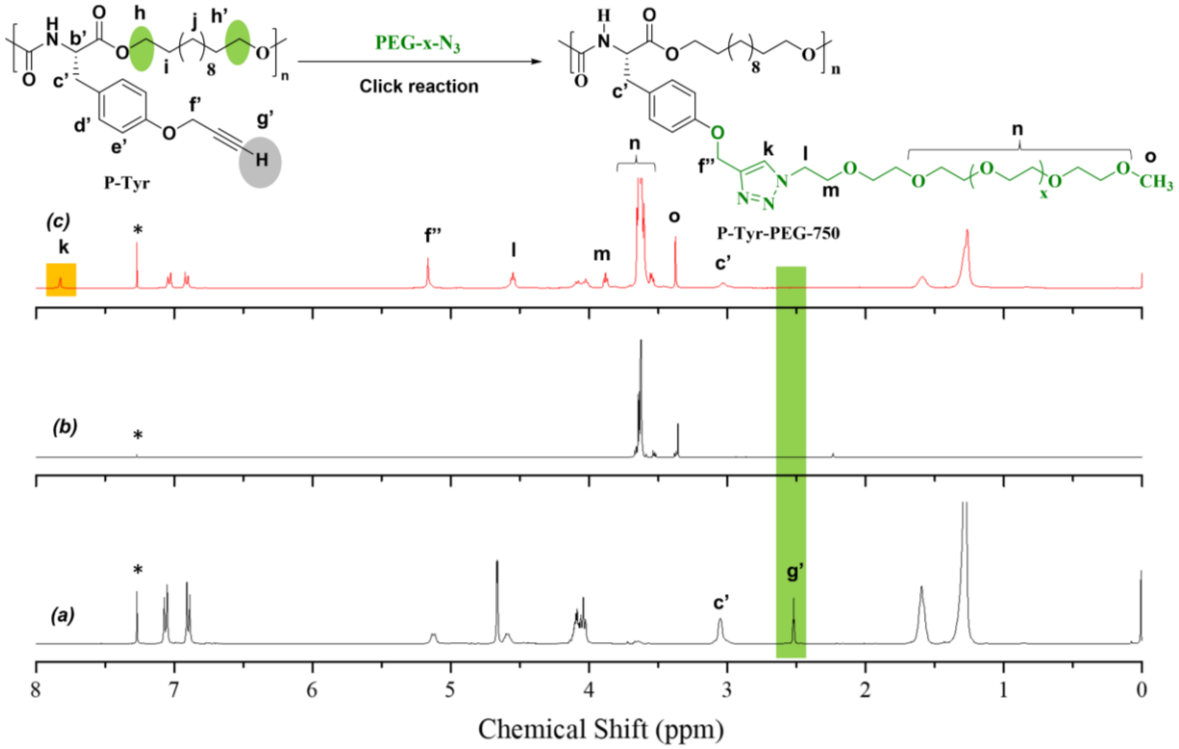

Figure 2.4 *(a) ^{1}H-NMR spectrum of homo polymer P-Tyr. (b) ^{1}H-NMR spectrum of PEG Azide, and (c) P-Tyr-PEG-750. All the spectra were recorded in $CDCl_3$.*

Further, the peaks corresponding to C**H**$_2$-triazole and triazole Ar-**H** at 5.20 and 7.75 ppm, respectively, which support the completeness of click reactions (other clicked polymer P-Tyr-PEG-350, P-Tyr-PEG-2000 and P-Tyr-PEG-5000 ^{1}H-NMR were showed in Appendix Figure S6).

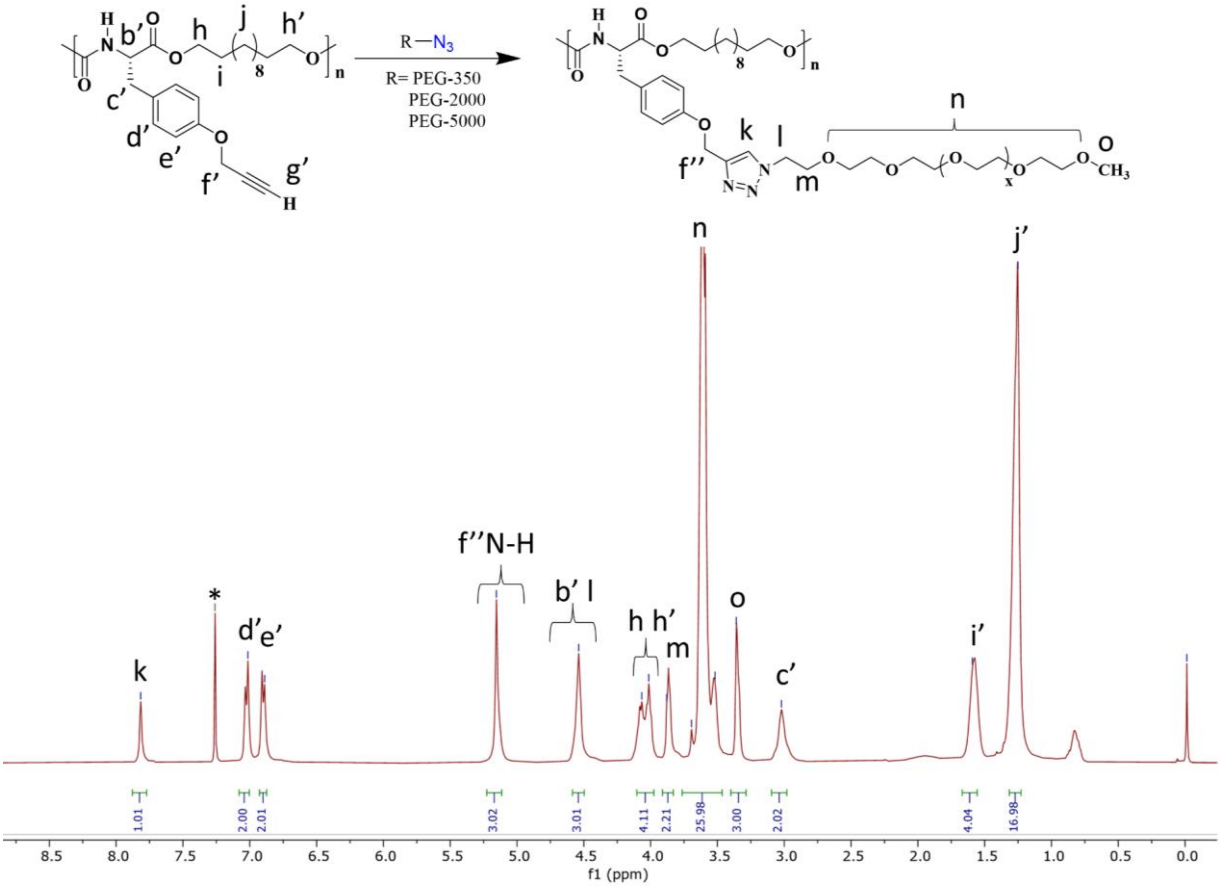

Figure 2.5 *^{1}H-NMR spectrum of P-Tyr-PEG-350 in $CDCl_3$. The peak integration values are given for each proton in the structure.*

The peak intensities of all other protons in the polymer backbone matched very well with expected structure. The comparison of NMR spectra of azide protons in PEG-OCH$_2$C**H**$_2$-N$_3$ (see Appendix Figure S2, 3.38 ppm) are completely disappeared in the synthesized polymer confirming the occurrence of more than 99 % of the click reactions. The NMR peak integration values at 3.3 ppm for the -OCH$_3$ protons (peak-o) matched with polymer benzyl-C**H**$_2$ protons (at 3.03 ppm, peak-c' in) having nearly 1:1 in ratio as expected (expanded NMR spectrum with complete peak integration details is shown in Figure 2.5). In Figure 2.5, the polymer backbone peaks in the NMR spectrum P-Tyr-PEG-350 is clearly visible since the mass contributed by the PEG-350 by click chemistry (40x350 = 14,000 g/mol) is comparable to that of its polymer backbone (16,000 g/mol). On the other hand, the number of PEG chains attached in P-Tyr-

PEG-5000 via click reaction account for the molecular weight of 200,000 g/mol in the total mass of 216,000 g/mol (40 repeating x repeating unit mass 427 = 16,000 g/mol). Due to the large mass added by the PEG chains in the P-Tyr-PEG-5000 sample, the NMR signals appeared very low for the backbone compared to the narrow PEG chain. FT-IR spectra in Figure 2.6a. and other clickable FT-IR spectra are shown in Appendix Figure S8a). clearly showed the disappearance of -N_3 stretching frequencies of PEG-azides at 2100 cm^{-1} in their click-polymer products and evident for the complete conversion of azide into triazole units. The FT-IR analysis in Figure 2.6a further support the completion of click chemistry in the polymer samples. SEC of the click-products P-Tyr-PEG-X were determined in DMF solvent (polymers were found to be soluble in DMF) using a triple detector setup consisting of a refractive index (RI) detector, light scattering detectors RALs and LALs. SEC chromatograms of the polymers are showed in Figure 2.6b and the molecular weights are reported in the table 2.1. The nascent propargyl-substituted polymer P-Tyr showed mono-model distribution in DMF and showed M_n = 13,500 g/mol, M_w = 40,800 with Đ =3.0 which is comparable to that of SEC values obtained in THF (see Appendix Figure S1). As expected, the SEC chromatograms of the PEG-chain clicked polymers appeared at low retention time in Figure 2.6b.

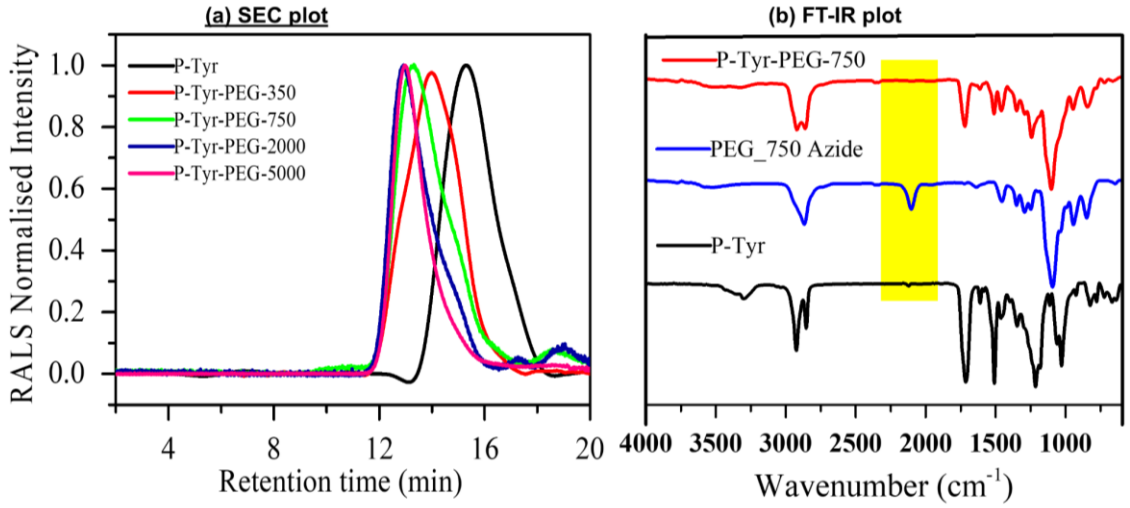

Figure 2.6 *(a) Size exclusion chromatograms of polymers in DMF. (b) FT-IR spectra of PEG azide and their Clickable polymer.*

The NMR based molecular weights (M_n) for each PEGylated polymers were estimated by the formula Mn = 40 x (each polymer repeating units + click PEG-X units), where x= 350, 750, 2000 and 5000 g/mol). This estimated the expected molecular weights for the PEGylated polymers from moderate (M_n = 31 x10^3 for PEG 350) to ultra-high molecular weights (M_n =

217x10^3 g/mol for PEG-5000). The dn/dc values for the PEGylated samples were determined by Omnisec software in SEC as 0.031, 0.032, 0.051 and 0.011 for P-Tyr-PEG-X (X = 350, 750, 2000 and 5000 g/mol), respectively (see in Appendix Figure S7). By applying these values, the M_n and M_w of the samples were determined and given in the table 2.1. The M_n determined by SEC and NMR were matching very well upto PEG-2000 side chains substitution; however, the SEC underestimate the PEG-5000 sample which is beyond our SEC column limit. Based on the above NMR, FT-IR and triple detector SEC analysis, the complete occurrence of the post-polymerization click chemistry is confirmed in the L-tyrosine based polymers.

Table 2.1. *containing the molecular weights of the Polymers*

Sample	^{1}H-NMR[a] M_n (g/mol)	SEC Triple Detector[b] M_n (g/mol)	M_w (g/mol)	Đ
P-Tyr	17000	13500	40800	3.0
P-Tyr-PEG-350	31000	31600	94600	2.9
P-Tyr-PEG-750	47000	44000	139200	3.1
P-Tyr-PEG-2000	97000	87700	200900	2.2
P-Tyr-PEG-5000	217000	116800	386400	3.3

a)1H-NMR NMR molecular weights are calculated using the expression: M_n = (DP × repeating unit mass). b) Number (M_n) and weight average molecular weight (M_w), and dispersity (Đ) were determined by size exclusion chromatography in DMF at 70 ºC using triple detector (RI, RALS and LALS).

2.3.3 Thermal properties of polymers

Thermogravimetric analysis (TGA) confirmed the high thermal stability of the polymers up to 350-400 ℃ as shown in Figure 2.7a. Differential scanning calorimetry (DSC) analysis was performed to study the thermal transitions in P-Tyr and P-Tyr-PEG-X samples, and the heating cycle thermograms are shown in Figure 2.7b (see Appendix Figure S8b for cooling cycle data).

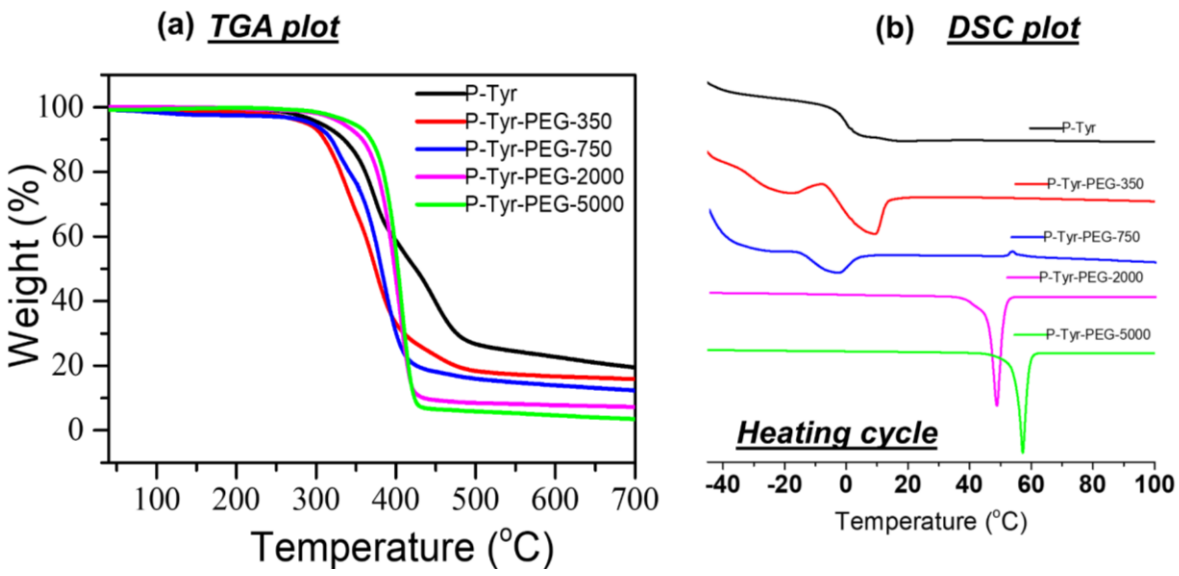

Figure 2.7 *(a) TGA thermograms of polymers. TGA was performed at 10 °/min under N_2 atmosphere. (b) DSC thermograms of the polymers recorded at 10 °/min under nitrogen atmosphere.*

The propargyl polymer P-Tyr was found to be amorphous and showed only glass transition temperature at -4°C. The PEGylated P-Tyr-PEG-X polymers were found to be semi-crystalline in nature; however, they significantly vary their enthalpies of melting (ΔH_m) or crystallization (ΔH_c). For instance, the P-Tyr-PEG-2000 and P-Tyr-PEG-5000 polymers showed higher enthalpies of melting (ΔH_m 106 J/g and 120 J/g) with respect to their higher degree of packing in the polymer matrix. On the other hand, the lower PEGylated analogues P-Tyr-PEG-350 and P-Tyr-PEG-750 showed relatively low crystallinity. The parent polymer backbone is amorphous; thus, the semi-crystallinity in the polymer matrix is predominantly associated with the side-chain packing of the PEG units, as shown in **Table 2.2.**

Table 2.2. *containing the thermal stability of Polymers*

Sample	T_D[a] (°C)	T_g[b] (°C)	T_m[c] (°C)	ΔH_m[d] (J/g)	T_C[e] (°C)	ΔH_C[f] (J/g)
P-Tyr	315	-4.0	-	-	-	-
P-Tyr-PEG-350	300	-	4.0	12.00		11.00
P-Tyr-PEG-750	305	-	0	4.43		3.25
P-Tyr-PEG-2000	336	-	48	106.7		105.2
P-Tyr-PEG-5000	346	-	57	120.3		118.9

a) Temperature of decomposition (Td) determined from TGA. [b)] The glass transition temperature (Tg) was determinedfrom second heating cycle of DSC thermogram. [c)] Melting point (Tm) of the polyester determined heating cycle. [d)] Enthalpy of melting determined from area under the curve of heating cycle. [e)] Temperature of crystallization (Tc) of the polyester determined cooling cycle. [f)] Enthalpy of

The polymers samples were subjected to PXRD and their diffraction patterns are shown in Figure 2.8a. P-Try and P-Tyr-PEG-750 showed a broad pattern centered at 4.52 Å indicating their highly amorphous state as observed in their DSC profiles. On the other hand, the long chain PEGylated polymers P-Tyr-PEG-2000 and P-Tyr-PEG-5000 exhibited side chain crystallization; as a result, two sharp peaks appeared at 4.66 Å and 3.94 Å corresponding to the PEG chain crystallization and this observation was also reflected in their DSC thermograms. Further, the enthalpies of crystallization are plotted along with the P-Tyr-PEG-X and shown in Figure 2.8b with appropriate model diagram for the short and long-PEGylated polymer brushes. The % crystallinity was estimated by considering the (ΔH_c) of PEG-5000 as maximum for packed chain length using the formula: % Crystallinity = [ΔH_c of P-Tyr-PEG-X / ΔH_c of PEG-5000] x 100; and the values are indicated in Figure 2.8b. It is very clear from this plot that the PEG-350 and PEG-750 chains were not capable of undergoing side-chain packing (only 2-7 % crystalline) and the amorphous backbone do not allow them to back-fold. Interestingly, this influence by the chain backbone is overcome by the side-chain packing at longer PEG chains and the P-Tyr-PEG-2000 and P-Tyr-PEG-5000 polymers retained almost 65-70 % of the semi-crystallinity. This phenomenon is represented by the diagram in Figure 2.8b.

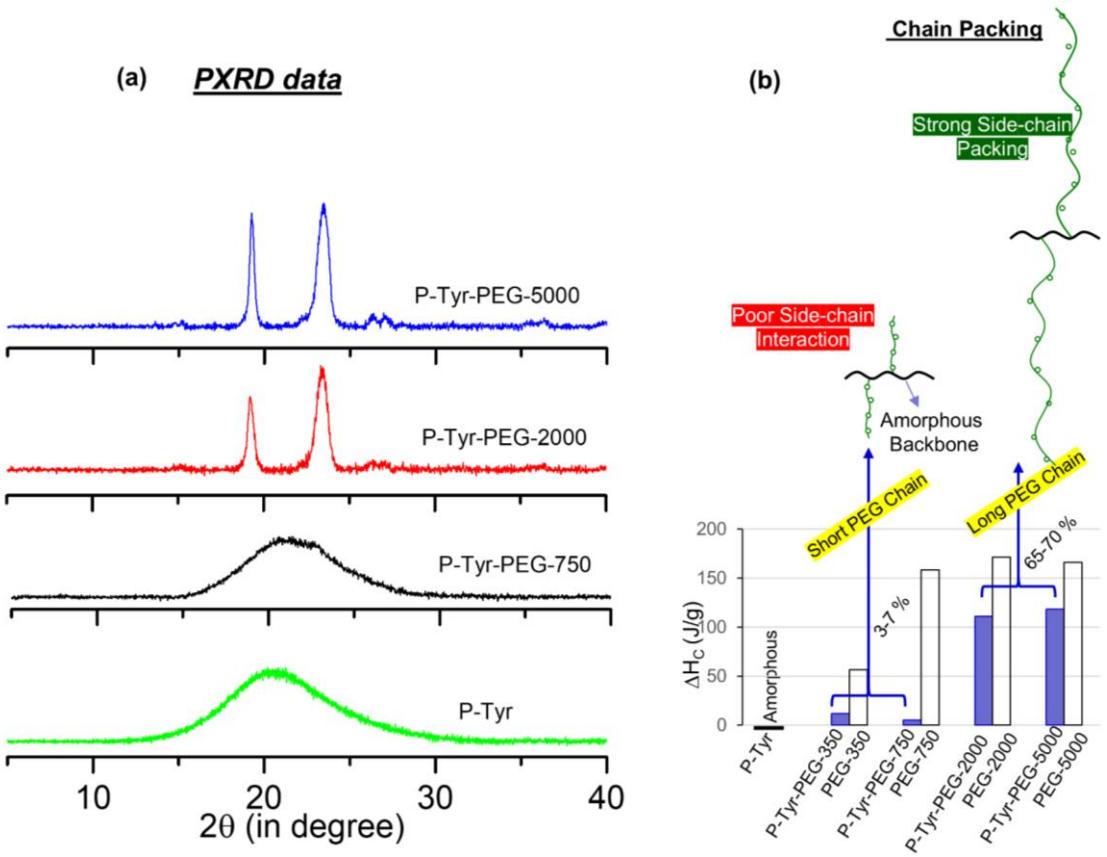

Figure 2.8 *(a) PXRD patterns of the polymers were recorded in dry powder sample at 25 ℃. (b) Schematic diagrams showing the chains packing of polymer brushes having short and long PEG side arms. The plot showed the enthalpy of melting for PEGx-OH alcohols and their corresponding polymer brushes.*

Based on thermal analysis, one could conclude that the PEG chain length played a very crucial role in determining the packing ability of the click-chemistry strategy to induce semi-crystallinity in polymer matrix. In general, this approach is very useful fine-tuning thermal properties and other mechanical of polymers, more specifically for manipulating semi-crystalline for long-term in engineering thermoplastics. Since the present work is mainly focused to explore the L-tyrosine PEGylated polymers amphiphilicity for biomedical applications, the influence of the side-chain interaction in the aqueous self-assembly properties is investigated in detail. The newly designed L-tyrosine based polymers have unique structural geometry with hydrophobic poly(ester-urethane) backbone and an average number of 40 hydrophilic PEGylated side chains with variable molecular weights. The average mass of the polymers varies from 30 kDa to 220 kDa and provide very good opportunity to study the self-assembly aspects in terms of hydrophilic-hydrophobic content, molecular weight, etc. To understand the hydrophilic-hydrophobic nature of the polymer brushes, they were subjected to water contact angle measurements LB-ADSA method.[30] The polymer films were drop-caste

on the glass substrate and the photographs of the water drop on the film are shown in Figure 2.9a.

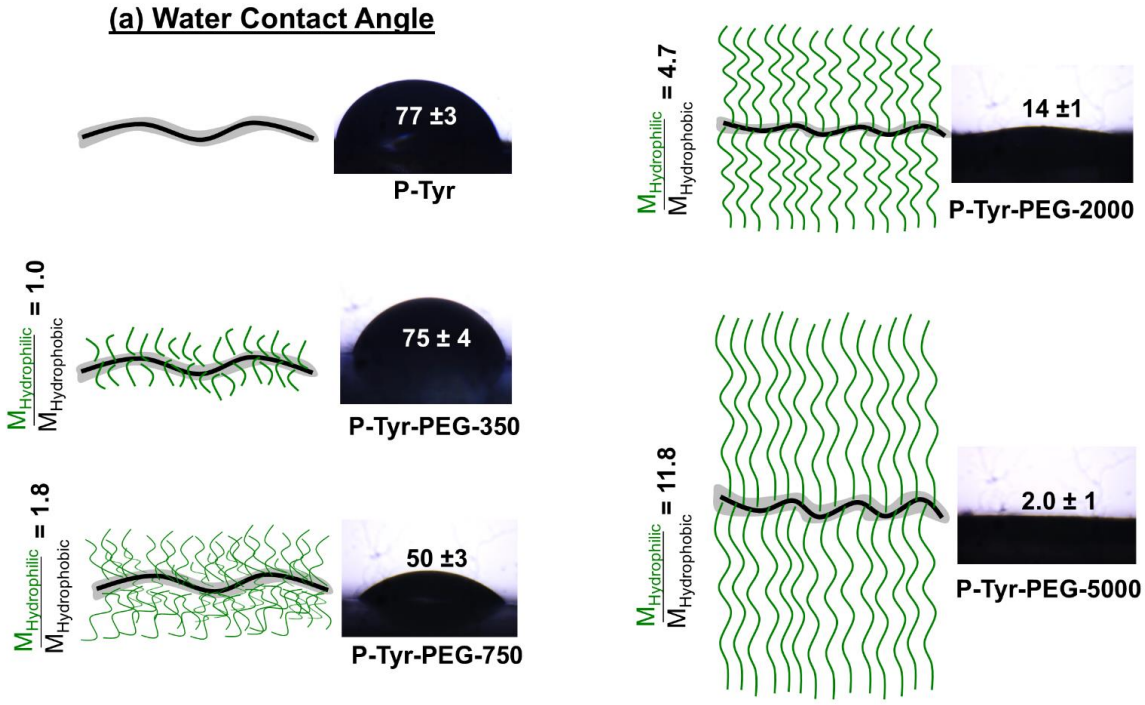

Figure 2.9. *(a) Schematic representation of polymer brushes having various PEG side chains. The ratio of $M_{Hydrophobic}$ and $M_{Hydrophilic}$ represents the molecular weights of the polymers in the polymer backbone and PEG-chains contributed to the total mass of each polymer brush. The photographs show the water contact angle (LB-ADSA method) recorded for the polymer brush drop-caste film on glass substrate.*

The WCA values were found to decrease with increase in the PEG-chain lengths in the polymer brushes from 77° to 2° indicating that the polymer brushes transformed from hydrophobic to highly hydrophilic surfaces. The hydrophobic-to-hydrophilic ratio ($M_{Hydrophobic}/M_{Hydrophilic}$) of the polymer brushes were estimated by comparing the molecular mass of the polymer backbone to that of the total PEG content in the side chains. The values were found to be varied from 1.0 to 11.0 with increase in the PEG chain lengths PEG-350 to PEG-5000 g/mol, respectively as shown in Figure 2.9a. The aqueous solubility or dispersibility of the polymers were found to be highly dependent on the PEG chain lengths.

2.3.4 Self-Assembly behavior

For instance, the P-Tyr-PEG-2000 and P-Tyr-PEG5000 were readily soluble in water whereas the lower PEG analogues do not dissolve and require further dialysis. Tyr-PEG-350 and Tyr-PEG-750 were dissolved in DMSO+water (2:3 v/v) and dialyzed against large amount of water using 3.5 kDa semipermeable dialysis membrane to get clear polymer dispersions (see vials in Appendix Figure S9). P-Tyr-PEG-350 sample was not stable at higher concentration for CAC measurements and it is not included for further analysis. The PEGylated polymers significantly vary in side chain interaction which leads to their difference in packing energies (as evident from the DSC analysis, Figure 2.7b); thus, one would anticipate such difference could eventually reflect in their aqueous phase segregation of hydrophilic-hydrophobic at the nano-confinement. The schematic representation of self-assembly is shown in Figure 2.10a. To measure the size of the aggregated micellar nanoparticles, they were subjected to dynamic light scattering (DLS) and electron (FESEM and HR-TEM) and atomic force microscopic imaging. The DLS histograms of P-Try-PEG-750 showed monomodal distribution corresponding to homogeneous particle formation with size of 250 nm (PDI Average= 0.466) (for three independent data, (see Appendix Figure S10a). The critical micelle concentration (CAC) of polymer amphiphiles is an elegant method to differentiate the aqueous self-assembly behaviors. The CAC of the PEGylated polymers were determined by pyrene probe method using steady fluorescence method.[30] The pyrene concentration was fixed (0.6 μM) and the polymer concentrations were varied from 0.5 mg/mL to $1x10^{-6}$ mg/mL. Fluorescence spectra were recorded using 337 nm excitation (see emission spectra in Figure 2.11a) and the ratio of vibrionic I_1/I_3 were plotted and showed for P-Tyr-PEG-750 in Figures 2.10b. From the break-point, the CMC of the polymer brush was estimated to be $1x10^{-3}$ mg/mL. AFM images exhibit the formation of short rod-like one-dimensional polymer brushes having average length 220 ± 6 and width 50 ± 6 (for more images see Appendix Figure S9b). This suggests that at least few polymer brushes have aggregated together to produce the rod-like nano-assemblies as shown in Figure 2.10b. FE-SEM images showed the existence of rod-like nano-assemblies with average 200 ± 8 nm and diameter 60 ± 8 nm. HR-TEM images clearly provided proof for the

existence of polymer brush nano-rods having length 210 ± 10 nm and diameter 70 ± 10 nm in Figure 2.10b.

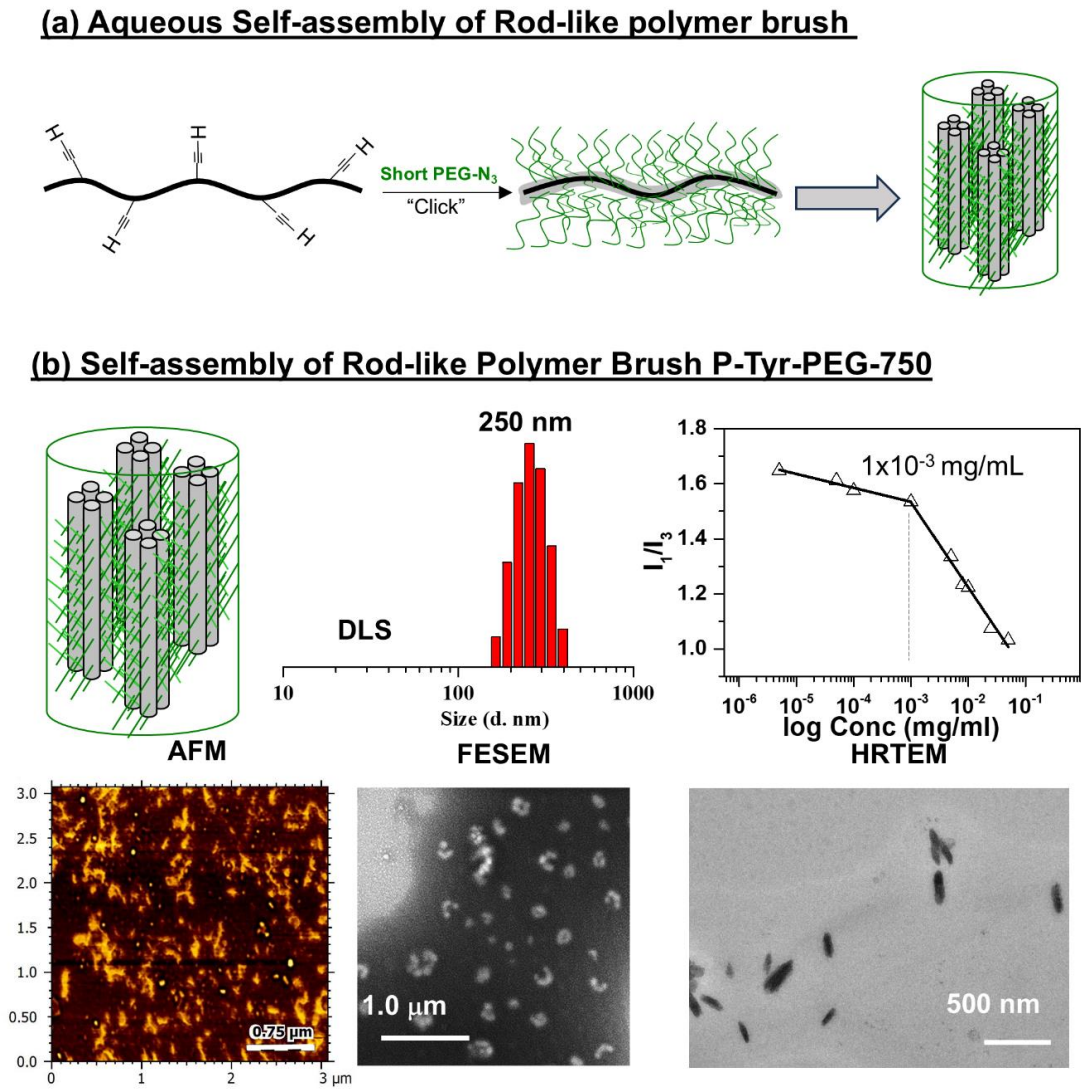

Figure 2.10 *(a) Schematic aqueous Self-assembly of P-Tyr-PEG-750 polymer brush. (b) DLS histogram and Critical aggregation concentration (CAC) was determined by pyrene-probe. P-Tyr-PEG-750 brush characterization by AFM, FE-SEM and HR-TEM images.*

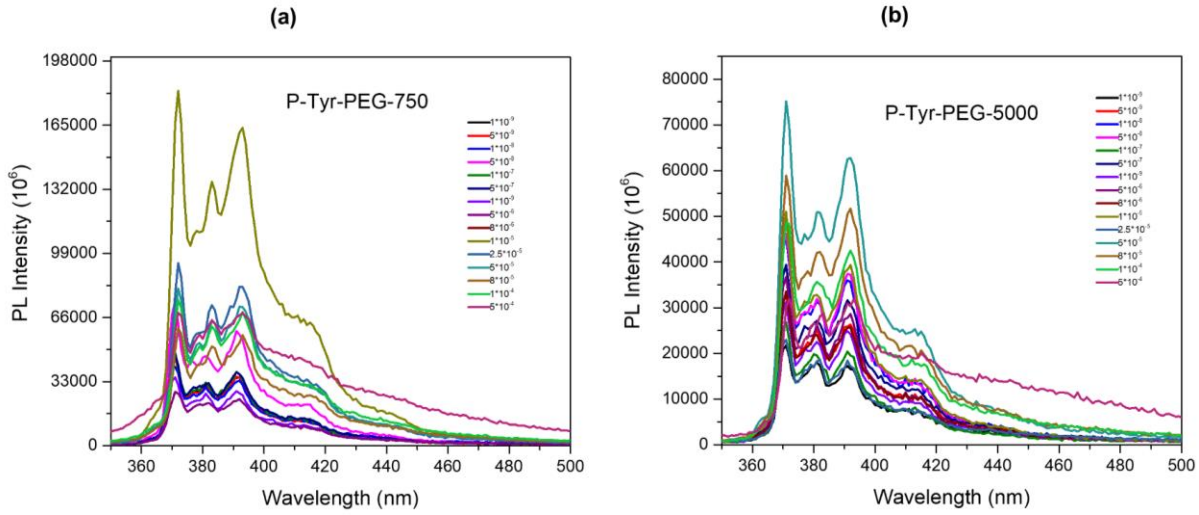

Figure 2.11 *Pyrene emission spectra for CMC determination. Pyrene chromophore was excited at λEx= 337nm and emission was collected from 350-500 nm. (a) P-Tyr-PEG-750, (b) P-Tyr-PEG-5000.*

Schematic representation of sphere-like polymer brush as shown in Figure 2.12a. Self-assembly of the P-Try-PEG-5000 sample was shown in Figure 2.2b. PEG-5000 substitution in the polymer chains leads to the formation of tightly packed tiny nanoparticles and this observation is attributed to that fact that long PEG chains have high tendency to undergo inter-chain packing (as supported by DSC analysis as well). DLS measurements for P-Tyr-PEG-5000 nanoparticles depicted the monomodal histogram with hydrodynamic diameter of 40 nm having (PDI Average=0.401) (for three independent data, (see Appendix Figure S10b) as shown in Figure 2.12b. Further CAC plot suggested the break point at 0.2 mg/mL.

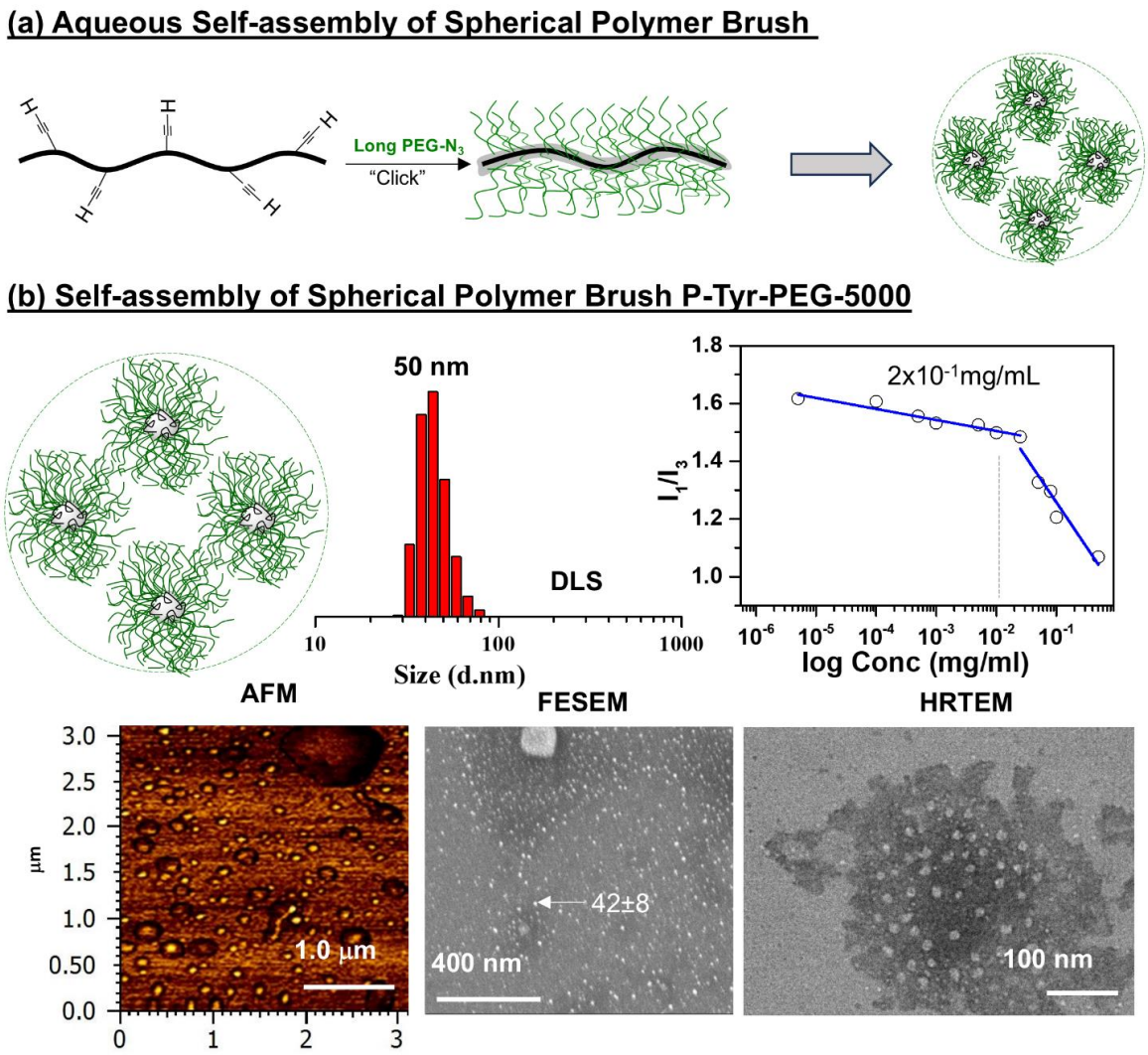

Figure 2.12 *(a) Schematic aqueous Self-assembly of P-Tyr-PEG-5000 polymer brush. (b) DLS histogram and Critical aggregation concentration (CAC) was determined by pyrene-probe. P-Tyr-PEG-5000 brush characterization by AFM, FE-SEM and HR-TEM images.*

In Figure 2.12b which is much higher than CAC of P-Tyr-PEG-750 (Figure 2.11b). Interestingly AFM and FE-SEM images revealed the formation of spherical nanoparticles for P-Tyr-PEG-5000 with 50 ± 6 nm diameter. This data was further supported by HR-TEM which also exhibited presence of 40 ± 8 nm nanoparticles with spherical morphology. All the characterization data of morphology for polymer brushes is tabulated in the **Table 2.3**.It is important to note the as the chain length of PEG is increased from 750 to 5000 the morphology of nanoparticles is shifted from rod -like to spherical nanoparticles. P-Try-PEG-2000 sample is showed the formation of 60 ± 10 nm tiny nanoparticles and the data are shown in Appendix Figure S11a. And pyrene emission spectra see Appendix Figure S12.

Table 2.3. *Size and DLC of rod-like and spherical Polymer Brushes*

Sample	DLS (nm)	AFM (nm)	FE-SEM (nm)	HR-TEM (nm)	CMC mg/mL	DLC for DOX (%)	Size of DOX loaded NP (nm)	DLC for NIR IR-780 (%)	Size of IR-780 loaded NP (nm)
P-Tyr-PEG-750	250	220±10	200±8	210±10	$1x10^{-3}$	5.5	200±10	4.4	190±10
P-Tyr-PEG-2000	60	60±8	40±6	45±6	$7x10^{-2}$	2.9	40±10	2.2	75±6
P-Tyr-PEG-5000	40	50±6	42±8	50±8	$2x10^{-1}$	2.9	40±6	2.2	50±5

2.3.5 Drug Encapsulation

Schematic representation of Dox encapsulation in the rod-like polymer brush as shown in Figure 2.13a. Schematic representation of Dox encapsulation in the sphere-like polymer brushes see Figure 2.13b. vials photograph of Dox-loaded polymer brushes see Figure 2.13c. To investigate the encapsulation capability of P-Tyr-PEG-x NPs, the clinical anticancer drug doxorubicin was chosen as a model system. The drug loading test was done by three independent methods such as dialysis, nanoprecipitation, solvent evaporation, and the detail procedures are given in the experimental section. In this process, the DOX molecules would eventually occupy the hydrophobic pocket in the aggregated micelles as shown in Figure 2.13a.

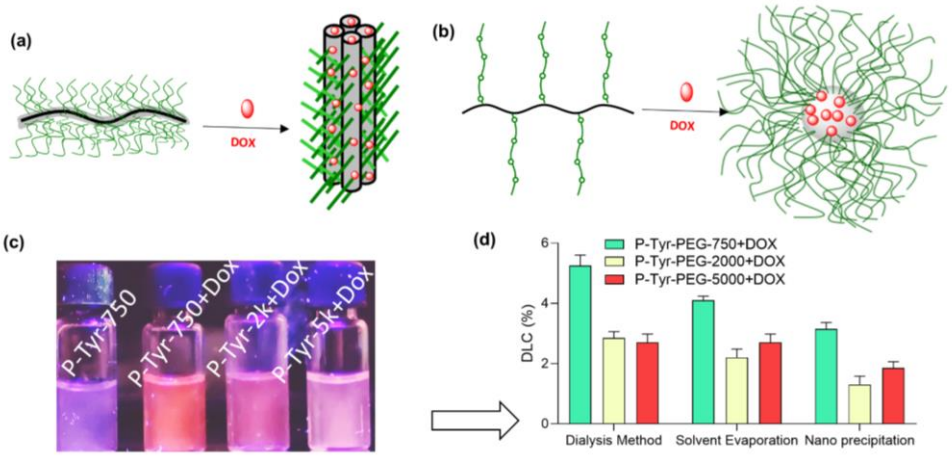

Figure 2.13 *(a) schematic representation of P-Tyr-PEG-750 brush polymer and loaded the DOX. (b) schematic representation of P-Tyr-PEG-5000 brush polymer and loaded the DOX. (c) photograph of vials DOX loaded polymers. (d) Drug loaded by three different methods dialysis, solvent evaporation and nano precipitation methods.*

For this purpose, 0.5 mg of the drug and 5.0 mg of the polymer were used in the feed, and the drug loading content (DLC) and drug loading efficiencies were determined by absorption spectroscopy. In the **table 2.3,** the DLC values are reported. The DLC decrease with the increase in the PEG-content in the polymer, the P-Tyr-PEG-750 samples showed better loading capabilities. The trend is almost same irrespective of the method of encapsulation and among all three procedures (Figure 2.14d),

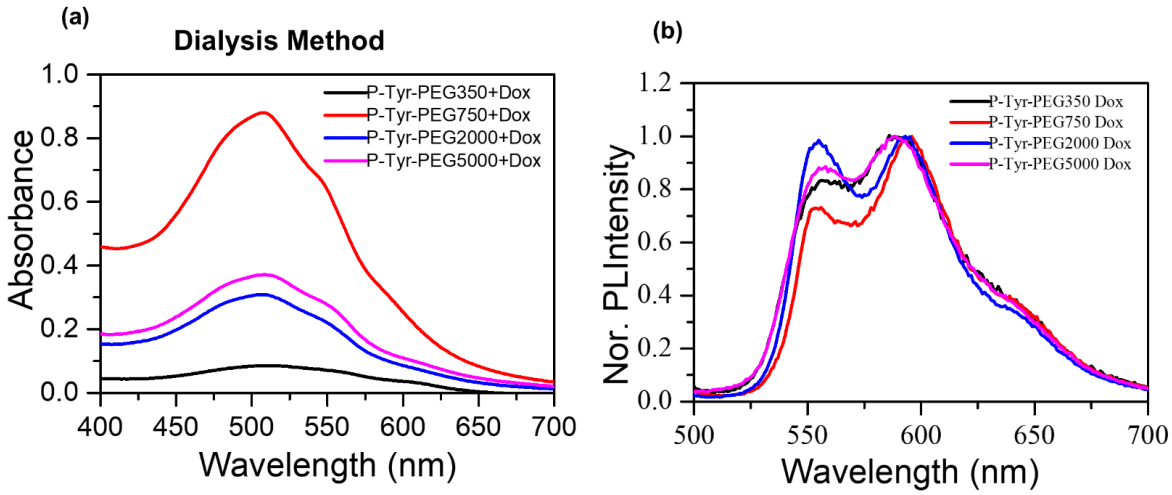

Figure 2.14 *(a) Absorbance spectra of DOX loaded samples for dialysis method. (b) emission spectra of DOX encapsulated P-Tyr-PEG-X Nanoparticles. (λ_{exc}=absorbance maxima).*

Dialysis method seems to be very good in loading higher DOX content with 5.5 % DLC. The photophysical studies revealed that the drug loaded polymers having same properties as for nascent form and confirmed the stability of drug molecules in the nanocavity (see Figure 2.14a and 2.14b) and other spectra are shown in Appendix FigureS13a and S13b. The DOX loaded samples were referred as P-Tyr-PEG-750-DOX, P-Tyr-PEG-2000-DOX, and P-Tyr-PEG-5000-DOX. DLS, of the P-Tyr-PEG-750-DOX nanoparticles confirmed the size as 200 ± 10 nm (see Figure 2.15a). The AFM and FE-SEM images of Dox-loaded polymer brushes were matches with nascent polymer brushes and the images are shown in Figure 2.15b.

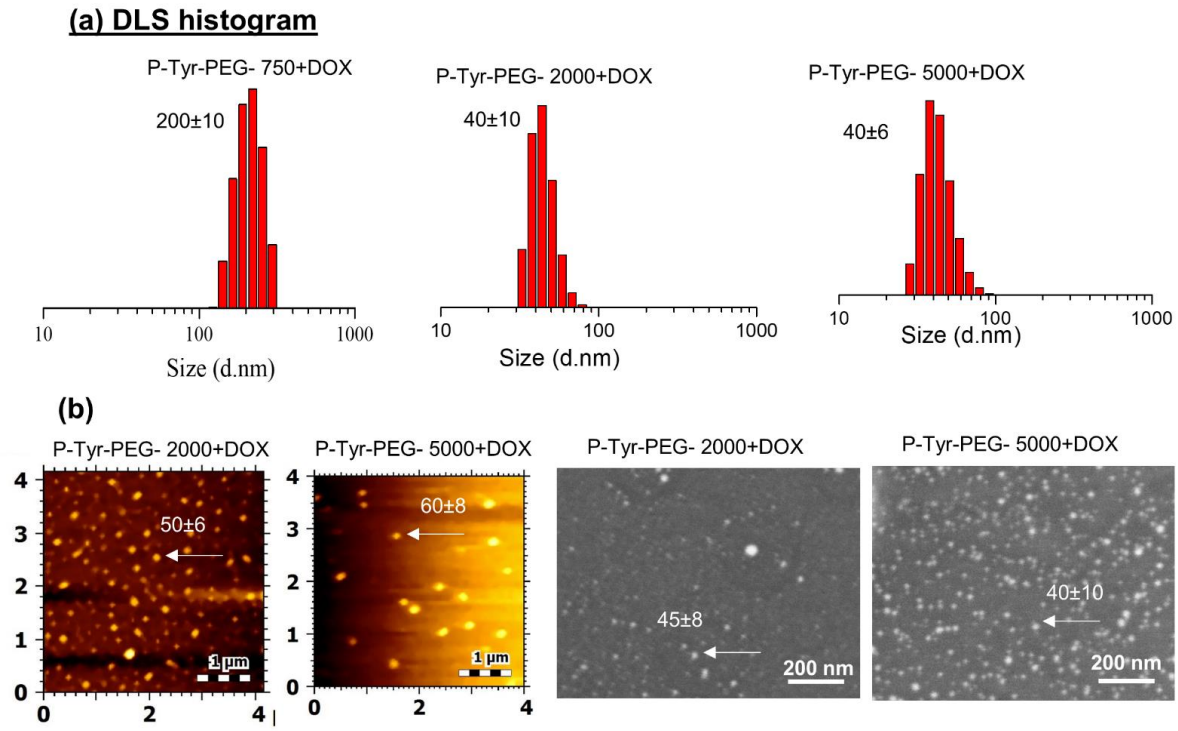

Figure 2.15 *DLS Histogram (a) P-Tyr-PEG-750-DOX, P-Tyr-PEG-2000-DOX, and P-Tyr-PEG-5000-DOX, (b) AFM images of P-Tyr-PEG-2000-DOX, AFM images of P-Tyr-PEG-5000-DOX, FE-SEM images of P-Tyr-PEG-2000-DOX, and FE-SEM images of P-Tyr-PEG-5000-DOX. Concentration = 0.1mg/mL.*

2.3.6 Enzymatic degradation studies

The enzymatic-biodegradation of the polymer was carried out in the presence of horse live esterase in PBS at 37 °C and aliquots were collected at various time intervals to subject SEC analysis. With increase in the incubation time, the SEC chromatograms in Figure 2.16a showed disappearance of polymer abundance and appearance of low molecular weight oligomers at the higher retention time. After 48 h incubation, the polymer sample exhibited complete biodegradation and only small molecules or oligomers are left in the SEC traces.

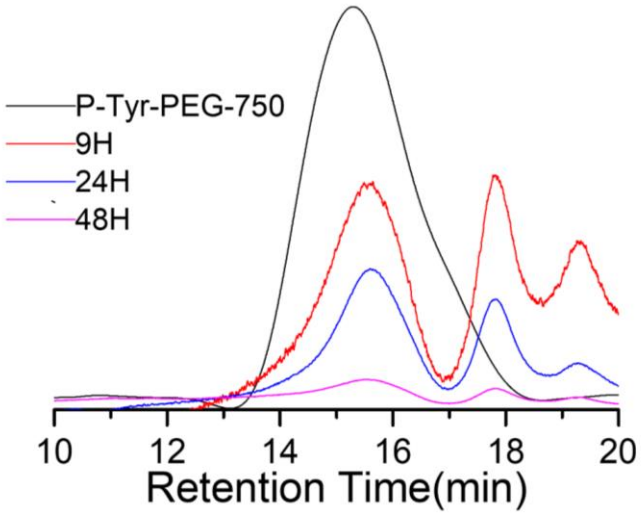

Figure 2.16 *(a) the enzyme-degradation of the P-Tyr-PEG-750 polymer was carried out in the presence of horse live peroxidase in PBS at 37 ℃ and aliquots were collected at various time intervals to subject SEC analysis in Chloroform as eluent at 25 ℃.*

The degraded polymer products (48 h sample) were subjected to MALDI-TOF analysis and the spectrum in Figure 2.17 showed the presence of low molecular weight chains having < 1200 g/mol indicating the formation of short oligomers upon biodegraded by the enzymes. These experiments further support the enzymatic-biodegradation of the tailor-made polymer brushes.

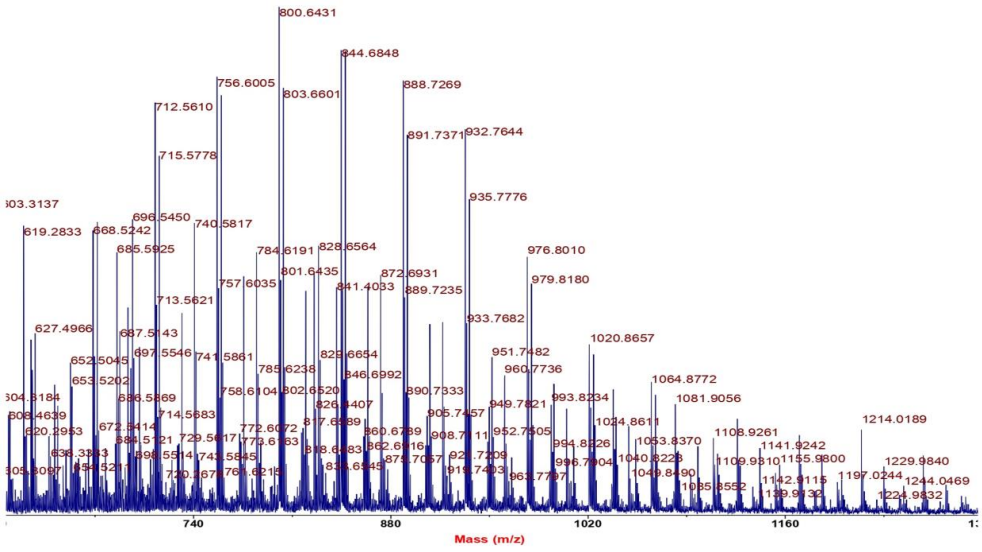

Figure 2.17 *MALDI-TOF mass spectrum of enzyme-degraded P-Tyr-PEG-750 samples (48h incubation).*

To evaluate the biodegradability of currently designed polymers, *in vitro* release kinetics studies of DOX loaded nanoparticles have been investigated and details are mentioned in experimental section. Aliphatic polyester urethanes are known to undergo enzymatic biodegradation into lysosomal compartment of cells.[51]

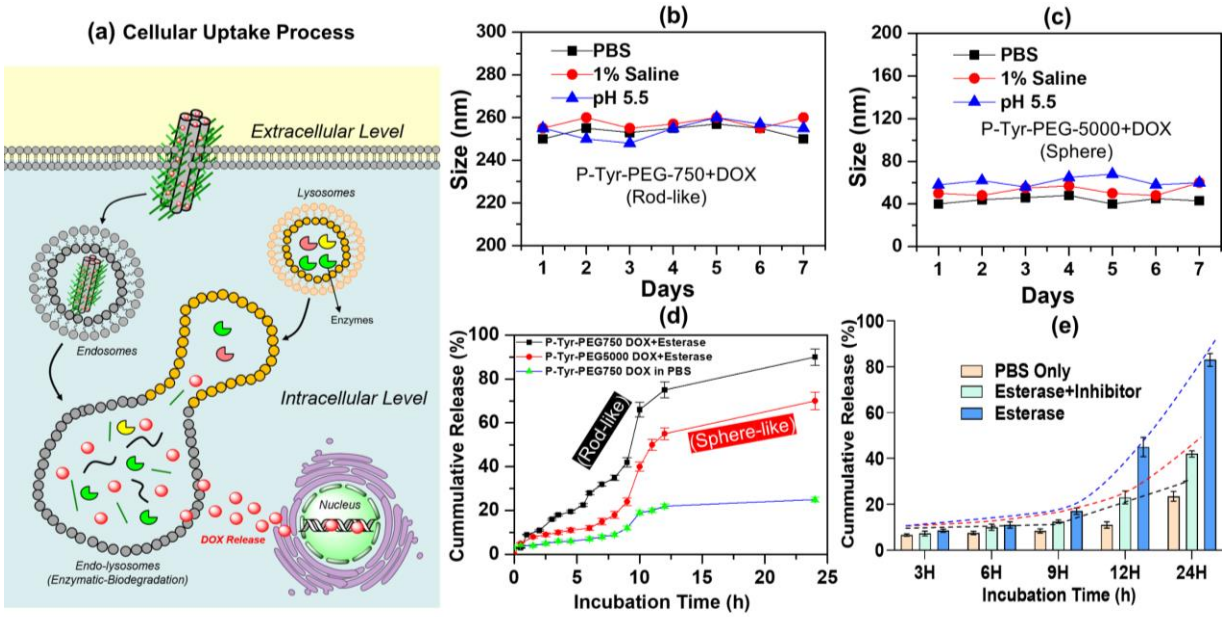

Figure 2.18 *(a) Schematic representation of rod-like polymer brush uptake in the cells and enzyme-biodegradation for DOX release in lysosomal compartment. (b) DLS size of the PTry-PEG-750+DOX loaded rod-like polymer brushes in PBS 7.4, 1% saline and pH=5.5 at 37 ℃. (c) DLS size of the PTry-PEG-5000+DOX loaded sphere-like polymer brushes in PBS 7.4, 1% saline and pH=5.5 at 37 ℃. (d) Cumulative drug release profiles of DOX-loaded P-Tyr-PEG-750 and P-Tyr-PEG-5000 samples in the presence of horse-liver esterase enzyme 10 U in PBS, pH 7.4 at* 37°C. *Drug release profiles of DOX-loaded P-Tyr-PEG-750 samples in the absence of enzyme in PBS, pH 7.4 at* 37°C. *(e) Enzyme-inhibition assay was performed in presence of (4-nitrophenyl-octyl-carbamate) and horse liver esterase enzyme in PBS 7.4 at 37 ℃ for the release of DOX in the polymer brush PTry-PEG-750+DOX. PTry-PEG-750+DOX in PBS (alone) and PTry-PEG-750+DOX in the presence of enzyme (without inhibitor) are used as controls.*

Typically, these nanoparticles internalized into cells via endocytosis pathway and localized into endosomes and subsequently undergo endo-lysosome compartmentalization as shown in Figure 2.18a. Endo-lysosome compartments are acidic pH 4-6 with plenty of hydrolytic enzymes are present such has esterase which will subsequently act upon aliphatic polyester-urethane backbone and degrade it into smaller units in controlled manner which results into chopping of nanoparticles and release of cargo into cytosol as shown in Figure 2.18a. Further the fate of release cargo such as DOX which is DNA intercalator essentially ends to nucleus where it undergoes DNA intercalation and disrupt the DNA replication which

eventually inhibit the cell growth. The stability of the polymer nanoparticles is investigated in various pH and salt concentration by DLS. The data is shown in Figures 2.18b and 2.18c revealed that the polymer nanoparticles are stable in various pH and salt concentration Briefly, P-Tyr-PEG-DOX nanoparticles were incubated with Horse liver esterase enzyme into dialysis membrane (1 kDa) in PBS pH 7.4 at 37 ºC and release of DOX was monitored by UV-spectrophotometry and the results are plotted as cumulative release versus concentration as shown in Figure 2.18d. In the control experiment, P-Tyr-PEG-DOX nanoparticles were incubated in PBS pH 7.4 to evaluate the stability in buffer at physiological conditions. From the Figure 2.18d, it can be clearly depicted that the polymer brushes underwent enzymatic degradation to release more than 80 % of the DOX in less than 24h. Whereas in case of PBS pH 7.4, the P-Tyr-PEG-DOX nanoparticles were stable and only 20 % release of DOX was observed in 24h and this is attributed to fact that PBS salts effect on the nanoparticles.[58] P-Tyr-PEG2000-DOX polymer brush was also investigated for release studies and data is shown in Appendix Figure S14. It is interesting to note that the rod-like polymer brush P-Tyr-PEG750-DOX exhibited much faster release of DOX compared to that of the spherical polymer brush P-Tyr-PEG5000-DOX. This difference is attributed that rod-like nano-assemblies could be degraded enzymatically much faster due to that fact that the enzymes could adhere on the middle biodegradable backbone readily due to the less shielding effect by the short chains. On the other hand, the long PEG chains hamper the enzyme accessibility to the backbone of the spherical nanoparticles in P-Try-PEG-5000; thus, relatively slow down the kinetic aspects. Even though, both polymer brushes have identical backbone length and chemical structures; the rod-like polymer brush exhibited 80 % DOX release which is nearly 20 % higher than the spherical polymer brush. Enzyme-inhibitor 4-nitrophenyl-octyl-carbamate was chosen based on our earlier investigation, and the DOX loaded polymer nanoparticles were tested for releases kinetics. The cumulative release data in Figure 2.18e were estimated for P-Tyr-PEG-750+DOX sample in PBS alone, in the presence of enzyme without inhibitor, and with the combination of enzymes+ enzyme inhibitor. The data clearly evident that the enzyme inhibitor slowed down the release kinetics and only 40 % of the drug was released at 24 h incubation which is almost half compared to the action by the enzyme. This data validated the action of lysosomal-enzymes on the polymer backbone and its biodegradation aspects.

3.2.7 Temperature dependent endocytosis experiment

Polymer nanoparticles are typically endocytosed across the cell membranes at 37 °C, i e. at the biological temperature by ATP-assisted energy driven transportation pathways.[43] Two control experiments are carried out to study endocytosis of the nano-rod and spherical polymer brushes; (i) incubation of polymer nano-objects at 37 ºC and 4 ºC so that the ATP energy-assisted endocytosis across the cell membranes could be traced, and (ii) pre-treat the cells at 37 ºC with NaN_3 which is a well-known electron transport inhibitor for ATP synthase.[61] This second experiment affect the ATP-driven uptake mechanism; thus it would indirectly diminish the uptake of the nano-objects.

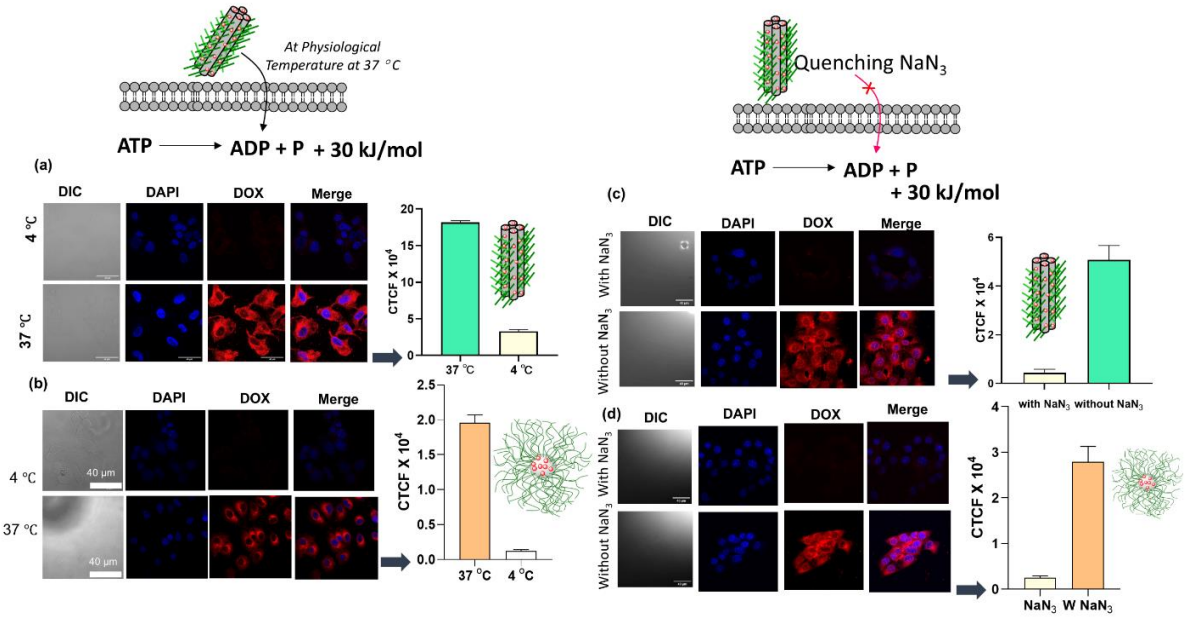

Figure 2.19 *(a) CLSM images of PTyr-PEG-750+DOX sample treated at 4 ℃ and 37 ℃ (6h incubation, DOX concentration 5 µg/mL) in WT-MEF cells. CTCF plots estimated from the CLSM images at 4 ℃ and 37 ℃ incubated sample. (b) CLSM images of PTyr-PEG-5000+DOX sample treated at 4 ℃ and 37 ℃ (6h incubation, DOX concentration 5 µg/mL) in WT-MEF cells. CTCF plots estimated from the CLSM images at 4 ℃ and 37 ℃ incubated sample. (c) CLSM images of PTyr-PEG-750+DOX sample incubated with cells that are pre-treated with NaN_3 at 37 ℃ (NaN_3 concentration =6.5 µg/mL incubation 30 minute) in WT-MEF cells. A control experiment was carried out without NaN_3 at 37 ℃. CTCF plots estimated from the CLSM images of NaN_3 experiment. (d) CLSM images of PTyr-PEG-5000+DOX sample incubated with cells that are pre-treated with NaN_3 at 37 ℃ (NaN_3 concentration =6.5 µg/mL incubation 30 minute) in WT-MEF cells. A control experiment was carried out without NaN_3 at 37 ℃. CTCF plots estimated from the CLSM images of NaN_3 experiment.*

Temperature dependent cellular uptake of polymer brush was carried out in WT-MEF cell line at 37 ºC and 4 ºC, and the CLSM images are reported in Figure 2.19a (see Figure 2.19b for spherical brush P-Tyr-PEG-5000+DOX). The CLSM clearly depict that the P-Tyr-PEG-

750+DOX nano-rod have been taken up by the cells predominantly at 37 ºC whereas negligible uptake was observed at 4 ºC. This trend was supported by CTCF values in Figure 2.19a and 2.19b, the P-Tyr-PEG-2000+Dox data are shown in Appendix Figure S15a and S15b, which further evident for ATP-assisted temperature dependent cellular uptake. In the second control experiment, the cells were first pre-treated with NaN_3 (6.5 µg/mL, ATP inhibitor) for 30 minutes; then the cells were administrated with DOX loaded polymer brushes for 6 h at 37 ºC prior. A control experiment was carried out without NaN_3 pre-treatment under identical conditions (see Figure 2.19c for NaN_3 experiment pretreated cellular uptake of spherical brush P-Tyr-PEG-5000+DOX). CLSM images in Figure 2.19c and 2.19d showed the substantial reduction in the uptake of the DOX loaded nano-rods in the NaN_3 pretreated cells. This trend was supported by CTCF values in Figure 2.19c and Figure 2.19d. Both these control experiments validated the endocytosis of the polymer brushes by the ATP-assisted energy driven process under physiological temperature.

2.3.8 Live cell real time biodegradation

The difference in the uptake of the nano-rod versus spherical polymer brush objects were investigated by the live-cell bioimaging and the details are reported in Figure 6. Based on these studies one could summarize that the polymer brushes are endocytosed across the cellular membranes and digested in the endo-lysosomal compartments by enzymatic-biodegradation. Real time live-cell bioimaging technique was employed to study the biodegradation aspects of DOX loaded polymer brushes in Figure 2.20a. Briefly, WT-MEF cells were treated with P-Tyr-PEG750-DOX nanoparticles and lysosomes were stained with lysotracker green DND-26 and cells were visualized by confocal laser scanning microscopy (CLSM) using 488 nm laser for lysotracker and 561 nm laser for DOX.

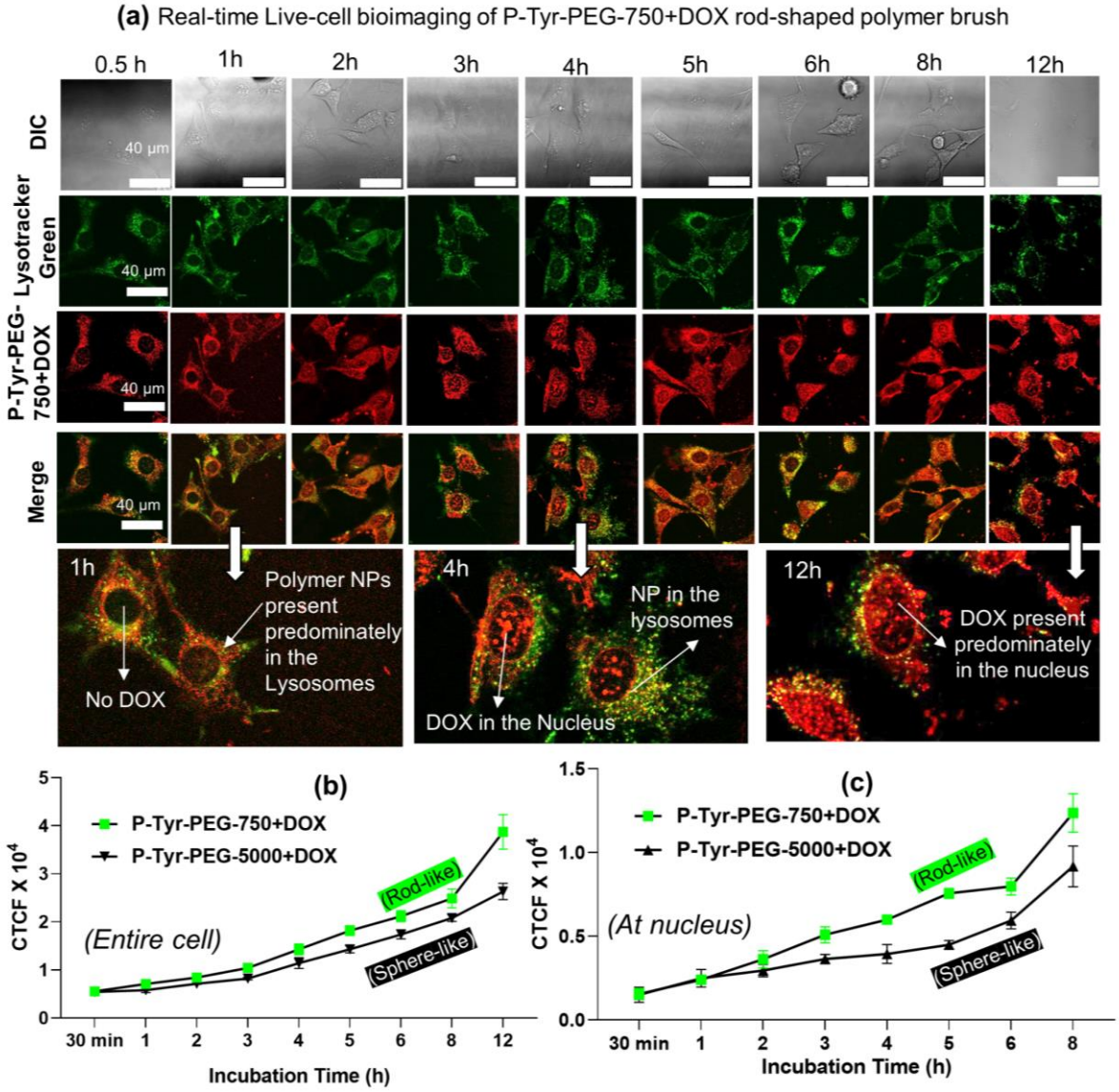

Figure 2.20. *(a) Time dependent live-cell imaging of P-Tyr-PEG-750+DOX at time point 30 min, 1h, 2h, 3h, 4h, 5h, 6h, 8h, and 12h incubation in WET-MEF cell lines. (b) Corrected total cell fluorescence (CTCF) of entire cell P-Tyr-PEG-750+DOX uptake. (c) CTCF in the P-Tyr-PEG-750+DOX at nucleus region only. The concentration of DOX was maintained as 5 µg/mL. The scale bar represents 40 µm in cell images.*

It is evident from confocal images that P-Tyr-PEG750-DOX nanoparticles were internalized into cells at 30 minutes of incubation evident from DOX emission in red channel and enhanced emission can be seen as incubation time progressed. P-Tyr-PEG750-DOX nanoparticles were predominantly localized into lysosomal compartment at initial timepoints of incubation (30 minutes to 2h) evident from yellow color in the cytoplasmic region in merge image which is resulted form of lysosome (green) and DOX (red) colocalization as shown in expanded image of 1h. Furthermore, nanoparticle underwent lysosomal degradation to release

of DOX into cytoplasm resulted into localization of DOX into nuclei which can be seen as DOX emission from nucleus as well as from lysosomes at 4h of incubation and onwards as shown as expanded image of 4h. As the time of incubation progressed, the DOX predominantly localized into nucleus as shown in expanded image of 12h.

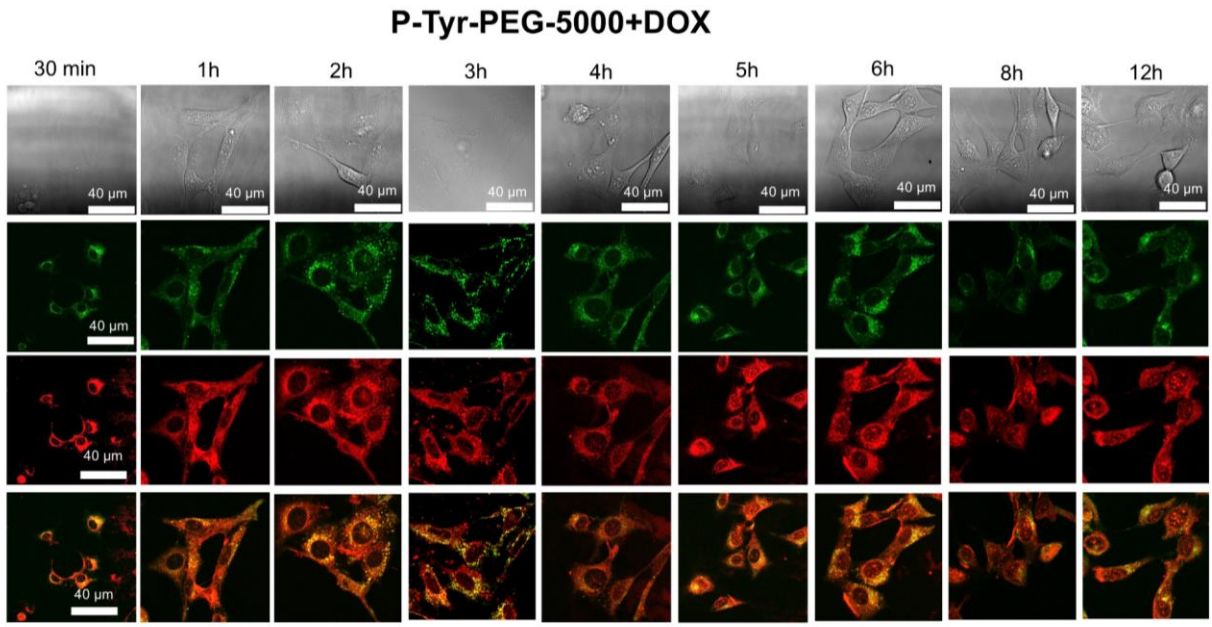

Figure 2.21. *(a) Time dependent live-cell imaging of P-Tyr-PEG-5000+DOX at time point 30 min, 1h, 2h, 3h, 4h, 5h, 6h, 8h, and 12h incubation in WET-MEF cell lines.*

Live cell imaging clearly depicted that P-Tyr-PEG750-DOX nanoparticles and the results are in consistent with the expected biodegradation. Whereas free DOX underwent the diffusion pathway and directly went to nucleus from initial time of incubation upon internalization see Appendix S16. In similar manner live-cell imaging were carried out for P-Tyr-PEG5000-DOX nanoparticles and data is shown Figure 2.21. Moreover, the mean corrected total cell fluorescence (CTCF) calculated by two methods: (i) by considering the total fluorescence in the entire cell which account for both the uptake in the cytosol plus the biodegraded polymer and subsequent accumulation of DOX at the nucleus, and (ii) fluorescence signals in the selective region of the nucleus to estimate exclusively the DOX amount only upon the biodegrading. By subtracting the CTCF values from (i) – (ii), the quantity of the drugs present in the polymer brushes that are yet to be biodegraded in the cytosol. The CTCF values estimated for the rod-like polymer brushes (from Figure 2.20a) and the spherical

polymer brushes (from Figure 2.21a) are plotted together in Figure 2.20b for the entire cells and in Figure 2.20c for the DOX in the nucleus. The data in Figure 2.20b suggests that the one-dimensional rod-like polymer brush was taken up much faster and also in higher amount compared to the three-dimensional spherical polymer brush. This trend is attributed to the fact that the 1D rod has higher penetration ability into the extracellular membranes compared to 3D objects. This trend is matched with the endocytosis of 1D and 3D silica based inorganic nanoparticles reported in the past.[59,60] The CTCF data in Figure 2.20c is corresponding to the DOX accumulated in the nucleus upon the enzymatic biodegradation of the polymer brushes in the cytosol; thus, the difference in the DOX content in the nucleus is the direct measure of the degradation ability of the shape-dependent polymer brushes. The DOX accumulation from the rod-like brushes and much higher than that of the spherical nano-objects and this data corroborated with the enzyme-degradation kinetics in Figure 2.18d. From this live-cell imaging, it can be concluded that the shape of the biodegradable polymer brushes played a major role both in uptake and biodegradation aspects; the rod-like polymer brushes seems to be better candidate than the spherical nanoobjects.

2.3.9 Cell viability and biocompatibility assay

To validate the biocompatibility of the polymers, MTT assays were performed in human breast cancer cells (MCF-7) and non-cancerous cells (WT-MEF). MCF-7 cells were treated with nascent nanoparticles for 72h, and data is shown as plot in Figure 2.22.From the plot it can be concluded that P-Tyr-PEG-750 nanoparticles has shown excellent compatibility with 100% cell viability and were non-toxic to cells up to 100 µg/mL. Similarly, P-Tyr-PEG-2000 and P-Tyr-PEG5000 nanoparticles were found to be non-toxic and cell viability plots are shown in Figure 2.22a. Further cytotoxicity evaluation of DOX loaded nanoparticles were investigated in DOX resistant MCF-7 cell line for 72h. The P-Tyr-PEG-750+DOX nanoparticles exhibited IC_{50} at 0.1 µg/mL which is comparable to Free DOX (IC_{50} 0.1 µg/mL) as shown in Figure 2.22d whereas IC_{50} was obtained at 0.2 µg/mL concentration for P-Tyr-PEG-5000+DOX nanoparticles as shown in Figure 2.22f. Both DOX loaded nanoparticle systems exhibited 80% cell killing at 1 µg/mL comparable to Free DOX. In similar manner nascent nanoparticles were found to be non-toxic to WT-MEF cells and cell viability plots are shown in Figure 2.23 and DOX loaded nanoparticles were equally efficient in killing cells compared to free DOX. The polymers are also now tested in ovarian cancer cell lines (SKOV3) and the data is shown in

Appendix Figure S17. It is clear evident that DOX loaded polymer nanoparticles could able to suppress the cell growth efficiently.

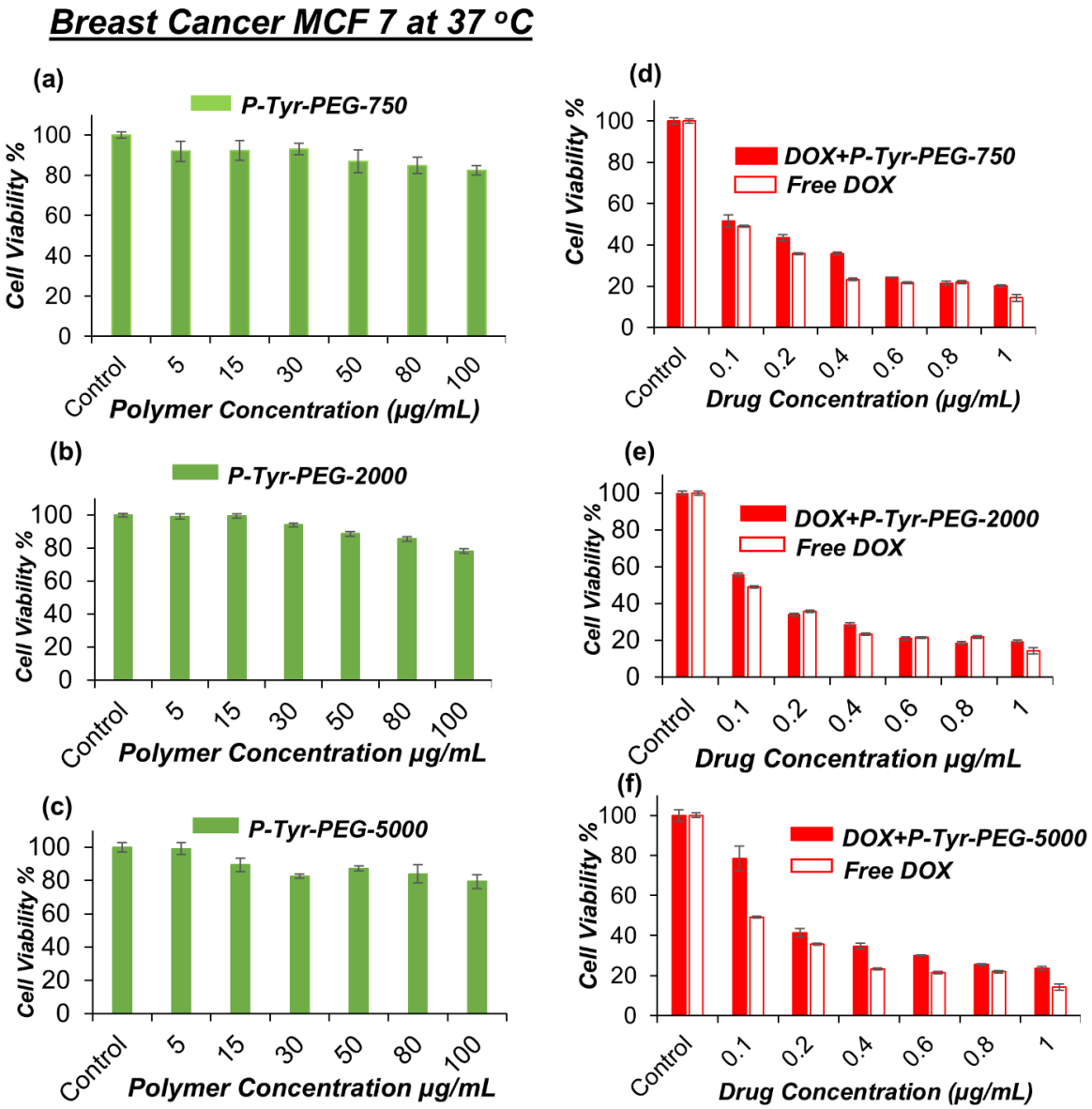

Figure 2.22 *(a) Plot showing the cytotoxicity of P-Tyr-PEG-750 in breast cancer MCF-7 cell line. (b) Plot showing the cytotoxicity of P-Tyr-PEG-2000 in breast cancer MCF-7 cell line. (c) Plot showing the cytotoxicity of P-Tyr-PEG-5000 in breast cancer MCF-7 cell line. (d) Plot showing the cytotoxicity of DOX loaded P-Tyr-PEG-750 and free DOX in breast cancer MCF-7 cell line. (e) Plot showing the cytotoxicity of DOX loaded P-Tyr-PEG-2000 and free DOX in breast cancer MCF-7 cell line. (f) Plot showing the cytotoxicity of DOX loaded P-Tyr-PEG-5000 and free DOX in breast cancer MCF-7 cell line.*

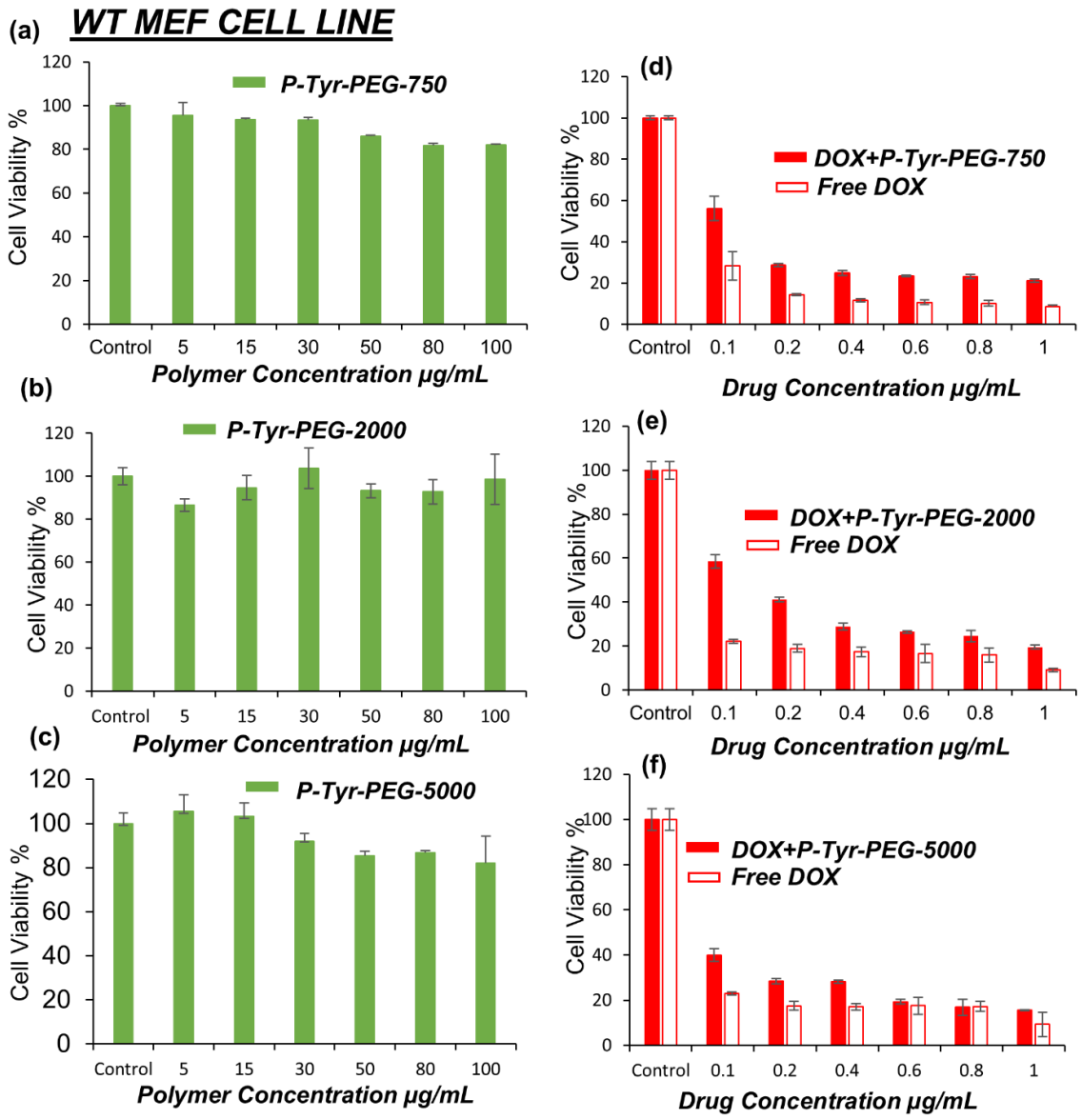

Figure 2.23 *(a) Plot showing the cytotoxicity of P-Tyr-PEG-750 in breast cancer M cell line. (b) Plot showing the cytotoxicity of P-Tyr-PEG-2000 in WT-MEF cell line. (c) Plot showing the cytotoxicity of P-Tyr-PEG-5000 in WT-MEF cell line. (d) Plot showing the cytotoxicity of DOX loaded P-Tyr-PEG-750 and free DOX in WT-MEF cell line. (e) Plot showing the cytotoxicity of DOX loaded P-Tyr-PEG-2000 and free DOX WT-MEF cell line. (f) Plot showing the cytotoxicity of DOX loaded P-Tyr-PEG-5000 and free DOX WT-MEF cell line.*

2.3.10 Cellular uptake studies

The delivery capability of DOX loaded nanoparticles was examined by cellular uptake studies in multidrug resistant breast cancer cell line MCF-7 and details are mentioned in experimental section. Time-dependent cellular uptake studies has been carried out in MCF-7 from 30 min to 12h incubation and compiled images are shown Figure 2.24a to 2.26a and 6h time point data are shown in Appendix Figure S18. From the images it can be seen that all the DOX loaded nanoparticles were taken by cells evident from DOX emission in DOX channel in Figure 2.24. The cells were treated with DOX loaded nanoparticles and fixed at the endpoint of experiment and visualized by using 405 nm (blue channel for DAPI) and 488 nm (red channel for DOX) laser excitation and CLSM images for 9h incubation is shown Figure 2.26a Furthermore, the nanoparticles were successfully degraded in lysosomal compartment (supported by live-cell imaging) and released DOX to nucleus indicated by magenta color of colocalized (merged) image of blue (nucleus, DAPI) and red (DOX) channels as shown in Figure 2.26a. The mean CTCF for DOX loaded nanoparticles calculated and plot is shown in Figure 2.26a, which clearly suggest better uptake of all nanoparticles compared to free DOX (statistically significant) as well as the rod-shaped P-Tyr-PEG-750+DOX compared to spherical P-Tyr-PEG-2000+DOX and P-Tyr-PEG-5000+DOX nanoparticles.

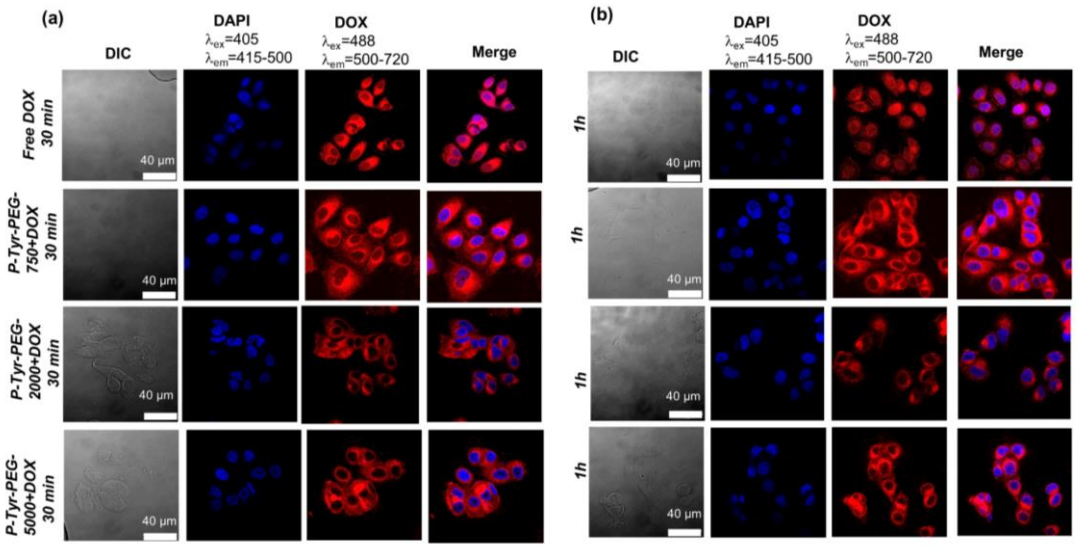

Figure 2.24 *Time-dependent cellular uptake fixed cell imaging in MCF-7 cell line. (a) incubation time point 30 min, and (b) incubation time 1h. The concentration of DOX was maintained as 5.0 µg/mL*

.

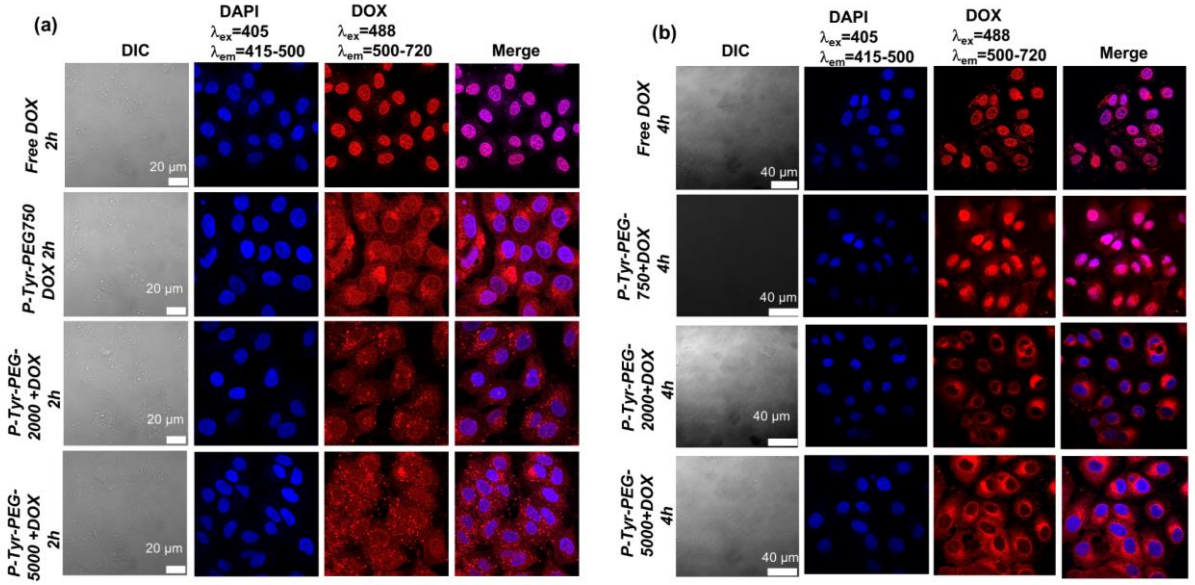

Figure 2.25 *Time-dependent cellular uptake fixed cell imaging in MCF-7 cell line. (a) incubation time point 2h, and (b) incubation time 4h. The concentration of DOX was maintained as 5.0 µg/mL.*

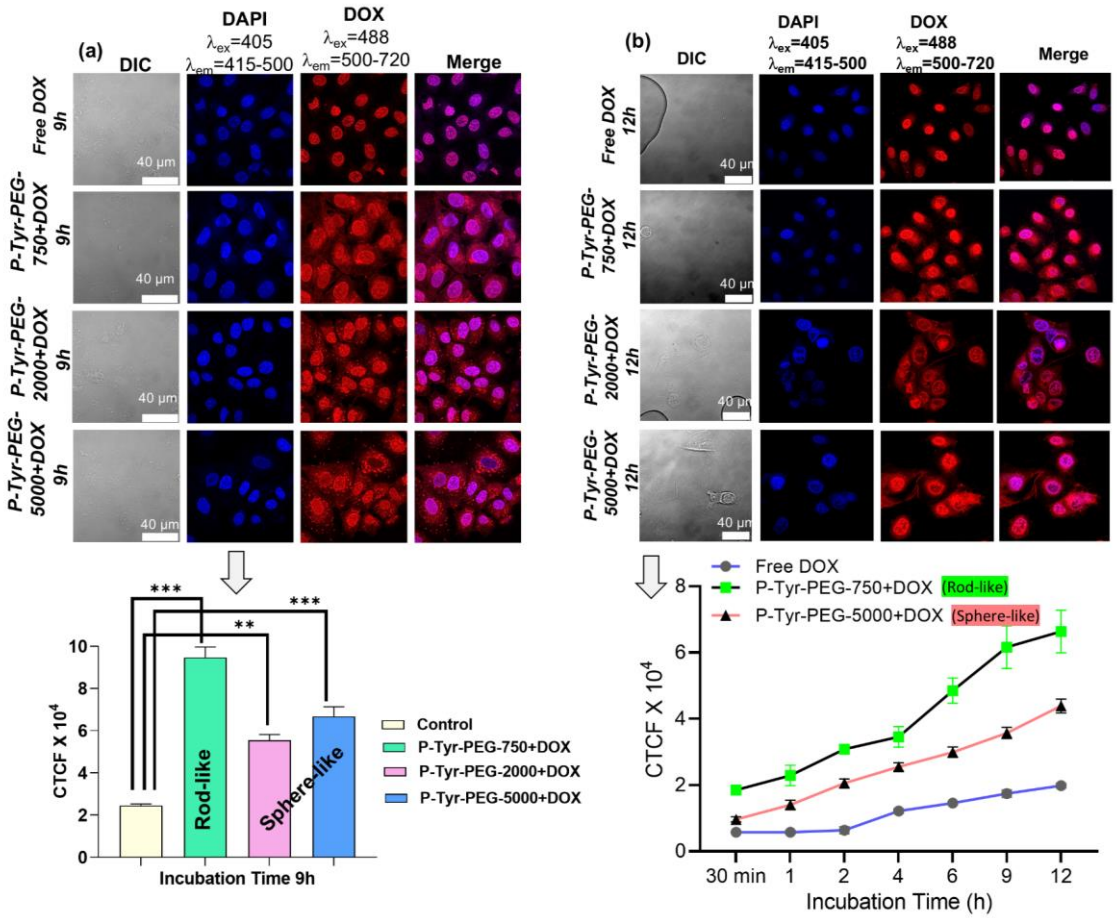

Figure 2.26 *Time-dependent cellular uptake fixed cell imaging in MCF-7 cell line. (a) incubation time point 9h, and (b) incubation time 12h. corresponding their CTCF values of Free DOX, P-Tyr-PEG-750-DOX, and P-Tyr-PEG-5000-DOX. The concentration of DOX was maintained as 5.0 µg/mL.*

Time-dependent studies indicated that the initially DOX loaded nanoparticles were localized in cytoplasm and 3h onwards resulted in DOX accumulation into nucleus evident from magenta color in merge panel. These results support the lysosomal degradation and release mechanism. More ever CTCF calculations suggest the superiority of rod-shaped P-Tyr-PEG-750+DOX over spherical P-Tyr-PEG-5000+DOX nanoparticles in terms of DOX delivery capabilities see Figure 2.26b.

2.3.11 NIR probe Encapsulation

NIR dyes are fluorophores that can be excited by near-infrared radiation. They are commonly used in in vivo imaging studies due to their ability to penetrate tissues more effectively than UV-visible light, and their low autofluorescence in the near-infrared region.[62]To enable in vivo imaging and investigate the biodistribution of currently designed pegylated P-Tyr-PEG polymer scaffold, an NIR dye (IR-780 iodide) was encapsulated into polymer scaffold, as shown in Figure 2.27a. The encapsulation of the dye was performed using a similar method to that for DOX, and the drug loading content was found to be 4.2 %, which is suitable for in vivo imaging applications. The photograph of the IR-780 loaded polymer sample is shown in Figure 2.27a. DLS measurements of the IR-780 loaded nanoparticles revealed the presence of nano-assemblies with sizes of ~200 nm. The photophysical studies revealed that the dye loaded polymers having same properties as for nascent form and confirmed the stability of dye molecules in the nanocavity shown in Figure 2.27b and 2.27c.

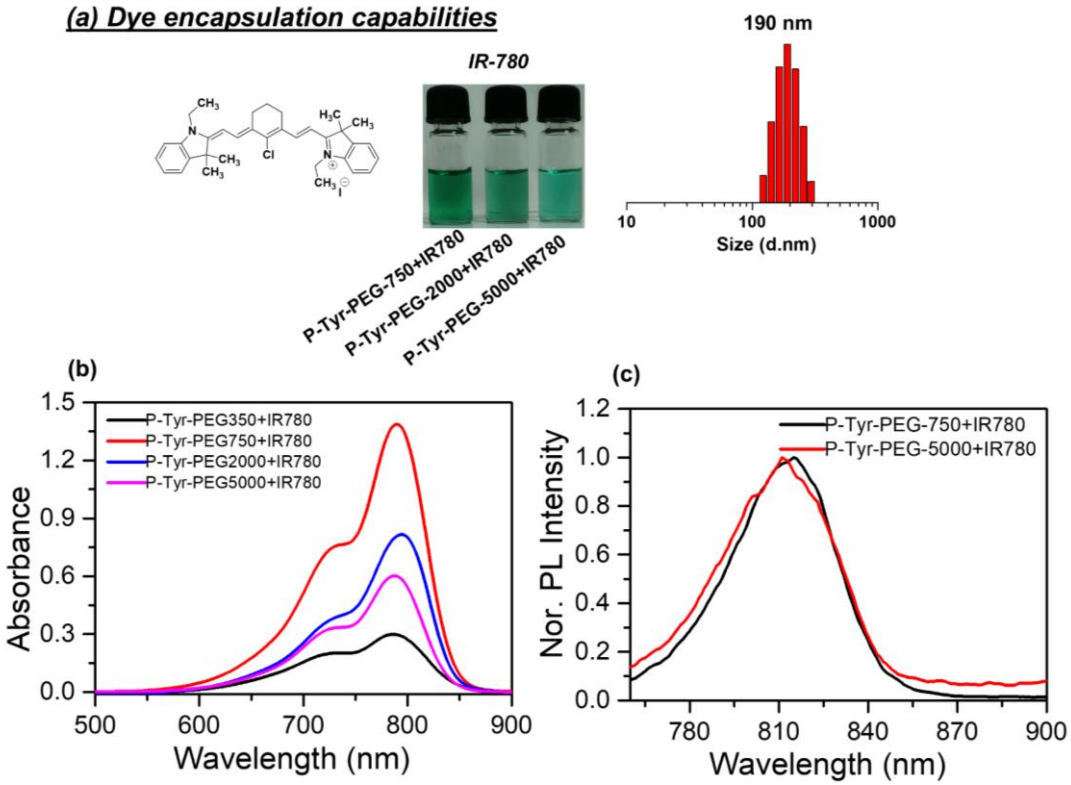

Figure 2.27*. (a) Schematic for encapsulation of IR-780 dye and DLS histogram for IR-780 loaded P-Tyr-PEG-750 polymer brush nanoparticles. (b) Absorbance spectra of IR-780 loaded polymers, and (c) emission spectra of fluorophore encapsulated P-Tyr-PEG-X Nanoparticles. (λ_{exc}=absorbance maxima).*

2.3.12 Hemolysis assay

The non-hemolytic nature of drug delivery vehicle is important for its use in nano-formulations for *in vivo* drug delivery application. A hemolysis assay was conducted, in which the polymer sample was incubated with a solution of red blood cells (RBCs) in phosphate-buffered saline (PBS), followed by centrifugation to separate the RBCs. If the sample is non-hemolytic, the RBCs remain intact and form a red pellet at the bottom, while the supernatant remains colorless. In the event of RBC rupture caused by polymer interaction, hemoglobin is released, resulting in red coloration of the supernatant liquid, and quantified by measuring absorbance. The negative control was PBS which do not cause any RBC rupture and Triton X-100 which is a nonionic surfactant that causes RBC lysis through osmosis were used as a positive control. The results proved that all the nanoparticles did not cause hemolysis of RBCs, as evidenced by the stable RBC pellet and lack of red coloration in the supernatant, photographs shown in Figure

2.28a. The percentage of hemolysis was quantified and shown in a histogram in Figure 2.28a, which confirmed the non-hemolytic nature of all the nanoparticles.

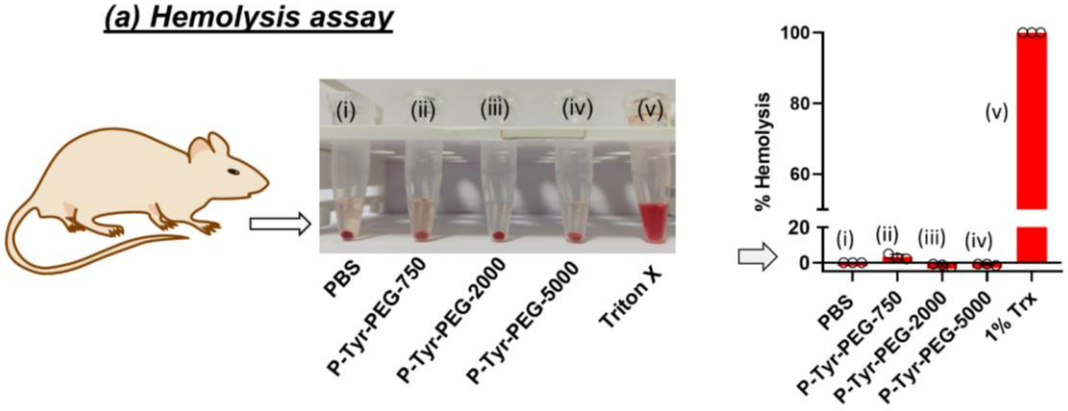

Figure 2.28. *(a) Photographs of centrifuge tubes post incubation of sample with RBC solution. Appearance of intact pellet indicate RBC stability. Plot showing % hemolysis for polymer (P-Tyr-PEG) along with PBS (negative control) and 1% Triton X-100 (positive control), (****P<0.0001) each point represents mean ± SEM, n=3).*

2.3.13 In-vivo Biodistribution Studies

For the in vivo imaging and biodistribution studies, three group of mice were used in each experiment (with the experiment performed in triplicate). One group was injected intraperitoneally with IR-780 loaded polymer nanoparticles, the second group was injected intraperitoneally with free IR-780 dye, and the third group was injected intraperitoneally with 1X PBS as a control. In vivo whole-body imaging was carried out at 4 h, 24 h, 48 h, and 72 h post-injection with the help of In Vivo Imaging System (IVIS, PerkinElmer) for biodistribution analysis, and the images are shown in Figure 2.29a for dorsal view and similar images were captured for ventral view as shown in Figure 2.29b.

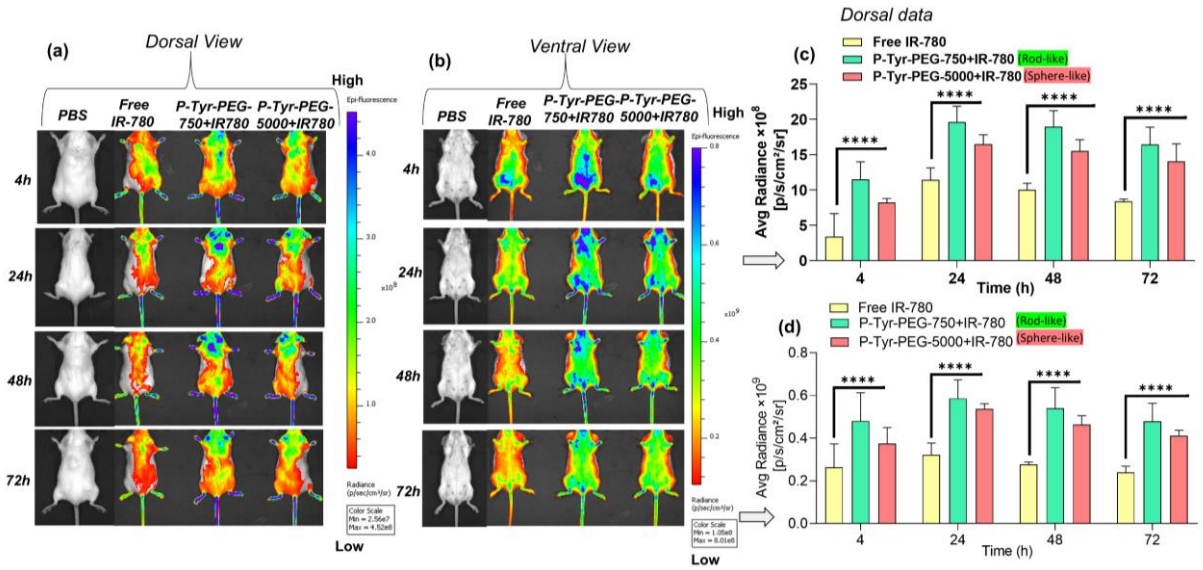

Figure 2.29. *(a). Time-dependent IVIS images (dorsal view) of mice injected with PBS (control), free IR-780 dye and IR-780 loaded polymer nanoparticles. (b) Time-dependent IVIS images (Ventral view) of mice injected with PBS (control), free IR-780 dye and IR-780 loaded polymer nanoparticles. (c) Histogram representing amount of IR-780 dye (quantified as average radiance) at various time points in the body of mouse injected with free IR-780 and IR-780 loaded polymer nanoparticles. (d) Histogram representing amount of IR-780 dye (quantified as average radiance) at various time points in the body of mouse injected with free IR-780 and IR-780 loaded polymer nanoparticles.*

As expected, no fluorescence was observed in the control mouse injected with PBS. Conversely, intense fluorescence was observed from the mouse injected with IR-780 loaded nanoparticles or free IR-780 dye. The fluorescence signal was quantified by measuring the average radiance over time, as shown in Figure 2.29c. For ventral the fluorescence signal was quantified by measuring the average radiance over time see Figure 2.29d. The signal was consistently higher in the mouse injected with IR-780 loaded particles compared to the mouse injected with free IR-780 dye at all time points, indicating better uptake of IR-780 loaded nanoparticles. The total radiance of the mouse injected with free IR-780 dye at 72 h was slightly less than that at 24 h, indicating clearance of IR-780 dye from the body. In contrast, the total radiance of the mouse injected with IR-780 loaded polymer nanoparticles were the same at 72 h and 24 h, indicating the greater in vivo stability of IR-780 loaded nanoparticles. The comparison of the signal intensities revealed that the rod-like polymer brush are good candidates for biomedical application.

The duration of circulation time in the bloodstream is an essential aspect of any drug formulation. To assess the ability of polymer nanoparticles to remain in the bloodstream, plasma samples were collected from mice injected with IR-780-loaded nanoparticles, free IR-780 dye, or PBS at 4 h, 24 h, 48 h, and 72 h post-injection. The isolated plasma was imaged in a 96-well plate using IVIS, and the resulting image is shown in Figure 2.30a.

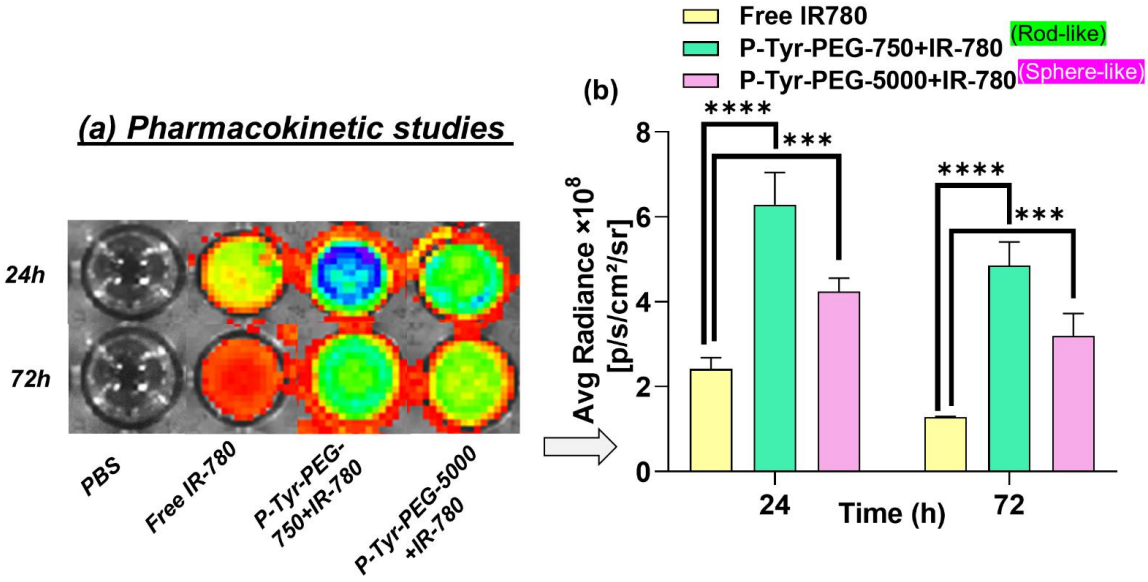

Figure 2.30 *(a) Representative time-dependent photograph of the plasma samples captured in a 96-well plate using IVIS. (b) Histogram representing the amount of IR-780 dye (quantified as average radiance) at various time points in plasma samples.*

The fluorescence signal from the plasma samples was quantified and plotted as a histogram for each time interval in Figure 10b. These results indicate that IR-780 loaded nanoparticles remained in the bloodstream for a longer period compared to free IR-780 dye, suggesting better circulation time and in vivo stability of the nanoparticles. To examine the probable toxicity of polymer brushes, biochemical analysis was done. Figure 2.31 shows no significant change in the apparent toxicity.

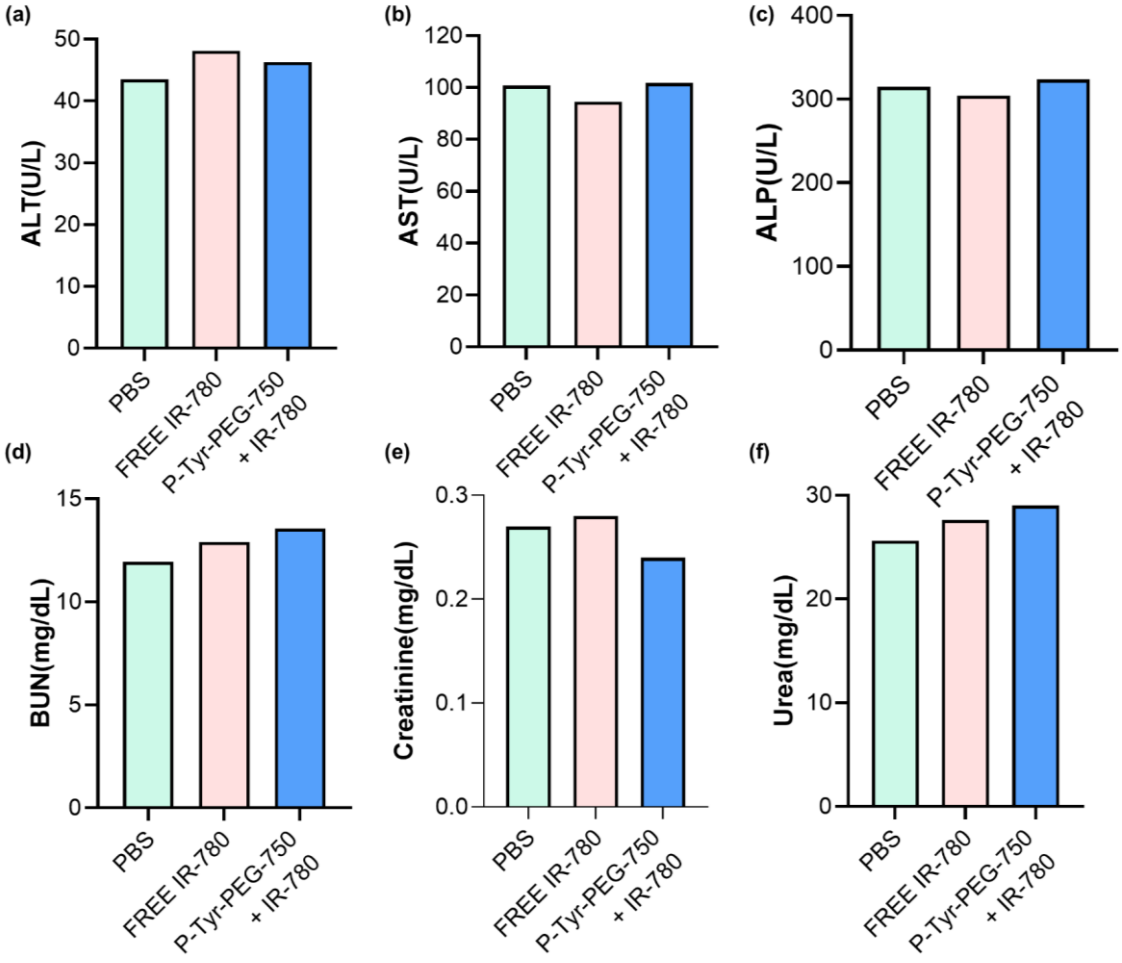

Figure. 2.31. *In vivo toxicity study for liver and kidney biomarker: (a) alanine transaminase (ALT), (b) aspartate transaminase (AST), (c) (c) Alkaline Phosphatase (ALP), (d) blood urea and nitrogen (BUN), (e) creatinine, (f) urea.*

These findings suggest that the nanoparticles did not induce any significant adverse effects on the kidney and liver based on the assessed biochemical markers. The stability in the levels of liver and kidney function markers implies a lack of substantial toxicity in these organs under the conditions of the study. These results contribute valuable insights into the safety profile of the nanoparticles, supporting the notion that they may not pose a notable risk to the kidney and liver. To investigate biodistribution in more detail, mice were sacrificed 72 hours post-injection, the mice were euthanized using an overdose of anesthesia (isoflurane) and perfused with PBS prior to organ harvesting. And their organs were collected and imaged using

IVIS. The resulting image is shown in Figure 2.32a, and fluorescence signal quantification from the image was plotted in the form of a histogram in Figure 2.32b.

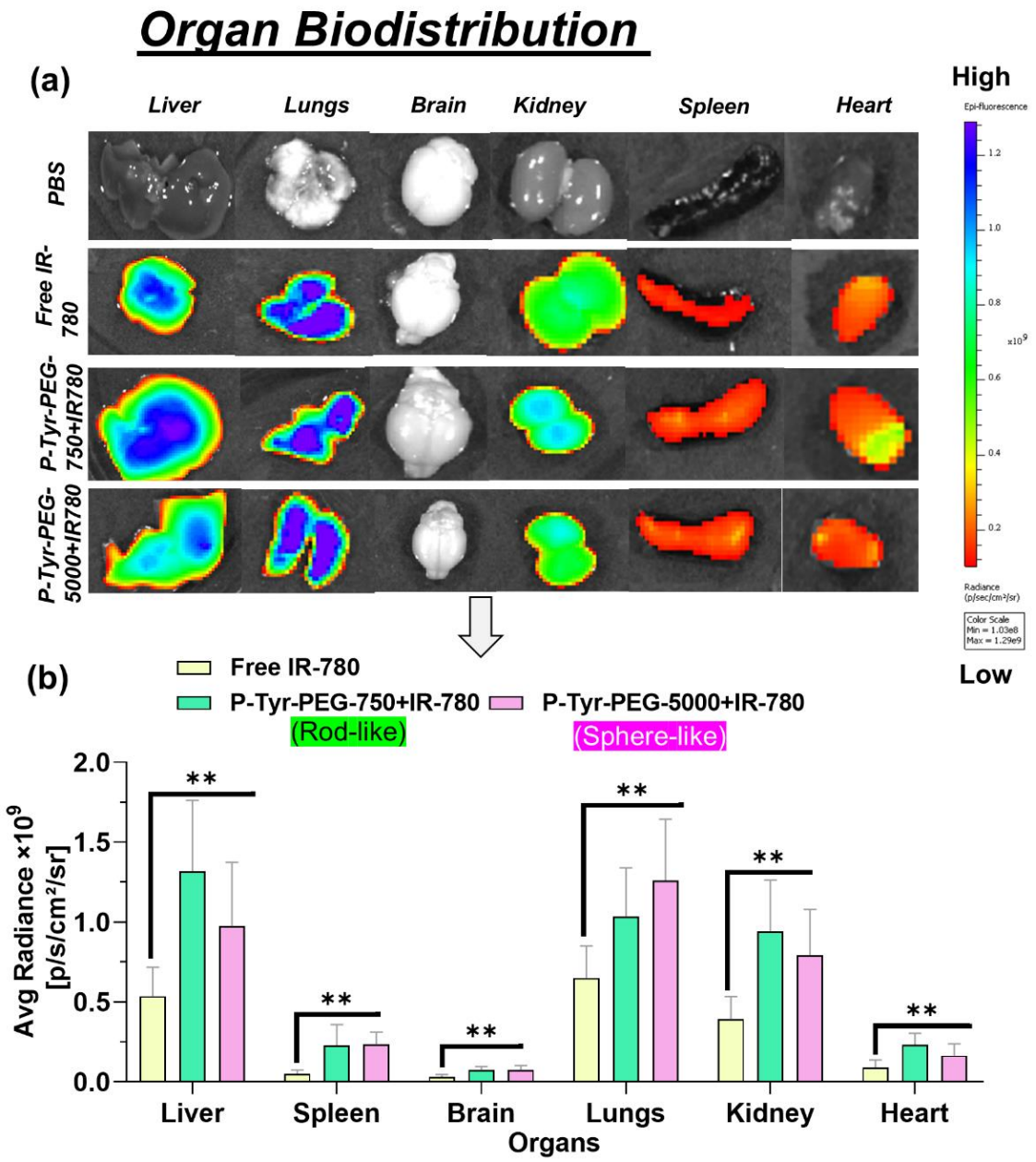

Figure 2.32 *(a) Photographs of the various organs (harvested post 72 h injection) captured using IVIS. (b) Histogram representing the amount of IR-780 dye (quantified as average radiance) in various organs.*

The fluorescence signals from free IR-780 injected mice were lower than those from IR-780 loaded polymer nanoparticles injected mice, reaffirming the better in vivo stability of polymer brushes. Again, the rod-like polymer showed stronger signals with respect to their higher penetration ability. Additionally, the kidney, liver, lungs, and heart showed more fluorescence signals, indicating greater uptake of IR-780 loaded rod-like polymer brush in these organs. The in vivo safety of the organs in liver, kidney, and lungs were validated by histopathological analysis (H&E staining). For this purpose, experiments were carried out by treating the mice with free IR-780, polymer PTyr-PEG-750, and PTyr-PEG-750+IR780 using PBS as a control.

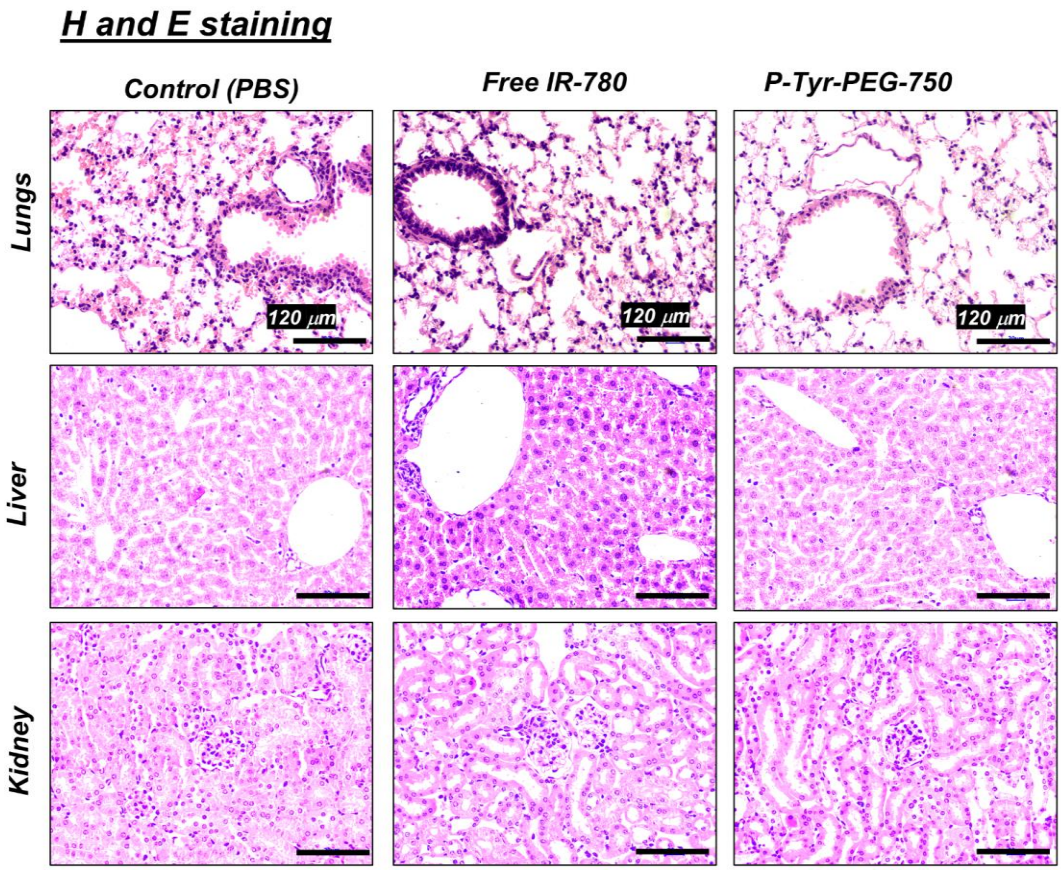

Figure 2.33 *Histopathological analysis (H & E staining) of the tissues after treatment with PBS alone, free IR-780, P-Tyr-PEG-750. Representative images (40X). Scale bar represents 120 μm.*

The organs were harvested after 72 h of injection and they were sliced and subjected to H & E staining. The tissues in Figure 2.33 revealed that the tissues are intact and they were not damaged by the polymer treatment. Microscopic examination of all the observed tissues viz.,

liver, kidneys and lungs did not reveal any lesion of pathological significance of all the treated groups PBS, P-Tyr-PEG-750, P-Tyr-PEG-750+IR-780 loaded and Free IR780. Data presented in this report suggestive of treatment of test drugs did not produce abnormalities in the observed organs.These exciting results demonstrate the potential of Tyrosine-based polymer architectures for biomedical applications. To further study the deep tissue penetration of the polymer brushes, the liver, kidney and lungs tissues were sliced from periphery-to-deep under cryotome conditions and these multiple locations cut tissues were subjected to IVIS imaging.

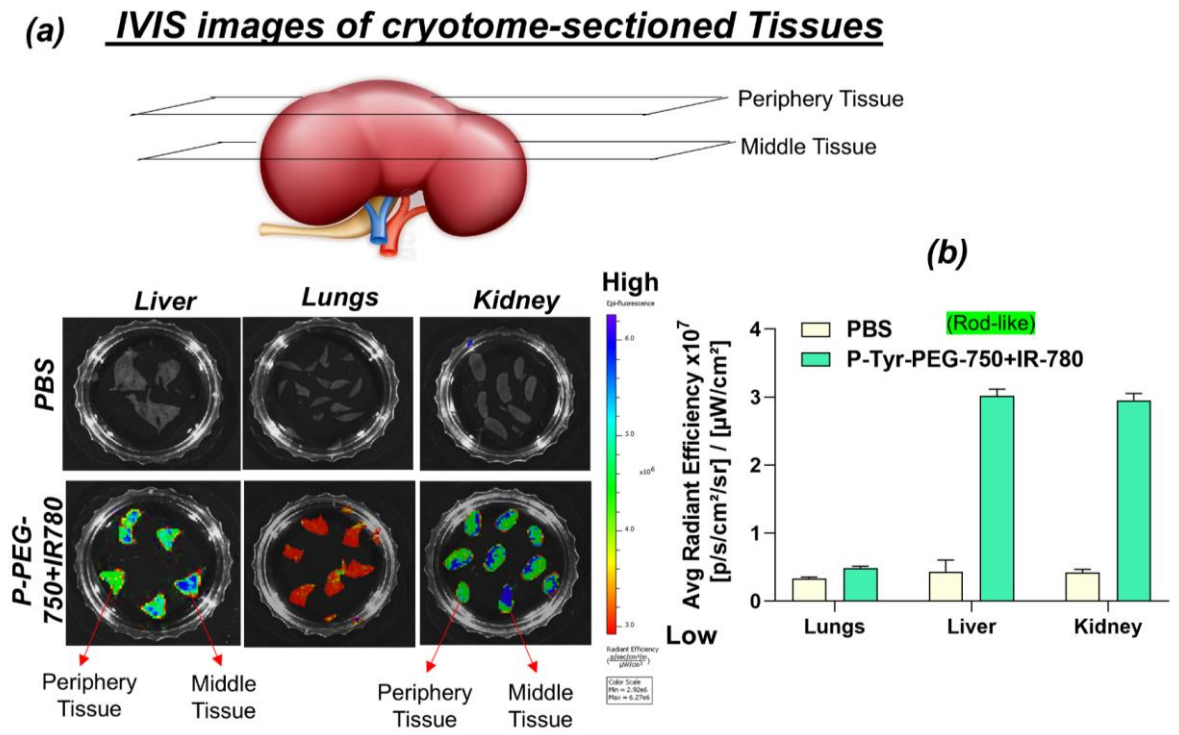

Figure 2.34 *(a) IVIS images of cryotome-tissue slices at periphery and middle portion of the Lungs, Liver and Kidney. The IVIS images showed the PBS treated tissues (as control) and PTyr-PEG-750+IR780 sample. The tissues collected at the periphery and middle portions are indicated. (b) IVIS Fluorescent signals of cryotome slices tissues of lungs, liver and kidney tissues. Sizes of slices tissue 100 µm thickness.*

The NIR IR-780 dye loaded polymer brush treated tissue slices were excited at 745 nm and the emission were collected from 800 nm. In this excitation and emission range, blood vessels do not show any fluorescence signals. Further, to rule out the possibility of the blood vessel emission signals in the IVIS imaging, the tissue slices that are collected followed by PBS injection were also subjected to IVIS analysis. This second set of samples would provide information of the background signals that are contributed by blood vessel, if any. The IVIS

images of the multiple slices for each organ are shown in Figure 2.34a for both PBS and NIR IR-780 dye loaded polymer brush. The IR signals from the tissues were quantified and plotted against in Figure 2.34b. The following trends are clearly evident by this analysis: (i) the PBS treated tissues do not show any signal in the IVIS imaging which rule out the possibility of fluorescent signals by blood vessels, and (ii) the NIR IR-780 polymer treated samples showed strong fluorescent signals and confirmed the delivery of the payloads. The enhanced and strong signals from the tissues sliced at the middle of the kidney was clearly much better than those slices of tissues from the periphery. This directly support the ability of the newly designed polymer brushes for tissue penetration to deliver the payload in the organs.

2.4 Conclusion

In summary, a novel class of biodegradable propargyl-functional poly(ester-urethane)s based on L-amino acids was developed using a solvent-free melt polycondensation method starting from L-tyrosine resources. These innovative poly(ester-urethane)s were created through the design of a multifunctional monomer derived from L-tyrosine, featuring a phenolic propargyl unit and carboxylic ester urethane. Methyl ester-urethane of the tyrosine monomer was subjected to melt-transesterification with commercially available diols, resulting in the production of high-molecular-weight poly(ester-urethane)s with propargyl functionalization via the melt-transesterification process. Subsequent post-polymerization approach was adopted for that various PEG monomethyl ether azides were synthesized and stitched to the polymer via a click reaction to form an amphiphilic polymer. These amphiphilic polymers self-assembled into nanoparticles to form brush rod-like morphology and DLS size measuring approximately 250 ± 10 nanometers and exhibited exceptional capabilities for encapsulating anticancer drugs such as doxorubicin (DOX) and NIR probe IR-780 dye. In vitro studies demonstrated that the drug-loaded polymer brush rod nanoparticles underwent enzymatic biodegradation and were released faster by 90 % than spherical nanoparticle 65 % brushes at the intracellular level to release the encapsulated drugs. remained stable under extracellular conditions. Temperature-dependent endocytosis experiments were performed at 37 ℃ and 4 ℃ degrees. Endocytosis is an energy-dependent process the polymeric brush rod degrades faster and the uptake of the rod is significant than the polymeric spherical nanoparticles. Cytotoxicity studies revealed that the newly developed brushes were non-toxic in nascent form whereas their DOX loaded Nano vectors exhibited excellent efficacy against cancer cells.

Confocal microscopic imaging confirmed the cellular uptake of drug-loaded brush nano-rod was significantly higher than spherical nanoparticles, showing that cells absorbed a significantly higher quantity of drugs when delivered from the brush L-tyrosine nano-rod platform than the free drug form. Time-dependent live cell experiment analysis demonstrated that DOX-loaded polymer nanoscaffolds internalized drugs at rates higher than the free DOX. Fix cell Confocal data also matches with live cell data, suggesting that polymeric brush rod has better uptake and faster release. *In-vivo* biodistribution studies reveal that polymeric brush nano-rod has better blood circulation time as well as in vivo stability of the nanoparticles. This research represents a pioneering exploration of untapped potential in L-amino acid bioresources, unveiling a new avenue for PEGylated brush poly(ester-urethane)s and their drug-delivery capabilities in cancer cells, and are expected to have a long-lasting impact.

2.5 References

(1) Chen, W.-L.; Cordero, R.; Tran, H.; Ober, C. K. *50th Anniversary Perspective* : Polymer Brushes: Novel Surfaces for Future Materials. *Macromolecules* **2017**, *50* (11), 4089–4113.

(2) Lamping, S.; Buten, C.; Ravoo, B. J. Functionalization and Patterning of Self-Assembled Monolayers and Polymer Brushes Using Microcontact Chemistry. *Acc Chem Res* **2019**, *52* (5), 1336–1346.

(3) Quadir, M. A.; Martin, M.; Hammond, P. T. Clickable Synthetic Polypeptides—Routes to New Highly Adaptive Biomaterials. *Chemistry of Materials* **2014**, *26* (1), 461–476.

(4) Riachi, C.; Schüwer, N.; Klok, H.-A. Degradable Polymer Brushes Prepared via Surface-Initiated Controlled Radical Polymerization. *Macromolecules* **2009**, *42* (21), 8076–8081.

(5) Wang, R.; Wei, Q.; Sheng, W.; Yu, B.; Zhou, F.; Li, B. Driving Polymer Brushes from Synthesis to Functioning. *Angewandte Chemie International Edition* **2023**, *62* (27), e202219312.

(6) Pelras, T.; Mahon, C. S.; Müllner, M. Synthesis and Applications of Compartmentalised Molecular Polymer Brushes. *Angewandte Chemie International Edition* **2018**, *57* (24), 6982–6994.

(7) Sheiko, S. S.; Sumerlin, B. S.; Matyjaszewski, K. Cylindrical Molecular Brushes: Synthesis, Characterization, and Properties. *Prog Polym Sci* **2008**, *33* (7), 759–785.

(8) Degirmenci, A.; Sanyal, R.; Sanyal, A. Plug-and-Play Biointerfaces: Harnessing Host–Guest Interactions for Fabrication of Functional Polymeric Coatings. *Biomacromolecules* **2023**, *24* (8), 3568–3579.

(9) Gevrek, T. N.; Degirmenci, A.; Sanyal, R.; Klok, H.-A.; Sanyal, A. Succinimidyl Carbonate-Based Amine-Reactive Polymer Brushes: Facile Fabrication of Functional Interfaces. *ACS Appl Polym Mater* **2021**, *3* (5), 2507–2517.

(10) Storti, G.; Jauhola-Straight, R.; Hannigan, J. R.; Sidorenko, A. Design of Amphiphilic, Biodegradable Functionalized Polyoxazoline Hybrid-Block Graft Copolymers Using Click Reactions. *Macromolecules* **2023**, *56* (10), 3538–3549.

(11) Al Nakeeb, N.; Willersinn, J.; Schmidt, B. V. K. J. Self-Assembly Behavior and Biocompatible Cross-Linking of Double Hydrophilic Linear-Brush Block Copolymers. *Biomacromolecules* **2017**, *18* (11), 3695–3705.

(12) Braga, C. B.; Pilli, R. A.; Ornelas, C.; Weck, M. Near-Infrared Fluorescent Micelles from Poly(Norbornene) Brush Triblock Copolymers for Nanotheranostics. *Biomacromolecules* **2021**, *22* (12), 5290–5306.

(13) Milatz, R.; Duvigneau, J.; Vancso, G. J. Dopamine-Based Copolymer Bottlebrushes for Functional Adhesives: Synthesis, Characterization, and Applications in Surface Engineering of Antifouling Polyethylene. *ACS Appl Mater Interfaces* **2023**, *15* (28), 34023–34030.

(14) Zhang, L.; Zhang, Z.; Liu, C.; Zhang, X.; Fan, Q.; Wu, W.; Jiang, X. NIR-II Dye-Labeled Cylindrical Polymer Brushes for in Vivo Imaging. *ACS Macro Lett* **2019**, *8* (12), 1623–1628.

(15) Wang, R.; Yin, C.; Liu, C.; Sun, Y.; Xiao, P.; Li, J.; Yang, S.; Wu, W.; Jiang, X. Phenylboronic Acid Modification Augments the Lysosome Escape and Antitumor Efficacy of a Cylindrical Polymer Brush-Based Prodrug. *J Am Chem Soc* **2021**, *143* (49), 20927–20938.

(16) Truong, V.; Blakey, I.; Whittaker, A. K. Hydrophilic and Amphiphilic Polyethylene Glycol-Based Hydrogels with Tunable Degradability Prepared by "Click" Chemistry. *Biomacromolecules* **2012**, *13* (12), 4012–4021.

(17) Engler, A. C.; Lee, H.; Hammond, P. T. Highly Efficient "Grafting onto" a Polypeptide Backbone Using Click Chemistry. *Angewandte Chemie* **2009**, *121* (49), 9498–9502.

(18) Geng, Z.; Shin, J. J.; Xi, Y.; Hawker, C. J. Click Chemistry Strategies for the Accelerated Synthesis of Functional Macromolecules. *Journal of Polymer Science* **2021**, *59* (11), 963–1042.

(19) Li, G. L.; Yu, R.; Qi, T.; Möhwald, H.; Shchukin, D. G. Double-Shelled Polymer Nanocontainers Decorated with Poly(Ethylene Glycol) Brushes by Combined Distillation Precipitation Polymerization and Thiol–Yne Surface Chemistry. *Macromolecules* **2016**, *49* (3), 1127–1134.

(20) Yuksekdag, Y. N.; Gevrek, T. N.; Sanyal, A. Diels-Alder "Clickable" Polymer Brushes: A Versatile Catalyst-Free Conjugation Platform. *ACS Macro Lett* **2017**, *6* (4), 415–420.

(21) Müllner, M.; Dodds, S. J.; Nguyen, T. H.; Senyschyn, D.; Porter, C. J. H.; Boyd, B. J.; Caruso, F. Size and Rigidity of Cylindrical Polymer Brushes Dictate Long Circulating Properties in Vivo. *ACS Nano* **2015**, *9* (2), 1294–1304.

(22) Bratek-Skicki, A.; Cristaudo, V.; Savocco, J.; Nootens, S.; Morsomme, P.; Delcorte, A.; Dupont-Gillain, C. Mixed Polymer Brushes for the Selective Capture and Release of Proteins. *Biomacromolecules* **2019**, *20* (2), 778–789.

(23) Ercole, F.; Kim, C.-J.; Dao, N. V.; Tse, W. K. L.; Whittaker, M. R.; Caruso, F.; Quinn, J. F. Synthesis of Thermoresponsive, Catechol-Rich Poly(Ethylene Glycol) Brush Polymers for Attenuating Cellular Oxidative Stress. *Biomacromolecules* **2023**, *24* (1), 387–399.

(24) Psarra, E.; Foster, E.; König, U.; You, J.; Ueda, Y.; Eichhorn, K.-J.; Müller, M.; Stamm, M.; Revzin, A.; Uhlmann, P. Growth Factor-Bearing Polymer Brushes - Versatile Bioactive Substrates Influencing Cell Response. *Biomacromolecules* **2015**, *16* (11), 3530–3542.

(25) Rautio, J.; Kumpulainen, H.; Heimbach, T.; Oliyai, R.; Oh, D.; Järvinen, T.; Savolainen, J. Prodrugs: Design and Clinical Applications. *Nat Rev Drug Discov* **2008**, *7* (3), 255–270.

(26) Surnar, B.; Jayakannan, M. Structural Engineering of Biodegradable PCL Block Copolymer Nanoassemblies for Enzyme-Controlled Drug Delivery in Cancer Cells. *ACS Biomater Sci Eng* **2016**, *2* (11), 1926–1941.

(27) Rainbolt, E. A.; Washington, K. E.; Biewer, M. C.; Stefan, M. C. Recent Developments in Micellar Drug Carriers Featuring Substituted Poly(ε-Caprolactone)s. *Polym Chem* **2015**, *6* (13), 2369–2381.

(28) Surnar, B.; Jayakannan, M. Stimuli-Responsive Poly(Caprolactone) Vesicles for Dual Drug Delivery under the Gastrointestinal Tract. *Biomacromolecules* **2013**, *14* (12), 4377–4387.

(29) Surnar, B.; Jayakannan, M. Triple Block Nanocarrier Platform for Synergistic Cancer Therapy of Antagonistic Drugs. *Biomacromolecules* **2016**, *17* (12), 4075–4085.

(30) Malhotra, M.; Surnar, B.; Jayakannan, M. Polymer Topology Driven Enzymatic Biodegradation in Polycaprolactone Block and Random Copolymer Architectures for Drug Delivery to Cancer Cells. *Macromolecules* **2016**, *49* (21), 8098–8112.

(31) Ghosh, R.; Jayakannan, M. Theranostic FRET Gate to Visualize and Quantify Bacterial Membrane Breaching. *Biomacromolecules* **2023**, *24* (2), 739–755.

(32) Ghosh, R.; Malhotra, M.; Sathe, R. R. M.; Jayakannan, M. Biodegradable Polymer Theranostic Fluorescent Nanoprobe for Direct Visualization and Quantitative Determination of Antimicrobial Activity. *Biomacromolecules* **2020**, *21* (7), 2896–2912.

(33) Mincheva, R.; Jasmani, L.; Josse, T.; Paint, Y.; Raquez, J.-M.; Gerbaux, P.; Eyley, S.; Thielemans, W.; Dubois, P. Binary Mixed Homopolymer Brushes Tethered to Cellulose Nanocrystals: A Step Towards Compatibilized Polyester Blends. *Biomacromolecules* **2016**, *17* (9), 3048–3059.

(34) Yu, Y.; Chen, C.-K.; Law, W.-C.; Mok, J.; Zou, J.; Prasad, P. N.; Cheng, C. Well-Defined Degradable Brush Polymer–Drug Conjugates for Sustained Delivery of Paclitaxel. *Mol Pharm* **2013**, *10* (3), 867–874.

(35) Teske, N. S.; Voigt, J.; Shastri, V. P. Clickable Degradable Aliphatic Polyesters via Copolymerization with Alkyne Epoxy Esters: Synthesis and Post functionalization with Organic Dyes. *J Am Chem Soc* **2014**, *136* (29), 10527–10533.

(36) Borchmann, D. E.; Tarallo, R.; Avendano, S.; Falanga, A.; Carberry, T. P.; Galdiero, S.; Weck, M. Membranotropic Peptide-Functionalized Poly(Lactide)- *Graft* -Poly(Ethylene Glycol) Brush Copolymers for Intracellular Delivery. *Macromolecules* **2015**, *48* (4), 942–949.

(37) Bej, S.; Dhayani, A.; Vemula, P.; Ramakrishnan, S. Fine-Tuning Crystallization-Induced Gelation in Amphiphilic Double-Brush Polymers. *Langmuir* **2021**, *37* (5), 1788–1798.

(38) Chakraborty, S.; Ramkumar, S. G.; Ramakrishnan, S. Amphiphilic Double-Brush Polymers Based on Itaconate Diesters. *Macromolecules* **2017**, *50* (13), 5004–5013.

(39) Mandal, J.; Krishna Prasad, S.; Rao, D. S. S.; Ramakrishnan, S. Periodically Clickable Polyesters: Study of Intrachain Self-Segregation Induced Folding, Crystallization, and Mesophase Formation. *J Am Chem Soc* **2014**, *136* (6), 2538–2545.

(40) Roy, R. K.; Ramakrishnan, S. Thiol-ene Clickable *Hyperscaffolds* Bearing Peripheral Allyl Groups. *J Polym Sci A Polym Chem* **2011**, *49* (8), 1735–1744.

(41) Chanda, S.; Ramakrishnan, S. Controlling Interlamellar Spacing in Periodically Grafted Amphiphilic Copolymers. *Macromolecules* **2016**, *49* (9), 3254–3263.

(42) Mandal, J.; Ramakrishnan, S. Periodically Grafted Amphiphilic Copolymers: Effects of Steric Crowding and Reversal of Amphiphilicity. *Langmuir* **2015**, *31* (22), 6035–6044.

(43) Saxena, S.; Jayakannan, M. Development of L-Amino-Acid-Based Hydroxyl Functionalized Biodegradable Amphiphilic Polyesters and Their Drug Delivery Capabilities to Cancer Cells. *Biomacromolecules* **2020**, *21* (1), 171–187.

(44) Anantharaj, S.; Jayakannan, M. Amyloid-Like Hierarchical Helical Fibrils and Conformational Reversibility in Functional Polyesters Based on L-Amino Acids. *Biomacromolecules* **2015**, *16* (3), 1009–1020.

(45) Anantharaj, S.; Jayakannan, M. Polymers from Amino Acids: Development of Dual Ester-Urethane Melt Condensation Approach and Mechanistic Aspects. *Biomacromolecules* **2012**, *13* (8), 2446–2455.

(46) Anantharaj, S.; Jayakannan, M. Catalysts and Temperature Driven Melt Polycondensation Reaction for Helical Poly(Ester-Urethane)s Based on Natural L-Amino Acids. *J Polym Sci A Polym Chem* **2016**, *54* (8), 1065–1077.

(47) Anantharaj, S.; Jayakannan, M. Melt Polycondensation Approach for Reduction Degradable Helical Polyester Based on L-cystine. *J Polym Sci A Polym Chem* **2016**, *54* (18), 2864–2875.

(48) Aluri, R.; Jayakannan, M. One-Pot Two Polymers: ABB′ Melt Polycondensation for Linear Polyesters and Hyperbranched Poly(Ester-Urethane)s Based on Natural L-Amino Acids. *Polym Chem* **2015**, *6* (25), 4641–4649.

(49) Chandra Joshi, D.; Ashokan, A.; Jayakannan, M. L-Amino Acid Based Phenol- and Catechol-Functionalized Poly(Ester-Urethane)s for Aromatic π-Interaction Driven Drug Stabilization and Their Enzyme-Responsive Delivery in Cancer Cells. *ACS Appl Bio Mater* **2022**, *5* (11), 5432–5444.

(50) Joshi, D. C.; Saxena, S.; Jayakannan, M. Development of L-Lysine Based Biodegradable Polyurethanes and Their Dual-Responsive Amphiphilic Nanocarriers for Drug Delivery to Cancer Cells. *ACS Appl Polym Mater* **2019**, *1* (7), 1866–1880.

(51) Aluri, R.; Jayakannan, M. Development of L-Tyrosine-Based Enzyme-Responsive Amphiphilic Poly(Ester-Urethane) Nanocarriers for Multiple Drug Delivery to Cancer Cells. *Biomacromolecules* **2017**, *18* (1), 189–200.

(52) Aluri, R.; Saxena, S.; Joshi, D. C.; Jayakannan, M. Multistimuli-Responsive Amphiphilic Poly(Ester-Urethane) Nanoassemblies Based on L-Tyrosine for

Intracellular Drug Delivery to Cancer Cells. *Biomacromolecules* **2018**, *19* (6), 2166–2181.

(53) Khuddus, M.; Jayakannan, M. Melt Polycondensation Strategy for Amide-Functionalized L-Aspartic Acid Amphiphilic Polyester Nano-Assemblies and Enzyme-Responsive Drug Delivery in Cancer Cells. *Biomacromolecules* **2023**, *24* (6), 2643–2660.

(54) Saxena, S.; Jayakannan, M. Enzyme and PH Dual Responsive L-Amino Acid Based Biodegradable Polymer Nanocarrier for Multidrug Delivery to Cancer Cells. *J Polym Sci A Polym Chem* **2016**, *54* (20), 3279–3293.

(55) Saxena, S.; Jayakannan, M. π-Conjugate Fluorophore-Tagged and Enzyme-Responsive L-Amino Acid Polymer Nanocarrier and Their Color-Tunable Intracellular FRET Probe in Cancer Cells. *Biomacromolecules* **2017**, *18* (8), 2594–2609.

(56) Saxena, S.; Pradeep, A.; Jayakannan, M. Enzyme-Responsive Theranostic FRET Probe Based on L-Aspartic Amphiphilic Polyester Nanoassemblies for Intracellular Bioimaging in Cancer Cells. *ACS Appl Bio Mater* **2019**, *2* (12), 5245–5262.

(57) Saxena, S.; Pradeep, A.; Jayakannan, M. Enzyme-Responsive Theranostic FRET Probe Based on L-Aspartic Amphiphilic Polyester Nanoassemblies for Intracellular Bioimaging in Cancer Cells. *ACS Appl Bio Mater* **2019**, *2* (12), 5245–5262.

(58) Pranav, U.; Malhotra, M.; Pathan, S.; Jayakannan, M. Structural Engineering of Star Block Biodegradable Polymer Unimolecular Micelles for Drug Delivery in Cancer Cells. *ACS Biomater Sci Eng* **2023**, *9* (2), 743–759.

(59) Kolhar, P.; Doshi, N.; Mitragotri, S. Polymer Nanoneedle-Mediated Intracellular Drug Delivery. *Small* **2011**, *7* (14), 2094–2100.

(60) Champion, J. A.; Mitragotri, S. Role of Target Geometry in Phagocytosis. *Proceedings of the National Academy of Sciences* **2006**, *103* (13), 4930–4934.

(61) Yang, L.; Ma, H.; Lin, S.; Zhu, Y.; Chen, H.; Zhang, N.; Feng, X. Nucleus-Selective Codelivery of Proteins and Drugs for Synergistic Antitumor Therapy. *Chem Sci* **2022**, *13* (35), 10342–10348.

(62) Chen, Y.; Li, Z.; Wang, H.; Wang, Y.; Han, H.; Jin, Q.; Ji, J. IR-780 Loaded Phospholipid Mimicking Homopolymeric Micelles for Near-IR Imaging and Photothermal Therapy of Pancreatic Cancer. *ACS Appl Mater Interfaces* **2016**, *8* (11), 6852–6858.

Chapter 3

L-Tyrosine Sugar based Biodegradable Hybrid Polymer Brushes

Abstract

We developed Biodegradable polymer brushes derived from bio-based resources that are in high demand for creating sustainable polymer brush systems, both for everyday plastic applications and advancements in the biomedical sector. Here, the propargyl, functionalized L-tyrosine monomer was polymerized via solvent-free melt polymerization strategy to yield a hydrophobic biodegradable poly(ester-urethane)s. Further, sugar azides were synthesized by a protection deprotection strategy to yield free hydroxyl sugar azides. These sugar azides were subsequently characterized by ^{1}H NMR and ^{13}C NMR. The post-polymerization click chemistry strategy was utilized to get fully amphiphilic biodegradable sugar hybrid polymer brushes. Further, these sugar polymer brushes showed higher glass transition temperature (Tg ≥ 107 ℃) as compared to their homopolymer; these polymer brushes were self-assembled into nanoparticles with sizes below 100 nm in aqueous environments. The nanoparticles were capable of encapsulating various fluorescent dyes such as HPTS and therapeutic agents like CPT, TPT, and CUR. The photophysical properties were analyzed using absorbance and emission spectroscopy and retained their photophysical properties. These sugar polymer brushes were performed on their biocompatibility and cytotoxicity assay. We found that these sugar polymer brushes are non-toxic to the cancerous as well as normal cell lines at higher concentrations of 100 µg/mL. Further, the drug-loaded polymer brushes showed comparable cytotoxicity as a free drug in the cancerous cell line MCF-7 as well as the HEK-293 cell line. The nanoparticles exhibited excellent biocompatibility with both normal and cancer cell lines and showed non hemolytic in nature. Drug-loaded polymer bioimaging studies using confocal laser scanning microscopy (CLSM) confirmed the interaction between the polymer and its cargo at the cellular level. In vivo, biodistribution studies showed that ICG-loaded nanoparticles demonstrated prolonged nanoparticle retention compared to free ICG.

3.1 Introduction

Glycopolymers, synthetic polymers functionalized with carbohydrate (glyco) units, represent a fascinating class of materials at the intersection of polymer science and glycobiology.[1] Glycopolymers are particularly attractive for biomedical applications due to their biocompatibility, bioactivity, and ability to interact specifically with lectins,[2] proteins that recognize carbohydrate structures.[3] These polymers mimic natural glycoproteins[4] and polysaccharides,[5] which play critical roles in biological processes such as cell signaling,[6] immune response,[7,8] and pathogen recognition.[9] This specificity enables glycopolymers to serve as multivalent ligands,[10] The ability to design and synthesize glycopolymers with controlled architectures and tailored functionalities has enabled their application in various fields, including drug delivery,[11–13] amplifying binding interactions for applications in targeted drug delivery,[14–17] cancer therapy,[18–20] antiviral treatments,[21] and materials science.[22] Additionally, glycopolymers have shown promise in the design of hydrogels, [23–25]nanoparticles,[26] and emphasizing their versatility. The synthesis of glycopolymers typically involves the polymerization of glycosylated monomers or post-polymerization modification of pre-formed polymers with carbohydrate groups. Advances in living polymerization techniques, such as reversible addition-fragmentation chain transfer (RAFT) polymerization,[27–29] atom transfer radical polymerization (ATRP),[30] and ring-opening polymerization (ROP),[31–34] have facilitated the precise control of glycopolymer composition, molecular weight, and architecture. In recent years, efforts have focused on developing environmentally friendly and sustainable glycopolymer synthesis methods, incorporating renewable carbohydrate resources such as glucose, mannose, and galactose. These advancements align with the global push toward green chemistry and sustainable materials.[35] L-amino acid bioresources have been transformed into N-carboxyanhydride (NCA) monomers and subsequently polymerized through ring-opening polymerization to produce synthetic polypeptides. However, these synthetic polypeptides lack the ability to melt or flow, rendering them unsuitable for use as thermoplastic engineering polymers. Additionally, the protease enzyme systems in living organisms exhibit high specificity for cleaving particular peptide linkages, which limits the biodegradability of long-chain polypeptides under physiological conditions.[36,37] Interestingly, the literature contains very few reports of synthetic approaches that combine sugars and L-amino acids, containing melt polycondensation. This presents a promising pathway for creating sugar-amino acid hybrid thermoplastic materials with potential applications in biomedical and industrial fields. Over the past decade, our research group has focused on developing solvent-

free melt polycondensation methods for L-amino acid resources to synthesize various polymers, including linear and hyperbranched,[38] polyesters,[39–41] poly(ester-urethane)s,[42–46] and polyurethanes.[47] This approach has been further extended to multifunctional L-amino acid monomers, yielding thermo-responsive,[48,49] pH-sensitive,[50] and enzyme-responsive nano-architectures for applications such as drug delivery in cancer therapy. Our laboratory's efforts have created a unique opportunity to integrate L-amino acids and carbohydrates into a one-pot click reaction, paving the way for the synthesis of previously unexplored sugar-amino acid hybrid engineering thermoplastics. This breakthrough represents a significant step toward achieving what has long been an ambitious goal for synthetic chemists.

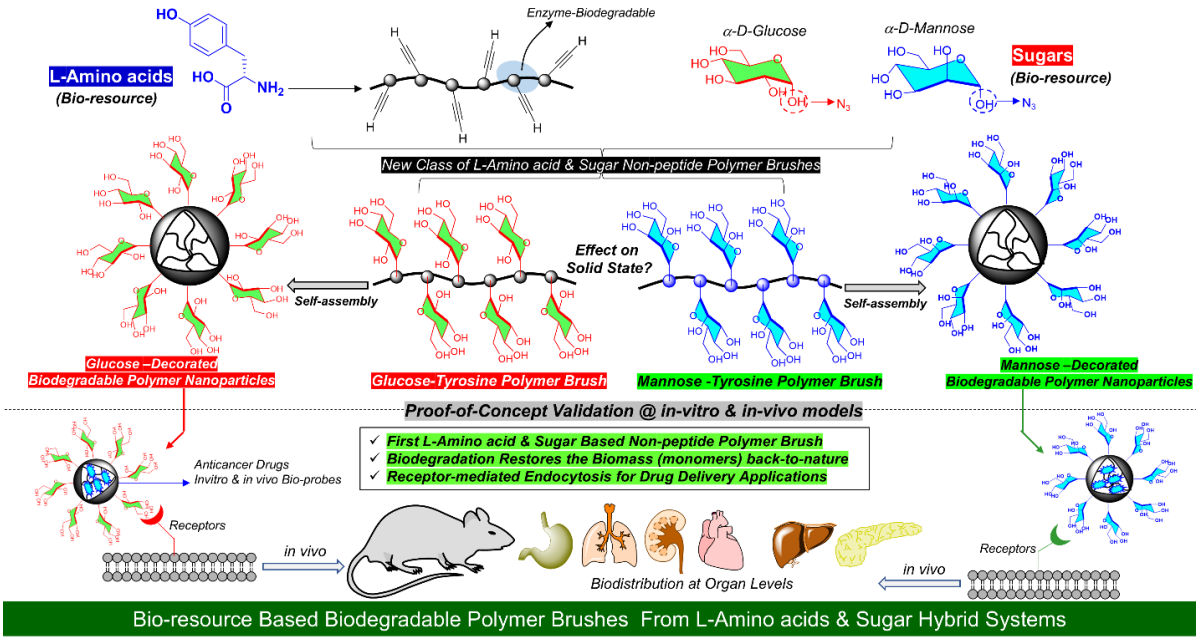

Figure 3.1. *Design and development of L-amino acid based biodegradable polymer brushes with precise control in size. Drug Encapsulated Polymer brush nanocarrier and in-vitro studies. Organ level in-vivo biodistribution of the polymer brushes.*

In this work, we provide one of the pioneering efforts to synthesize hybrid polymers from two essential natural resources, L-amino acids and sugars, using an eco-friendly, click-reaction approach, as illustrated in Figure 3.1. During biodegradation, the long polymer chains decompose into their original building blocks, L-amino acids, and (D-glucose/D-mannose), effectively restoring them to their natural forms.

L-amino acid ester-urethane monomers were successfully melt-polymerized with diols, resulting in high molecular weight aliphatic poly(ester-urethane)s. Furthermore, D-glucose and D-mannose were reacted with poly(ester-urethane) to synthesize a hybrid sugar polymer. These poly(ester-urethane) brushes were characterized for structural and thermal properties and self-

assembled into 100±10 nm sized spherical nanoparticles in an aqueous medium. The nano-assemblies showed excellent encapsulation capabilities for anticancer drug camptothecin (CPT), Topotecan (TPT), anti-inflammatory drug curcumin (CUR), biomarkers such as 8-hydroxypyrene-1,3,6-trisulfonic acid trisodium salt (HPTS), Cardiogreen (ICG), etc. These hybrid polymer brushes were nontoxic to cancerous as well as normal cell lines. These polymers are non-hemolytic in nature. The anticancer drug CPT validates their enzymatic biodegradation within intracellular compartments of mammalian cell lines. Confocal laser scanning microscopy (CSLM) assisted time-dependent cellular uptake analysis directly evident for the of CPT loaded polymer NP endocytosis and their internalization for biodegradation. Further, In-vivo live animal bio-imaging for biodistribution was carried out using cardio green biomarker labelled polymer brushes. The polymer brushes exhibited longer blood circulation time as well and harvested organs showed larger accumulation of polymer brushes in major excretory organs after 24h. This synthetic strategy introduces a novel pathway for developing fully bio-based and biodegradable polymers derived from L-amino acids and sugars, marking a significant addition to the field of sustainable polymer research.

3.2 Experimental Section

3.2.1 Materials and Methods

L-Tyrosine, α-D-Glucose, α-D-Mannose, 1,12-dodecane diol, Titanium (IV) butoxide [$Ti(OBu)_4$], Trimethylsilyl Azide (TMS-N_3), $SnCl_4$, 4-(Dimethylamino)pyridine (DMAP), Sodium methoxide, paraformaldehyde, glycerol, and HPLC-grade dimethyl sulfoxide (DMSO) were obtained from Sigma-Aldrich. Additional reagents including Dowex-450 resin, methyl chloroformate, acetic anhydride, pyridine, propargyl bromide, thionyl chloride, copper sulfate pentahydrate ($CuSO_4 \cdot 5H_2O$), sodium ascorbate, PBS (1×), pyrene, 8-Hydroxypyrene-1,3,6-trisulfonic acid trisodium salt (HPTS), Nile Red, the near-infrared probe Indocyanine green (ICG), curcumin, camptothecin (CPT), topotecan (TPT), horse liver esterase enzyme, and 3-(4,5-dimethylthiazol-2-yl)-2,5-diphenyltetrazolium bromide (MTT) were also purchased from Sigma-Aldrich. Other solvents, reagents, and salts were obtained locally and used as received without further purification. Cell culture reagents, including 4% paraformaldehyde, DMEM media with phenol red, 10% (v/v) fetal bovine serum (FBS), 1% (v/v) penicillin-streptomycin, were also obtained from Sigma-Aldrich. The following cancer cell lines were maintained at 37 °C in a 5% CO_2 atmosphere human breast cancer (MCF-7), wild-type mouse embryonic fibroblasts (WT-MEF), human embryonic kidney (HEK-293), breast cancer (MDA-MB-468), and human pancreatic cancer (MIA PaCa-2).

3.2.2 General Procedures

The following instruments and procedures were used for the analysis of monomers and polymers NMR Spectroscopy Both 400-MHz Bruker and Bruker Neo 400-MHz spectrometers were utilized to obtain the ^{13}C NMR and ^{1}H NMR spectra. $CDCl_3$ and DMSO d6 were used as the solvents, and TMS served as the internal standard. Mass Spectrometry The monomer mass was determined using a Biosystems 4800 PLUS MALDI TOF/TOF Analyzer. Size Exclusion Chromatography (SEC): SEC was performed with a Viscotek VE 1122 pump and VE 3580 RI detector using tetrahydrofuran (THF) as the mobile phase and polystyrene as the standard. For SEC analysis in DMF, Agilent PLgel 10 µm MIXED-B columns (7.5 × 300 mm) were used at 70 °C. Thermal Analysis A Perkin Elmer STA 6000 thermal analyzer was used to study the thermal degradation of polymers under a nitrogen atmosphere at a heating rate of 10 °C/min. Thermal characterization of all polymers was performed with a TAQ20 differential scanning calorimeter (DSC), calibrated using an indium standard. Polymer thermograms were recorded by heating and cooling at 10 °C/min under a nitrogen atmosphere. FT-IR Spectroscopy FT-IR spectra were recorded using a Bruker AlphaT Fourier-transform infrared spectrophotometer. Dynamic Light Scattering (DLS) A Malvern Instruments Nano ZS-90 device equipped with a 633 nm red laser was used for DLS measurements. Scanning Electron Microscopy (SEM) Field emission SEM (FE-SEM) images were captured with a Zeiss UltraPlus SEM. Samples were drop-casted onto silicon wafers, and a gold coating was applied for imaging. Atomic Force Microscopy (AFM) AFM images were taken using a Veeco Nanoscope IV in tapping mode. Samples were drop-cast on mica sheets. Confocal Microscopy Confocal microscopic analysis was performed using a Leica SP8 (or Zeiss LSM 710) microscope.

3.2.3 Synthesis of Methyl (methoxycarbonyl)-L-tyrosinate (Compound 2):

L-Tyrosine (15.0 g, 0.082 mol) was dissolved in 70 mL of anhydrous methanol in a 250 mL two-neck round bottom flask. Thionyl chloride (10.7 g, 6.7 mL, 0.091 mol) was added dropwise while maintaining the mixture at an ice-cold temperature. The reaction mixture was gradually brought to room temperature and refluxed for 12 hours under a nitrogen atmosphere. After completion, thionyl chloride and methanol were removed via vacuum distillation, yielding a white solid residue of the L-tyrosine ester amine salt (Compound 1). This residue was neutralized using 90 mL of a 15% sodium carbonate solution, kept under ice-cold conditions. A solution of methyl chloroformate (7.1 mL, 0.0911 mol) in 90 mL of dichloromethane was added dropwise, and the reaction was stirred at room temperature for 12 hours. The solvent

was removed using a rotary evaporator, and the residue was diluted with dichloromethane, then passed through anhydrous Na_2SO_4. The product was purified by column chromatography using a chloroform-methanol mixture (9:1 v/v) as the eluent, yielding a white solid product. Yield = 18.0 g (85%). ^{1}H NMR (400 MHz, $CDCl_3$): δ ppm: 3.01–3.05 (m, 2H, Ph-CH_2), 3.67 (s, 3H, -NH-$COOCH_3$), 3.73 (s, 3H, -$COOCH_3$), 4.61 (s, 1H, Ph-CH_2CH), 5.19 (s, 1H, NH), 6.73–6.75 (m, 2H, Ph), 6.96–6.98(m,2H, Ph). ^{13}C NMR (100 MHz, $CDCl_3$): δ ppm: 173, 157, 156, 131, 128, 116, 55, 53, 38. FT-IR (cm^{-1}): 3291, 2954, 1713, 1610, 1508, 1441, 1358, 1262, 1213, 1059, 1023, 700.

3.2.4 Synthesis of Methyl(S)-2-(Methoxycarbonylamino)-3-(4-(prop-2-yn-1-yloxy)phenyl)propanoate (Compound 3, Monomer):

Compound 2 (5.0 g, 0.019 mol) was dissolved in 70 mL of dry acetonitrile in a clean 100 mL two-neck round bottom flask. Potassium carbonate (K_2CO_3) (3.26 g, 0.023 mol) was then added, and the mixture was refluxed under nitrogen for 30 minutes. Afterward, propargyl bromide (2.6 mL, 0.023 mol) was introduced, and the reaction was further refluxed for 12 hours under a nitrogen atmosphere. The solvent was evaporated using a rotary evaporator, and the residue was treated with water. The aqueous layer was extracted three times with ethyl acetate. The resulting organic layer was dried and the product was purified using column chromatography with a dichloromethane-methanol eluent (9:1 v/v) to yield a white solid. Yield = 5.2 g (91%). ^{1}H NMR (400MHz ,DMSO) d = 7.65 (d, *J* = 8.1 Hz, 1 H), 7.17 (d, *J* = 8.6 Hz, 2 H), 6.89 (d, *J* = 8.8 Hz, 2 H), 4.75 (d, *J* = 2.4 Hz, 2 H), 4.24 - 4.09 (m, 1H), 3.62 (s, 3 H), 3.53 (t, *J* = 2.3 Hz, 1 H), 3.49 (s, 3 H), 2.96 (dd, *J* = 4.9, 13.9 Hz, 1 H), 2.85 - 2.73 (m, 1 H). ^{13}C NMR (100 MHz, DMSO) d = 173.0, 157.0, 156.4, 130.5, 115.1, 79.8, 78.6, 56.2, 55.8, 52.4, 52.0, 36.1. FT-IR (cm^{-1}): 3291, 2954, 2120, 1713, 1610, 1508, 1441, 1358, 1262, 1213, 1059, 1023, 700. HR-MS (ESI): m/z calculated for $C_{15}H_{17}NO_5$ $[M + H]^+$, 291.1107; found $[M + Na]^+$, 314.1002.

3.2.5 Synthesis of Propargyl-Substituted L-Tyrosine Poly(ester-urethane)s (P-Tyr):

L-Tyrosine monomer 3 (0.75 g, 0.0025 mol) and 1,12-dodecanediol (0.52 g, 0.0025 mol) were placed in a polymerization tube and heated to 100 °C until melted. The mixture was purged with nitrogen and then subjected to vacuum, repeating the degassing process three times to ensure the removal of oxygen and moisture. Titanium (IV) butoxide [$Ti(OBu)_4$], 1 mol%] was added as a catalyst, and the reaction was stirred under a nitrogen atmosphere at 150 °C for 4 hours. Following this, the reaction was placed under high vacuum at 150 °C for an additional

two hours. During this time, methanol, the condensation byproduct, was removed alongside the nitrogen flow. After polymerization, the resulting viscous melt was subjected to high vacuum (10^{-2} mbar) for 2 hours at 150 °C. The polymer (P-Tyr) was obtained as a viscous material, which was then purified by dissolving it in THF and precipitating it into methanol. The final yield was 0.98 g (89%). ^{1}H NMR (400 MHz,DMSO-d6) Shift δ = 7.53 (d, J = 8.1 Hz, 1 H), 7.16 - 7.14 (d, 2 H), 6.88 - 6.86 (d, 2 H), 4.73 - 4.72 (d, 2 H), 4.15 - 4.10 (m, 1 H), 4.00 - 3.96 (m, 2 H), 3.93 - 3.80 (m, 2 H), 3.52 - 3.48 (t, 1 H), 2.95 - 2.90 (dd, 1 H), 2.83 - 2.77 (m, 1 H), 1.49 - 1.46 (m, 4 H), 1.22 (m, 16 H). ^{13}C NMR (100 MHz DMSO) δ = 172.5, 156.6, 156.4, 130.5, 115.0, 79.7, 78.4, 64.9, 64.4, 61.2, 56.3, 55.8, 36.1, 33.0, 29.5, 29.2, 28.5, 26.0, 25.8. FT-IR (cm^{-1}): 3303, 2924, 2853, 1713, 1610, 1508, 1441, 1358, 1262, 1213, 1112, 1059, 1028.

3.2.6 Synthesis of α-D-Glucose (2S,3R,4S,5S,6R)-6-(hydroxymethyl)tetrahydro-2H-pyran-2,3,4,5-tetraol:

α-D-Glucose (8.0 g, 0.044 mol) was dissolved in 70 mL of dry pyridine in a clean 250 mL two-neck round-bottom flask. A catalytic amount of DMAP was added to the solution. Once the solution became clear, acetic anhydride (34.0 g, 0.333 mol) was slowly added under ice-cold conditions. The reaction mixture was stirred for 12 hours at room temperature under a nitrogen atmosphere. After completion, the reaction mixture was extracted three times with ethyl acetate, followed by washes with 1N HCl. The organic phase was dried over Na_2SO_4, and the solvents were removed using a rotary evaporator, yielding 16.0 g (92%) of the product. ^{1}H NMR (400 MHz CHLOROFORM-d) δ = 6.33 (d, *J* = 3.7 Hz, 1 H), 5.50 - 5.45 (t, 1 H), 5.17 - 5.08 (m, 2 H), 4.32 - 4.22 (dd, 1 H), 4.16 - 4.05 (m, 2 H), 2.19 (s, 3 H), 2.10 (s, 3 H), 2.05 (s, 3 H), 2.03 (s, 3 H), 2.02 (s, 3 H). ^{13}C NMR (100 MHz, $CDCl_3$) δ = 170.61, 170.20, 169.63, 169.35, 168.73, 89.03. 69.78, 69.14, 67.85, 61.42, 20.84, 20.66, 20.62, 20.53, 20.40. HRMS (TOF): [M + Na]+ calcd for $C_{16}H_{22}O_{11}$ found 413.1059.

3.2.7 Synthesis of (2R,3R,4S,5R,6R)-2-(acetoxymethyl)-6-azidotetrahydro-2H-pyran-3,4,5-triyl triacetate:

Glucose pentaacetate (8.0 g, 0.025 mol) was dissolved in 130 mL of dry dichloromethane (DCM) in a clean 250 mL round-bottom flask. Under ice-cold conditions and a nitrogen atmosphere, $SnCl_4$ (4.80 g, 2.1 mL, 0.0184 mol) was added, followed by the addition of trimethylsilyl azide (2.69 g, 3 mL, 0.0233 mol). The reaction mixture was stirred at room temperature for 6 hours. After completion, DCM was removed using a rotary evaporator, and the mixture was extracted with ethyl acetate. The organic layer was washed twice with a basic

solution, and the product was purified by column chromatography using a petroleum ether/ethyl acetate mixture (7:3 v/v) to obtain the pure product. Yield: 6.0 g (78%). 1H NMR (400 MHz, $CDCl_3$) δ 5.23 (t, *J* = 9.5 Hz, 1H), 5.11 (t, *J* = 9.7 Hz, 1H), 4.96 (t, *J* = 9.2 Hz, 1H), 4.66 (d, *J* = 8.9 Hz, 1H), 4.27 (dd, *J* = 12.5, 4.8 Hz, 1H), 4.19 (dd, *J* = 12.5, 2.3 Hz, 1H), 3.80 (ddd, *J* = 10.0, 4.8, 2.3 Hz, 1H), 2.11 (s, 3H), 2.08 (s, 3H), 2.04 (s, 3H), 2.02 (s, 3H); ^{13}C NMR (100 MHz, CDCl3) δ 170.61, 170.11, 169.30, 169.19, 87.90, 74.01, 72.58, 70.62, 67.86, 61.64, 20.68, 20.53 (3 X $COCH_3$); FT-IR: 2113, 1747, 1214, 1036 cm−1 HRMS (TOF): [M + Na]+ calcd for $C_{14}H_{19}O_9N_3Na$ 396.1019, found 396.1022.

3.2.8 Synthesis of (2R,3R,4S,5S,6R)-2-azido-6-(hydroxymethyl)tetrahydro-2H-pyran-3,4,5-triol:

Glucose tetraacetate azide (4.0 g, 0.0107 mol) was dissolved in 20 mL of dry dichloromethane (DCM) in a clean 100 mL two-neck round-bottom flask. To this, 40 mL of dry methanol was added. Once the starting materials were fully dissolved, sodium methoxide (0.58 g, 0.0107 mol) was introduced into the mixture. The reaction was stirred at room temperature for 6 hours. For product purification, Dowex-450 resin was added to the mixture to neutralize the pH. The reaction mixture was filtered using Whatman filter paper, and the filtrate, containing the product in methanol, was collected. The excess methanol was evaporated using a rotary evaporator, yielding the final product. Yield: 1.9 g (90%). ^1H NMR (400 MHz, DMSO-d6): δ ppm ^1H NMR (400 MHz DMSO-d_6) d = 4.46 (d, *J* = 8.8 Hz, 1 H), 3.68 (dd, *J* = 2.0, 12.0 Hz, 1 H), 3.45 (dd, *J* = 5.9, 12.0 Hz, 1 H), 3.26 - 3.20 (m, 2 H), 3.20 - 3.15 (m, 1 H), 3.11 - 3.03 (m, 1 H), 3.02 - 2.95 (t, 1 H). ^{13}C NMR (100 MHz, DMSO-d_6) d ppm 90.61, 79.64, 77.01, 73.81, 70.01, 61.25. FT-IR= HRMS (TOF): [M + Na]+calcd for $C_6H_{11}N_3O_5Na$ 228.0699, found 228.0596.

3.2.9 Synthesisof α-D-Mannose (2R,3S,4S,5R,6R)-6-(acetoxymethyl)tetrahydro-2H-pyran-2,3,4,5-tetrayl tetraacetate

α-D-Mannose (8.0 g, 0.044 mol) was dissolved in 70 mL of dry pyridine in a clean 250 mL two-neck round-bottom flask. A catalytic amount of DMAP was added to the solution. Once the solution became clear, acetic anhydride (34.0 g, 0.333 mol) was slowly added under ice-cold conditions. The reaction mixture was stirred for 12 hours at room temperature under a nitrogen atmosphere. After completion, the reaction mixture was extracted three times with ethyl acetate, followed by washes with 1N HCl. The organic phase was dried over Na_2SO_4, and the solvents were removed using a rotary evaporator, yielding 16.0 g (92%) of the product. ^1H

NMR (400 MHz ,CHLOROFORM-D) d = 6.07 (d, *J* = 2.3 Hz, 1 H), 5.35 - 5.31 (m, 2 H), 5.26 - 5.23 (t, 1 H), 4.26 (dd, *J* = 5.0, 12.6 Hz, 1 H), 4.12 - 4.08 (dd, 1 H), 4.07 - 4.00 (m, 1 H), 2.16 (s, *J* = 3.1 Hz, 3 H), 2.15 (s, *J* = 3.1 Hz, 3 H), 2.07 (s, 3 H), 2.03 (s, 3 H), 1.99 (s, 3 H) ^{13}C NMR (100 MHz, $CDCl_3$) δ 170.62, 169.97, 169.72, 169.51, 168.04, 90.56, 70.56, 68.70, 68.29, 65.48, 62.06, 20.83, 20.74, 20.69, 20.63, 20.61. HRMS (TOF): [M + Na]+ calcd for $C_{16}H_{22}O_{11}$ found 413.1059.

3.2.10 Synthesis of (2R,3R,4S,5S,6S)-2-(acetoxymethyl)-6-azidotetrahydro-2H-pyran-3,4,5-triyl triacetate

Mannose pentaacetate (8.0 g, 0.025 mol) was dissolved in 130 mL of dry dichloromethane (DCM) in a clean 250 mL round-bottom flask. Under ice-cold conditions and a nitrogen atmosphere, $SnCl_4$ (4.80 g, 2.1 mL, 0.0184 mol) was added, followed by the addition of trimethylsilyl azide (2.69 g, 3 mL, 0.0233 mol). The reaction mixture was stirred at room temperature for 6 hours. After completion, DCM was removed using a rotary evaporator, and the mixture was extracted with ethyl acetate. The organic layer was washed twice with a basic solution, and the product was purified by column chromatography using a petroleum ether/ethyl acetate mixture (7:3 v/v) to obtain the pure product. Yield: 6.0 g (78%). ^{1}H NMR (400 MHz, $CDCl_3$) δ 5.39 (d, *J* = 1.8 Hz, 1H), 5.32 – 5.23 (m, 2H), 5.16 (dd, *J* = 2.8, 2.0 Hz, 1H), 4.29 (dd, *J* = 12.4, 5.5 Hz, 1H), 4.19-4.10 (m, 2H), 2.17 (s, 3H), 2.12 (s, 3H), 2.06 (s, 3H), 2.0 (s, 3H); ^{13}C NMR (100 MHz, $CDCl_3$) δ 170.66, 169.89, 169.79, 169.68, 87.41, 70.57, 69.13, 68.21, 65.58, 62.13, 20.79, 20.70, 20.65, 20.58 DEPT-135 87.46, 70.64, 69.19, 68.25, 65.63, 62.17, 20.62, 20.72, 20.68, 20.63. FT-IR 2116, 1742, 1207, 1045 cm^{-1} HRMS (TOF): [M + Na] + calcd for $C_{14}H_{19}O_9N_3Na$ 396.1019, found 396.1019

3.2.11 Synthesis of (2S,3S,4S,5S,6R)-2-azido-6-(hydroxymethyl)tetrahydro-2H-pyran-3,4,5-triol

Mannose tetraacetate azide (4.0 g, 0.0107 mol) was dissolved in 20 mL of dry dichloromethane (DCM) in a clean 100 mL two-neck round-bottom flask. To this, 40 mL of dry methanol was added. Once the starting materials were fully dissolved, sodium methoxide (0.58 g, 0.0107 mol) was introduced into the mixture. The reaction was stirred at room temperature for 6 hours. For product purification, Dowex-450 resin was added to the mixture to neutralize the pH. The reaction mixture was filtered using Whatman filter paper, and the filtrate, containing the product in methanol, was collected. The excess methanol was evaporated using a rotary evaporator, yielding the final product. Yield: 1.9 g (90%). ^{1}H NMR (400 MHz, DMSO-d6): δ

ppm ^{1}H NMR (400 MHz DMSO) d = 5.35 (d, *J* = 2.0 Hz, 1 H), 5.06 (br. s., 1 H), 4.86 (br. s., 1 H), 4.76 (br. s., 1 H), 4.58 (br. s., 1 H), 3.68 (d, *J* = 11.5 Hz, 1 H), 3.55 - 3.45 (m, 2 H), 3.40 (m, 3 H). ^{13}C NMR (100 MHz, DMSOd_6) δ 90.72, 77.15, 70.71, 70.32, 66.91, 61.45. DEPT-135 90.73, 77.15, 70.70, 70.31, 66.90, 61.45. HRMS (TOF): [M + Na]+ calcd for $C_6H_{11}N_3O_5Na$ 228.0699, found 228.0596.

3.2.12 Post-Polymerization Click Chemistry

3.2.13 P-Tyr-G click reaction

A representative procedure for the click chemistry reaction between Glucose azide and P-Tyr was as follows. P-Tyr (100 mg, 0.234 mmol) and Glucose azide (217.0 mg, 0.281 mmol) were placed in a polymerization tube and dissolved in 5 mL of DMSO. Once the solution became clear, copper sulfate (29.0 mg, 0.117 mmol) and sodium ascorbate (46.0 mg, 0.234 mmol) were added. The reaction mixture was stirred for 24 hours at 70 °C. After cooling, the mixture was dialyzed using a 3.5 kDa semipermeable membrane for 48 hours, with frequent changes of fresh water. EDTA was regularly checked in the reservoir to ensure the complete removal of copper residues. The final product was obtained with a yield of 260 mg (92%). ^{1}H NMR (400 MHz ,DMSO-d_6) δ = 8.37 (s, 1 H), 7.51 (d, *J* = 8.4 Hz, 1 H), 7.12 (d, *J* = 8.4 Hz, 2 H), 6.91 (d, *J* = 8.4 Hz, 2 H), 5.51 (d, *J* = 9.2 Hz, 1 H), 5.36 (d, *J* = 6.1 Hz, 1 H), 5.24 (d, *J* = 4.6 Hz, 1 H), 5.11 (d, *J* = 5.3 Hz, 1 H), 5.05 (s, 2 H), 4.59 (t, *J* = 5.7 Hz, 1 H), 4.09 (q, *J* = 6.1 Hz, 1 H), 3.98 - 3.95 (m, 2 H), 3.88 - 3.86 (m, 1 H), 3.80 - 3.69 (m, 2 H), 3.65 (dd, *J* = 5.3, 9.9 Hz, 1 H), 3.45 - 3.32 (m, 3 H), 3.24 - 3.18 (m, 1 H), 2.87 (dd, *J* = 5.3 Hz, 1 H), 2.75 (m, *J* = 3.8 Hz, 1 H), 1.53 - 1.34 (m, 4 H), 1.19 (m, 16 H). ^{13}C NMR (100 MHz, DMSO d6): δ = 172.68, 157.46, 156.85, 143.28, 134.56, 130.76, 130.39, 124.47, 115.12, 114.94, 88.12, 80.60, 77.58, 72.67, 70.18, 65.02, 64.58, 61.52, 61.36, 56.48, 36.23, 29.67, 29.39, 29.32, 29.25, 28.71, 25.95, 25.88. FT-IR (cm^{-1}): 2974, 1647, 1459, 1056, 897, 658.

3.2.14 P-Tyr-M click reaction

A representative procedure for the click chemistry reaction between Mannose azide and P-Tyr was as follows. P-Tyr (100 mg, 0.234 mmol) and Mannose azide (217.0 mg, 0.281 mmol) were placed in a polymerization tube and dissolved in 5 mL of DMSO. Once the solution became clear, copper sulfate (29.0 mg, 0.117 mmol) and sodium ascorbate (46.0 mg, 0.234 mmol) were added. The reaction mixture was stirred for 24 hours at 70 °C. After cooling, the mixture was dialyzed using a 3.5 kDa semipermeable membrane for 48 hours, with frequent changes of fresh water. EDTA was regularly checked in the reservoir to ensure the complete removal of

copper residues. The final product was obtained with a yield of 258 mg (90%). ^{1}H NMR (400MHz ,DMSO-d_6) δ = 8.29 (s, 1 H), 7.50 (d, *J* = 8.4 Hz, 1 H), 7.11 (d, *J* = 8.4 Hz, 2 H), 6.91 (d, *J* = 8.4 Hz, 2 H), 5.88 (d, *J* = 4.6 Hz, 1 H), 5.23 (d, *J* = 5.3 Hz, 1 H), 5.06 (s, 2 H), 5.01 (d, *J* = 5.3 Hz, 1 H), 4.96 (d, *J* = 5.3 Hz, 1 H), 4.57 (t, *J* = 6.1 Hz, 1 H), 4.39 - 4.36 (m, 1 H), 4.09 (d, *J* = 6.1 Hz, 1 H), 3.97 - 3.94 (m, 2 H), 3.90 - 3.84 (m, 2 H), 3.88 - 3.77 (m, 3 H), 3.61 - 3.48 (m, 3 H), 2.91 - 2.86 (dd, 1 H), 2.78 - 2.73 (m, 1 H), 1.54 - 1.35 (m, 4 H), 1.18 (m, 16 H). ^{13}C NMR (100 MHz, DMSO d6): δ = 172.52, 158.14, 154.97, 143.21, 130.59, 124.79, 114.83, 86.25, 78.80, 71.67, 68.61, 68.06, 64.43, 61.42, 61.18, 31.18, 29.7, 29.24, 28.57, 25.82. FT-IR (cm^{-1}): 2974, 1647, 1459, 1056, 897, 658.

3.2.15 Self-Assembly of Polymers

5.0 mg of polymer and 0.5 mg of curcumin, camptothecin (CPT), topotecan (TPT), were placed in 15 mL vials. To this, 2 mL of HPLC-grade dimethyl sulfoxide (DMSO) was added, dissolving both the polymer and the drug. After complete dissolution, 3 mL of Milli-Q water was gradually introduced, and the solution was stirred at 25 °C for 4 hours. The resulting mixture was transferred into a 1 kDa dialysis membrane and dialyzed against Milli-Q water for 48 hours to remove unencapsulated drug/dye and DMSO. Drug loading content and efficiency were measured via UV absorbance spectroscopy as previously described. A similar method was followed for the encapsulation of the Indocyanine green (ICG).

3.2.16 Critical Aggregation Concentration (CAC) Measurements

The CAC of the polymer was determined using pyrene as a probe, as previously reported. The pyrene concentration was set at 0.6 µM while the polymer concentration was varied from 0.5 mg/mL to $1x10^{-6}$ mg/mL. The polymer solution with pyrene was sonicated for 3 hours and allowed to equilibrate for 12 hours. Nitrogen purging was performed to eliminate O_2 from the sample. Fluorescence spectra were recorded, and the ratio of vibronic bands I_1 and I_3 was plotted to determine the CAC. The pyrene was excited at 337 nm, and emissions were collected in the range of 347-500 nm.

3.2.17 Release Kinetics

Camptothecin (CPT), loaded samples (1 mL) were combined with 10 U of esterase enzyme and placed in a 1 kDa dialysis tube. The tube was incubated in 3 mL of 1x PBS at 37 °C for 24 hours. Samples were periodically taken from the reservoir and analyzed using UV absorbance

spectroscopy to determine CPT release, with cumulative release profiles calculated as previously reported. A control experiment without the enzyme was conducted similarly.

3.2.18 Cell Viability Assay

Cell viability was assessed using the MTT assay, as described in prior studies. MDA-MB-468, MIA PaCa-2, MCF-7 breast cancer cells and HEK-293 cells were seeded at 1000 cells per well in a 96-well plate, using 100 µL of complete media per well. After a 16-hour incubation, the media was aspirated and replaced with samples dissolved in 300 µL of complete media. The media comprised DMEM with 1% penicillin-streptomycin and 10% fetal bovine serum. The plates were incubated for 72 hours at 37 °C, with 5 % CO_2 and 70 % humidity. After incubation, the media was removed, and the MTT reagent, dissolved at a concentration of 0.5 mg/mL in complete media, was added and incubated for 4 hours. Media was then carefully aspirated, leaving the formazan crystals, which were dissolved in 100 µL of HPLC-grade DMSO. The plate was kept in the dark and shaken for 10 minutes. Absorbance was measured at 570 nm using a Varioscan microplate reader. Experiments were performed in triplicate, and cell viability was calculated against control cells.

3.2.19 Cellular Uptake Studies

Fixed-cell imaging was performed to evaluate the cellular uptake of drug or dye-loaded polymer nanoparticles. MCF-7 cells were seeded at 10^5 cells per well in 6-well plates, along with 2 mL of complete media. After 16 hours of incubation at 37 °C, with 5 % CO_2 and 1 % O_2, lyophilized polymeric samples were re-dispersed in complete media and added to the wells. The cells were incubated for various time intervals, and after incubation, the media was removed and cells were washed twice with 1 mL of PBS. The cells were fixed with 4 % paraformaldehyde at 4 °C for 15 minutes and washed twice with PBS. phalloidin was then added to the wells and incubated for 2 minutes. Excess phalloidin was washed away, and slides were prepared with 70 % glycerol. The slides were dried for 12-18 hours and then imaged using confocal microscopy (Zeiss LSM 710), with HPTS, CPT, TPT, and CUR excited at 405 nm and phalloidin at 488 nm. Images were analyzed with Fiji software.

3.2.20 Hemolysis Assay

To determine the hemolytic activity of the polymer, a hemolysis assay was conducted following established protocols. Fresh blood from C57BL/6 mice was centrifuged to separate red blood cells (RBCs), and a 5 % v/v RBC suspension was prepared in PBS. Polymer samples (100

μg/mL) were mixed with 100 μL of RBC suspension and incubated at 37 °C for 1 hour. Triton-X (1 %) was used as a positive control, and PBS served as a negative control. The samples were centrifuged at 8000 rpm for 5 minutes. The presence of a pellet indicated the biocompatibility of the polymer. Hemolysis percentage was calculated based on previously reported methods.

3.2.21 IVIS-Mediated Biodistribution Studies

For biodistribution studies, 8 female Balb/c mice (8-12 weeks old, ~25 g) were divided into three groups. Group 1 (n=3) received intraperitoneal injections of free Indocyanine green (ICG) dye (0.5 mg/kg) in 100 μL of PBS, group 2 (n=3) received ICG-loaded polymer nanoparticles (0.5 mg/kg) in 100 μL of PBS, and group 3 (n=2) received 100 μL of PBS. Blood samples were collected at 2-, 6- and 24-hours post-injection via retro-orbital plexus puncture. Mice were imaged at 2, 4, 6, and 24 hours using IVIS, with λexc = 745 nm and λem = 800 nm. After 24 hours, the mice were euthanized, perfused with PBS, and organs were harvested for whole-organ imaging. Plasma samples were collected from the blood and diluted with PBS for IVIS imaging. Radiance was measured and quantified using the instrument's software.

3.3 Results and Discussion

L-Tyrosine was modified into a multifunctional monomer with methyl ester, urethane, and propargyl-functionalized phenolic hydroxyl groups. NMR confirmed its structure and thermal stability (up to 250 °C), supporting melt polymerization with 1,12-dodecanediol (1:1 molar ratio) at 150 °C for 4 hours under nitrogen purge, using 1 mol % catalyst. High vacuum (0.01 mbar) yielded high molecular weight polymers. ^{1}H-NMR showed polymerization by the disappearance of methoxy protons (3.71–3.66 ppm) and new ester peaks (4.07–4.10 ppm), with the propargyl group (2.5 ppm) remaining unaffected. The degree of polymerization (DPn = 40) corresponded to ~98% reaction, with Mn ~17,000 g/mol. ^{13}C-NMR confirmed the conversion of methoxy carbons (52–53 ppm) to ester carbons (62–63 ppm). SEC analysis showed Mn = 18,200 g/mol, Mw = 46,800 g/mol, and Đ = 2.5, Further details about this synthesis and characterization are provided in Chapter 2.

.3.3.1 Synthesis of Sugar Azide (Glucose and Mannose)

Azide-functionalized sugars, particularly glucose and mannose, were synthesized through a multi-step process designed to selectively modify the sugar molecules while protective their core structure. The procedure started with the protection of the hydroxyl groups in the sugar

molecules, which was essential to prevent side reactions and enhance the yield of the desired product. The hydroxyl groups were converted into acetate esters using acetic anhydride under acidic or catalytic conditions, forming fully acetylated sugar derivatives. This protection step not only stabilized the sugars but also rendered the anomeric carbon more reactive toward subsequent nucleophilic substitution. In the next step, the acetylated sugars were reacted with trimethylsilyl azide, a mild and efficient reagent for introducing azide groups. This reaction occurred specifically at the anomeric position of the sugar, leading to the formation of the corresponding anomeric glucose azide. The structure is shown in Scheme 3.1.

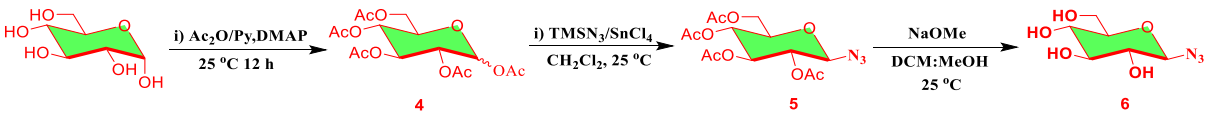

Scheme 3.1 *Multistep synthesis of Glucose Azide.*

A similar procedure was used for the D-mannose azide, and the structure is shown in Scheme 3.2.

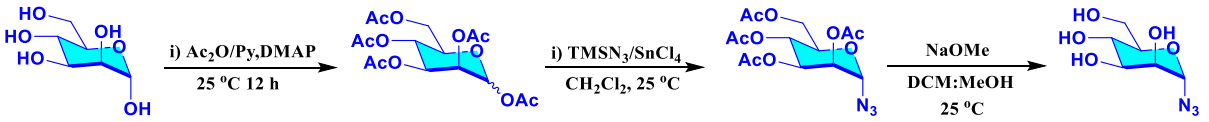

Scheme 3.2 *Synthesis of Mannose Azide.*

The final sugar-azides derivatives were characterized using ^{1}H-NMR, and ^{13}C-NMR, the glucose azide data are shown in Figure 3.3. The first step protection of 1 and 2 hydroxyl group by using acetic anhydride in 1H NMR clearly see that the peak at 2.0 to 2.20 ppm five methyl peak corresponding to Acetate group and the anomeric proton comes at 6.3 ppm see Figure 3.2a. Further, the selective azidation of anomeric position by using Lewis's acid $SnCl_4$ confirmed by proton NMR the anomeric peak at 6.63 ppm completely vanished, and new peaks appeared at 4.66 ppm confirming the formation of Azide (see Figure 3.2b).

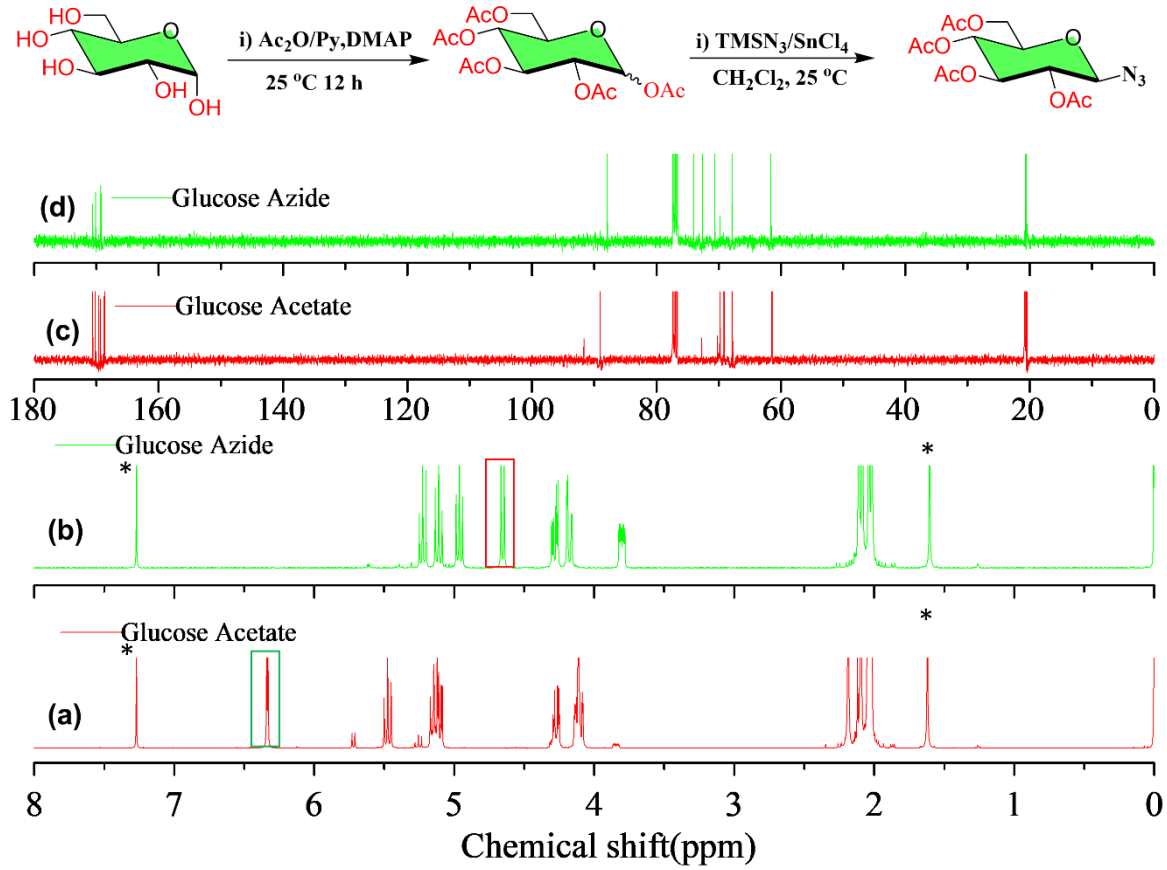

Figure 3.2 *(a) ^{1}H NMR of Glucose Acetate, (b) ^{1}H NMR of Glucose Acetate Azide, and (c) ^{13}C NMR of Glucose Acetate and (d) ^{13}C NMR of Glucose Acetate azide. All the spectra were recorded in the $CDCl_3$. The peaks corresponding to solvents are assigned by asterisks.*

Further, the Glucose pentaacetate structure was confirmed by ^{13}C, NMR in this the five Acetate peak coming at range of 168 ppm to 170 ppm. The spectra are shown in Figure 3.2c. and after selective azidation of the anomeric position, one acetate peak vanished, confirming the formation of anomeric azidation completely (see Figure 3.2d). In a similar way, the Mannose tetra Azide was characterized by ^{1}H and ^{13}C NMR, and the data are shown in (Appendix Figure S19). Further, the glucose tetra acetate group were deprotected by using sodium methoxide to get Glucose Azide; this structure was confirmed by ^{1}H NMR and ^{13}C NMR in glucose tetra acetate azide the peak at 2.0 to 2.11 ppm corresponding to four methyl peaks after deprotection the methyl peak completely vanished and all the CH proton of glucose ring also shifted to up filed region it confirms the successful deprotection of acetate group the spectra are shown in (Figure 3.3a).

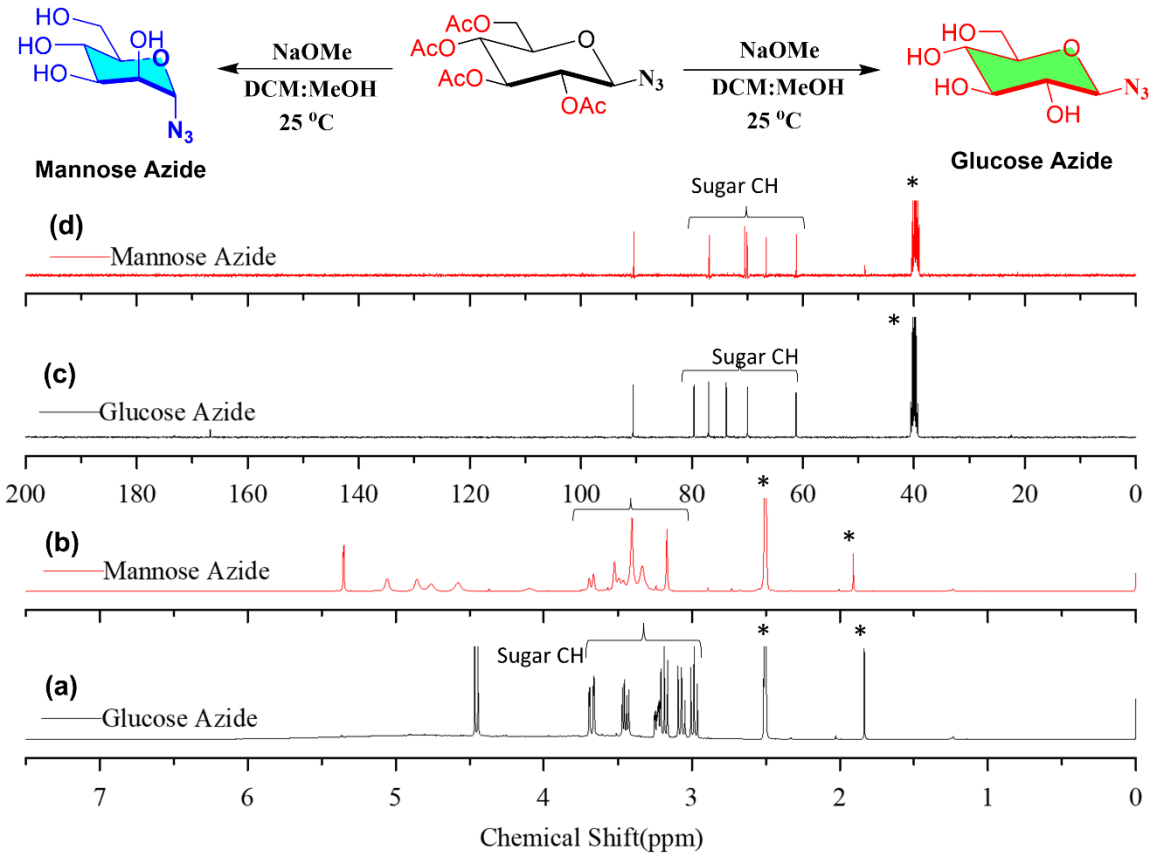

Figure 3.3. *(a) ^{1}H NMR of β-D-glucose azide, (b) ^{1}H NMR of α-D-Mannose azide, and (c) ^{13}C NMR of β-D-glucose Azide (d) ^{13}C NMR of α-D-Mannose azide. All the spectra were recorded in the DMSO d6. The peaks corresponding to solvents are assigned by asterisks.*

Similarly, the D-mannose azide also confirmed by proton NMR and spectra are shown in (Figure 3.3b). Further, D-glucose azide was confirmed by ^{13}C NMR and in ^{13}C, the Glucose tetraacetate, the acetate peak coming at a range of 171-169 ppm completely disappeared and it confirmed the deprotection of the acetate group completely spectra in (Figure 3.3c). Similarly, the D-mannose azide structure was also confirmed by ^{13}C NMR and spectra are shown in (Figure 3.3d). After that, The DEPT-135 NMR was also recorded to distinguish between CH_2, group for that Glucose pentaacetate azide, Glucose azide and mannose pentaacetate Azide, mannose azide all the spectra are shown in (Appendix Figure S20-21).

3.3.3 Click reaction of P-Tyr-G and P-Tyr-M

The propargyl-functionalized P-Tyr polymer was subjected to click chemistry with the synthesized sugar azides in DMSO, using copper (II) sulfate and sodium ascorbate as catalytic agents. After the reaction, Following the reaction, the resulting sugar-functionalized polymers were purified to remove unreacted reagents, byproducts, and residual copper. Continuous dialysis was performed using a 3.5 kDa molecular weight cut-off (MWCO) membrane to retain

the high molecular weight polymer while eliminating smaller impurities. To ensure the complete removal of residual copper, ethylenediaminetetraacetic acid (EDTA) was employed, which chelates copper ions effectively. The purification process was carefully monitored to confirm that no trace of copper remained in the final product. The purified polymers were subsequently lyophilized to obtain a dry, stable form, which was stored under appropriate conditions for further characterization and use. These sugar-functionalized polymers were named P-Tyr-X, where X corresponds to the attached sugar (glucose or mannose), as shown in Scheme 3.3.

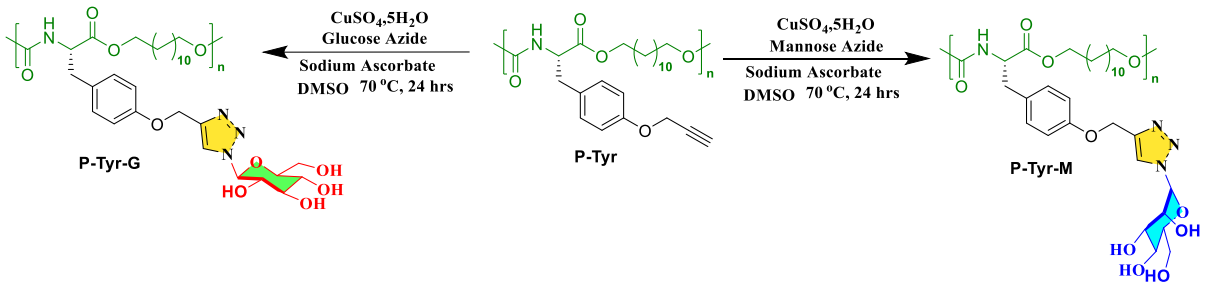

Scheme 3.3. *Synthesis of clickable L-tyrosine poly(ester-urethane) and its clicked Sugar amphiphilic polymers.*

First, the stack plot of NMR the P-Tyr is shown in Figure 3.4a. The Clickable polymers were characterized by the ^{1}H-NMR spectrum of the sugar-functionalized polymer (P-Tyr-G), shown in Figure 3.4b, confirming the successful completion of the click reaction. The disappearance of the propargyl proton signals at 3.5 ppm and the clear indication -O-**CH$_2$**-propargyl peak coming at 4.72 ppm and after click reaction, the O-**CH$_2$**-propargyl peak completely vanished and shifted towards the downfield region -O-**CH$_2$**-triazole peak at 5.00 ppm indicated that over 99% of the reaction had proceeded. Additionally, the appearance of characteristic peaks for the triazole group at 8.37 ppm (triazole Ar-**H**) provided further evidence of reaction completion. Similar results were observed for the spectrum of the mannose-clicked polymer (P-Tyr-M), as shown in Figure 3.4c. Characterization by ^{1}H-NMR spectroscopy confirmed the successful completion of the click reaction. For the mannose-functionalized polymer (P-Tyr-M), the disappearance of propargyl proton signals at 3.5 ppm indicated near-complete consumption of the alkyne groups, with a reaction efficiency exceeding 99%. The appearance of new peaks corresponding to the -O-**CH$_2$**-Propargyl 4.72 ppm shifted to 5.00 ppm -O-**CH$_2$**-triazole group

specifically at 5.20 ppm and 8.28 ppm (triazole Ar-**H**) provided clear evidence of the formation of the triazole linkage.

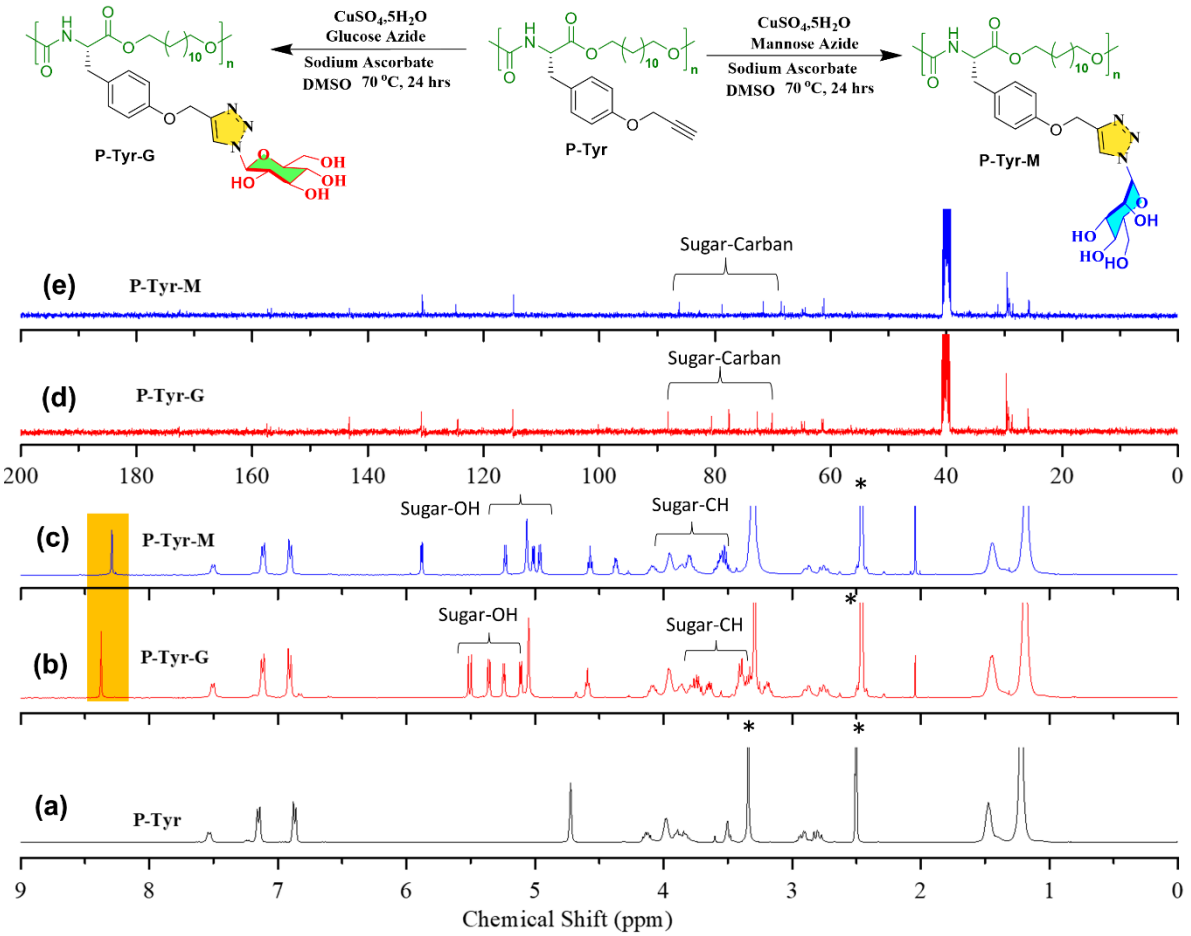

Figure 3.4 *(a) ^{1}H-NMR spectrum of homo polymer P-Tyr. (b) ^{1}H-NMR spectrum of P-Tyr-G (c) ^{1}H-NMR spectrum of P-Tyr-M (d) ^{13}C-NMR spectrum of P-Tyr-G and (e) ^{13}C-NMR spectrum of P-Tyr-M. All the spectra were recorded in DMSO d6. The peaks corresponding to solvents are assigned by asterisks.*

The disappearance of sugar azide proton signals from the sugar derivative (Sugar-O-**CH**-N_3 anomeric proton) at 4.5 ppm (Figure 3.3a) confirmed the conversion of azide groups into triazole units. Integration of the NMR peaks corresponding to -O**CH**- protons at 5.5 ppm (peak-anomeric-**H**) and the benzyl-CH_2 protons of the polymer at 2.90-2.80 ppm (peak-c') demonstrated a near 1:1 ratio. The clicked sugar-functionalized polymers were further analyzed using size exclusion chromatography (SEC) in dimethylformamide (DMF) at 70 °C. Polystyrene standards were used for calibration, and the sugar-polymer samples were prepared at a concentration of 3 mg/mL. The SEC analysis revealed a shift in retention time to lower values after the click reaction, consistent with an increase in molecular weight. The chromatograms exhibited monomodal distributions, confirming the consistency of the polymers. The chromatograph is shown in Figure 3.5a.

(a) SEC Plot

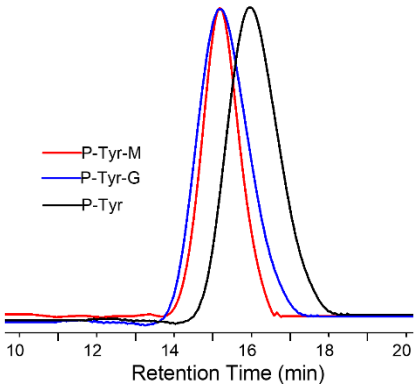

(b) Table containing the molecular weights and thermal properties of the Polymers

Sample	^{1}H-NMR[a] M_n (g/mol)	SEC RI Detector[b] M_n (g/mol)	M_w (g/mol)	Đ	T_D[c] (°C)	T_g[d] (°C)
P-Tyr	17000	15500	35000	2.2	315	-4
P-Tyr-G	25000	20000	46000	2.3	265	107
P-Tyr-M	25000	20000	46000	2.3	215	91

[a] ^{1}H-NMR NMR molecular weights are calculated using the expression: M_n = (DP × repeating unit mass). [b] Number (M_n) and weight average molecular weight (M_w), and dispersity (Đ) were determined by size exclusion chromatography in DMF at 70 °C using RI detector. [c] Temperature of decomposition (Td) determined from TGA. [d] The glass transition temperature (Tg) was determined from second heating cycle of DSC thermogram.

Figure 3.5 *(a) Size exclusion chromatograms of polymers in DMF. (b) The table containing the molecular weight and thermal properties of Clickable polymers.*

The molecular weight of the sugar-functionalized polymers was estimated by considering the contribution of the sugar chains. Based on the repeating unit calculation for the polymer (40 repeating units × 427 g/mol per unit = 16,000 g/mol), the addition of sugar chains contributed approximately 8,200 g/mol to the final molecular weight, resulting in a total molecular weight of approximately 25,000 g/mol for the sugar-functionalized polymer. The number average molecular weight (M_n) of clickable polymers P-Tyr-G showed the =20,000 g/mol), and polydispersity sugar polymer showed mono-model distribution in DMF and showed M_n = 20,000 g/mol, M_w = 46,000 with Đ =2.3 which is comparable to ^{1}H NMR. The SEC data are shown in Figure 3.5b.

3.3.4 FT-IR Analysis

The inter-chain hydrogen bonding schematic structure is shown in Figure 3.6a. FT-IR spectroscopy provided complementary evidence for the reaction's success. The Sugar azide stretching frequency at 2100 cm^{-1}, after the click reaction, the azide stretching frequency 2100 cm^{-1} completely vanished in the spectra of the sugar-functionalized polymers, indicating the complete conversion of sugar azide groups into triazole units. Furthermore, the presence of triazole-specific absorption bands and other characteristic functional group vibrations confirmed the successful formation of the sugar-functionalized polymers. Detailed FT-IR data, shown in Figure 3.6b, supported the conclusion that the click reaction was highly efficient and complete for all samples.

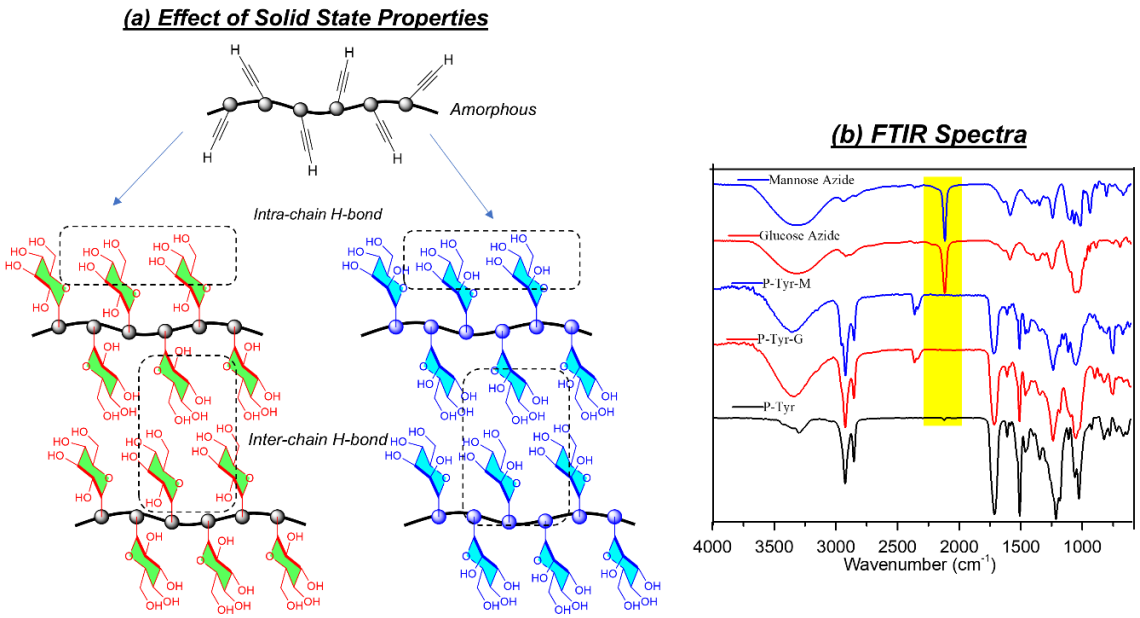

Figure 3.6. *(a) Schematic diagram of intermolecular hydrogen bonding. (b) FT-IR stack plot of Sugar azide and their clickable polymer spectra.*

The integration of sugar moieties onto the P-Tyr polymer via click chemistry was successful, as evidenced by comprehensive characterization using NMR, SEC and FT-IR spectroscopy. The highly efficient purification process ensured the removal of impurities and residual copper, yielding sugar-functionalized polymers with well-defined structures and properties.

3.3.5 Thermal properties of Sugar polymer brushes

The thermal stability of the P-Tyr-G polymer was evaluated using thermogravimetric analysis (TGA) at a heating rate of 10 °C/min under a nitrogen atmosphere. The results showed that the polymer was stable up to 265 °C., and on the other hand, the P-Tyr-M polymer was stable up to 215 C. The T_D values is shown in table Figure 3.5b. The initial thermal degradation corresponded to the sugar side chains, as indicated by a characteristic first hump in the TGA curve, followed by the degradation of the poly(ester-urethane) backbone. The P-Tyr-M polymer degraded faster as compared to P-Tyr-G see Figure 3.7a. Differential scanning calorimetry (DSC) was used to measure the glass transition temperature (Tg) of the polymers at 10 °C/min under a nitrogen atmosphere. The homopolymer exhibited a Tg of -4°C. After sugar conjugation, the Tg increased significantly to 107 °C for the glucose-clicked polymer and 90 °C for the mannose-clicked polymer. The T_g values are shown in the table Figure 3.5b. The increase in Tg was attributed to inter-chain hydrogen bonding between the sugar moieties. The 17 °C difference between the glucose and mannose polymers was attributed to variations in the geometric arrangement of the sugar side chains.

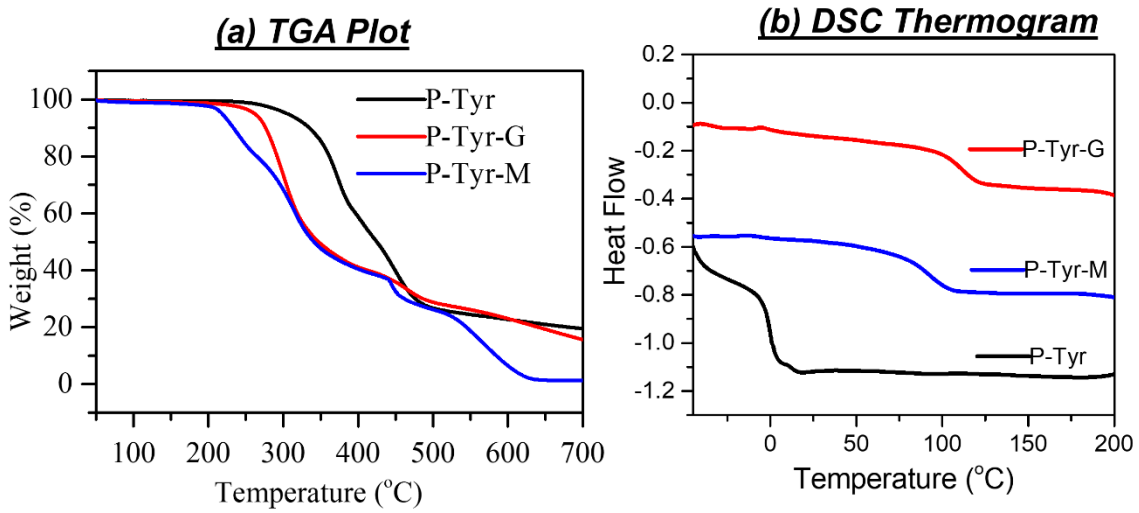

Figure 3.7. *(a) TGA thermograms of polymers. TGA was performed at 10 °/min under N_2 atmosphere. (b) DSC thermograms of the polymers recorded at 10 °/min under nitrogen atmosphere.*

Influence of Sugar Conjugation on T_g The increase in T_g after sugar functionalization is primarily attributed to the introduction of inter-chain hydrogen bonding facilitated by the sugar moieties. The hydroxyl groups in the sugar side chains engage in extensive hydrogen bonding with inter-chains, creating a more tightly packed and constrained polymer matrix. This inter-chain interaction reduces chain mobility, thereby increasing the energy required for the polymer to transition from the glassy state to the rubbery state, as reflected in the higher T_g. The substantial increase in Tg after sugar conjugation suggests that these sugar-functionalized polymers possess enhanced thermal stability and rigidity, making them promising candidates for thermoplastic applications.

3.3.5 Aqueous Self Assembly of Sugar polymer

The aqueous self-assembly behavior of the sugar-functionalized polymer brushes was investigated to evaluate their potential for forming stable nanostructures in water; 5 mg of polymer and 0.5 mg of drug or dye were dialyzed in a 3.5 kDa molecular weight cutoff (MWCO) cellulose membrane against Milli-Q water for 48 hours. The resulting assemblies were found to be stable in aqueous conditions for both glucose and mannose-functionalized polymers. After dialysis, the resulting assemblies were stable in aqueous conditions for both glucose-functionalized (P-Tyr-G) and mannose-functionalized (P-Tyr-M) polymers. The schematic representation of self-assembly behavior is shown in Figure 3.8a. The stability of the assemblies can be attributed to several key factors: such as hydrophilic sugar shell, intermolecular interactions, and hydrophobic core formation. The hydroxyl-rich glucose and

mannose groups formed a hydrophilic outer shell around the self-assembled nanostructures. Hydrogen bonding between the sugar moieties further contributed to the stability of the assemblies.

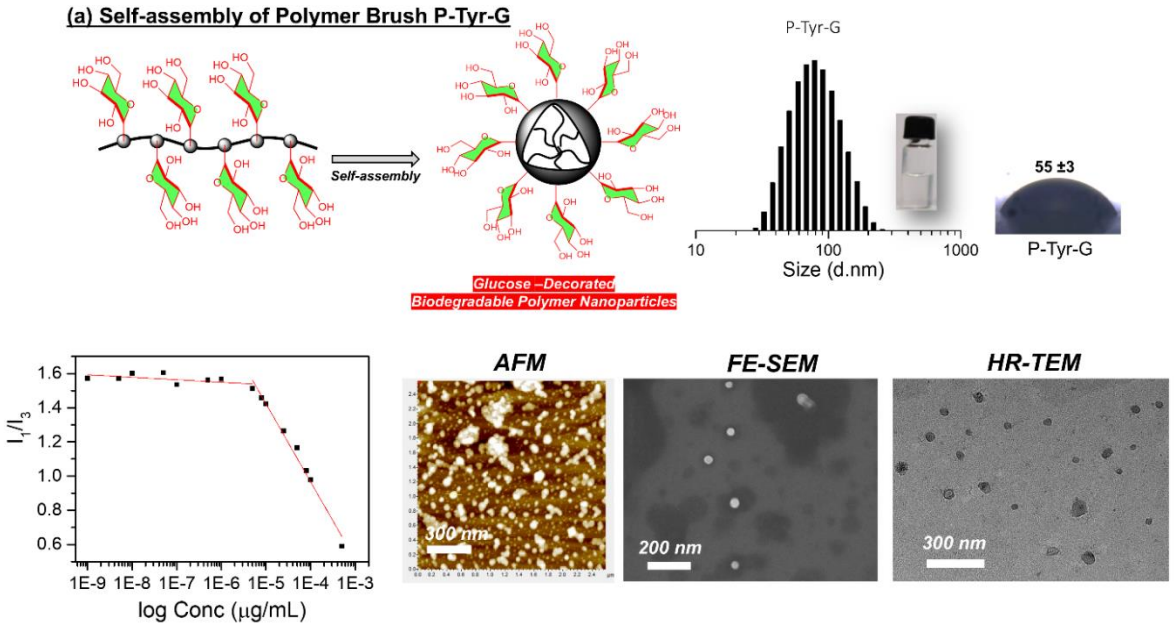

Figure 3.8 *(a) Schematic aqueous Self-assembly of P-Tyr-G polymer brush. (b) DLS histogram and the photographs show the water contact angle (LB-ADSA method) recorded for the polymer brush drop-caste film on glass substrate. Critical aggregation concentration (CAC) was determined by pyrene-probe. P-Tyr-G brush characterization by AFM, FE-SEM and HR-TEM images.*

The hydrophobic interactions between the polymer backbone and the encapsulated drug or dye facilitated the formation of a stable hydrophobic core. Dynamic light scattering (DLS) measurements revealed nanoparticle sizes of 90±10 nm see Figure 3.8a. To assess the amphiphilic nature of the polymers, water contact angle measurements were performed. Polymer films coated on glass slides exhibited a contact angle of 55 °, confirming their amphiphilic character and suitability for self-assembly applications, as shown in Figure 3.8a. The critical micelle concentration (CMC) of the polymers was determined using pyrene encapsulation studies. A fixed concentration of pyrene (0.6 µM) was used, and the polymer concentration was varied from 0.5 mg/mL to 1 mg/mL. Pyrene emission spectra were recorded from 447 to 500 nm upon excitation at 337 nm, and spectra are shown in Figure 3.9a. The I_1/I_3 vibronic intensity ratio was plotted against polymer concentration, yielding CMC values of 5 µg/mL for the glucose-functionalized polymer (P-Tyr-G) see Figure 3.8a and 5 µg/mL for the mannose-functionalized polymer (P-Tyr-M). Atomic force microscopy (AFM) analysis of drop-cast solutions on mica sheet confirmed the formation of nanoparticle brushes with sizes of 90±10 nm, consistent with the DLS results. High-resolution transmission electron

microscopy (HR-TEM) image showed nanoparticle sizes of 80±10 nm, further corroborating with the DLS and AFM data shown in Figure 3.8a.

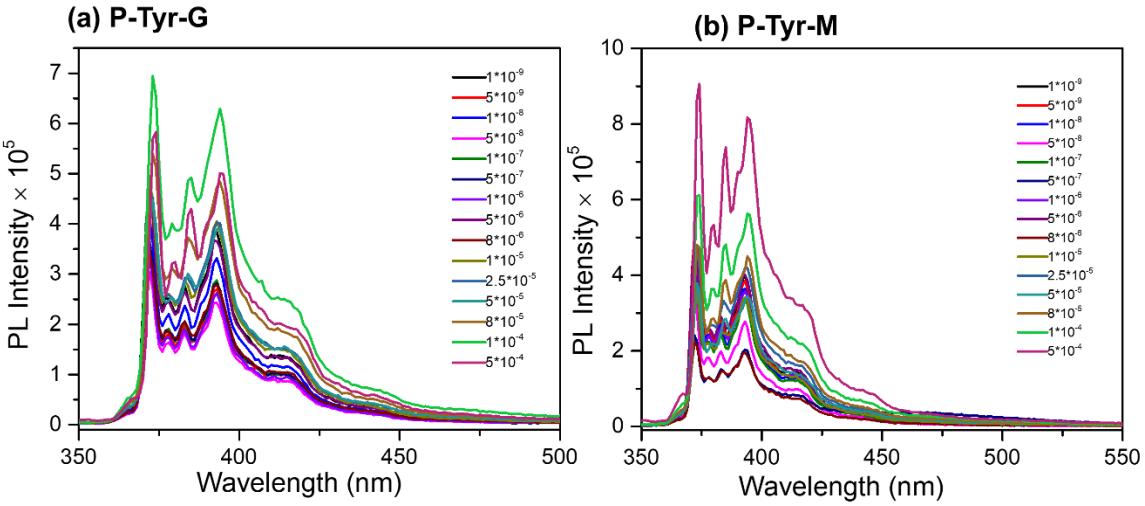

Figure 3.9 *Pyrene emission spectra for CMC determination. Pyrene chromophore was excited at λEx= 337nm and emission was collected from 350-500 nm. (a) P-Tyr-G, (b) P-Tyr-M.*

The schematic representation of self-assembly nanoarchitecture is shown in Figure 3.10a. the P-Tyr-M polymers were recorded DLS and sizes of 80±10 nm, and the water contact angle showed 55°. The polymer is amphiphilic in nature, and it can be used for self-assembly behavior. Further, for Critical micellar concentrations, the pyrene probe was used, the pyrene concentration was fixed at 0.6 µM, and the polymer (P-Tyr-M) concentration was varied from 0.5 mg to 1 mg/mL. The pyrene was excited at 337 nm, and their emission was collected from 347-500 nm, and their emission spectra are shown in Figure 3.9b.

The I_1/I_3 intensity was plotted against polymer concentration. The breakpoint of CMC showed 5 µg/mL, and the data are shown in Figure 3.10a. AFM, FE-SEM and HR-TEM images showed the formation of spherical nanoparticles and their sizes matched with dynamic light scattering (DLS) and the images are shown in figure 3.10a.

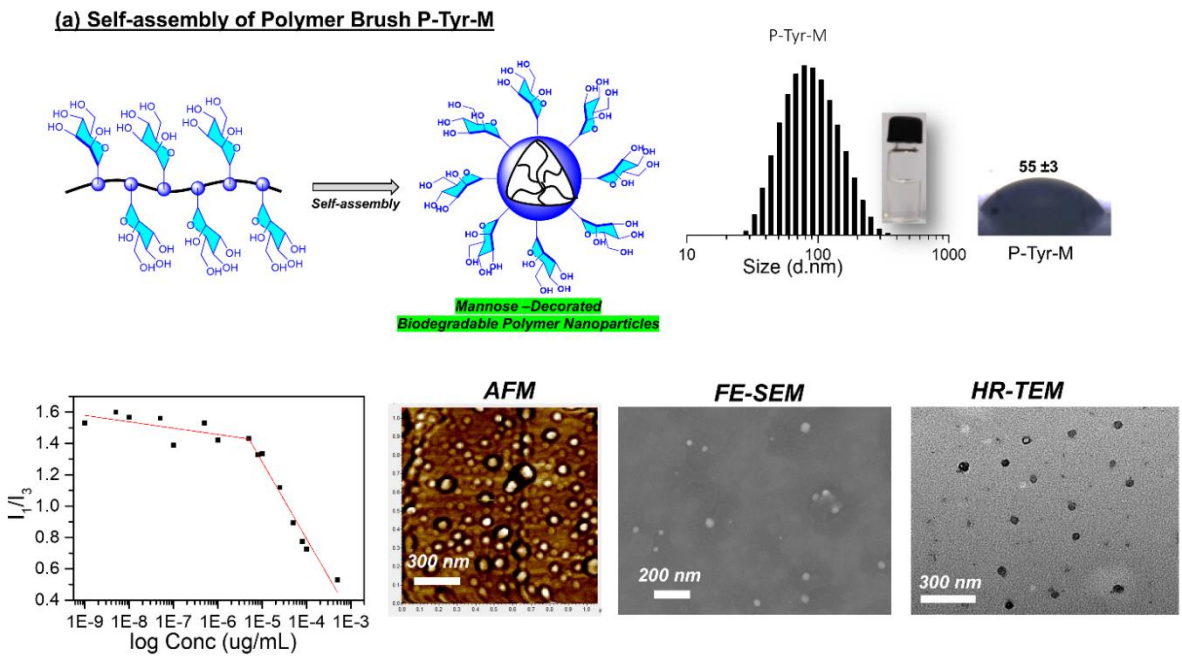

Figure 3.10 *(a) Schematic aqueous Self-assembly of P-Tyr-M polymer brush. (b) DLS histogram and the photographs show the water contact angle (LB-ADSA method) recorded for the polymer brush drop-caste film on glass substrate. Critical aggregation concentration (CAC) was determined by pyrene-probe. P-Tyr-M brush characterization by AFM, FE-SEM and HR-TEM images.*

3.3.6 Encapsulation Capabilities of Drug/dye

To prepare the self-assembled structures, a mixture of 5 mg of sugar-functionalized polymer and 0.5 mg of drugs a hydrophobic drug or dye, was dissolved in DMSO, ensuring homogeneous mixing. This solution was then subjected to dialysis against Milli-Q water using a 3.5 kDa molecular weight cutoff (MWCO) cellulose membrane for 48 hours. Dialysis facilitated the gradual removal of the DMSO, such as CPT, TPT, CUR, and biomarker HPTS and NR, which are capable of loading in the sugar polymer brushes, inducing encapsulation of the drug in polymer brushes into well-defined nanostructures. The schematic representation of drug encapsulation is shown in Figure 3.11a. The aqueous environment encouraged the hydrophobic interactions between polymer chains and the encapsulated drug or dye, while the hydrophilic sugar moieties-oriented outward, stabilizing the assemblies in water. The sugar-polymer brushes were evaluated for their drug and dye encapsulation capacities. The drug/dye encapsulation vial photographs in visible and under UV light, the photographs are shown in Figure 3.11b. Various molecules, including camptothecin (CPT), topotecan (TPT), curcumin, HPTS, and Nile red, DLS measurements of the drug-loaded nanoparticles showed sizes comparable to the native polymer brushes, as shown in Figure 3.11c and other DLS histograms

of drug-loaded polymer are shown in Appendix Figure S22 and AFM, HR-TEM images showed the sizes were matches with the nascent polymer brushes the images are shown in Figure 3.11d comparable analyses confirmed that the morphology remained unchanged after encapsulation. were successfully loaded into the polymers. Drug loading efficiencies were as follows: 2.5% for CPT, 4-5% for TPT and curcumin, 3-4% for HPTS, and 0.5-1% for Nile red. The DLC plot are shown in Figure 3.11e.

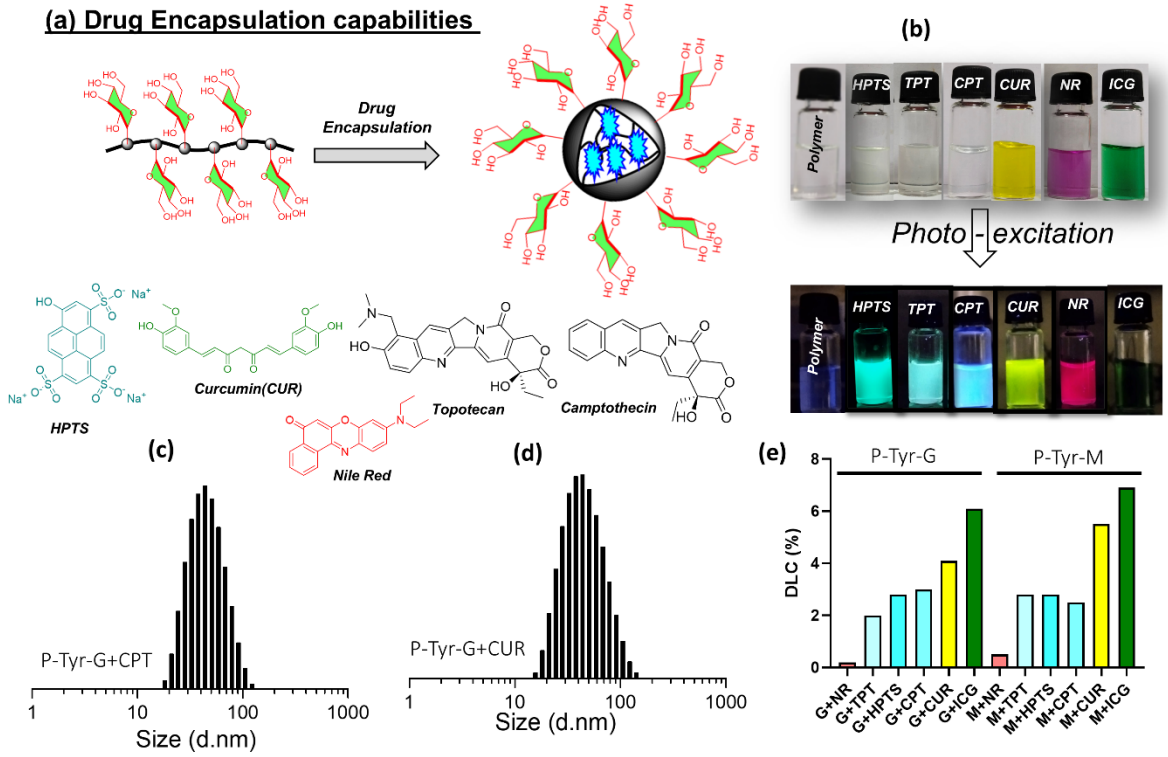

Figure 3.11 *(a) Schematic representation of P-Tyr-G brush polymer loaded with various drugs and dyes. (b) photograph of vials drug-loaded polymers brushes. (c) DLS histogram of P-Tyr-G+CPT, (d) DLS histogram of P-Tyr-G+CUR, (e) Drug loading content of P-Tyr-G and P-Tyr-M.*

The photophysical properties of the drug/dye were recorded in their absorbance and emission spectra, and we found out that the Drug/dye encapsulated nascent forms retain their photophysical properties after being effectively encapsulated by the drug or dye within the hydrophobic core encapsulated in the polymeric nanoarchitecture, as confirmed by subsequent characterization the absorbance spectra are shown in Figure 3.12a. Further, the emission spectra of drug/dye-loaded polymers are shown in Figure 3.12b. Biocompatibility: The use of glucose and mannose, naturally occurring and biocompatible sugars, enhances the likelihood of the assemblies being well-tolerated in biological systems. Mannose-functionalized assemblies, in particular, could target mannose receptors on immune cells, suggesting potential for targeted drug delivery. The study revealed that the glucose- and mannose-functionalized polymer

brushes are capable of forming stable self-assembled nanostructures in aqueous conditions. Their hydrophilic sugar shell and hydrophobic core provide a versatile platform for encapsulating and stabilizing hydrophobic drugs/dye, making these materials highly promising for diverse applications in biomedicine and nanotechnology.

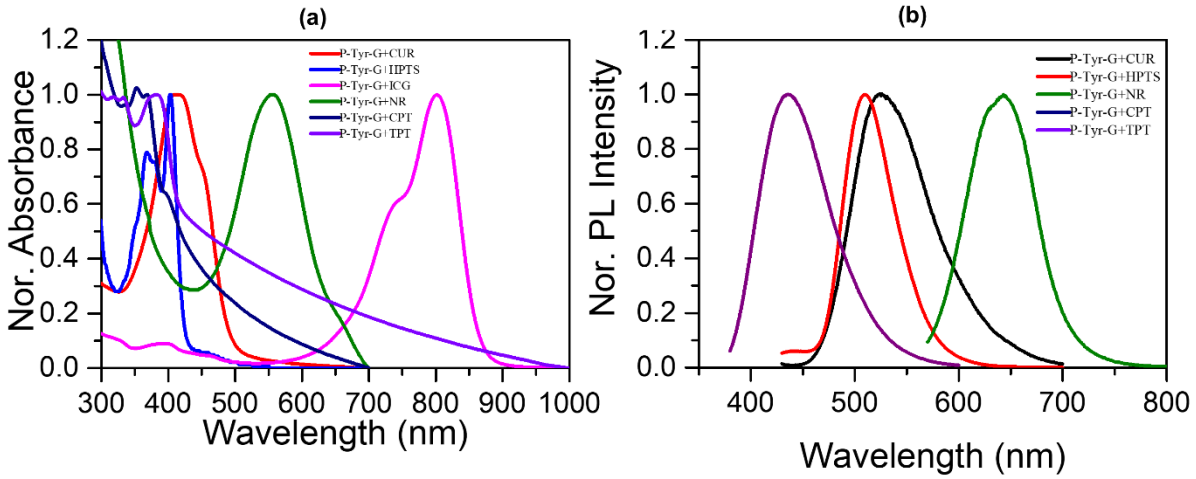

Figure 3.12 *(a) photophysical properties of drug-loaded samples. (b) emission spectra of drug-encapsulated P-Tyr-G+X Nanoparticles. (λ_{exc}=absorbance maxima).*

3.3.7 Release Kinetics experiments

The drug release kinetics of the loaded polymeric nanoparticle brushes were evaluated using a previously established procedure, detailed in the experimental section. The release kinetic experiment utilized camptothecin (CPT)-loaded polymer brushes with the enzyme horse liver esterase to simulate enzymatic degradation. The polymer's aliphatic ester backbone facilitates degradation during the endocytic process, mimicking cellular pathways. During endocytosis, nanoparticles transition from the extracellular matrix to the intracellular membrane, progressing through the early and late endosomes before reaching lysosomes, where enzymes such as esterase, lipase, and protease degrade the polymer backbone, leading to drug release. This mechanism allows the released drugs to intercalate with DNA as shown in Figure 3.13a. Further the fate of release cargo such as CPT which is DNA intercalator essentially ends to nucleus where it undergoes DNA intercalation and disrupt the DNA replication which eventually inhibit the cell growth. The stability of the polymer nanoparticles is investigated in various pH and salt concentration by DLS. The data is shown in Figures 2.17b and 2.17c revealed that the polymer nanoparticles are stable in various pH and salt concentration The CPT loaded polymer release cargo such as CPT which intercalate the essentially reach to nucleus where it intercalates and disturb the DNA replication which inhibit the cell growth.

The stability of the CPT loaded polymeric nanoparticles is investigated in various pH and salt concentration by Dynamic light scattering method (DLS) the data are shown in Figure 3.13b and 3.13c.

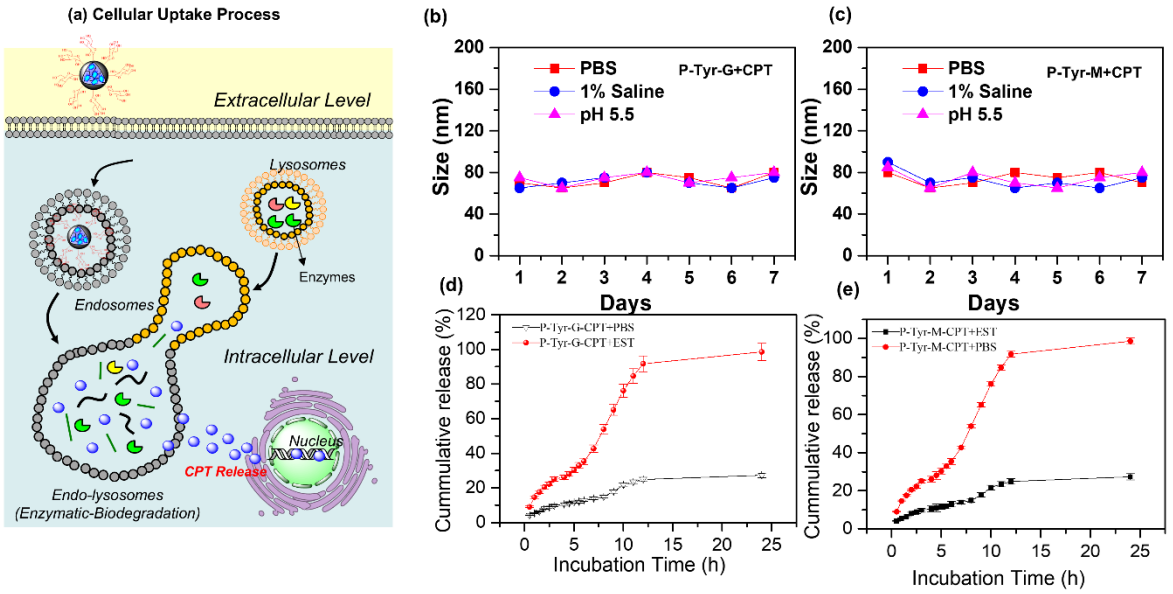

Figure 3.13 *(a) Schematic representation of sphere-like polymer brush uptake in the cells and enzyme-biodegradation for CPT release in lysosomal compartment. (b) DLS size of the PTry-G+CPT loaded sphere-like polymer brushes in PBS 7.4, 1% saline and pH=5.5 at 37 ℃. (c) DLS size of the P-Try-M+CPT loaded sphere-like polymer brushes in PBS 7.4, 1% saline and pH=5.5 at 37 ℃. (d) Cumulative drug release profiles of CPT-loaded P-Tyr-G samples in the presence of horse-liver esterase enzyme 10 U in PBS, pH 7.4 at* 37°C. *Drug release profiles of CPT-loaded P-Tyr-G samples in the absence of enzyme in PBS, pH 7.4 at* 37°C. *(e) Cumulative drug release profiles of CPT-loaded P-Tyr-M samples in the presence of horse-liver esterase enzyme 10 U in PBS, pH 7.4 at* 37 °C. *Drug release profiles of CPT-loaded P-Tyr-G samples in the absence of enzyme in PBS, pH 7.4 at* 37°C.

In the experiment, CPT-loaded polymer brushes were combined with 10 U of esterase enzyme in a 3.5 kDa molecular weight cutoff (MWCO) dialysis membrane and incubated in 1X PBS at 37 °C. A control experiment without the enzyme was performed under the same conditions. Aliquots were collected at various time intervals, and absorbance spectra were recorded to quantify drug release. The results, plotted as polymer concentration versus cumulative drug release, are shown in Figure 3.13d. Enzyme-mediated degradation resulted in 90 % drug release within 24 hours, compared to only 25 % release in the absence of the enzyme, confirming that drug release followed an enzymatic pathway.

3.3.8 Cell Viability assay (MTT assay)

The biocompatibility and cytotoxicity of the polymeric nanoparticle brushes were assessed using various cell lines, including HEK-293, MCF-7 breast cancer cells, MDA-MB-468 breast cancer cells, and MIA PaCa pancreatic cancer cells. Firstly, the complete media were prepared

for that 1 % penicillin-streptomycin, 10 % fetal bovine serum, and culture media were prepared. Nearly 1000 cells per well were seeded in 96-well plates and incubated for 16 hours. After media removal, different concentrations of polymer brushes were added, and the cells were incubated for 72 hours. Following incubation, media were aspirated, and an MTT assay was performed by adding 0.5 mg/mL MTT solution to each well, followed by a 4-hour incubation. The enzymatic reduction of MTT by mitochondrial nitro reductase formed formazan crystals, which were dissolved in DMSO. Absorbance was recorded at 570 nm, and the percentage of cell viability was plotted against polymer concentration. The polymer brushes were tested at concentrations ranging from 5 µg/mL to 100 µg/mL and showed no significant toxicity to either cancerous or normal cells at higher concentrations. To validate the biocompatibility and cytotoxicity of P-Tyr-G polymer were nontoxic to the Human kidney (HEK-293) cell line. The P-Tyr-G polymer at a higher concentration of 100 µg/mL as shown in Figure 3.14a. Similarly, the P-Tyr-M showed excellent compatibility at higher concentrations of 100 ug/mL 90 % of cells are viable and non-toxic to HEK-293 cell lines shown in Figure 3.14a.

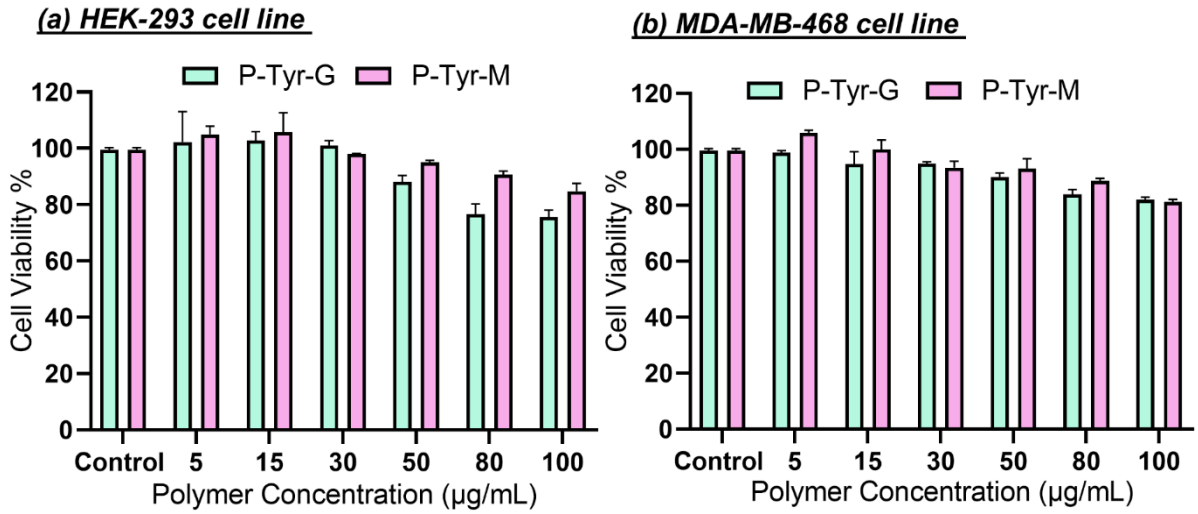

Figure 3.14 (a) *Plot showing the cytotoxicity of P-Tyr-G and P-Tyr-M in a normal HEK-293 cell line. (b) Plot showing the cytotoxicity of P-Tyr-G and P-Tyr-M in breast cancer MDA-MB-468 cell line.*

Similarly, the P-Tyr-G polymer alone was varied in concentration, and at a higher concentration of 100 ug/mL, the sugar polymers are 85 % cells are viable. These sugar polymers are compatible and non-toxic to cancer cell line MDA-MB-264 data, as shown in Figure 3.14b.

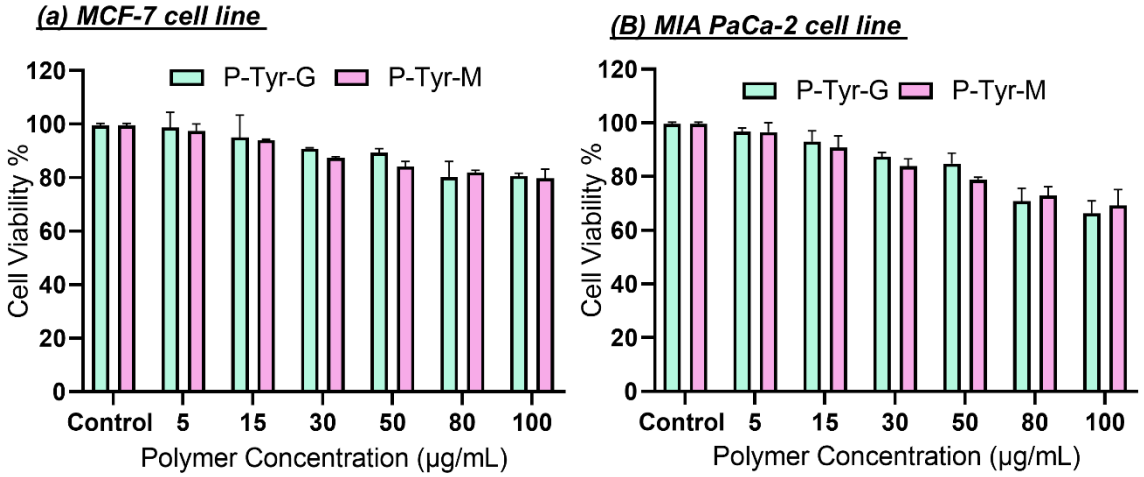

Figure 3.15 (a) *Plot showing the cytotoxicity of P-Tyr-G and P-Tyr-M in breast cancer MCF-7 cell line. (b) Plot showing the cytotoxicity of P-Tyr-G and P-Tyr-M in pancreatic MIA PaCa-2 cell line.*

Further, the sugar polymers alone were good compatibility at higher concentrations of 100 ug/mL, and 90 % of cells are viable and non-toxic to cancerous MCF-7 cell lines as shown in Figure 3.15a. Similarly, the sugar polymers are non-toxic to 2 pancreatic MIA PaCa-2 cell lines at a higher concentration of 100 ug/mL 75 % of cells are viable data is shown in Figure 3.15b it concluded that the Sugar polymers are non-toxic to various cell lines like HEK-293,MCF-7, MDA-MB-468, and MIA PaCa and very good biocompatibility and it can be used for drug delivery application. The cytotoxicity of drug-loaded polymer brushes was compared with free drugs, including camptothecin (CPT), topotecan (TPT), and curcumin, across various cell lines data are shown in Figure 3.16. The CPT-loaded P-Tyr-G polymers are showing similar killing to free CPT, but the P-Tyr-M polymers are not killing similarly to free CPT in cancerous cell line MCF-7 the data are shown in Figure 3.16a. Further, CUR-loaded polymers showed similar killing as free CUR at 1 ug/mL concentration in cancerous cell line MCF-7 see Figure 3.16b. However, the CPT-loaded polymers also showed similar killing as free CPT at a higher concentration of 1 ug/mL in the HEK-293 cell line, and data are shown in Figure 3.16c.

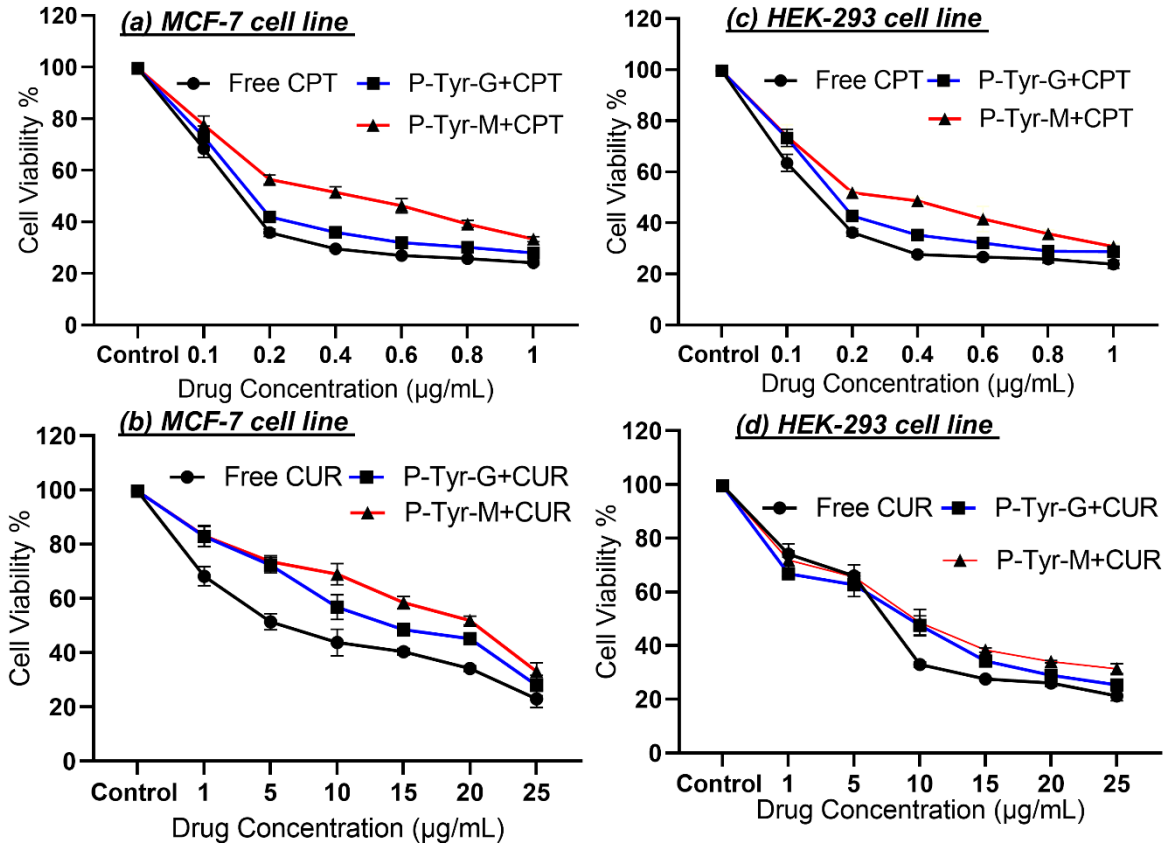

Figure 3.16 *(a) Plot showing the cytotoxicity of CPT loaded P-Tyr-G, and P-Tyr-M free CPT in breast cancer MCF-7 cell line. (b) Plot showing the cytotoxicity of CUR loaded P-Tyr-G, and P-Tyr-M free CUR in breast cancer MCF-7 cell line. (c) Plot showing the cytotoxicity of CPT loaded P-Tyr-G, and P-Tyr-M free CPT in normal human kidney HEK-293 cell line. (d) Plot showing the cytotoxicity of CPT loaded P-Tyr-G, and P-Tyr-M free CUR in normal human kidney HEK-293 cell line.*

After that, the CUR-loaded polymer showed similar killing as free CUR in normal HEK cell lines see Figure 3.16d. Similarly, the TPT loaded polymers data are shown in Appendix Figure S23. The IC_{50} values were determined to be 0.2 µg/mL for CPT, 5 µg/mL for TPT, and 10 µg/mL for curcumin. Free drugs at 1 µg/mL concentration showed only 20 % cell viability, and the drug-loaded polymer brushes demonstrated similar levels of cell killing, highlighting their potential for biomedical applications.

3.3.9 Cellular Uptake studies.

Cellular uptake studies were performed in wild-type MEF, HEK-293, and MCF-7 cell lines, as detailed in the experimental section. Approximately 10^5 cells per well were seeded in six-well plates and incubated for 16 hours. Firstly, Wild-type MEF cells were used. The 10^5 cells were seeded per well and incubated for 16 hours. After that, media were aspirated, and the HPTS-loaded sugar polymer brushes were incubated for various times like 3h and 6h. First, the HPTS

dye laser power at 405 nm. And 488 nm (for phalloidin) labelled actin filaments in cells. We found that the HPTS-loaded polymer brushes showed better uptake as compared to free HPTS. As the incubation time increased, the uptake also increased. The confocal images are shown in Figures 3.17a and 3.17b. The CTCF data clearly show that the HPTS-loaded polymers showed better uptake as compared to free HPTS data, as shown in Figure 3.17c.

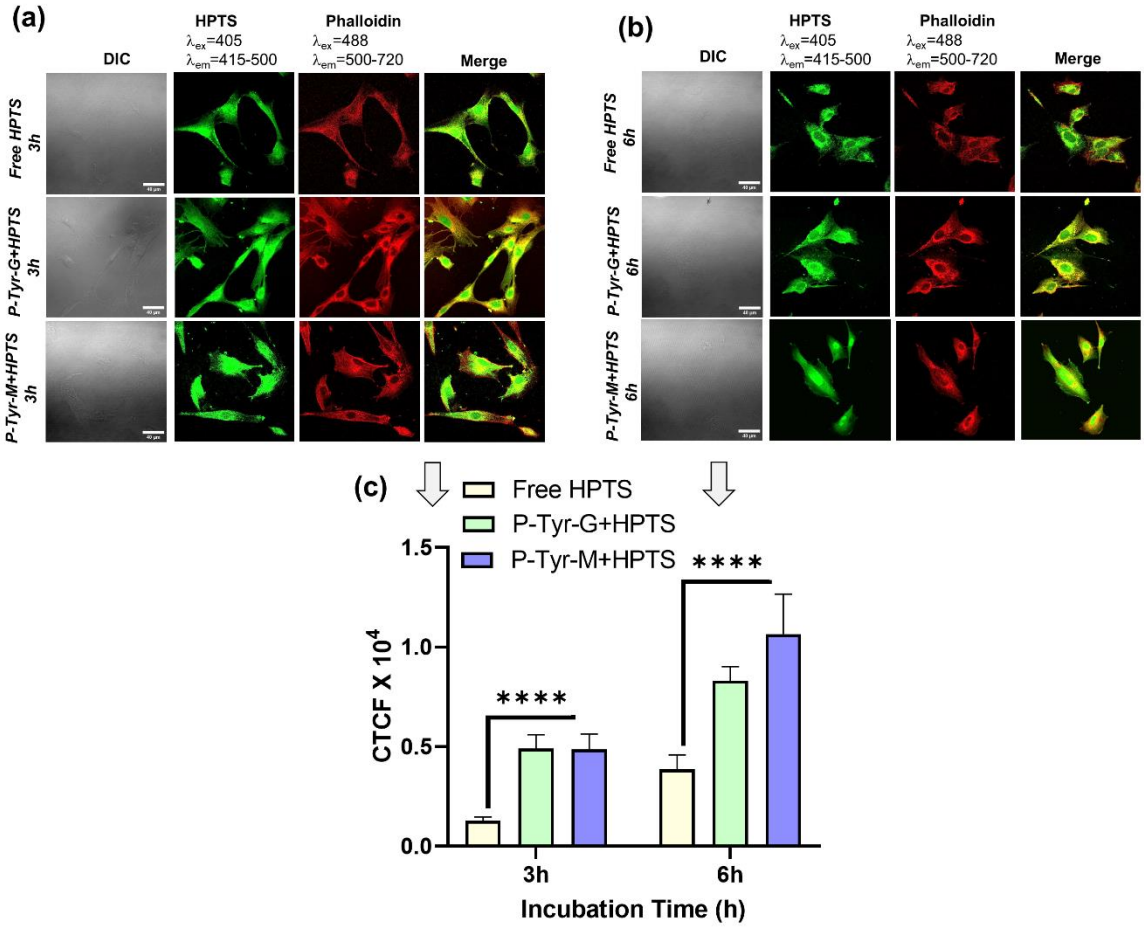

Figure 3.17 *Time-dependent cellular uptake fixed cell imaging in WET MEF cell line. (a) incubation time point 3 h, and (b) incubation time 6h. (c) Corrected total cell fluorescence (CTCF) of entire cell P-Tyr-G+HPTS uptake. The concentration of HPTS was maintained as 5 µg/mL. The scale bar represents 40 µm in cell images.*

For time-dependent cellular uptake studies, the cancerous MCF-cell line was used. After that, media removal was done, and cells were treated with CPT-loaded polymer brushes and incubated for various time points (2, 6, and 9 hours). Following incubation, cells were fixed and imaged using confocal laser scanning microscopy (LSM). For imaging, the CPT laser 405 nm and 488 nm (for phalloidin), the 2h and 9h confocal images are shown in Appendix Figure S24. The 6h incubation data of all the drugs like, CPT, TPT, and CUR were incubated in various cell lines like HEK-293 and in MCF-7 cancerous cell lines. In the HEK-293, cells were seeded in 10^5 per well and incubated for 16 hours, and media were aspirated. Further; the CPT-loaded

sugar polymers were given to cells and incubated for 6h. the cells were fixed, and the confocal images were captured through CSLM. The CPT laser 405 and 488 nm (for phalloidin) the CSLM images are shown in Figure 3.18a, and their CTCF calculation showed that the CPT-loaded sugar polymers better uptake as compared to free CPT data is shown in Figure 3.18b.

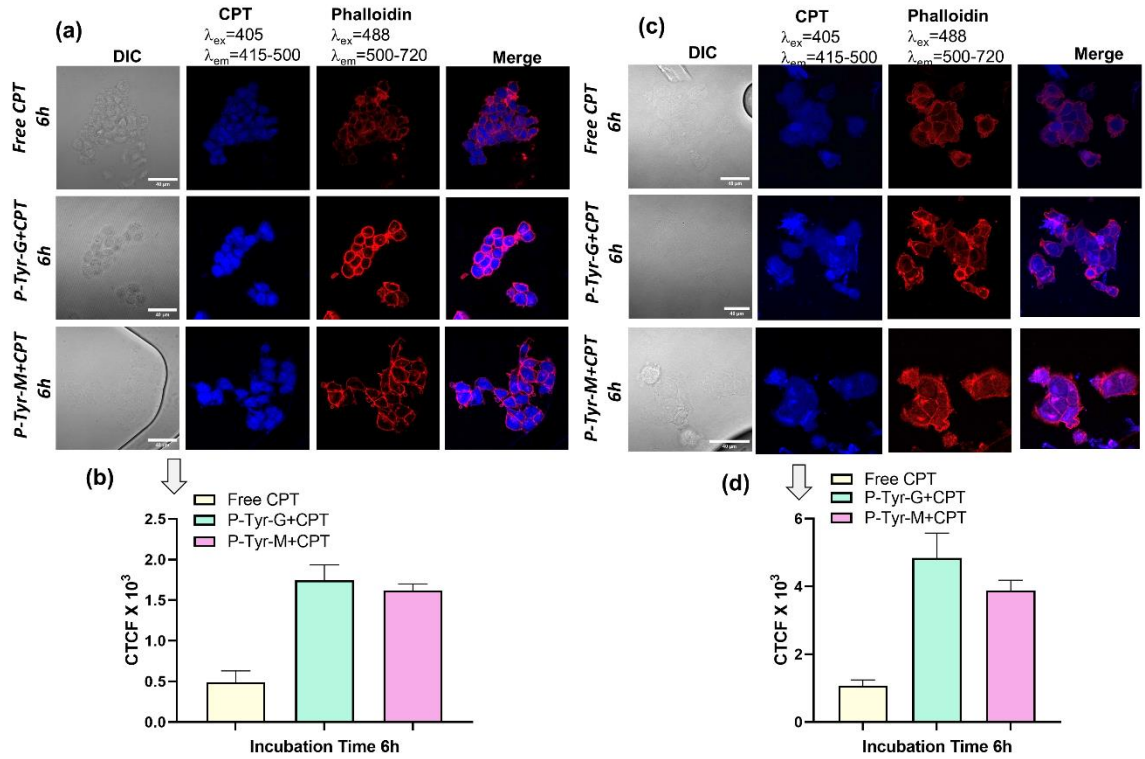

Figure 3.18. *(a) Cellular uptake studies of fixed cell imaging in HEK-293 cell line. (b) Corrected total cell fluorescence (CTCF) of entire cell uptake (c) Cellular uptake studies of fixed cell imaging in MCF-7 cell line. (d) Corrected total cell fluorescence (CTCF) of entire cell uptake. The concentration of CPT was maintained as 5 µg/mL. The scale bar represents 40 µm in cell images.*

Similarly, the CUR-loaded sugar polymers were incubated for a six-hour time point in the HEK-293 cell line. Further, the confocal images first Pannel CUR and second Pannel phalloidin and merge images clearly show that the phalloidin is labelled as actin filaments in cells data shown in Figure 3.19a. the CTCF calculation shows that the CUR-loaded sugar polymers have better uptake as compared to free CUR data are shown in Figure 3.19b. After that, the MCF-7 cancerous cells 10^5 cells were seeded in a six-well plate and incubated for 16 hours. Further, the CUR-loaded sugar polymers were given to cells and incubated for 6 hours. The fixed cells CSLM images captured and data are shown in Figure 3.19c. The CTCF calculation showed that the CUR-loaded sugar polymers have better uptake as compared to free CUR data, which are shown in Figure 3.19d.

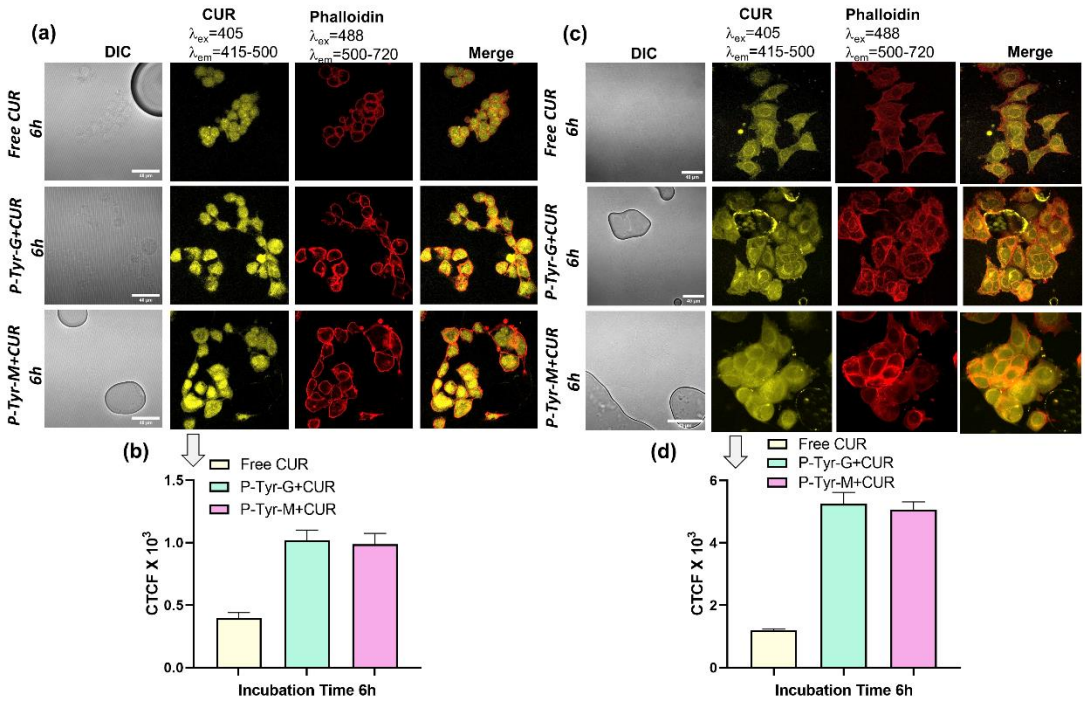

Figure 3.19. *(a) Cellular uptake studies of fixed cell imaging in HEK-293 cell line. (b) Corrected total cell fluorescence (CTCF) of entire cell uptake (c) Cellular uptake studies of fixed cell imaging in MCF-7 cell line. (d) Corrected total cell fluorescence (CTCF) of entire cell uptake. The concentration of CUR was maintained as 5 µg/mL. The scale bar represents 40 µm in cell images.*

The TPT-loaded sugar polymers were incubated for 6 hours in HEK-293 cells, and after that, cells were fixed, and CSLM images were captured the data are shown in Figure 3.20a. Further, the CTCF calculation clearly showed that the TPT-loaded sugar polymers have better uptake as compared to free TPT, and data are shown in Figure 3.20b. Further, the TPT-loaded sugar polymers were incubated for 6 hours in cancerous cells MCF-7. Further cells were fixed, and CSLM images were captured, as shown in Figure 3.20c. The CTCF calculation shows that the TPT-loaded sugar polymers have better uptake compared to free TPT data, are shown in Figure 3.20d. For various drugs, and dyes were used, including CPT, TPT, curcumin, HPTS, and Nile red. Laser sources at 405 nm (for CPT, TPT, curcumin, HPTS), 488 nm (for phalloidin), and 561 nm (for Nile red) were employed. Over time, an increase in polymer brush uptake was observed. The uptake of free drugs and dyes was significantly lower compared to that of drug-loaded polymer brushes. Both glucose- and mannose-functionalized sugar polymer brushes exhibited similar uptake behavior, suggesting effective biodegradation of the polymer brushes at the cellular level.These studies collectively demonstrate that sugar-functionalized polymer brushes are biocompatible, effectively deliver encapsulated drugs, and degrade at the cellular level, making them promising candidates for biomedical applications.

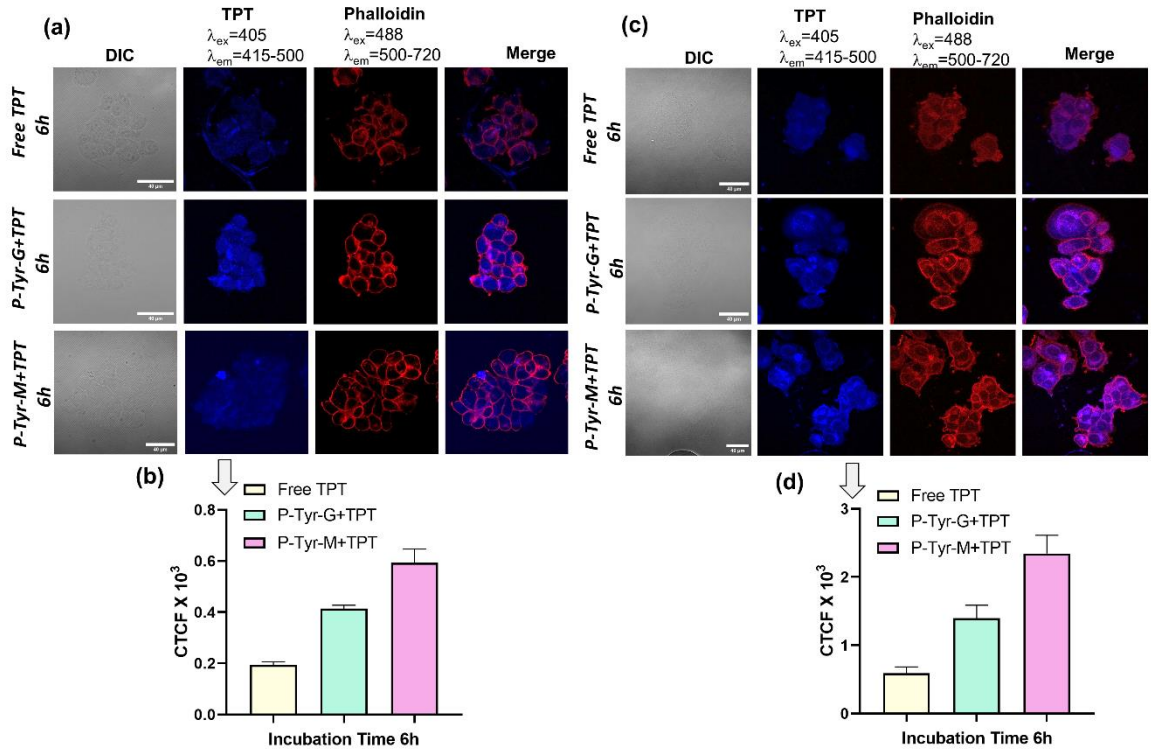

Figure 3.20. *(a) Cellular uptake studies of fixed cell imaging in HEK-293 cell line. (b) Corrected total cell fluorescence (CTCF) of entire cell uptake (c) Cellular uptake studies of fixed cell imaging in MCF-7 cell line. (d) Corrected total cell fluorescence (CTCF) of entire cell uptake. The concentration of TPT was maintained as 5 µg/mL. The scale bar represents 40 µm in cell images*.

3.3.10 Dye Encapsulation and Hemolysis Assay

Near-infrared (NIR) dyes are fluorophores activated by near-infrared radiation, widely used in *in vivo* imaging because of their superior tissue penetration compared to UV-visible light and their low autofluorescence in the NIR region. To enable *in vivo* imaging and examine the biodistribution of the synthesized sugar P-Tyr-G polymer scaffold, the NIR dye ICG was encapsulated into the polymer matrix, as illustrated in Figure 3.21a. The encapsulation procedure followed a method similar to that used for loading camptothecin (CPT), and the drug loading content was determined to be 6.2%, which is suitable for imaging applications. A photograph of the ICG-loaded polymer sample is provided in Figure 3.21a. Dynamic light scattering (DLS) measurements of the ICG-loaded nanoparticles indicated the formation of nano-assemblies with an average size of approximately 100 nm Figure 3.21a. Photophysical analysis confirmed that the encapsulated dye retained the same properties as in its free form, verifying the dye's stability within the nanocavities, as depicted in To evaluate the hemolytic

potential of the polymer samples, a hemolysis assay was conducted in which red blood cells (RBCs) were incubated with the polymer solution in phosphate-buffered saline (PBS), followed by centrifugation to separate the RBCs. In the absence of hemolysis, the RBCs remain intact, forming a red pellet at the bottom of the tube, while the supernatant stays clear. If the polymer induces RBC rupture, hemoglobin is released into the supernatant, resulting in a red coloration, which can be quantified by absorbance measurement. PBS served as a negative control, showing no RBC lysis, while Triton X-100, a nonionic surfactant known to disrupt RBCs osmotically, was used as a positive control. The results indicated that none of the polymer samples caused RBC hemolysis, as evidenced by the intact RBC pellet and the clear supernatant, as shown in Figure 3.21b. The percentage of hemolysis was calculated and presented in a histogram (Figure 3.21b), confirming that all nanoparticle samples exhibited non-hemolytic behavior.

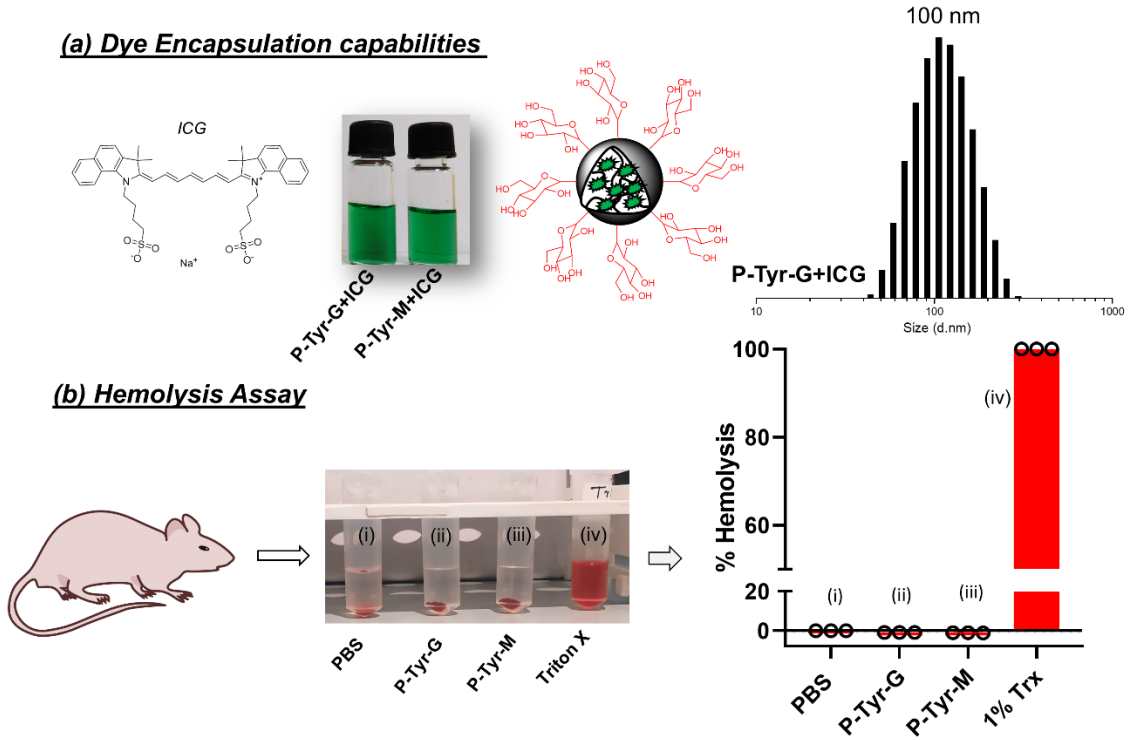

Figure 3.21. *(a) Schematic for encapsulation of ICG GREEN dye and DLS histogram for ICG loaded P-Tyr-G polymer brush nanoparticles. (b) Photographs of centrifuge tubes post incubation of sample with RBC solution. Appearance of intact pellet indicate RBC stability. Plot showing % hemolysis for polymer (P-Tyr-PEG) along with PBS (negative control) and 1% Triton X-100 (positive control), (****P<0.0001) each point represents mean ± SEM, n=3).*

3.3.11 In Vivo Biodistribution studies

For *in vivo* imaging and biodistribution studies, three groups of mice were used for each experimental condition, with each experiment performed in triplicate. The first group received intraperitoneal injections of ICG-loaded polymer nanoparticles, the second group was injected with free ICG dye, and the third group, serving as a control, was injected with 1× PBS. Whole-body imaging was conducted at 2-, 4-, 6-, and 24-hours post-injection using the PerkinElmer In Vivo Imaging System (IVIS) for biodistribution analysis. Representative images from the dorsal view are shown in Figure 3.22a, with similar images from the ventral view presented in Figure 3.22b. As anticipated, no fluorescence was detected in the control group injected with PBS, while strong fluorescence signals were observed in the groups injected with either ICG-loaded nanoparticles or free ICG dye. The fluorescence intensity was quantified by measuring the average radiance efficiency over time, as shown in Figure 3.22c and 3.22d. At all-time points, the signal intensity was higher in the group injected with ICG-loaded sugar polymeric nanoparticles compared to the group injected with free ICG dye, indicating enhanced uptake of the nanoparticles. By 24 hours, the total radiance efficiency in the group injected with free ICG dye had decreased substantially compared to the 2-hour time point, indicating the clearance of the dye from the body. In contrast, the total radiance efficiency in the group injected with ICG-loaded P-Tyr-G nanoparticles remained constant between 6 and 24 hours, but with the ICG loaded P-Tyr-M average radiant efficiency was decreased substantially suggesting the greater stability of the P-Tyr-G nanoparticle formulation in *in vivo* conditions.

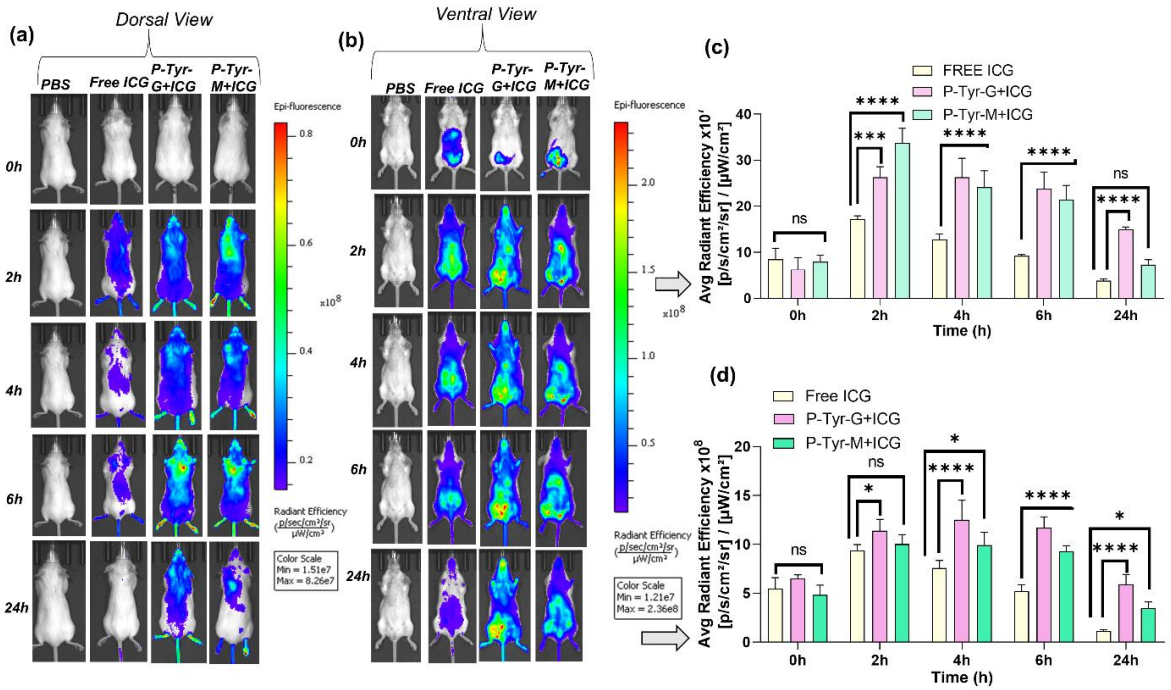

Figure 3.22. *(a). Time-dependent IVIS images (dorsal view) of mice injected with PBS (control), free ICG dye and ICG loaded polymer nanoparticles. (b) Time-dependent IVIS images (Ventral view) of mice injected with PBS (control), free ICG dye and ICG loaded polymer nanoparticles. (c) Histogram representing amount of ICG dye (quantified as average radiance) at various time points in the body of mouse injected with free ICG and ICG loaded polymer nanoparticles. (d) Histogram representing amount of ICG dye (quantified as average radiance) at various time points in the body of mouse injected with free ICG and ICG loaded polymer nanoparticles.*

The comparison of fluorescence intensities demonstrated that the sugar nanoparticle polymer brush shows significant potential for biomedical applications. The duration of circulation within the bloodstream is a critical factor in evaluating the efficacy of drug formulations. To assess the retention ability of the polymer nanoparticles, plasma samples were collected from mice at 2-, 6-, and 24-hours post-injection after administering ICG-loaded nanoparticles, free ICG dye, or PBS. These plasma samples were imaged in a 96-well plate using an In Vivo Imaging System (IVIS), as displayed in Figure 3.23a. Fluorescence signals from these plasma samples were then quantified and plotted in a histogram, shown in Figure 3.23b. The results demonstrated that the Free ICG leach out very faster because of their half life time is very low but ICG-loaded P-Tyr-G nanoparticles exhibited prolonged circulation

compared to the free ICG dye and P-Tyr-M, suggesting enhanced circulation time and stability *in vivo*.

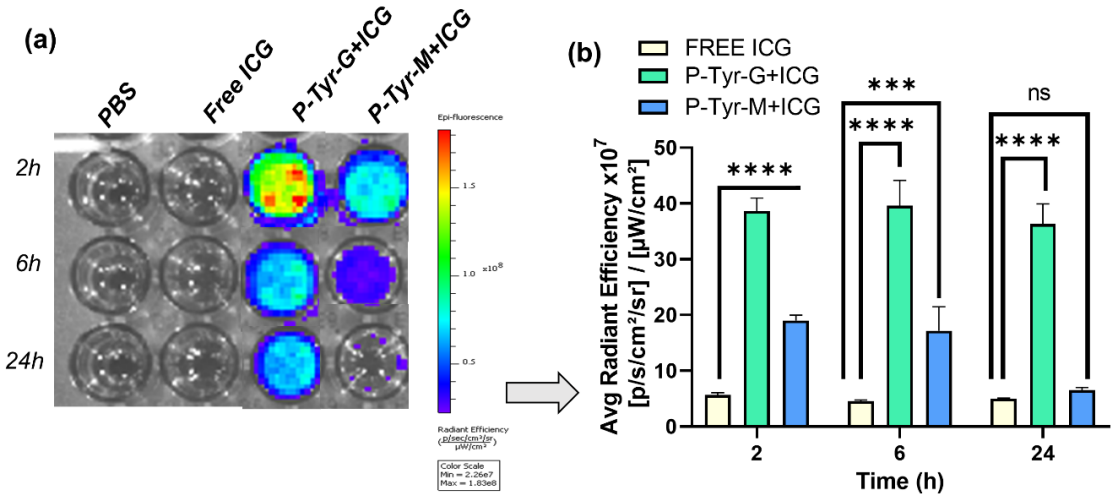

Figure 3.23 *(a) Representative time-dependent photograph of the plasma samples captured in a 96-well plate using IVIS. (b) Histogram representing the amount of ICG dye (quantified as average radiance efficiency) at various time points in plasma samples.*

To further explore the biodistribution, mice were sacrificed 24 hours after injection, euthanized via an overdose of isoflurane anesthesia, and perfused with PBS before organ collection. The organs were imaged using IVIS, and the results are obtained in Figure 3.24a. Fluorescence signal quantification from these organs is shown in the form of a histogram in Figure 3.25b. The data confirmed that mice injected with ICG-loaded nanoparticles showed stronger fluorescence signals compared to those injected with free ICG dye, supporting the enhanced stability of the polymer nanoparticles. Additionally, the nanoparticle polymer brushes demonstrated superior signal intensity due to their better blood circulation capabilities. High fluorescence signals were observed in organs such as the kidney, liver, lungs, and pancreas, indicating higher uptake of the ICG-loaded sugar polymer nanoparticles in these tissues.

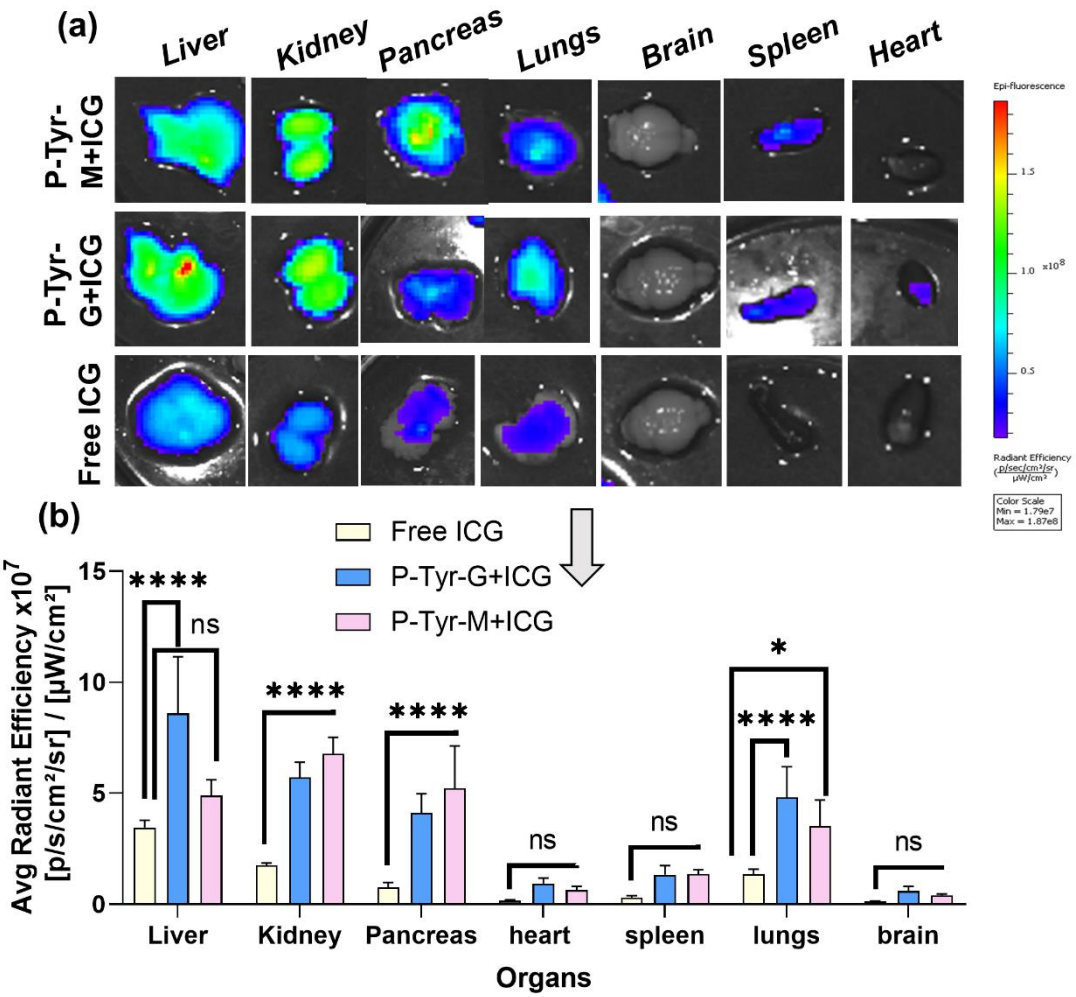

Figure 3.24 *(a) Photographs of the various organs (harvested post 24 h injection) captured using IVIS. (b) Histogram representing the amount of ICG Green dye (quantified as average radiance efficiency) in various organs.*

3.4 Conclusion

A novel synthetic approach has been established for the making of fully biobased poly(ester urethane)s utilizing two abundant natural resources. D-glucose and D-mannose are widely available and were transformed into protection and deprotection chemistry to form selective azidation to the anomeric position of glucose and mannose sugar through a multistep synthesis process. The secondary hydroxyl groups of D-glucose were protected as acetate linkages, resulting in two isomeric sugars, α and β. Comprehensive structural analysis, including ^{1}H and ^{13}C NMR structure determination, confirmed the formation of sugar azide molecules. The second monomeric component was derived from amino acids and modified to produce ester urethane monomers. Followed by the thermal stability of the monomer, a melt polymerization reaction was conducted at 150 ^{o}C to form poly(ester-urethane)s. Detailed thermal property analysis revealed that the rigid structure of the poly(ester-urethane)s. these amino acid polymer were clicked with sugar to formed hybrid poly(ester-urethane)s. Sugar polymer contributed to an elevated glass transition temperature in the resulting polymers. Subsequently, the amphiphilic amino acid-sugar hybrid poly(ester-urethane)s was self-assembled in aqueous solutions to form nanoparticles about 100 ± 10 nm in size. Enzymatic drug release of CPT with enzyme 90 % drug release and without enzyme only 25 % drug release and cytotoxicity assessments in human kidney HEK-293 cell and breast cancer MCF-7, MDA-MB-264 and MIA PaCa-2 pancreatic cell lines demonstrated the biocompatibility of the amino acid-sugar hybrid polymers. The cellular uptake studies revealed that the CPT, TPT and CUR-loaded polymer exhibited good uptake in cancer cell MCF-7 and HEK-293 cell lines. Further, the NIR probe ICG-green loaded polymer brushes live In Vivo biodistribution imaging IVIS technique emphasizes that the glucose polymer brushes have good blood circulation stability as compared to Mannose polymer. This study represents the first example of a polymer synthesized entirely from natural resources, specific sugar and amino acids. These innovative polymers hold promise as sustainable alternatives to traditional petroleum-based materials.

3.5 References:

(1) Varki, A.; Angata, T. Siglecs—the Major Subfamily of I-Type Lectins. *Glycobiology* **2006**, *16* (1), 1R-27R.

(2) Ambrosi, M.; Cameron, N. R.; Davis, B. G. Lectins: Tools for the Molecular Understanding of the Glycocode. *Organic and Biomolecular Chemistry*. May 7, 2005, pp 1593–1608.

(3) Wibowo, A.; Peters, E. C.; Hsieh-Wilson, L. C. Photoactivatable Glycopolymers for the Proteome-Wide Identification of Fucose-∝(1-2)-Galactose Binding Proteins. *J Am Chem Soc* **2014**, *136* (27), 9528–9531.

(4) Bonduelle, C.; Lecommandoux, S. Synthetic Glycopolypeptides as Biomimetic Analogues of Natural Glycoproteins. *Biomacromolecules*. September 9, 2013, pp 2973–2983.

(5) Deshpande, N. U.; Jayakannan, M. Cisplatin-Stitched Polysaccharide Vesicles for Synergistic Cancer Therapy of Triple Antagonistic Drugs. *Biomacromolecules* **2017**, *18* (1), 113–126.

(6) You, M.; Xie, Z.; Zhang, N.; Zhang, Y.; Xiao, D.; Liu, S.; Zhuang, W.; Li, L.; Tao, Y. Signaling Pathways in Cancer Metabolism: Mechanisms and Therapeutic Targets. *Signal Transduct Target Ther* **2023**, *8* (1), 196.

(7) Anderluh, M.; Berti, F.; Bzducha-Wróbel, A.; Chiodo, F.; van Vliet, S. J. Emerging Glyco-Based Strategies to Steer Immune Responses. *FEBS Journal* **2021**, *288* (16), 4746–4772.

(8) Li, Z.; Sun, L.; Zhang, Y.; Dove, A. P.; O'Reilly, R. K.; Chen, G. Shape Effect of Glyco-Nanoparticles on Macrophage Cellular Uptake and Immune Response. *ACS Macro Lett* **2016**, *5* (9), 1059–1064.

(9) Díaz-Alvarez, L.; Ortega, E. The Many Roles of Galectin-3, a Multifaceted Molecule, in Innate Immune Responses against Pathogens. *Mediators of Inflammation*. Hindawi Limited 2017.

(10) Nagao, M.; Kichize, M.; Hoshino, Y.; Miura, Y. Influence of Monomer Structures for Polymeric Multivalent Ligands: Consideration of the Molecular Mobility of Glycopolymers. *Biomacromolecules* **2021**, *22* (7), 3119–3127.

(11) Beach, M. A.; Nayanathara, U.; Gao, Y.; Zhang, C.; Xiong, Y.; Wang, Y.; Such, G. K. Polymeric Nanoparticles for Drug Delivery. *Chemical Reviews*. American Chemical Society May 8, 2024, pp 5505–5616.

(12) Woythe, L.; Tito, N. B.; Albertazzi, L. A Quantitative View on Multivalent Nanomedicine Targeting. *Advanced Drug Delivery Reviews*. Elsevier B.V. February 1, 2021, pp 1–21.

(13) Suriano, F.; Pratt, R.; Tan, J. P. K.; Wiradharma, N.; Nelson, A.; Yang, Y. Y.; Dubois, P.; Hedrick, J. L. Synthesis of a Family of Amphiphilic Glycopolymers via Controlled

Ring-Opening Polymerization of Functionalized Cyclic Carbonates and Their Application in Drug Delivery. *Biomaterials* **2010**, *31* (9), 2637–2645.

(14) Chen, W.; Meng, F.; Cheng, R.; Deng, C.; Feijen, J.; Zhong, Z. Biodegradable Glycopolymer-b-Poly(ε-Caprolactone) Block Copolymer Micelles: Versatile Construction, Tailored Lactose Functionality, and Hepatoma-Targeted Drug Delivery. *J Mater Chem B* **2015**, *3* (11), 2308–2317.

(15) Yilmaz, G.; Guler, E.; Geyik, C.; Demir, B.; Ozkan, M.; Odaci Demirkol, D.; Ozcelik, S.; Timur, S.; Remzi Becer, C. PH Responsive Glycopolymer Nanoparticles for Targeted Delivery of Anti-Cancer Drugs. *Mol Syst Des Eng* **2018**, *3* (1), 150–158.

(16) Torres-Pérez, S. A.; Torres-Pérez, C. E.; Pedraza-Escalona, M.; Pérez-Tapia, S. M.; Ramón-Gallegos, E. Glycosylated Nanoparticles for Cancer-Targeted Drug Delivery. *Frontiers in Oncology*. Frontiers Media S.A. November 30, 2020.

(17) Bhattacharya, K.; Banerjee, S. L.; Das, S.; Samanta, S.; Mandal, M.; Singha, N. K. REDOX Responsive Fluorescence Active Glycopolymer Based Nanogel: A Potential Material for Targeted Anticancer Drug Delivery. *ACS Appl Bio Mater* **2019**, *2* (6), 2587–2599.

(18) Chen, H.; Jia, H.; Tham, H. P.; Qu, Q.; Xing, P.; Zhao, J.; Phua, S. Z. F.; Chen, G.; Zhao, Y. Theranostic Prodrug Vesicles for Imaging Guided Codelivery of Camptothecin and SiRNA in Synergetic Cancer Therapy. *ACS Appl Mater Interfaces* **2017**, *9* (28), 23536–23543.

(19) Zhao, J.; Babiuch, K.; Lu, H.; Dag, A.; Gottschaldt, M.; Stenzel, M. H. Fructose-Coated Nanoparticles: A Promising Drug Nanocarrier for Triple-Negative Breast Cancer Therapy. *Chemical Communications* **2014**, *50* (100), 15928–15931.

(20) Choi, K. Y.; Yoon, H. Y.; Kim, J. H.; Bae, S. M.; Park, Park, J. H. Smart Nanocarrier Based on PEGylated Hyaluronic Acid for Cancer Therapy. *ACS Nano* **2011**, *5* (11), 8591–8599.

(21) Liu, Y.; Liu, J.; Pang, X.; Liu, T.; Ning, Z.; Cheng, G. The Roles of Direct Recognition by Animal Lectins in Antiviral Immunity and Viral Pathogenesis. *Molecules*. MDPI AG February 1, 2015, pp 2272–2295.

(22) Delbianco, M.; Seeberger, P. H. Materials Science Based on Synthetic Polysaccharides. *Materials Horizons*. Royal Society of Chemistry April 1, 2020, pp 963–969.

(23) Cook, M. T.; Smith, S. L.; Khutoryanskiy, V. V. Novel Glycopolymer Hydrogels as Mucosa-Mimetic Materials to Reduce Animal Testing. *Chemical Communications* **2015**, *51* (77), 14447–14450.

(24) Tian, B.; Hua, S.; Tian, Y.; Liu, J. Chemical and Physical Chitosan Hydrogels as Prospective Carriers for Drug Delivery: A Review. *J Mater Chem B* **2020**, *8* (44), 10050–10064.

(25) Abasalizadeh, F.; Moghaddam, S. V.; Alizadeh, E.; Akbari, E.; Kashani, E.; Fazljou, S. M. B.; Torbati, M.; Akbarzadeh, A. Alginate-Based Hydrogels as Drug Delivery

Vehicles in Cancer Treatment and Their Applications in Wound Dressing and 3D Bioprinting. *Journal of Biological Engineering*. BioMed Central Ltd March 13, 2020.

(26) Wu, L.; Zhang, Y.; Li, Z.; Yang, G.; Kochovski, Z.; Chen, G.; Jiang, M. "sweet" Architecture-Dependent Uptake of Glycocalyx-Mimicking Nanoparticles Based on Biodegradable Aliphatic Polyesters by Macrophages. *J Am Chem Soc* **2017**, *139* (41), 14684–14692.

(27) Lowe, A. B.; Sumerlin, B. S.; McCormick, C. L. The Direct Polymerization of 2-Methacryloxyethyl Glucoside via Aqueous Reversible Addition-Fragmentation Chain Transfer (RAFT) Polymerization. *Polymer (Guildf)* **2003**, *44* (22), 6761–6765.

(28) Lu, M.; Khine, Y. Y.; Chen, F.; Cao, C.; Garvey, C. J.; Lu, H.; Stenzel, M. H. Sugar Concentration and Arrangement on the Surface of Glycopolymer Micelles Affect the Interaction with Cancer Cells. *Biomacromolecules* **2019**, *20* (1), 273–284.

(29) Song, E. H.; Manganiello, M. J.; Chow, Y. H.; Ghosn, B.; Convertine, A. J.; Stayton, P. S.; Schnapp, L. M.; Ratner, D. M. In Vivo Targeting of Alveolar Macrophages via RAFT-Based Glycopolymers. *Biomaterials* **2012**, *33* (28), 6889–6897.

(30) Ohno, K.; Tsujii, Y.; Fukuda, T. Synthesis of a Well-Defined Glycopolymer by Atom Transfer Radical Polymerization. *J Polym Sci A Polym Chem* **1998**, *36* (14), 2473–2481.

(31) Pati, D.; Kalva, N.; Das, S.; Kumaraswamy, G.; Sen Gupta, S.; Ambade, A. V. Multiple Topologies from Glycopolypeptide-Dendron Conjugate Self-Assembly: Nanorods, Micelles, and Organogels. *J Am Chem Soc* **2012**, *134* (18), 7796–7802.

(32) Pandey, B.; Patil, N. G.; Bhosle, G. S.; Ambade, A. V.; Gupta, S. Sen. Amphiphilic Glycopolypeptide Star Copolymer-Based Cross-Linked Nanocarriers for Targeted and Dual-Stimuli-Responsive Drug Delivery. *Bioconjug Chem* **2019**, *30* (3), 633–646.

(33) Pati, D.; Das, S.; Patil, Dhaware, V.; Ambade, A. V.; Sen Gupta, S. Tunable Nanocarrier Morphologies from Glycopolypeptide-Based Amphiphilic Biocompatible Star Copolymers and Their Carbohydrate Specific Intracellular Delivery. *Biomacromolecules* **2016**, *17* (2), 466–475.

(34) Deming, T. J. Synthesis of Side-Chain Modified Polypeptides. *Chemical Reviews*. American Chemical Society February 10, 2016, pp 786–808.

(35) Mperiju, T. M.; Silas, K.; Aji, M. M.; Abdulhalim Musa Abubakar; Budianto, A.; Indianraj N; Rezkallah Chafika. Renewable Carbohydrates: Advancements in Sustainable Glucose Production and Optimization. *Global Sustainability Research* **2023**, *2* (4), 77–124.

(36) Deng, C.; Wu, J.; Cheng, R.; Meng, F.; Klok, H. A.; Zhong, Z. Functional Polypeptide and Hybrid Materials: Precision Synthesis via α-Amino Acid N-Carboxyanhydride Polymerization and Emerging Biomedical Applications. *Progress in Polymer Science*. February 2014, pp 330–364.

(37) Deming, T. J. Synthetic Polypeptides for Biomedical Applications. *Progress in Polymer Science (Oxford)*. August 2007, pp 858–875.

(38) Aluri, R.; Jayakannan, M. One-Pot Two Polymers: ABB′ Melt Polycondensation for Linear Polyesters and Hyperbranched Poly(Ester-Urethane)s Based on Natural L-Amino Acids. *Polym Chem* **2015**, *6* (25), 4641–4649.

(39) Anantharaj, S.; Jayakannan, M. Melt Polycondensation Approach for Reduction Degradable Helical Polyester Based on L-cystine. *J Polym Sci A Polym Chem* **2016**, *54* (18), 2864–2875.

(40) Anantharaj, S.; Jayakannan, M. Amyloid-Like Hierarchical Helical Fibrils and Conformational Reversibility in Functional Polyesters Based on L-Amino Acids. *Biomacromolecules* **2015**, *16* (3), 1009–1020.

(41) Saxena, S.; Jayakannan, M. Development of L-Amino-Acid-Based Hydroxyl Functionalized Biodegradable Amphiphilic Polyesters and Their Drug Delivery Capabilities to Cancer Cells. *Biomacromolecules* **2020**, *21* (1), 171–187.

(42) Aluri, R.; Jayakannan, M. Development of L-Tyrosine-Based Enzyme-Responsive Amphiphilic Poly(Ester-Urethane) Nanocarriers for Multiple Drug Delivery to Cancer Cells. *Biomacromolecules* **2017**, *18* (1), 189–200.

(43) Chandra Joshi, D.; Ashokan, A.; Jayakannan, M. L-Amino Acid Based Phenol- and Catechol-Functionalized Poly(Ester-Urethane)s for Aromatic π-Interaction Driven Drug Stabilization and Their Enzyme-Responsive Delivery in Cancer Cells. *ACS Appl Bio Mater* **2022**, *5* (11), 5432–5444.

(44) Anantharaj, S.; Jayakannan, M. Polymers from Amino Acids: Development of Dual Ester-Urethane Melt Condensation Approach and Mechanistic Aspects. *Biomacromolecules* **2012**, *13* (8), 2446–2455.

(45) Anantharaj, S.; Jayakannan, M. Catalysts and Temperature Driven Melt Polycondensation Reaction for Helical Poly(Ester-Urethane)s Based on Natural L-Amino Acids. *J Polym Sci A Polym Chem* **2016**, *54* (8), 1065–1077.

(46) Gavhane, U. A.; Joshi, D. C.; Jayakannan, M. Size- and Shape-Controlled Biodegradable Polymer Brushes Based on L-Amino Acid for Intracellular Drug Delivery and Deep-Tissue Penetration. *Biomacromolecules* **2024**.

(47) Joshi, D. C.; Saxena, S.; Jayakannan, M. Development of L-Lysine Based Biodegradable Polyurethanes and Their Dual-Responsive Amphiphilic Nanocarriers for Drug Delivery to Cancer Cells. *ACS Appl Polym Mater* **2019**, *1* (7), 1866–1880.

(48) Aluri, R.; Saxena, S.; Joshi, D. C.; Jayakannan, M. Multistimuli-Responsive Amphiphilic Poly(Ester-Urethane) Nanoassemblies Based on L-Tyrosine for Intracellular Drug Delivery to Cancer Cells. *Biomacromolecules* **2018**, *19* (6), 2166–2181.

(49) Khuddus, M.; Jayakannan, M. Melt Polycondensation Strategy for Amide-Functionalized L-Aspartic Acid Amphiphilic Polyester Nano-Assemblies and Enzyme-Responsive Drug Delivery in Cancer Cells. *Biomacromolecules* **2023**, *24* (6), 2643–2660.

(50) Saxena, S.; Jayakannan, M. Enzyme and PH Dual Responsive L-Amino Acid Based Biodegradable Polymer Nanocarrier for Multidrug Delivery to Cancer Cells. *J Polym Sci A Polym Chem* **2016**, *54* (20), 3279–3293.

Chapter 4

Fluorophore-Tagged Theranostic FRET Polymer Brushes for Real-time Cellular Monitoring

Abstract

L-Tyrosine-based propargyl-functionalized, coumarin-tagged fluorescent polymer brushes were developed to investigate real-time drug delivery applications. The fluorophore was incorporated as a side chain via a click reaction to evaluate the influence of polymer topology on drug and fluorophore loading and release capabilities. This study focuses on the design and synthesis of biodegradable poly(ester-urethane)s. For this purpose, the tyrosine monomer was polymerized with 1,12-dodecanediol to produce poly(ester-urethane)s, which were subsequently functionalized with PEG and CUM in an 80:20 ratio to produce fluorescent amphiphilic polymer brushes. These polymer brushes were characterized using size exclusion chromatography (SEC) and proton nuclear magnetic resonance spectroscopy (^{1}H NMR). The brushes were then self-assembled in an aqueous medium, yielding particle sizes of 220 nm. These structures demonstrated the capability to encapsulate biomarkers such as Nile Red (NR). The photophysical properties of the nanoparticle were done using absorbance and emission spectroscopy, TCSPC, to establish the FRET probe. It was clearly demonstrated that there is the transfer of energy from the Coumarin molecule to Nile red (NR) in the hydrophobic nanocavity of the nanoparticle, which was further confirmed by determining the distance between donor and acceptor, FRET efficiency, etc. Enzymatic degradation using horse liver esterase validated the biodegradable nature of the polymer's brushes, showing the enzyme-responsive release of the encapsulated cargo. Biocompatibility assessments revealed that both the polymer brushes and its nanorods and nanoparticles exhibited non-cytotoxic toward normal or cancer cell lines, whereas NR-loaded nanoparticles were also non-toxic to cancer cells as well as normal cell lines. Time-dependent Cellular uptake studies were carried out, and it was found that the indeed the rod-like polymer brush had better uptake as compared to the sphere-like polymer brushes. FRET interactions between CUM and encapsulated cargos were visualized via live cell bioimaging in cancer cells. This study highlights the potential of these biodegradable and biocompatible CUM-tagged poly(ester-urethane)s brushes as advanced nanocarriers for cancer therapy and imaging applications.

4.1 Introduction

Fluorescent nanoprobes are becoming a vital biomaterial platform for the early detection of cancer.[1] Theragnostic self-assemblies represent an innovative class of nanosystems designed for the targeted delivery of therapeutic drugs or genes in cancer therapy.[2–6] These nanocarriers, constructed from fluorescent chromophores, leverage their distinctive absorbance and emission properties across the visible to infrared spectrum. By enabling effective treatment at lower concentrations, they enhance therapeutic efficiency.[7,8] Within the domain of fluorescent polymers, numerous strategies have been developed, including the conjugation of fluorescent molecules to polymers. These constructs are self-assembled in aqueous environments and exhibit responsiveness to external stimuli, such as variations in pH, enzymatic activity, or redox conditions, and facilitate precise analysis at the cellular level.[9–13]

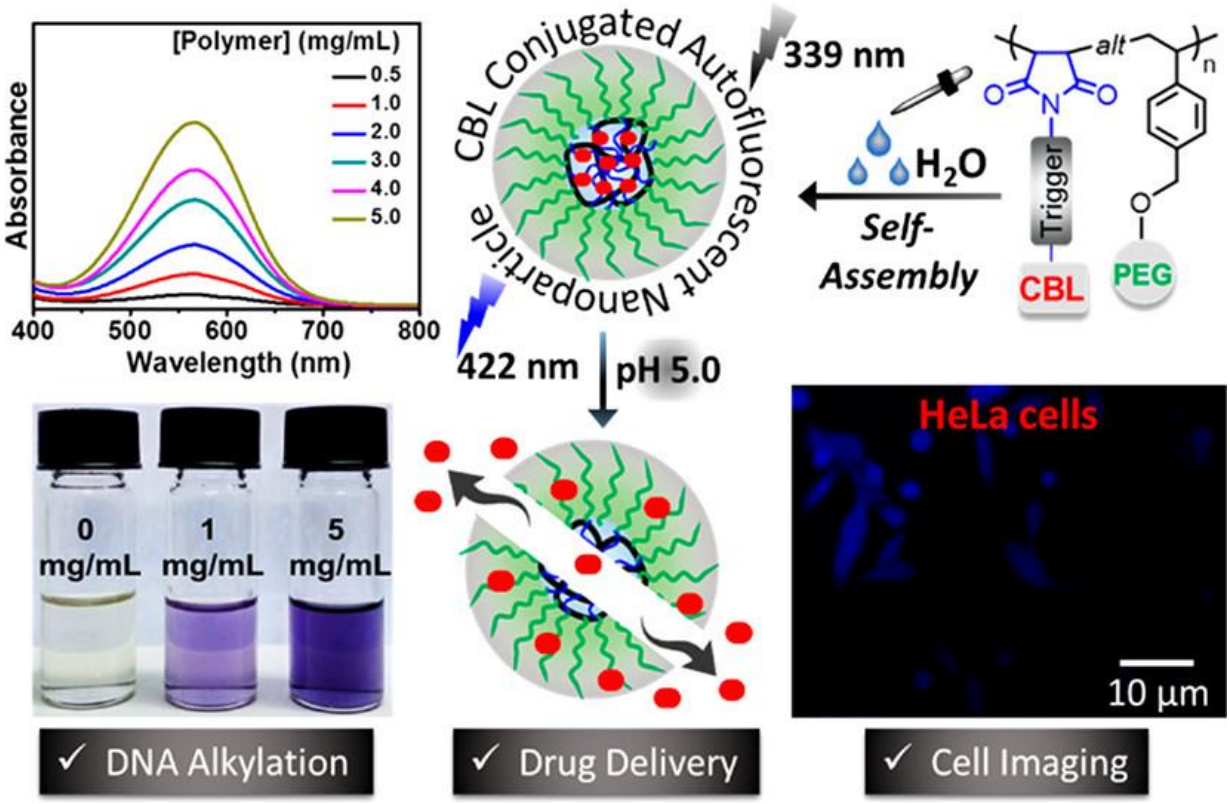

Figure 4.1 *Aromatic Nitrogen Mustard-Based Auto fluorescent Amphiphilic Brush Copolymer for pH-Responsive Drug Delivery Applications. (adopted from Biomacromolecules* ***2019****, 20, 1, 546–557).*

The diverse range of polymeric self-assemblies encompasses unimolecular micelles,[14] aggregated micelles,[15,16] polymersomes,[17–20] liposomes,[21,22] supramolecular assemblies,[23–25]

inorganic nanoparticles,[26] and more, offering versatile platforms for advanced biomedical applications. In the field of fluorescent polymer systems, polyaromatic molecules stand out as a significant category. Under aqueous conditions, these systems undergo π-π interactions among their chromophores, leading to a phenomenon known as aggregation-induced quenching (ACQ). This strong aggregation diminishes the emission intensity of the polymers, particularly affecting their performance in intracellular bioimaging applications.[27–29] When polyaromatic systems converge or come into close proximity within nanocavities during the formation of polymeric nanoparticles, they not only quench the fluorescence of the polymer but also reduce the signals emitted by the encapsulated cargo. Over the past decade, the concept of aggregation-induced emission (AIE), pioneered by Ben Zong Tong and colleagues, has garnered significant attention. This pioneering approach involves the synthesis of molecules that exhibit enhanced emission intensity upon aggregation, contrasting with the previously mentioned phenomenon of aggregation-caused quenching (ACQ). Notably, structures such as hexaphenylsilole were explored, demonstrating fluorescence when intramolecular rotation is restricted. The principles of AIE present exciting opportunities for advancing fluorescent-tagged nanoparticles, paving the way for innovative developments and applications in this field.[30–33] Förster or fluorescence resonance energy transfer (FRET) is a powerful and non-invasive fluorescence probing technique.[34] It relies on the principle of selective photoexcitation energy transfer between donor and acceptor chromophores within nano-confined spaces of ≤ 50 Å.[35] The versatility of FRET has facilitated its application across a wide range of fields, including real-time cellular imaging,[36–39] monitoring drug release kinetics,[40–43] investigating the self-assembly of amphiphilic block copolymers,[44] studying protein folding under physiological conditions,[45,46] exploring DNA,[47–49] quadruplex-to-duplex transitions,[50] probing molecular interactions at mammalian cell surfaces,[51] enabling two-photon imaging in cancers,[52,53] and sensing bilirubin in human serum,[54] among other significant uses. In recent decades, advancements in conducting polymers for optoelectronic devices have opened new avenues for the use of water-soluble cationic π-conjugated polymers as luminescent bio-probes.[55] Among these, cationic and water-soluble polyfluorenes have become key π-conjugated polymers for FRET applications.[56] Furthermore, polyacrylate-based random and block copolymers, incorporating optical chromophores into their side chains, have also been investigated for FRET-related uses. Despite these advancements, a major challenge remains: the non-biodegradability of the rigid C-C backbone in π-conjugated polymers and acrylates, which continues to impede their broader adoption in biomedical research.[57–59] There is a

growing need to develop fluorescent nanocarrier-based drug delivery systems that are both biodegradable and biocompatible. In our lab, we have synthesized biodegradable polymers derived from L-amino acid resources using a melt polycondensation strategy. This approach has led to the development of novel polymer classes, including polyesters,[60–64] polyurethanes,[65] and poly(ester-urethane)s,[66–70] from L-amino acids. Furthermore, this methodology has been extended to create stimuli-responsive polymers that respond to pH, redox conditions, enzymatic activity, and more. Building on this foundation, we have developed a biodegradable poly(ester-urethane)s derived from L-tyrosine. This innovative polymer not only facilitates bioimaging in cancer cells but also enables the investigation of intermolecular interactions between the polymer and its loaded cargo, utilizing FRET as an analytical tool.

This chapter developed the synthesis of biodegradable poly(ester-urethane) derived from L-tyrosine. The tyrosine-based monomer was polymerized with 1,12-dodecanediol via a melt polycondensation technique to produce poly(ester-urethane)s. Subsequently, the tyrosine-based polymer was functionalized with CUM and PEG via a click reaction, resulting in PEGylated-functionalized and CUM-tagged poly(ester-urethane)s. The hydrophilic-hydrophobic balance of the polymers was fine-tuned by varying the ratio (80:20) of PEG and CUM during click reaction. Thermal analysis revealed that the clickable polymers exhibited semi-crystalline behavior due to the polyethylene chain between CUM units and polyethylene groups, contributing to enhanced crystallinity, as illustrated in Figure 4.2

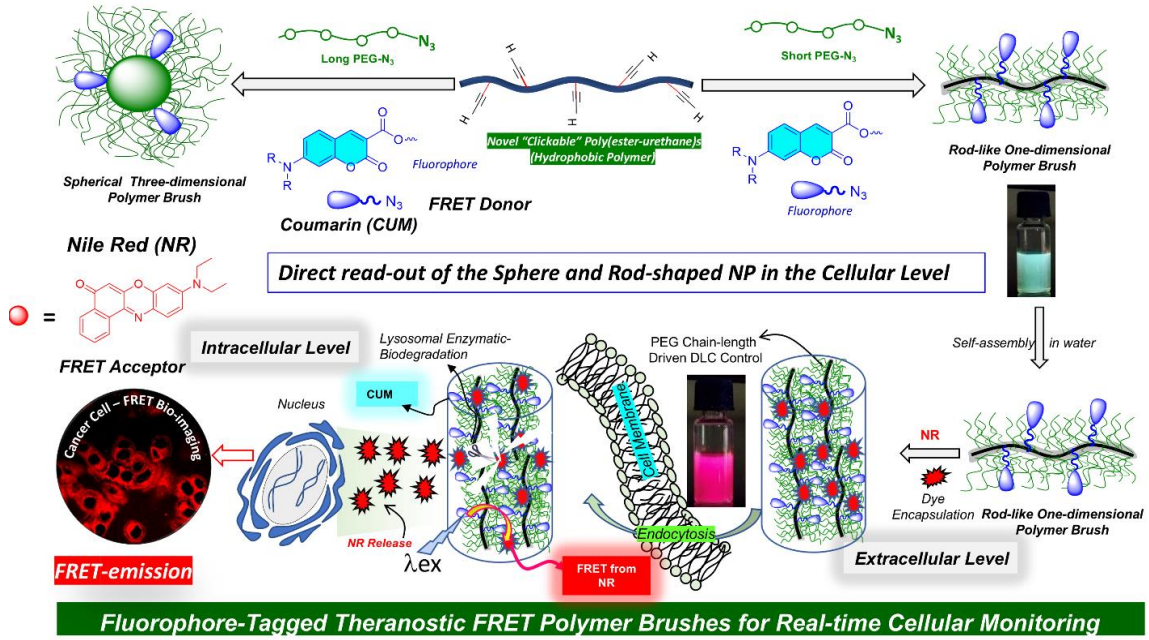

Figure 4.2 *Development of Enzyme-Responsive CUM-Tagged Poly(ester-urethane)s Brushes as Theranostic Fluorescent Probes for Drug Delivery in Cancer Cells*

. The CUM-functionalized polymer brushes self-assembled into nanoparticles (NPs) in water via a dialysis method, encapsulating hydrophobic cargos such as Nile Red (NR), within their nanocavities. Photophysical studies demonstrated FRET-based energy transfer between the CUM and Nile red. In the FRET pair, the CUM acts as a donor, and NR acts as an acceptor. Comprehensive characterization of FRET, including absorbance, emission spectra, and lifetime measurements, confirmed efficient energy transfer. The FRET efficiency, and donor lifetime in the presence and absence of the acceptor were calculated. Enzymatic degradation using horse liver esterase validated the biodegradable nature of the polymer's brushes, showing the enzyme-responsive release of the encapsulated cargo. Biocompatibility assessments revealed that both the polymer brushes and its nanorods and nanoparticles exhibited non-cytotoxic toward normal or cancer cell lines, whereas NR-loaded nanoparticles were also non-toxic to cancer cells as well as normal cell lines. Time-dependent Cellular uptake studies were carried out, and it was found that the indeed the rod-like polymer brush had better uptake as compared to the sphere-like polymer brushes. FRET interactions between CUM and encapsulated cargos were visualized via live cell bioimaging in cancer cells. This study highlights the potential of these biodegradable and biocompatible CUM-tagged poly(ester-urethane)s brushes as advanced nanocarriers for cancer therapy and imaging applications.

4.2 Experimental Section

4.2.1 Materials and Methods

L-Tyrosine, 1,12-dodecane diol, Titanium (IV) butoxide [$Ti(OBu)_4$], polyethylene glycol monomethyl ether (PEG-750, 5000), and 4-(Dimethylamino)pyridine (DMAP), 2,2-Dimethyl-1,3-dioxane-4,6-dione, 4-(Diethylamino)salicylaldehyde, N,N′-Dicyclohexylcarbodiimide (DCC), paraformaldehyde, glycerol, and HPLC-grade dimethyl sulfoxide (DMSO) were obtained from Sigma-Aldrich. Additional reagents including methyl chloroformate, dichloromethane (DCM), propargyl bromide, thionyl chloride, copper sulfate pentahydrate ($CuSO_4 \cdot 5H_2O$), sodium ascorbate, Triton-X, PBS (1×), Nile Red, horse liver esterase enzyme, and 3-(4,5-dimethylthiazol-2-yl)-2,5-diphenyltetrazolium bromide (MTT) were also purchased from Sigma-Aldrich. Other solvents, reagents, and salts were obtained locally and used as received without further purification. Cell culture reagents, including 4% paraformaldehyde, DMEM media with phenol red, 10% (v/v) fetal bovine serum (FBS), 1% (v/v) penicillin-streptomycin, were also obtained from Sigma-Aldrich. The following cancer cell lines were

maintained at 37 °C in a 5% CO_2 atmosphere: human breast cancer (MCF-7) and human embryonic kidney (HEK-293).

4.2.2 General Procedures

The following instruments and procedures were used for the analysis of monomers and polymers NMR Spectroscopy Both 400-MHz Bruker and Bruker Neo 400-MHz spectrometers were utilized to obtain the ^{13}C NMR and ^{1}H NMR spectra. $CDCl_3$ were used as the solvents, and TMS served as the internal standard. Mass Spectrometry The monomer mass was determined using a Biosystems 4800 PLUS MALDI TOF/TOF Analyzer. Size Exclusion Chromatography (SEC): SEC was performed with a Viscotek VE 1122 pump and VE 3580 RI detector using tetrahydrofuran (THF) as the mobile phase and polystyrene as the standard. For SEC analysis in DMF, Agilent PLgel 10 µm MIXED-B columns (7.5 × 300 mm) were used at 70 °C. Thermal Analysis A Perkin Elmer STA 6000 thermal analyzer was used to study the thermal degradation of polymers under a nitrogen atmosphere at a heating rate of 10 °C/min. Thermal characterization of all polymers was performed with a TAQ20 differential scanning calorimeter (DSC), calibrated using an indium standard. Polymer thermograms were recorded by heating and cooling at 10 °C/min under a nitrogen atmosphere. FT-IR Spectroscopy FT-IR spectra were recorded using a Bruker AlphaT Fourier-transform infrared spectrophotometer. PerkinElmer Lambda 45 UV-vis spectrophotometer provided the absorption spectra as well as SPEX Fluorolog HORIBA JOBIN VYON fluorescence spectrophotometer (with excitation source 420 W Xe lamp and double gating 0.22 m Spex 1680 monochromator) provided the fluorescence spectra for dye and drug-loaded polymers respectively. Dynamic Light Scattering (DLS) A Malvern Instruments Nano ZS-90 device equipped with a 633 nm red laser was used for DLS measurements. High-resolution transmission electron microscopy (HR-TEM) images were captured with a Zeiss UltraPlus HR-TEM. Samples were drop-casted onto a Copper grid. Atomic Force Microscopy (AFM) AFM images were taken using a Veeco Nanoscope IV in tapping mode. Samples were drop-cast on mica sheets. Confocal Microscopy Confocal microscopic analysis was performed using a Leica SP8 (or Zeiss LSM 710) microscope.

4.2.3 7-(diethylamino)-2-oxo-2H-chromene-3-carboxylic acid

An aldehyde (5 g, 0.0258 moles) was dissolved in 100 mL of ethanol in a clean 250 mL one-neck round-bottom flask. To this solution, Meldrum's acid (6.6 g, 0.0460 moles) was added, followed by the addition of piperidine (11.6 g, 13.5 mL, 0.1371 moles). Acetic acid (175 µL) was then introduced dropwise into the reaction mixture at room temperature. Once all the

reagents were added, the mixture was refluxed for 4 hours, with the reaction progress monitored by thin-layer chromatography (TLC). After completion, excess ethanol was removed using a rotary evaporator. The residue was treated with 100 mL of ice-cold water, resulting in the formation of a black solid, which was separated by filtration. The filtrate was acidified with 1 N HCl, leading to the precipitation of a yellow solid. This precipitate was collected using a Büchner funnel, yielding a yellow product that was confirmed by ^{1}H NMR analysis. Yield = 74 % 5 g. ^{1}H NMR (400 MHz, CHLOROFORM-*d*) δ ppm 1.25 - 1.29 (t, 6 H), 3.47 - 3.52 (q, 4 H), 6.54 (s, *J*=2.45 Hz, 1 H) 6.70 - 6.73 (dd, 1 H) 7.45-7.47 (dd, 1 H) 8.66 (s, 1 H). ^{13}C NMR (100 MHz, $CDCl_3$) δ 12.44, 45.16, 49.95, 63.38, 96.74, 107.66, 109.65, 131.30, 149.58, 153.17, 158.08, 158.63, 163.53. HRMS (ESI): m/z [M + H] calcd for $C_{14}H_{15}NO_4$, found 262.1079.

4.2.4 2-aminoethyl 7-(diethylamino)-2-oxo-2H-chromene-3-carboxylate

Coumarin acid (1 g, 0.00382 moles) was dissolved in 20 mL of dry dichloromethane (DCM) in a clean 50 mL two-neck round-bottom flask. Once the coumarin acid had completely dissolved, N,N′-Dicyclohexylcarbodiimide (DCC, 0.94 g, 0.00459 moles) was added to the solution, followed by 4-dimethylaminopyridine (DMAP, 0.46 g, 0.00382 moles). After ensuring all reagents were well-dissolved, azido ethanol (0.39 g, 0.0045 moles) was introduced to the reaction mixture under a nitrogen atmosphere. The reaction mixture was stirred at room temperature for 24 hours. The resulting product was purified using column chromatography with a solvent system of petroleum ether and ethyl acetate (70:30 v/v). Yield = 57 % 0.8 g. ^{1}H NMR (400 MHz, CHLOROFORM-*d*) δ ppm 1.24 – 1.26 (t, 6H) 3.42-3.48 (q, 4 H) 3.60 (t, 2 H) 4.47 (t, 2 H) 6.46 (d, *J*=2.45 Hz, 1 H) 6.60-6.63 (dd, *J*=8.93, 2.57 Hz, 1 H) 7.35-7.37 (d, *J*=9.05 Hz, 1 H) 8.46 (s, 1H) ^{13}C NMR (100 MHz, CHLOROFORM-*d*) δ ppm 163.53, 158.63, 158.08, 153.17, 131.30, 131.13, 109.65, 107.66, 96.74, 63.38, 49.95, 45.16, 12.44. FTIR. 2967, 2100, 1748, 1612, 1589, 1517, 1412, 1344, 1158, 1107, 830. HRMS (ESI): m/z [M + H] calcd for $C_{16}H_{18}N_4O_4$, found 331.1406.

4.2.5 Click reaction P-Tyr-PEG-750 CUM

P-Tyr polymer (100 mg, 0.234 mmol), PEG-750-N_3 (145 mg, 0.187 mmol), and CUM-Azide (16 mg, 0.046 mmol) were placed in a clean polymer tube. To this, 5 mL of HPLC-grade dimethyl sulfoxide (DMSO) was added, and the contents were stirred until fully dissolved. Copper sulfate (29 mg, 0.117 mmol) was then added to the mixture, followed by sodium ascorbate (46 mg, 0.234 mmol). The reaction mixture was maintained at 70 °C with stirring for 24 hours. The product was purified using a dialysis method with a 3.5 kDa membrane for 24

hours, followed by lyophilization to obtain the final pure product. Yield= 88 % ^{1}H NMR (400 MHz, CHLOROFORM-*d*) δ ppm 1.26-1.29 (m, *J*=10.07 Hz, 18 H) 1.59 - 1.60 (m, 5 H) 3.03 (d, *J*=4.12 Hz, 2 H) 3.38 (s, 2.40 H) 3.47 - 3.90 (m, 46 H) 4.03 - 4.09 (m, 4 H) 4.55 (d, *J*=5.50 Hz, 3 H) 4.76 (br. s., 1 H) 5.17 (br. s., 3 H) 6.46 (br. s., 0.20 H) 6.62 (dd., 0.20 H) 6.91 (d, *J*=8.24 Hz, 2 H) 7.04 (d, *J*=7.79 Hz, 2 H) 7.35 (d, 0.20 H) 7.83 (br. s., 0.80 H) 8.28 (br. s., 0.20 H) 8.43 (br. s., 0.20 H). 172, 158, 156, 131, 130, 115, 110, 72, 71, 70, 69, 66. 65, 62, 59, 55, 50, 45, 38, 29, 28, 26, 12. ^{13}C NMR (100 MHz, CHLOROFORM-*d*) δ ppm 12.73, 26.12, 28.04 - 31.14, 37.75, 45.47, 50.64, 55.08, 59.30, 62.29, 64.69 - 67.02, 68.57 - 71.28, 110.11, 115.14, 128.49 - 131.59, 156.32, 157.74, 172.10. FTIR 2857, 2850, 1716, 1609, 1588, 1515, 1463, 1344, 1234, 1223, 1089, 939, 855.

4.2.6 P-Tyr-PEG-5000 CUM

P-Tyr polymer (100 mg, 0.234 mmol), PEG-5000-N_3 (941 mg, 0.187 mmol), and CUM-Azide (16 mg, 0.046 mmol) were placed in a clean polymer tube. To this, 5 mL of HPLC-grade dimethyl sulfoxide (DMSO) was added, and the contents were stirred until fully dissolved. Copper sulfate (29 mg, 0.117 mmol) was then introduced to the mixture, followed by sodium ascorbate (46 mg, 0.234 mmol). The reaction was maintained at 70°C with stirring for 24 hours. The product was purified using a dialysis method with a 3.5 kDa membrane for 24 hours, followed by lyophilization to obtain the final pure product. Yield =85 % ^{1}H NMR (400 MHz, CHLOROFORM-*d*) δ ppm 1.26-1.29 (m, *J*=10.07 Hz, 18 H) 1.59 - 1.60 (m, 5 H) 3.03 (d, *J*=4.12 Hz, 2 H) 3.38 (s, 2.40 H) 3.47 - 3.90 (m, 46 H) 4.03 - 4.09 (m, 4 H) 4.55 (d, *J*=5.50 Hz, 3 H) 4.76 (br. s., 1 H) 5.17 (br. s., 3 H) 6.46 (br. s., 0.20 H) 6.62 (dd., 0.20 H) 6.91 (d, *J*=8.24 Hz, 2 H) 7.04 (d, *J*=7.79 Hz, 2 H) 7.35 (d, 0.20 H) 7.83 (br. s., 0.80 H) 8.28 (br. s., 0.20 H) 8.43 (br. s., 0.20 H). 172, 158, 156, 131, 130, 115, 110, 72, 71, 70, 69, 66. 65, 62, 59, 55, 50, 45, 38, 29, 28, 26, 12. ^{13}C NMR (100 MHz, CHLOROFORM-*d*) δ ppm 12.73, 26.12, 28.04 - 31.14, 37.75, 45.47, 50.64, 55.08, 59.30, 62.29, 64.69 - 67.02, 68.57 - 71.28, 110.11, 115.14, 128.49 - 131.59, 156.32, 157.74, 172.10. FTIR 2857, 2850, 1716, 1609, 1588, 1515, 1463, 1344, 1234, 1223, 1089, 939, 855.

4.2.7 Self-Assembly

For the solvent evaporation, 5.0 mg of the polymer was dissolved in 0.5 mL of tetrahydrofuran (THF) and mixed with 0.5 mg of Nile Red, dissolved in 0.25 mL of THF. This solution was added dropwise to 5.0 mL of Milli-Q water in a 15 mL vial under constant stirring for 30 minutes at ambient temperature. The mixture was heated in a water bath at 70 °C for 20 minutes

to remove THF. After centrifugation at 8000 rpm for 5 minutes, the unencapsulated drug/dye was filtered out.

4.3 Results and discussion

4.3.1 Synthesis of Coumarin Azide

Synthesis of coumarin derivative fluorescence Monomer (CUM): We have synthesized a novel coumarin fluorophore using a multi-step process. Initially, 4-(Diethylamino) salicylaldehyde was coupled with Meldrum's acid to form coumarin acid, which was subsequently subjected to DCC/DAMP coupling to yield coumarin ester azide (4), as illustrated in Scheme 4.1 The structure of the coumarin acid was confirmed using **^{1}H** NMR spectroscopy (Figure 4.3a).

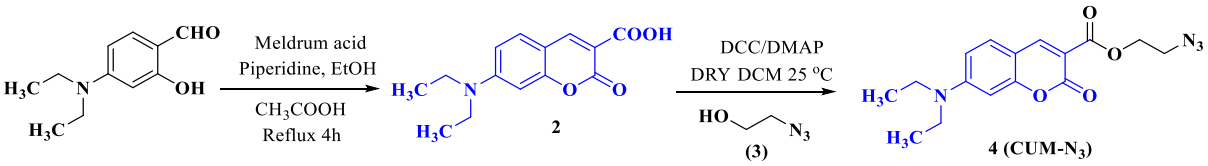

Scheme. 4.1 *Synthesis of Coumarin Azide (CUM-N_3).*

Further, coumarin azide (4) was confirmed by ^{1}H NMR spectrum; as shown in Figure 4.3b. The protons (g+h) coming at 4.73 and 3.60 ppm correspond to the two -O-**CH_2-CH_2-N_3** groups of azido ethanol. And Aromatic ring protons (c+d) were observed at 6.46 and 6.61 ppm and a proton (b) at 7.36 ppm, and a chromone ring proton (a) coming at 8.45 ppm it confirms the formation of CUM azide. Further, the CUM acid and CUM azide was confirmed by ^{13}C NMR and spectra are shown in 4.4a, the CUM acid ^{13}C NMR peak coming at 165 ppm after formation CUM azide the acid peak 165 ppm completely vanished, and other ethanol CH_2 carbons appeared at **49.95** ppm (-O-CH_2-**CH_2-N_3**) and **63.38** ppm (-O-**CH_2**-CH_2-N_3), confirming the successful formation of coumarin azide as shown in Figure 4.4b. FTIR analysis further verified this, with the azide functional group exhibiting a characteristic peak at 2100 cm^{-1}

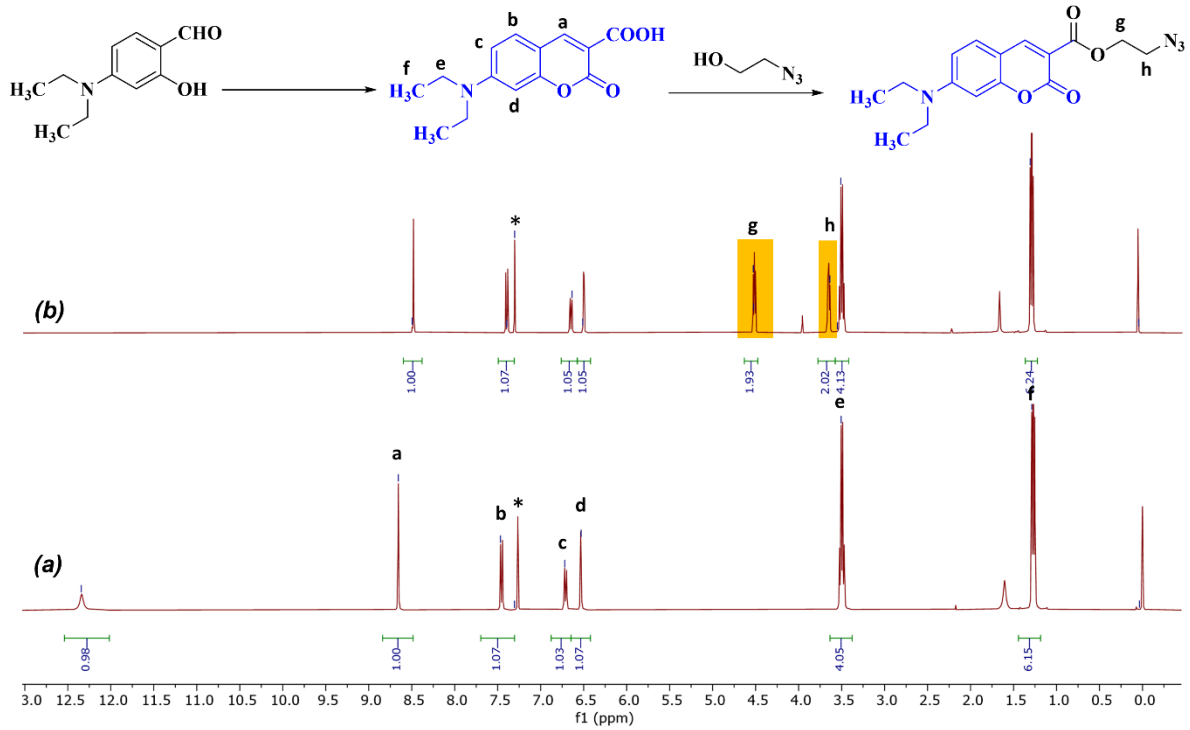

Figure 4.3 *(a) [1]H-NMR spectrum of coumarin acid, (b) [1]H-NMR spectrum of coumarin ester azide. All the spectra were recorded in $CDCl_3$.*

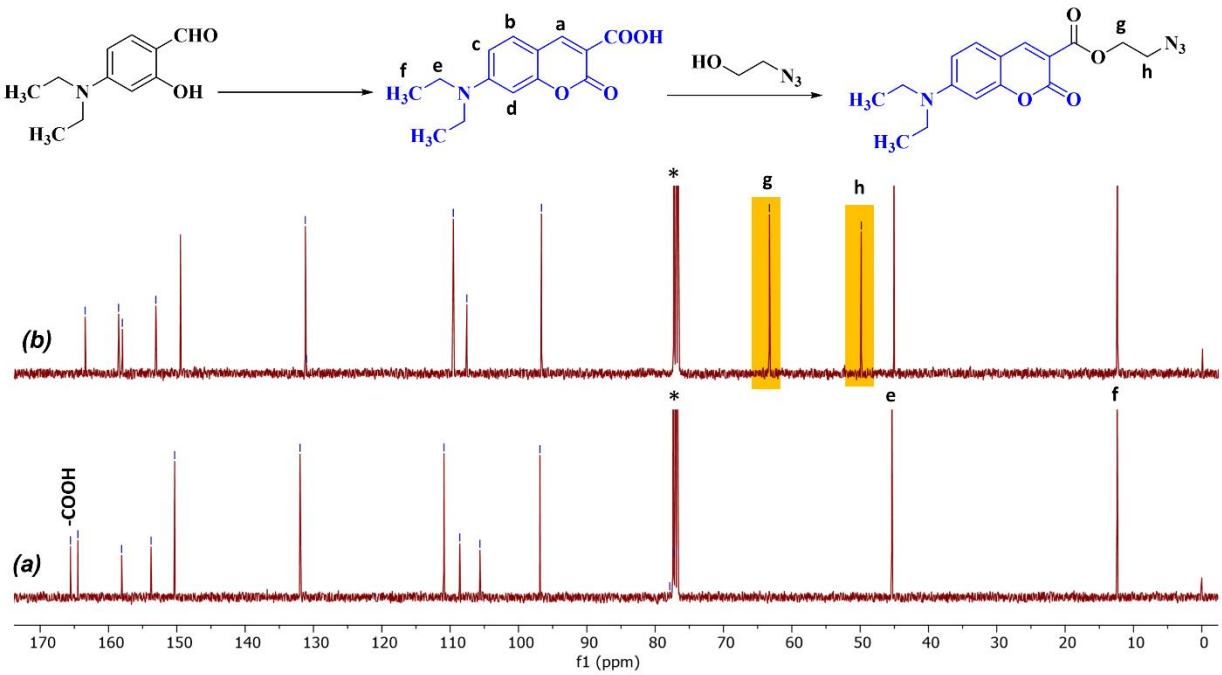

Figure 4.4 *(a) [13]C-NMR spectrum of coumarin acid, (b) [13]C-NMR spectrum of coumarin ester azide. All the spectra were recorded in $CDCl_3$.*

Next, L-Tyrosine was modified to create a multifunctional monomer with methyl ester, urethane, and propargyl-functionalized phenolic hydroxyl groups. NMR confirmed its structure and thermal stability (up to 250 °C), enabling solvent-free melt polymerization with 1,12-dodecanediol (1:1 molar ratio) at 150 °C for 4 hours under nitrogen, using 1 mol% titanium

tetra butoxide as a catalyst. High vacuum (0.01 mbar) produced high molecular weight polymers. ^{1}H-NMR showed polymerization via the disappearance of methoxy protons (3.71–3.66 ppm) and new ester peaks (4.07–4.10 ppm), with the propargyl group (2.5 ppm) remaining inert. ^{13}C-NMR confirmed methoxy-to-ester carbon conversion (52–53 ppm to 62–63 ppm). SEC analysis showed Mn = 18,200 g/mol, Mw = 46,800 g/mol, and Đ = 2.5, validating synthesis precision. Further details about this synthesis and characterization are provided in Chapter 2. Subsequently, polyethylene glycol monomethyl ether azides were taken from second chapter (M_n = 750, 5000) these clickable chains were incorporated using a post-polymerization click chemistry approach. Whereas the CUM-Azide and PEG chains varied the composition 80:20 ratio to get random copolymers with the side chain PEG as well as the hydrophobic CUM group. These copolymers were further purified by dialysis (3.5 kDa membrane) and lyophilized for further use. the copolymer structure is shown in Scheme, 4.2.

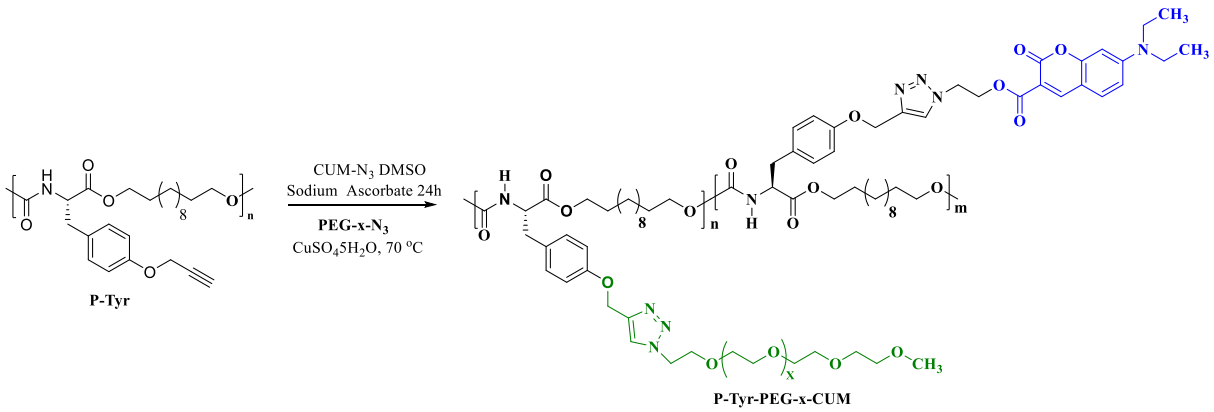

Scheme 4.2. *Synthesis of Random copolymers P-Tyr-PEG-750-CUM using Click chemistry.*

Further, the copolymer was termed as P-Tyr-PEG-750 CUM were characterized by ^{1}H and ^{13}C NMR where the homo polymer P-Tyr the propargyl CH peak coming at 2.5 ppm as shown in Figure 4.5a and after post polymerization, the propargyl CH peak completely vanish, and a new peak were appeared at 7.83 ppm corresponding to (triazole aromatic-**CH**) and the spectra were shown in Figure 4.5b. Coumarin protons are showed in the zoom spectrum whereas due to very small amount of CUM incorporation in the polymer that's why the peak intensity was less. The appeared protons region between 6.62 and 8.43 ppm with integrals corresponding to 0.20 for each proton. In comparison, the methoxy proton at 3.38 ppm had an integral of 2.40 ppm, indicating the successful incorporation of PEG (80%) and coumarin (20%) chains, as

shown in Figure 4.5b. Similarly, the other polymer P-Tyr-PEG-5000 CUM 1H NMR spectra are shown in Appendix Figure S25.

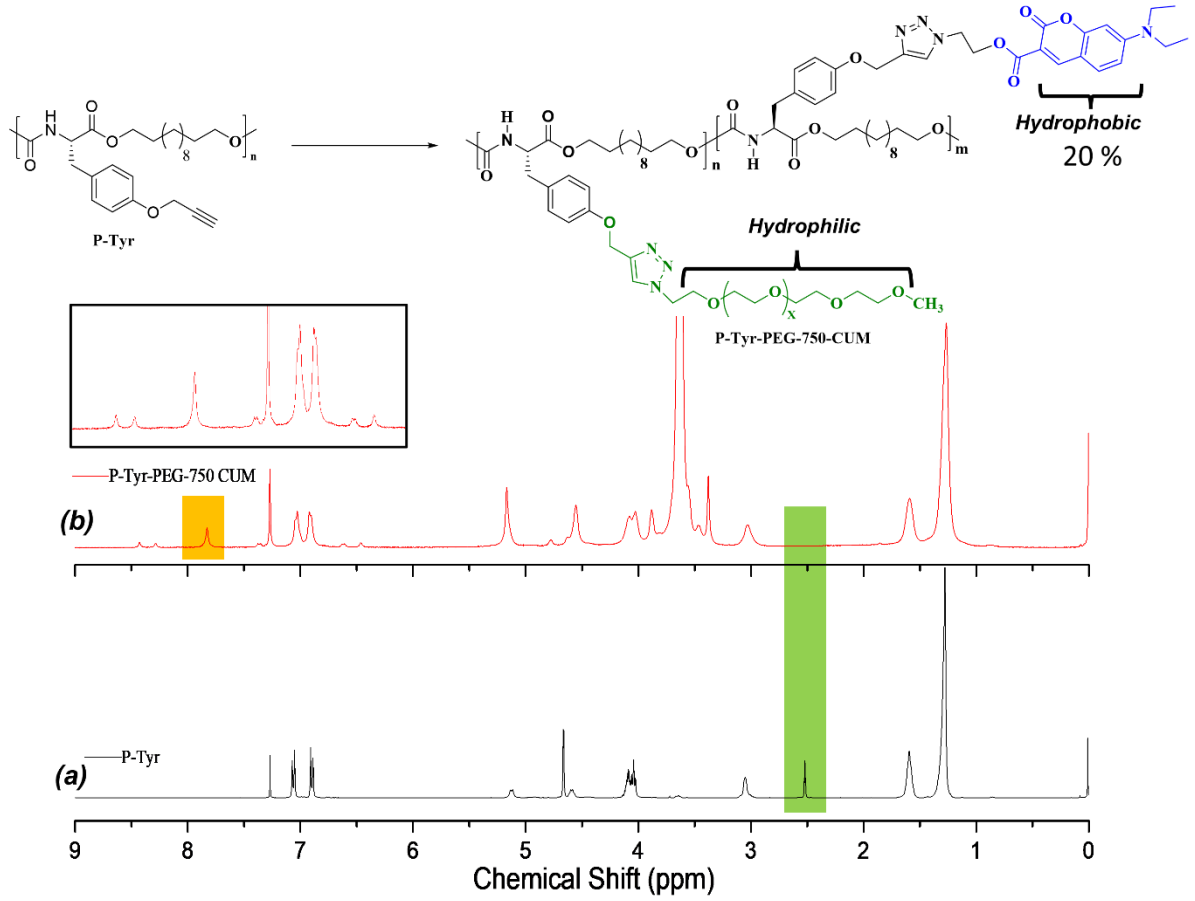

Figure 4.5 *(a) ^{1}H-NMR spectrum of homo polymer P-Tyr, (b) random copolymer P-Tyr-PEG-750 CUM. All the spectra were recorded in $CDCl_3$.*

Subsequently, the random copolymers were analyzed via size-exclusion chromatography (SEC). The chromatograms showed peaks shifted to lower retention times and exhibited monomodal distributions, confirming the successful formation of random copolymers, and the SEC chromatographs are shown in (Figure 4.6a). The number-average molecular weight (M_n) was determined to be 33,000 g/mol for P-Tyr-PEG-750 and 43,000 g/mol for P-Tyr-PEG-5000, as shown in (Figure 4.6b Table 1).

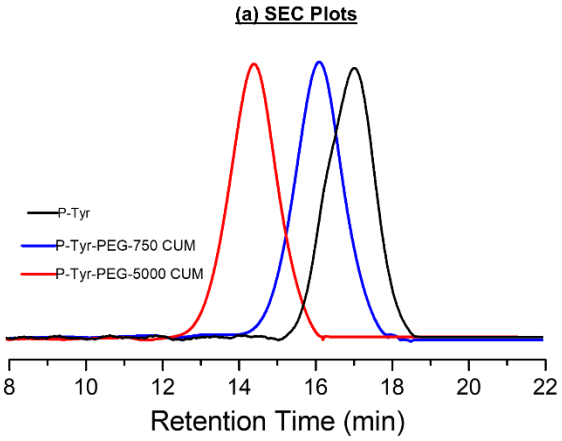

(b) Table containing the molecular weights of the Polymers

Sample	^{1}H-NMR[a] M_n (g/mol)	SEC RI Detector[b] M_n (g/mol)	M_w (g/mol)	Đ
P-Tyr	17000	15500	35000	2.2
P-Tyr-PEG-750-CUM	47000	31900	90000	2.8
PTyr-PEG-5000-CUM	217000	42000	125000	3.0

[a)]^{1}H-NMR NMR molecular weights are calculated using the expression: M_n = (DP × repeating unit mass). [b)]Number (M_n) and weight average molecular weight (M_w), and dispersity (Đ) were determined by size exclusion chromatography in DMF at 70 °C using RI detector.

Figure 4.6. *(a) Size exclusion chromatograms of polymers in DMF. (b) The table contains the molecular weight of the polymer by NMR and SEC.*

4.3.2 Thermal properties of polymers

thermogravimetric analysis (TGA) of random copolymers was conducted, and it revealed all the polymers are stable up to 350 °C as shown in (Figure 4.7a). The robustness of the click reaction was further confirmed by FTIR analysis, where the characteristic azide peak at 2100 cm^{-1} completely vanished, and it confirms the robustness of click reaction (see Figure 4.7b). Differential scanning calorimetry (DSC) showed amorphous behavior of homo polymer (Tg = −4 °C). and the random copolymer P-Tyr-PEG-750 CUM also shows amorphous in nature and their DSC thermograms, are shown in Figure 4.8a. The polymer showed (ΔHm=0.85) as shown in Figure 4.9a, and while the P-Tyr-PEG-5000 CUM shows semicrystalline behaviour (ΔHm = 68), and thermograms are shown in Figure 4.8b. the DSC properties of ΔH_m and ΔH_c are shown in Figure 4.9a.

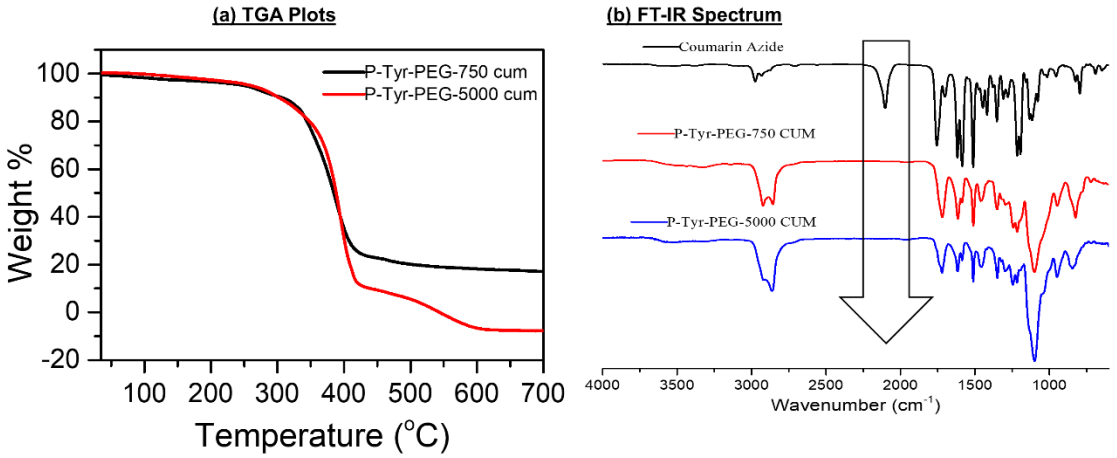

Figure 4.7. *(a) TGA thermograms of polymers. TGA was performed at 10 °/min under N_2 atmosphere. (b) FT-IR spectra of CUM, PEG azide and their Clickable polymer.*

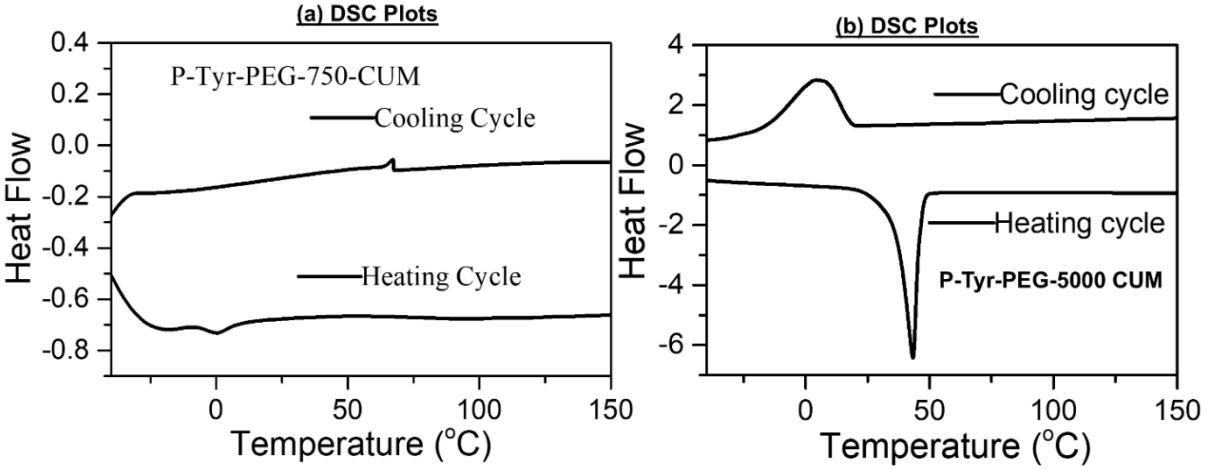

Figure 4.8 *(a) DSC thermograms of the P-Tyr-PEG-750 CUM polymers recorded at 10 °/min under nitrogen atmosphere. (b) DSC thermograms of the P-Tyr-PEG-5000 CUM polymers were recorded at 10/min under a nitrogen atmosphere.*

These amphiphilic random copolymers exhibit potential for thermoplastic and biomedical applications. Powder X-ray diffraction (PXRD) analysis was conducted on the polymer samples, and their diffraction patterns are shown in Figure 4.9b. P-Tyr and P-Tyr-PEG-750 displayed broad diffraction patterns centered around 4.52 Å, which is consistent with their highly amorphous nature as seen in the DSC profiles. In contrast, the longer-chain PEGylated polymers, P-Tyr-PEG-2000 and P-Tyr-PEG-5000, demonstrated side-chain crystallization. This was evidenced by two distinct peaks at 4.66 Å and 3.94 Å, which correspond to PEG chain crystallization and align with the findings from the DSC analysis.

(a) Table containing the thermal stability of Polymers

Sample	T_D[a] (°C)	T_g[b] (°C)	T_m[c] (°C)	ΔH_m[d] (J/g)	T_c[e] (°C)	ΔH_c[f] (J/g)
P-Tyr	315	-4.0	-	-	-	-
P-Tyr-PEG-750 CUM	328	-	0.85	0.47		0.13
P-Tyr-PEG-5000 CUM	328	-	43	82.26		66.55

a) Temperature of decomposition (Td) determined from TGA. [b] The glass transition temperature (Tg) was determined from second heating cycle of DSC thermogram. [c] Melting point (Tm) of the polyester determined heating cycle. [d] Enthalpy of melting determined from area under the curve of heating cycle. [e] Temperature of crystallization (Tc) of the polyester determined cooling cycle. [f] Enthalpy of crystallization determined from area under the curve of cooling cycle of the of DSC thermogram.

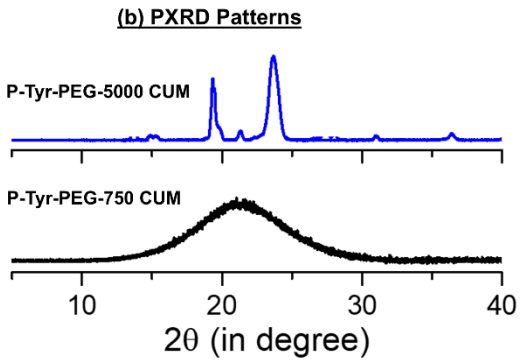

Figure 4.9 *(a) containing the thermal stability of Polymers. (b) PXRD patterns of the polymers were recorded in dry powder sample at 25 ℃.*

4.3.3 Aqueous Self-Assembly

confirming their amphiphilic nature. This amphiphilicity enables self-assembly, studied in water and DMSO (3:2 v/v). The detailed procedure is shown in the experimental section. The water contact angle of the polymers was measured by drop-casting on glass slides. The homopolymers showed a water contact angle of 78° as shown in our second chapter indicating hydrophobicity. After the click reaction, the random copolymers displayed reduced water contact angles 60° for P-Tyr-PEG-750-CUM and 15° for P-Tyr-PEG-5000-CUM, as shown in Figure 4.10a.

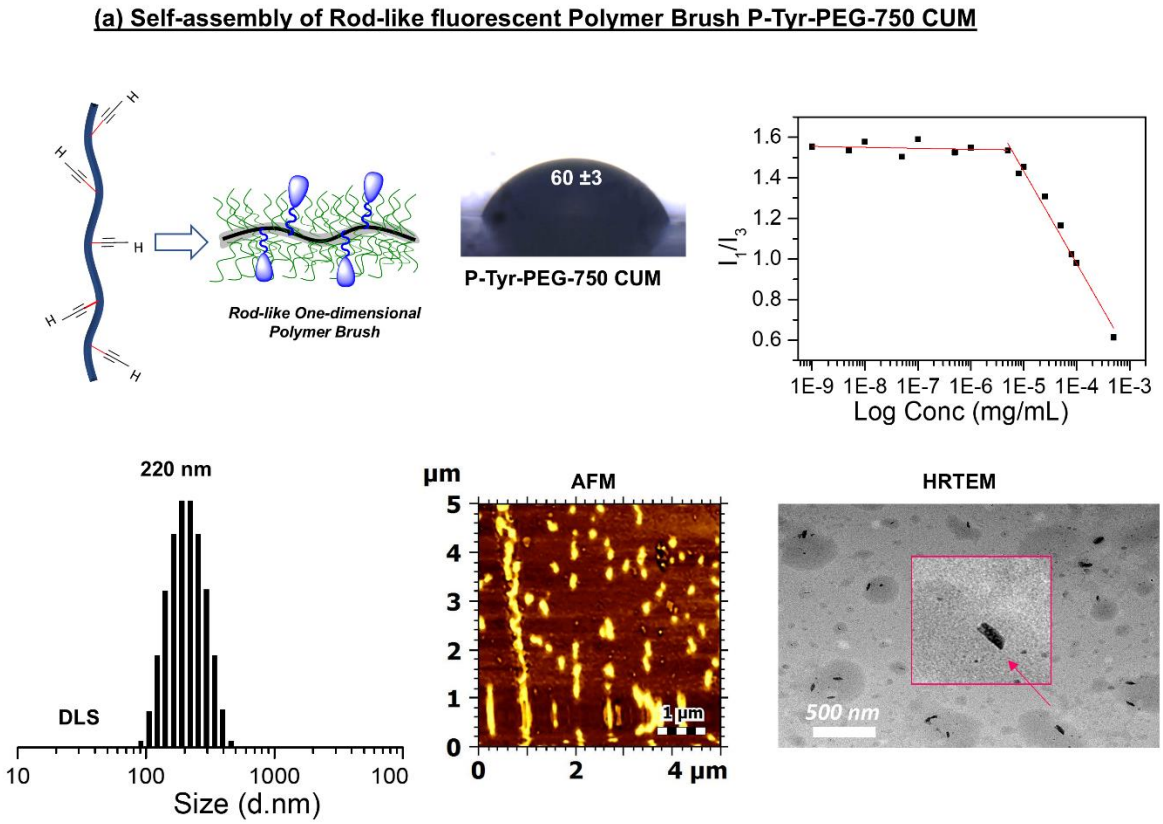

Figure 4.10 *(a) Schematic aqueous Self-assembly of P-Tyr-PEG-750 CUM polymer brush, and the photographs show the water contact angle (LB-ADSA method) recorded for the polymer brush drop-caste film on glass substrate. DLS histogram and Critical aggregation concentration (CAC) was determined by pyrene-probe. P-Tyr-G brush characterization by AFM, and HR-TEM images.*

The critical micellar concentration (CMC) of the self-assembled polymers P-Tyr-PEG-750 CUM was determined using pyrene as a fluorescent probe. Pyrene was fixed at 0.6 µM, while polymer concentrations varied from 0.5 mg/mL to 1 mg/mL. Excitation was performed at 337 nm, and emissions were recorded between 347–500 nm (emission spectra are shown in

Figure 4.11a). The CMC was found to be 5 µg/mL for P-Tyr-PEG-750-CUM, and the spectra are shown in Figure 4.10a.

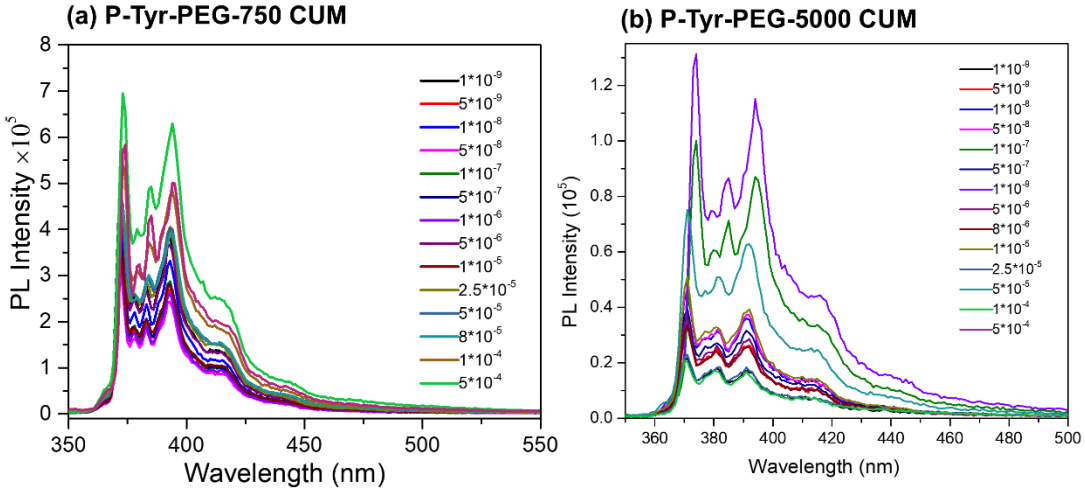

Figure 4.11. *Pyrene emission spectra for CMC determination. Pyrene chromophore was excited at λEx= 337nm and emission was collected from 350-500 nm. (a) P-Tyr-PEG-750 CUM, (b) P-Tyr-PEG-750 CUM.*

Dynamic light scattering (DLS) revealed that the P-Tyr-PEG-750-CUM formed assemblies with a hydrodynamic size of 220 nm, and the histogram is shown in Figure 4.10a. To study the morphology, of the polymers P-Tyr-PEG-750 CUM were drop-cast on mica sheets (0.1 mg/mL) and analyzed by atomic force microscopy (AFM). AFM images revealed that the smaller PEG chains formed rod-like morphologies, and their images are shown in Figure 4.10a, the sizes of the rod 250 nm. High-resolution transmission electron microscopy (HR-TEM) was also employed P-Tyr-PEG-750 CUM Polymer brush was drop-cast on copper grids (0.1 mg/mL) and dried. HR-TEM images showed rod-like fluorescent polymer brushes with sizes of 220 nm in the shorter PEG chains, as shown in Figure 4.10a. Further, the longer PEG chain P-Tyr-PEG-5000 CUM self-assembly schematic representation see Figure 4.12a. Further, the breaking point confirms the CMC of the P-Tyr-PEG-5000 CUM polymer brush was found to be 100 µg/mL, and the plot is shown in Figure 4.12b, and their emission spectra are shown in Figure 4.11b. performed DLS measurement, and it formed smaller nano assemblies with sizes 60 nm; the DLS histogram is shown in Figure 4.12b. While with longer PEG chains, P-Tyr-PEG-5000 CUM polymer brushes formed sphere-like structures in AFM and sizes 70 nm, and images were shown in Figure 4.12b;

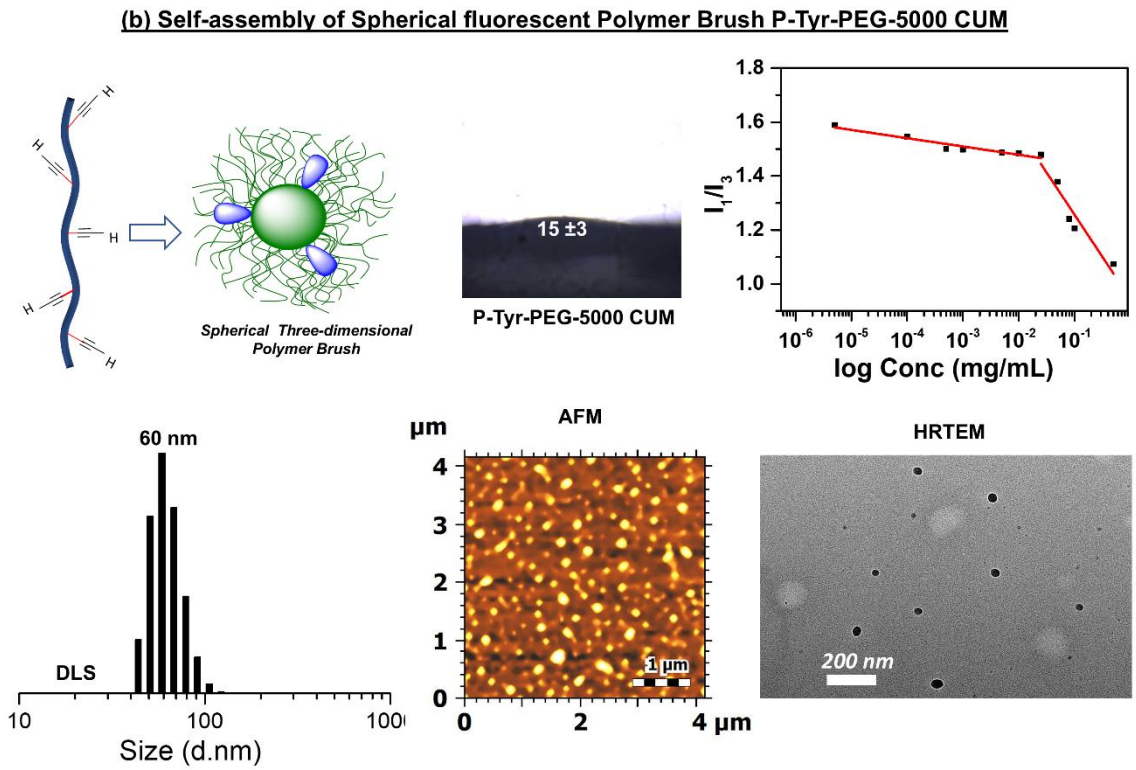

Figure 4.12 *(a) Schematic aqueous Self-assembly of P-Tyr-PEG-5000 CUM polymer brush, and the photographs show the water contact angle (LB-ADSA method) recorded for the polymer brush drop-caste film on glass substrate. DLS histogram and Critical aggregation concentration (CAC) was determined by pyrene-probe. P-Tyr-G brush characterization by AFM, and HR-TEM images.*

Further, the polymer was drop cast on a copper grid, and samples were recorded for their sizes 60 nm, and their HR-TEM images are shown in Figure 4.10b. consistent with our earlier reports, with the shorter PEG chain forming rod-like polymer brushes and the longer PEG chain forming sphere-like polymer brushes.

4.3.4 Encapsulation capabilities

The encapsulation capabilities of P-Tyr-PEG-CUM were evaluated for water-insoluble dye, such as Nile Red (NR). Using a dialysis method, 5 mg of florescent polymer brushes and 0.5 mg of dye/drug were dissolved in 2 mL HPLC grade DMSO, and 3 mL of Mili Q water was added slowly and stirred for 4h at 25 °C. Subsequently, this solution was transferred into the dialysis membrane 3.5 kDa MWCO and dialyzed against Mili Q for 48 hours. The polymer brushes successfully encapsulated commercial dyes, such as Nile Red (NR). The drug loading content efficiency varied depending on the morphology of the polymer brushes: rods achieved 2 % NR loading, while spheres achieved 1 % NR loading. The encapsulated dye/drug UV photographs are captured as shown in Figure 4.13a. Dynamic light scattering (DLS) analysis

of the dye/drug-loaded polymer brushes revealed sizes consistent with those of the nascent polymer brushes, sizes 220 nm and 65 nm and DLS histograms are shown in Figures 4.13b and 4.13c, indicating minimal structural changes during encapsulation. The drug loading capabilities (DLC) were calculated and shown in the table Figure 4.13d. Photophysical properties of the loaded samples were also assessed, demonstrating no significant alterations before and after encapsulation. Nile Red, due to its high molar extinction coefficient (38,000 M^{-1} cm^{-1}) and decent quantum yield ($\phi = 0.018$), NR is well-suited for bioimaging applications.

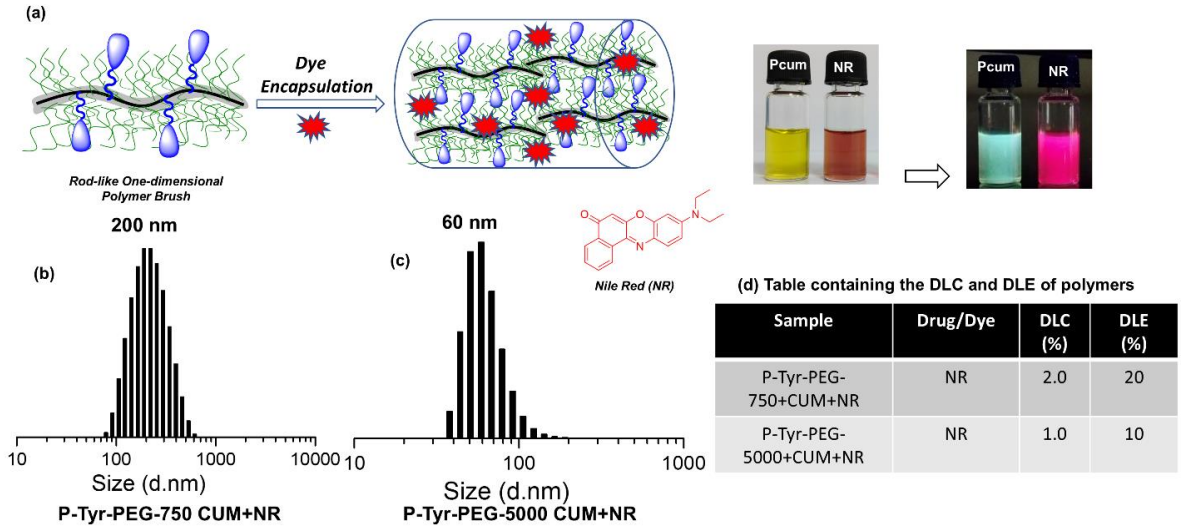

(d) Table containing the DLC and DLE of polymers

Sample	Drug/Dye	DLC (%)	DLE (%)
P-Tyr-PEG-750+CUM+NR	NR	2.0	20
P-Tyr-PEG-5000+CUM+NR	NR	1.0	10

Figure 4.13*.(a) Schematic representation of drug encapsulation Photograph of Drug/dye encapsulation, (b) DLS histogram of P-Tyr-PEG-750 CUM+NR and (c) P-Tyr-PEG-5000 CUM+NR. (d) Table containing the DLC and DLE.*

4.3.5 FRET probe based on NR and Coumarin polymer

Fluorescence Resonance Energy Transfer (FRET) between donor and acceptor fluorophores is a powerful yet challenging tool for cellular imaging in cancer treatment. In this context, a novel FRET probe was developed using a Coumarin-tagged L-tyrosine polymer brush nano scaffold for loading NR. After successful loading, efforts were directed toward constructing a FRET system between the Coumarin donor and NR acceptor for bioimaging applications. 0.1 OD concentration of polymer brushes P-Tyr-PEG-750 CUM were prepared and recorded their absorbance spectra, and similarly loaded samples were also prepared at 0.1 OD and for NR reference non-fluorescent polymer P-Tyr-PEG-750 were encapsulated NR and that polymer

brush was used for same OD concentration and the absorbance spectra are shown in Figure 4.14a.

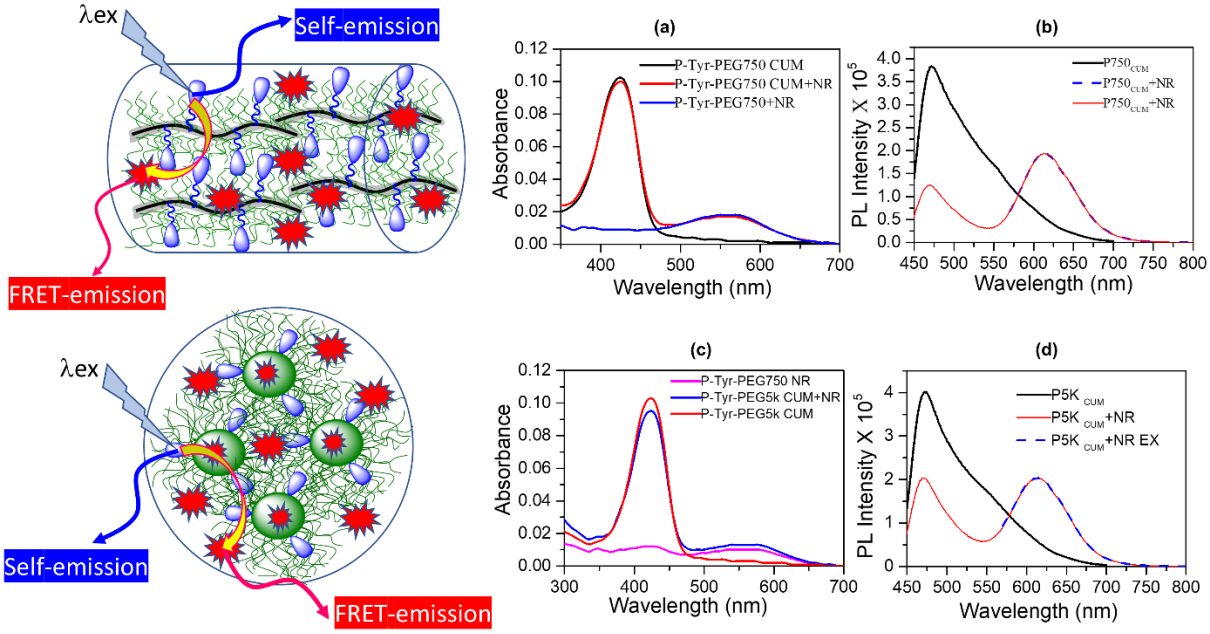

Figure 4.14 *(a) Absorbance spectra of P-Tyr-PEG-750 CUM and NR loaded polymer. (b) Emission spectra of P-Tyr-PEG-750 CUM and NR loaded polymer. (c) Absorbance spectra of P-Tyr-PEG-5000 CUM and NR loaded polymer. (d) Emission spectra of P-Tyr-PEG-5000 CUM and NR loaded polymer.*

same 0.1 OD polymer brushes were prepared that polymer P-Tyr-PEG-750 CUM were recorded their emission spectra for that the CUM were excited at 430 nm, and their emission was collected up to 440-600 nm. Whereas the NR-loaded P-Tyr-PEG-750 CUM+NR were excited at 430 nm and emission collected from 440-700 nm, in this case, we observe the CUM intensity was drastically decreased. The energy was transferred to the Acceptor molecule NR, confirming the FRET was happening with the donor molecule (CUM) and acceptor molecule (Nile Red). Spectra are shown in Figure 4.14b; 80 % of energy was transferred to the acceptor molecules. Further, the Nile red was excited at 561 nm, and emission was collected from 571-700 nm. The spectra are shown in Figure 4.14b. Further, the P-Tyr-PEG-5000 CUM and NR-loaded polymer brushes were prepared at 0.1 OD concentration and recorded their absorbance spectra are shown in Figure 4.14c. Similarly, P-Tyr-PEG-5000 CUM sample and NR loaded polymer brushes were recorded their emission spectra for that CUM was excited at 430 nm and emission spectra were collected up to 700 nm and found that the CUM self-intensity was decreased 50 % and the energy was transferred to accepter molecule NR confirms the FRET and spectra are shown in Figure 4.14d. The schematic energy diagram illustrates the FRET process between the CUM donor and the Nile Red (NR) acceptor. Upon selective photoexcitation at 430 nm, the excitation energy of CUM can follow two pathways: (i) radiative

self-emission by the CUM chromophores, producing blue fluorescence in the range of 440–525 nm, and (ii) energy transfer from CUM to NR via the FRET mechanism, resulting in red fluorescence emission from NR at 600 nm. In the second pathway, the blue emission from the CUM chromophores is expected to diminish or disappear due to the transfer of excitation energy to NR see figure 4.15a. whereas, the feasibility of FRET was evaluated by calculating the overlap integral between the emission spectrum of the donor (CUM) and the absorption spectrum of the acceptor (NR). Overlap spectra are shown in Figure 4.15b. The efficiency of the FRET process was estimated to exceed 80 % in the presence of a rod and 60 % efficiency in the presence of a sphere, indicating a highly efficient energy transfer.

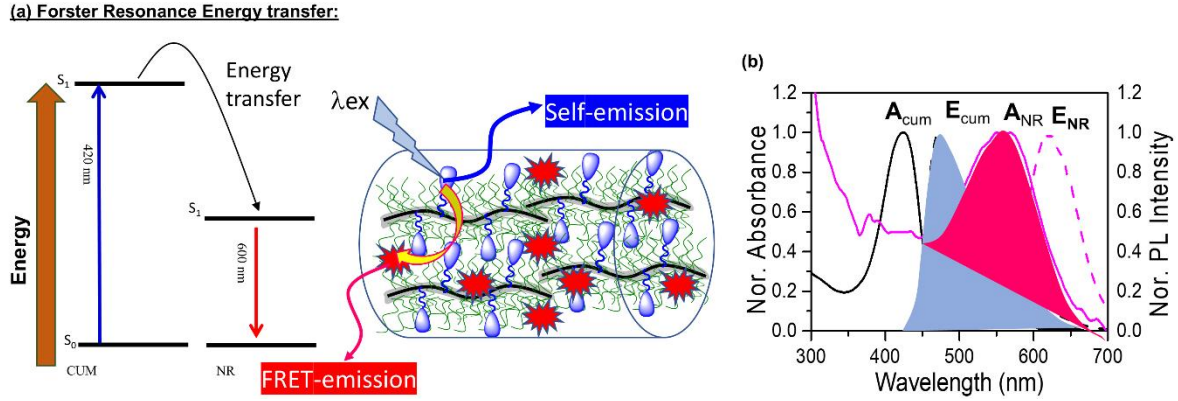

Figure 4.15 *(a) Energy diagram for the FRET process. (b) Overlap integral between the emission spectra of CUM and absorbance spectra of NR.*

TCSPC fluorescence decay profiles of CUM chromophore nanoparticle using 375 nm LED source for TCSPC in the nascent polymer P-Tyr-PEG750-CUM and in the presence of the FRET acceptor NR (in the P-Tyr-PEG750-CUM+NR sample) and P-Tyr-PEG-5k+NR were recorded (see Figure 4.17a and 4.16b). As anticipated, the fluorescence intensities of CUM decayed more rapidly in the presence of NR.

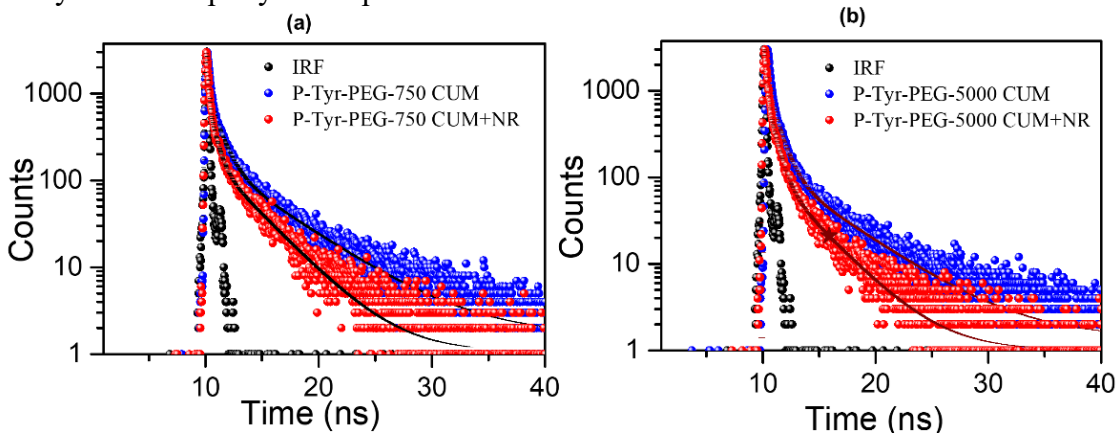

Figure 4.16 *(a) TCSPC decay profile of P-Tyr-PEG-750-CUM and P-Tyr-PEG-750-CUM+NR LED used 375 nm and emission collected at 510 nm (Concentration of CUM =0.1 OD). (b) TCSPC decay profile of P-Tyr-PEG-5000-CUM and P-Tyr-PEG-5000-CUM+NR LED used 375 nm and emission collected at 510 nm (Concentration of CUM =0.1 OD).*

The Förster distance between the donor and acceptor is a critical factor for achieving efficient FRET, as described by the equations in $E_{FRET} = (R_0^6) / [R_0^6 + R^6]$. The FRET efficiency is expressed as: where R and R_0 value the R_0 value of CUM is already reported,[37] the distance between the donor and acceptor molecules, and the Förster distance at which FRET efficiency is 50%. The FRET efficiency can also be determined using the donor fluorescence lifetimes, with the equation: $E = 1-[\tau_{DA}/\tau_D]$ is the lifetime of the donor molecule τ_D alone, and τ_{DA} is the lifetime of the donor in the presence of the acceptor. These values were calculated through detailed analysis, with the method provided in **Table 4.1.**

Table 4.1 *containing the FRET D and* D_A *details*

Sample	J (λ) (M^{-1} cm^{-1} nm^4	R_0 (Å)	τ_D (ns)	τ_{DA} (ns)	E_{FRET}	R (Å)
P-Tyr-P750	J (λ)= 3.54 × 10^{15}	39	3.84	2.39	0.38	44.2
P-Tyr-P5k	J (λ)= 3.54 × 10^{15}	39	4.11	2.80	0.32	42.3

were found to be 39 Å and 44.2 Å, respectively (see table 4.1), both of which are well below the 50 Å cutoff for efficient FRET. The FRET efficiency was estimated to be 38 %, with P-Tyr-PEG750+NR and P-Tyr-PEG-5k+NR estimated at 32 %, clearly demonstrating the efficient FRET process between the CUM chromophore and the encapsulated NR fluorophore within the L-tyrosine polymer brushes domain see table 4.1. Based on these detailed photophysical studies and energy calculations, it can be concluded that the newly designed CUM-tagged L-tyrosine polymer brushes provides the ideal nanoparticle geometry for an efficient FRET probe utilizing the CUM–NR donor–acceptor pair.

4.3.6 Release Kinetics studies

The schematic diagram of the endocytosis process is shown in Figure 4.17a. Release kinetics studies in the experiment, NR-loaded polymer brushes were combined with 10 U of esterase enzyme in a 3.5 kDa molecular weight cutoff (MWCO) dialysis membrane and incubated in 1X PBS at 37 °C. A control experiment without the enzyme was performed under the same conditions. Aliquots were collected at various time intervals, and absorbance spectra were recorded to quantify drug release. The results, plotted as polymer concentration versus cumulative drug release, are shown in Figure 4.17b. Enzyme-mediated degradation resulted in 90% drug release within 24 hours, compared to only 25% release in the absence of the enzyme, confirming that drug release followed an enzymatic pathway.

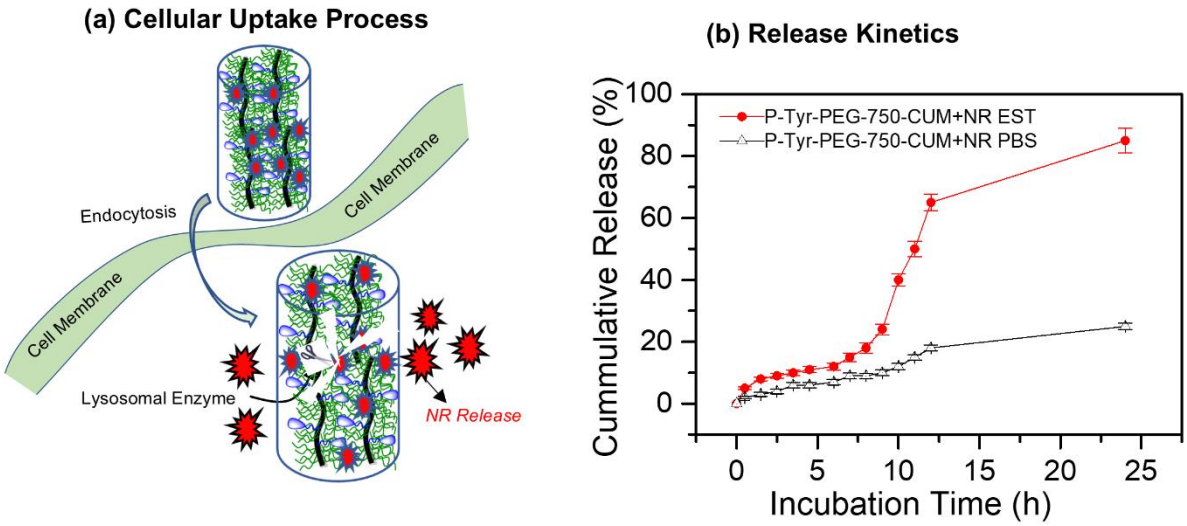

Figure 4.17 *(a) Schematic representation of rod-like polymer brush uptake in the cells and enzyme-biodegradation for NR release in the lysosomal compartment. (b) Cumulative drug release profiles of NR-loaded P-Tyr-PEG-750 sample in the presence of horse-liver esterase enzyme 10 U in PBS, pH 7.4 at 37°C. Drug release profiles of NR-loaded P-Tyr-PEG-750 samples in the absence of enzyme in PBS, pH 7.4 at 37°C.*

4.3.7 Hemolysis assay

To evaluate the hemolytic potential of the polymer samples, a hemolysis assay was conducted in which red blood cells (RBCs) were incubated with the polymer solution in phosphate-buffered saline (PBS), followed by centrifugation to separate the RBCs. In the absence of hemolysis, the RBCs remain intact, forming a red pellet at the bottom of the tube, while the supernatant stays clear. If the polymer induces RBC rupture, hemoglobin is released into the supernatant, resulting in a red coloration, which can be quantified by absorbance measurement. PBS served as a negative control, showing no RBC lysis, while Triton X-100, a nonionic surfactant known to disrupt RBCs osmotically, was used as a positive control. The results indicated that none of the polymer samples caused RBC hemolysis, as evidenced by the intact RBC pellet and the clear supernatant, as shown in Figure 4.18a. The percentage of hemolysis was calculated and presented in a histogram (Figure 4.18a), confirming that all polymer brushes exhibited non-hemolytic behavior.

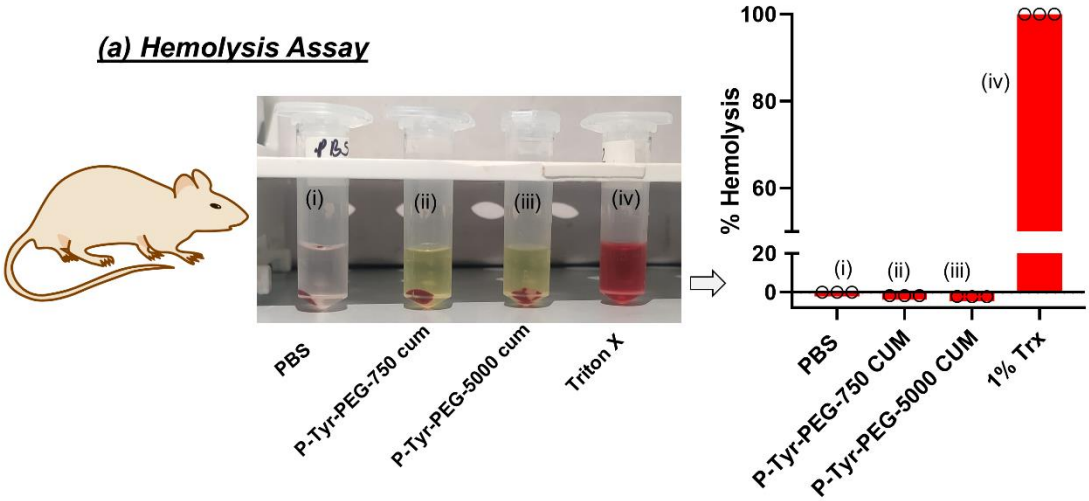

Figure 4.18 *(a) Photographs of centrifuge tubes post incubation of sample with RBC solution. Appearance of intact pellet indicate RBC stability. Plot showing % hemolysis for polymer (P-Tyr-PEG-CUM) along with PBS (negative control) and 1% Triton X-100 (positive control), (****P<0.0001) each point represents mean ± SEM, n=3).*

4.3.8 Cell viability assay

The polymer brushes' biocompatibility and Cytotoxicity were evaluated using the MTT molecule in the various cell lines such as breast cancer MCF-7, MDA-MB-268, human kidney HEK-293, and pancreatic MiaPaca. For the MTT assay, the details procedures were given in the experimental section. First, the polymer alone cytotoxicity was performed, and 96 well plates were used. Cells were seeded per well 10^3 and incubated for 16 hours under 5 % CO_2 at physiological temperature. Further, the CUM conjugated and NR samples were given to cells and incubated for 72 hours. The cytotoxicity data for MCF-7 cells is shown in Figure 4.19a, while data for HEK-293 cell lines are provided in Figure 4.19b . All polymer brushes, including P-Tyr-PEG750-CUM, P-Tyr-PEG750-CUM+NR, and P-Tyr-PEG5000-CUM, P-Tyr-PEG5000-CUM+NR, were found to be non-toxic to cells up to concentrations of 100 µg/mL, shown in Figure 4.20a and 4.20b indicating their biocompatibility highly desirable characteristic for biomedical applications.

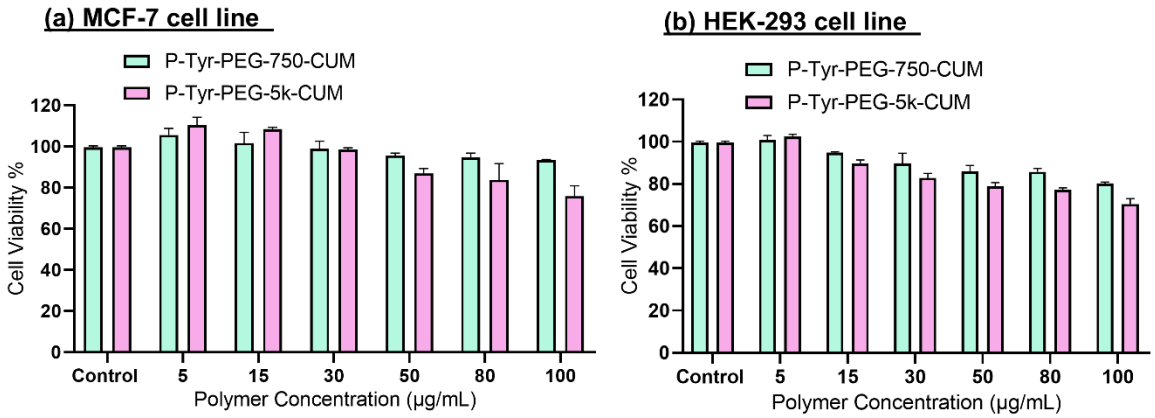

Figure 4.19 *(a) Plot showing the cytotoxicity of P-Tyr-PEG-750 CUM and P-Tyr-PEG-5000 CUM in a breast cancer MCF-7 cell line. (b) Plot showing the cytotoxicity of P-Tyr-PEG-750 CUM and P-Tyr-PEG-5000 CUM in a normal HEK-293 cell line.*

All polymer brushes, including P-Tyr-PEG750-CUM, P-Tyr-PEG750-CUM+NR, and P-Tyr-PEG5000-CUM, P-Tyr-PEG5000-CUM+NR, were found to be non-toxic to cells up to concentrations of 100 µg/mL, indicating their biocompatibility highly desirable characteristic for biomedical applications.

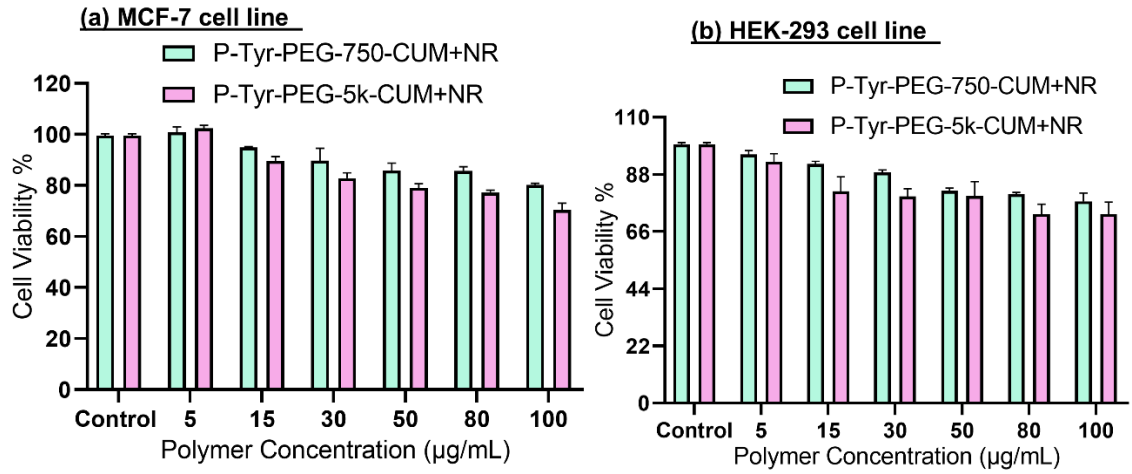

Figure 4.20. *(a) Plot showing the cytotoxicity of P-Tyr-PEG-750 CUM+NR and P-Tyr-PEG-5000 CUM+NR in a breast cancer MCF-7 cell line. (b) Plot showing the cytotoxicity of P-Tyr-PEG-750 CUM+NR and P-Tyr-PEG-5000 CUM+NR in a normal HEK-293 cell line.*

4.3.9 Cellular Uptake studies

The cellar uptake studies and the detailed procedure were included in the experimental section. To investigate cellular uptakes studies, first, the breast cancer (MCF-7) cells were grown in the six-well plates 10^5 cells were incubated for 16 hours. Time-dependent cellular uptake studies were then carried out. For that purpose, the CUM conjugated polymer brushes were incubated for various time points, such as 3h, 6h, and 9h. The CUM was excited at 405

nm, and the emission collected from 440 to 500 nm and the results are shown in Figure 4.21a and 4.21b. The CUM emission was predominantly observed in the cytoplasm. The merged images with the bright field and CUM indicate that CUM polymer brushes mainly accumulate in the cytoplasm rather than the nucleus. In the CTCF calculation, we found that the rod-like polymer brush accumulated more than the sphere polymer brush, as shown in Figure 4.21c.

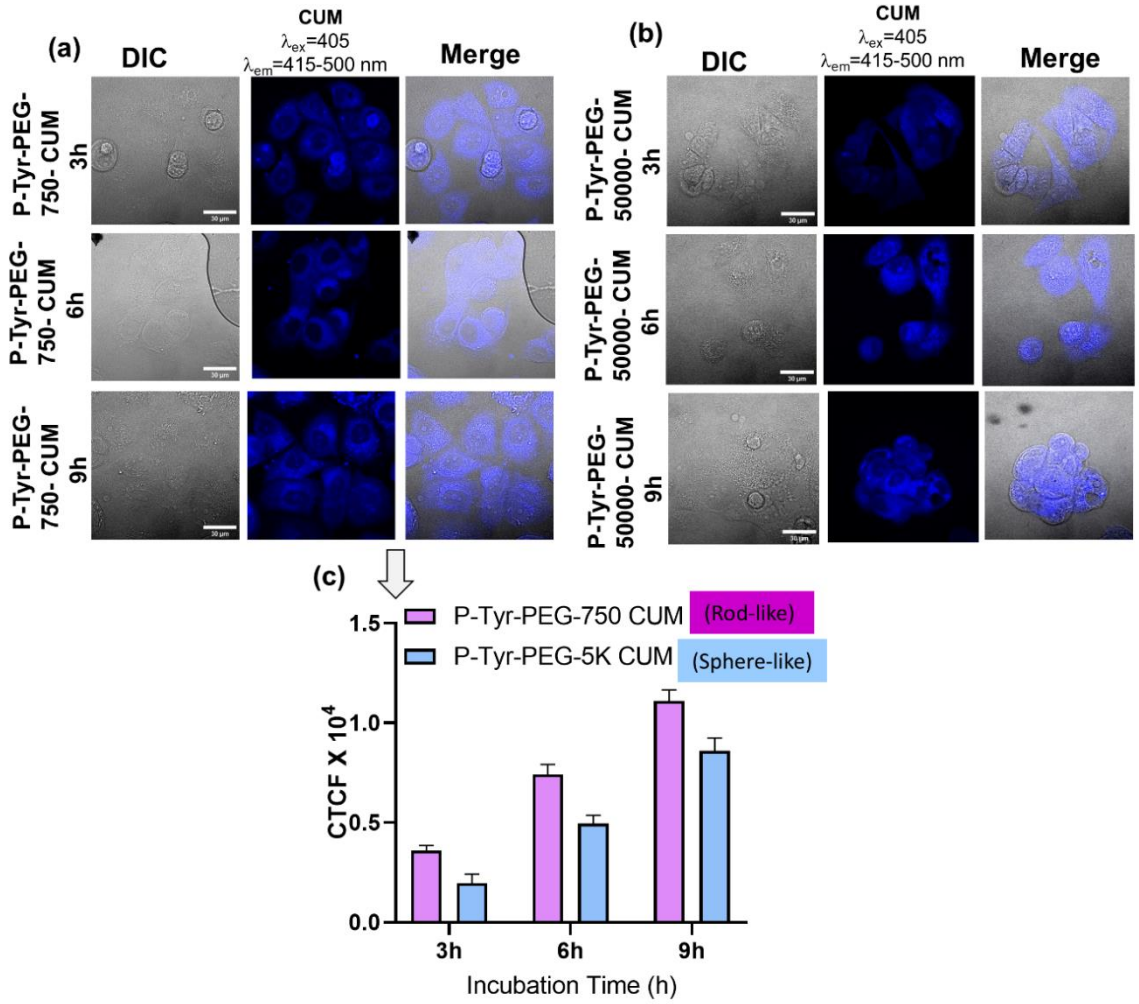

Figure 4.21. *(a) CLSM images of breast cancer MCF-7 cells incubated with P-Tyr-PEG-750-CUM. (b) CLSM images of breast cancer MCF-7 cells incubated with P-Tyr-PEG-5000-CUM.(c) CTCF intensity of P-Tyr-PEG-CUM at the cytoplasm of the cells.*

4.3.10 Live cell Imaging

For live cell imaging, breast cancer (MCF-7) cells were 25000 thousand cells seeded in the live cell chamber and incubated for 16 hours under 5 % CO2 at 37 C. The FRET behavior was further tested in living cells. When the CUM-loaded polymer brushes were introduced to cells, no fluorescence from CUM was detected because its emission energy was entirely transferred to NR, which fluoresced in the red region (see Figure 4.22a).

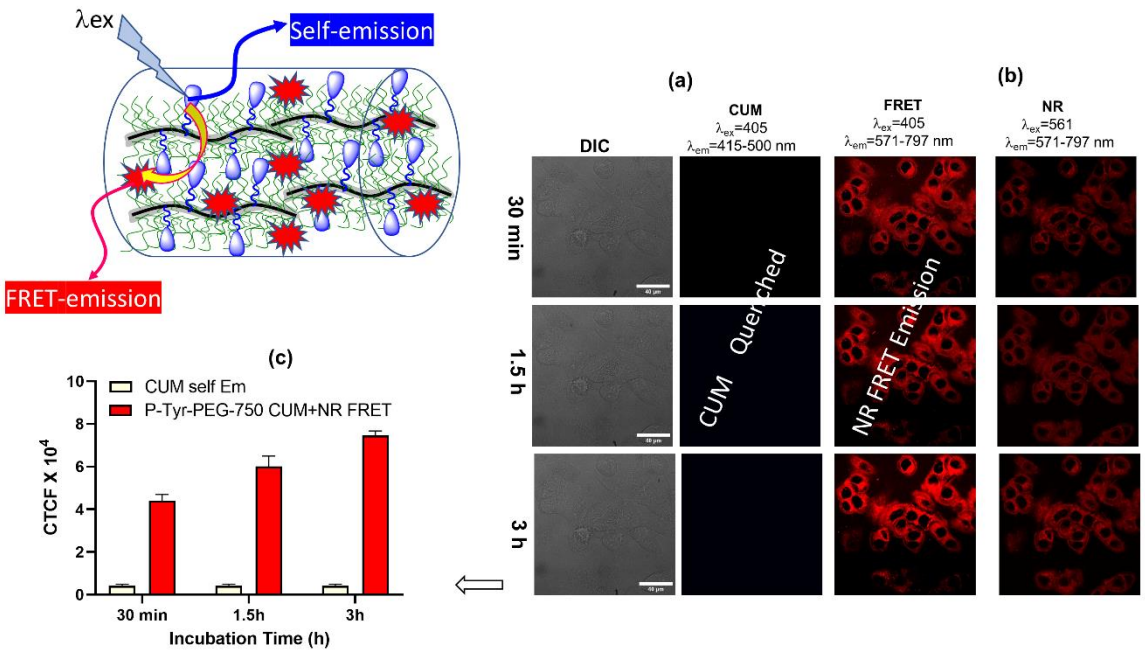

***Figure 4.22**. (a) Real time FRET monitoring by live cell confocal imaging in MCF-7 cell line. (b) Real-time live cell bioimaging self-emission of NR. (c) CTCF intensity of P-Tyr-PEG-750 CUM+NR.*

The FRET signal persisted for three hours inside the cellular environment. Additionally, NR alone showed reduced self-emission; see confirming its interaction with CUM within the FRET pair see Figure 4.22b These observations are corroborated by Corrected Total Cell Fluorescence (CTCF) calculations, see Figure 4.22c. demonstrated that the FRET pair remained stable and functional within cells for a prolonged period This study highlights the potential of these fluorescent polymer brushes for bioimaging and drug delivery applications.

4.4 Conclusion

A new class of monomers based on L-tyrosine was designed and polymerized using a melt polycondensation approach to synthesize a poly(ester-urethanes)s and subsequently clicked with PEG azide and CUM azide to get fluorescently tagged poly(ester-urethane)s. Comprehensive structural characterization of the copolymer was performed, and **^{1}H NMR** analysis validated the method's precision in achieving the desired composition. Size exclusion chromatography (SEC) indicated the formation of a moderate molecular weight polymer. The propargyl groups in the polymer were subsequently clicked with PEG and CUM azides to yield PEG-functionalized polymers tagged with coumarin (CUM), which exhibited thermal stability up to 300 °C. Differential Scanning Calorimetry (DSC) revealed unique thermal properties, highlighting semi-crystalline behaviour in the polymer. This crystallinity was attributed to PEG within the polymer chains, which created nucleation sites. Upon clicking, the semi-crystalline nature was further enhanced due to the synergistic effects of the PEG chain. The fluorescent polymer shows Emission behaviour in solution studies, and the Critical Aggregation Concentration (CAC) was determined using this property. In aqueous environments, the polymer brushes formed nano-assemblies capable of encapsulating hydrophobic dye. These polymer brushes nano-rod and sphere-like nanoparticles were characterized for size and shape using Field Atomic Force Microscopy (AFM) and High-Resolution Transmission Electron Microscopy (HR-TEM), revealing the shorter polyethene glycol formed rod-like polymer brush morphology, and the larger polyethene glycol (PEG-5000) formed spherical particle polymer brush with sub-nanometer dimensions. Photophysical studies, including emission spectra and fluorescence lifetime measurements, confirmed the occurrence of Förster Resonance Energy Transfer (FRET) within the nanoparticles' nanocavities. Biocompatibility assays demonstrated that the polymer nanoparticles were non-toxic to normal and cancer cells, making them effective drug delivery carriers. Cellular studies also utilized FRET to investigate interactions between the polymer chains and encapsulated cargo. Live cell experiments monitored the real-time drug delivery application.

4.5 References

(1) Lv, F.; Qiu, T.; Liu, L.; Ying, J.; Wang, S. Recent Advances in Conjugated Polymer Materials for Disease Diagnosis. *Small*. Wiley-VCH Verlag February 10, 2016, pp 696–705.

(2) Sharma, A.; Verwilst, P.; Li, M.; Ma, D.; Singh, N.; Yoo, J.; Kim, Y.; Yang, Y.; Zhu, J. H.; Huang, H.; Hu, X. Le; He, X. P.; Zeng, L.; James, T. D.; Peng, X.; Sessler, J. L.; Kim, J. S. Theranostic Fluorescent Probes. *Chemical Reviews*. American Chemical Society March 13, 2024, pp 2699–2804.

(3) Kelkar, S. S.; Reineke, T. M. Theranostics: Combining Imaging and Therapy. *Bioconjug Chem* **2011**, *22* (10), 1879–1903.

(4) Chen, H.; Jia, H.; Tham, H. P.; Qu, Q.; Xing, P.; Zhao, J.; Phua, S. Z. F.; Chen, G.; Zhao, Y. Theranostic Prodrug Vesicles for Imaging Guided Codelivery of Camptothecin and SiRNA in Synergetic Cancer Therapy. *ACS Appl Mater Interfaces* **2017**, *9* (28), 23536–23543.

(5) Lim, E. K.; Kim, T.; Paik, S.; Haam, S.; Huh, Y. M.; Lee, K. Nanomaterials for Theranostics: Recent Advances and Future Challenges. *Chemical Reviews*. American Chemical Society January 14, 2015, pp 327–394.

(6) Ghosh, R.; Malhotra, M.; Sathe, R. R. M.; Jayakannan, M. Biodegradable Polymer Theranostic Fluorescent Nanoprobe for Direct Visualization and Quantitative Determination of Antimicrobial Activity. *Biomacromolecules* **2020**, *21* (7), 2896–2912.

(7) Kumar, R.; Santa Chalarca, C. F.; Bockman, M. R.; Bruggen, C. Van; Grimme, C. J.; Dalal, R. J.; Hanson, M. G.; Hexum, J. K.; Reineke, T. M. Polymeric Delivery of Therapeutic Nucleic Acids. *Chemical Reviews*. American Chemical Society September 22, 2021, pp 11527–11652.

(8) Kamaly, N.; Xiao, Z.; Valencia, P. M.; Radovic-Moreno, A. F.; Farokhzad, O. C. Targeted Polymeric Therapeutic Nanoparticles: Design, Development and Clinical Translation. *Chem Soc Rev* **2012**, *41* (7), 2971–3010.

(9) Liu, G.; Wang, X.; Hu, J.; Zhang, G.; Liu, S. Self-Immolative Polymersomes for High-Efficiency Triggered Release and Programmed Enzymatic Reactions. *J Am Chem Soc* **2014**, *136* (20), 7492–7497.

(10) Saha, B.; Choudhury, N.; Seal, S.; Ruidas, B.; De, P. Aromatic Nitrogen Mustard-Based Autofluorescent Amphiphilic Brush Copolymer as PH-Responsive Drug Delivery Vehicle. *Biomacromolecules* **2019**, *20* (1), 546–557.

(11) Zou, J.; Yu, Y.; Li, Y.; Ji, W.; Chen, C.-K.; Law, W.-C.; Prasad, P. N.; Cheng, C. Well-Defined Diblock Brush Polymer–Drug Conjugates for Sustained Delivery of Paclitaxel. *Biomater Sci* **2015**, *3* (7), 1078–1084.

(12) Maiti, C.; Parida, S.; Kayal, S.; Maiti, S.; Mandal, M.; Dhara, D. Redox-Responsive Core-Cross-Linked Block Copolymer Micelles for Overcoming Multidrug Resistance in Cancer Cells. *ACS Appl Mater Interfaces* **2018**, *10* (6), 5318–5330.

(13) Saha, B.; Bhattacharyya, S.; Mete, S.; Mukherjee, A.; De, P. Redox-Driven Disassembly of Polymer–Chlorambucil Polyprodrug: Delivery of Anticancer Nitrogen Mustard and DNA Alkylation. *ACS Appl Polym Mater* **2019**, *1* (9), 2503–2515.

(14) Pranav, U.; Malhotra, M.; Pathan, S.; Jayakannan, M. Structural Engineering of Star Block Biodegradable Polymer Unimolecular Micelles for Drug Delivery in Cancer Cells. *ACS Biomater Sci Eng* **2023**, *9* (2), 743–759.

(15) Bak, J. M.; Lee, H. Use of Core-Cross-Linked Polymeric Micelles Induced by the Selective Detection of Cu(II) Ions for the Sustained Release of a Model Drug. *ACS Appl Mater Interfaces* **2019**, *11* (15), 14368–14375.

(16) Surnar, B.; Jayakannan, M. Stimuli-Responsive Poly(Caprolactone) Vesicles for Dual Drug Delivery under the Gastrointestinal Tract. *Biomacromolecules* **2013**, *14* (12), 4377–4387.

(17) Gao, Y.; Gao, C.; Fan, Y.; Sun, H.; Du, J. Physically and Chemically Compartmentalized Polymersomes for Programmed Delivery and Biological Applications. *Biomacromolecules* **2023**, *24* (12), 5511–5538.

(18) Iqbal, S.; Blenner, M.; Alexander-Bryant, A.; Larsen, J. Polymersomes for Therapeutic Delivery of Protein and Nucleic Acid Macromolecules: From Design to Therapeutic Applications. *Biomacromolecules*. American Chemical Society April 13, 2020, pp 1327–1350.

(19) Wei, Y.; Weng, X.; Wang, Y.; Yang, W. Stimuli-Responsive Polymersomes: Reshaping the Immunosuppressive Tumor Microenvironment. *Biomacromolecules* **2024**, *25* (8), 4663–4676.

(20) Bej, R.; Achazi, K.; Haag, R.; Ghosh, S. Polymersome Formation by Amphiphilic Polyglycerol- *b* -Polydisulfide- *b* -Polyglycerol and Glutathione-Triggered Intracellular Drug Delivery. *Biomacromolecules* **2020**, *21* (8), 3353–3363.

(21) Miyazaki, M.; Yuba, E.; Hayashi, H.; Harada, A.; Kono, K. Hyaluronic Acid-Based PH-Sensitive Polymer-Modified Liposomes for Cell-Specific Intracellular Drug Delivery Systems. *Bioconjug Chem* **2018**, *29* (1), 44–55.

(22) Lee, S.-M.; Nguyen, S. T. Smart Nanoscale Drug Delivery Platforms from Stimuli-Responsive Polymers and Liposomes. *Macromolecules* **2013**, *46* (23), 9169–9180.

(23) Ji, X.; Li, Y.; Wang, H.; Zhao, R.; Tang, G.; Huang, F. Facile Construction of Fluorescent Polymeric Aggregates with Various Morphologies by Self-Assembly of Supramolecular Amphiphilic Graft Copolymers. *Polym Chem* **2015**, *6* (28), 5021–5025.

(24) Li, Z.; Ma, J.; Lee, N. S.; Wooley, K. L. Dynamic Cylindrical Assembly of Triblock Copolymers by a Hierarchical Process of Covalent and Supramolecular Interactions. *J Am Chem Soc* **2011**, *133* (5), 1228–1231.

(25) Li, Y.; Liu, Q.; Ding, J.; Zou, J.; Yang, B. Responsive Supramolecular Nanomicelles Formed through Self-Assembly of Acyclic Cucurbit[*n*]Uril for Targeted Drug Delivery to Cancer Cells. *Mol Pharm* **2024**, *21* (11), 5784–5796.

(26) Peng, H.; Xu, Z.; Wang, Y.; Feng, N.; Yang, W.; Tang, J. Biomimetic Mesoporous Silica Nanoparticles for Enhanced Blood Circulation and Cancer Therapy. *ACS Appl Bio Mater* **2020**, *3* (11), 7849–7857.

(27) Hua, B.; Zhang, C.; Zhou, W.; Shao, L.; Wang, Z.; Wang, L.; Zhu, H.; Huang, F. Pillar[5]Arene-Based Solid-State Supramolecular Polymers with Suppressed Aggregation-Caused Quenching Effects and Two-Photon Excited Emission. *J Am Chem Soc* **2020**, *142* (39), 16557–16561.

(28) Pan, D.; Maity, S.; Parshi, N.; Ganguly, J. Remarkable Solvent Tunable Aggregation Caused Quenching for Fluorochromic Chitosan Based Hydrogel. *J Mol Liq* **2021**, *322*, 114565.

(29) Zuo, Y.; Wang, X.; Wu, D. Uniting Aggregation-Induced Emission and Stimuli-Responsive Aggregation-Caused Quenching, Single Molecule Achieved Multicolour Luminescence. *J Mater Chem C Mater* **2019**, *7* (46), 14555–14562.

(30) Hong, Y.; Lam, J. W. Y.; Tang, B. Z. Aggregation-Induced Emission. *Chemical Society Reviews*. Royal Society of Chemistry October 17, 2011, pp 5361–5388.

(31) Naghibi, S.; Sabouri, S.; Hong, Y.; Jia, Z.; Tang, Y. Brush-like Polymer Prodrug with Aggregation-Induced Emission Features for Precise Intracellular Drug Tracking. *Biosensors (Basel)* **2022**, *12* (6).

(32) Mei, J.; Leung, N. L. C.; Kwok, R. T. K.; Lam, J. W. Y.; Tang, B. Z. Aggregation-Induced Emission: Together We Shine, United We Soar! *Chemical Reviews*. American Chemical Society November 11, 2015, pp 11718–11940.

(33) Yuan, Y.; Zhang, C.-J.; Kwok, R. T. K.; Mao, D.; Tang, B. Z.; Liu, B. Light-up Probe Based on AIEgens: Dual Signal Turn-on for Caspase Cascade Activation Monitoring. *Chem Sci* **2017**, *8* (4), 2723–2728.

(34) Chen, J.; Zhong, W.; Tang, Y.; Wu, Z.; Li, Y.; Yi, P.; Jiang, J. Amphiphilic BODIPY-Based Photoswitchable Fluorescent Polymeric Nanoparticles for Rewritable Patterning and Dual-Color Cell Imaging. *Macromolecules* **2015**, *48* (11), 3500–3508.

(35) Sahoo, H. Förster Resonance Energy Transfer - A Spectroscopic Nanoruler: Principle and Applications. *Journal of Photochemistry and Photobiology C: Photochemistry Reviews*. March 2011, pp 20–30.

(36) Yuan, L.; Lin, W.; Zheng, K.; Zhu, S. FRET-Based Small-Molecule Fluorescent Probes: Rational Design and Bioimaging Applications. *Acc Chem Res* **2013**, *46* (7), 1462–1473.

(37) Shrestha, D.; Jenei, A.; Nagy, P.; Vereb, G.; Szöllősi, J. Understanding FRET as a Research Tool for Cellular Studies. *Int J Mol Sci* **2015**, *16* (4), 6718–6756.

(38) Jia, X.; Chen, Q.; Yang, Y.; Tang, Y.; Wang, R.; Xu, Y.; Zhu, W.; Qian, X. FRET-Based Mito-Specific Fluorescent Probe for Ratiometric Detection and Imaging of Endogenous Peroxynitrite: Dyad of Cy3 and Cy5. *J Am Chem Soc* **2016**, *138* (34), 10778–10781.

(39) Deshpande, N. U.; Virmani, M.; Jayakannan, M. An AIE-Driven Fluorescent Polysaccharide Polymersome as an Enzyme-Responsive FRET Nanoprobe to Study the Real-Time Delivery Aspects in Live Cells. *Polym Chem* **2021**, *12* (10), 1549–1561.

(40) Saxena, S.; Pradeep, A.; Jayakannan, M. Enzyme-Responsive Theranostic FRET Probe Based on L-Aspartic Amphiphilic Polyester Nanoassemblies for Intracellular Bioimaging in Cancer Cells. *ACS Appl Bio Mater* **2019**, *2* (12), 5245–5262.

(41) Lai, J.; Shah, B. P.; Garfunkel, E.; Lee, K. B. Versatile Fluorescence Resonance Energy Transfer-Based Mesoporous Silica Nanoparticles for Real-Time Monitoring of Drug Release. *ACS Nano* **2013**, *7* (3), 2741–2750.

(42) Pal, J.; Kola, P.; Samanta, P.; Mandal, M.; Dhara, D. Polymer Nanoparticles for Preferential Delivery of Drugs Only by Exploiting the Slightly Elevated Temperature of Cancer Cells and Real-Time Monitoring of Drug Release. *Biomacromolecules* **2024**, *25* (8), 5181–5197.

(43) Kayal, S.; Kola, P.; Pal, J.; Mandal, M.; Dhara, D. Self-Indicating Polymer Prodrug Nanoparticles for PH-Responsive Drug Delivery in Cancer Cells and Real-Time Monitoring of Drug Release. *ACS Appl Bio Mater* **2024**.

(44) Rajdev, P.; Basak, D.; Ghosh, S. Insights into Noncovalently Core Cross-Linked Block Copolymer Micelles by Fluorescence Resonance Energy Transfer (FRET) Studies. *Macromolecules* **2015**, *48* (10), 3360–3367.

(45) Lin, W.; Du, Y.; Zhu, Y.; Chen, X. A Cis-Membrane FRET-Based Method for Protein-Specific Imaging of Cell-Surface Glycans. *J Am Chem Soc* **2014**, *136* (2), 679–687.

(46) Kisley, L.; Miller, K. A.; Guin, D.; Kong, X.; Gruebele, M.; Leckband, D. E. Direct Imaging of Protein Stability and Folding Kinetics in Hydrogels. *ACS Appl Mater Interfaces* **2017**, *9* (26), 21606–21617.

(47) Chen, J.; Poddar, N. K.; Tauzin, L. J.; Cooper, D.; Kolomeisky, A. B.; Landes, C. F. Single-Molecule FRET Studies of HIV TAR-DNA Hairpin Unfolding Dynamics. *Journal of Physical Chemistry B* **2014**, *118* (42), 12130–12139.

(48) Heitz, M.; Zamolo, S.; Javor, S.; Reymond, J. L. Fluorescent Peptide Dendrimers for SiRNA Transfection: Tracking PH Responsive Aggregation, SiRNA Binding, and Cell Penetration. *Bioconjug Chem* **2020**, *31* (6), 1671–1684.

(49) Qu, X.; Trent, J. O.; Fokt, I.; Priebe, W.; Chaires, J. B. *Allosteric, Chiral-Selective Drug Binding to DNA*; 2002; Vol. 97.

(50) He, F.; Tang, Y.; Yu, M.; Feng, F.; An, L.; Sun, H.; Wang, S.; Li, Y.; Zhu, D.; Bazan, G. C. Quadruplex-to-Duplex Transition of G-Rich Oligonucleotides Probed by Cationic Water-Soluble Conjugated Polyelectrolytes. *J Am Chem Soc* **2006**, *128* (21), 6764–6765.

(51) Rana, S.; Elci, S. G.; Mout, R.; Singla, A. K.; Yazdani, M.; Bender, M.; Bajaj, A.; Saha, K.; Bunz, U. H. F.; Jirik, F. R.; Rotello, V. M. Ratiometric Array of Conjugated Polymers-Fluorescent Protein Provides a Robust Mammalian Cell Sensor. *J Am Chem Soc* **2016**, *138* (13), 4522–4529.

(52) Zhan, J.; Huang, J.; Xiao, Q.; Yu, Z.; Wang, Y.; Wang, X.; Liu, F.; Cai, Y.; Yang, Z.; Zheng, L. Optimized Two-Photon Imaging by Stimuli-Responsive Peptide Self-Assembly Facilitates Self-Assisted Counteraction of Cisplatin-Resistance in Cancer Cells. *Anal Chem* **2024**, *96* (31), 12630–12639.

(53) Zhu, M.-Q.; Zhang, G.-F.; Li, C.; Aldred, M. P.; Chang, E.; Drezek, R. A.; Li, A. D. Q. Reversible Two-Photon Photoswitching and Two-Photon Imaging of Immunofunctionalized Nanoparticles Targeted to Cancer Cells. *J Am Chem Soc* **2011**, *133* (2), 365–372.

(54) Senthilkumar, T.; Asha, S. K. Selective and Sensitive Sensing of Free Bilirubin in Human Serum Using Water-Soluble Polyfluorene as Fluorescent Probe. *Macromolecules* **2015**, *48* (11), 3449–3461.

(55) Hussain, S.; Chen, X.; Wang, C.; Hao, Y.; Tian, X.; He, Y.; Li, J.; Shahid, M.; Iyer, P. K.; Gao, R. Aggregation and Binding-Directed FRET Modulation of Conjugated Polymer Materials for Selective and Point-of-Care Monitoring of Serum Albumins. *Anal Chem* **2022**, *94* (30), 10685–10694.

(56) Senthilkumar, T.; Asha, S. K. Self-Assembly in Tailor-Made Polyfluorenes: Synergistic Effect of Porous Spherical Morphology and FRET for Visual Sensing of Bilirubin. *Macromolecules* **2013**, *46* (6), 2159–2171.

(57) Nhien, P. Q.; Chou, W. L.; Cuc, T. T. K.; Khang, T. M.; Wu, C. H.; Thirumalaivasan, N.; Hue, B. T. B.; Wu, J. I.; Wu, S. P.; Lin, H. C. Multi-Stimuli Responsive FRET Processes of Bifluorophoric AIEgens in an Amphiphilic Copolymer and Its Application to Cyanide Detection in Aqueous Media. *ACS Appl Mater Interfaces* **2020**, *12* (9), 10959–10972.

(58) Tsai, W.-K.; Lai, Y.-S.; Tseng, P.-J.; Liao, C.-H.; Chan, Y.-H. Dual Colorimetric and Fluorescent Authentication Based on Semiconducting Polymer Dots for Anticounterfeiting Applications. *ACS Appl Mater Interfaces* **2017**, *9* (36), 30918–30924.

(59) Tao, M.; Liang, X.; Guo, J.; Zheng, S.; Qi, Q.; Cao, Z.; Mi, Y.; Zhao, Z. Dynamic Photochromic Polymer Nanoparticles Based on Matrix-Dependent Förster Resonance Energy Transfer and Aggregation-Induced Emission Properties. *ACS Appl Mater Interfaces* **2021**, *13* (28), 33574–33583.

(60) Saxena, S.; Jayakannan, M. π-Conjugate Fluorophore-Tagged and Enzyme-Responsive L-Amino Acid Polymer Nanocarrier and Their Color-Tunable Intracellular FRET Probe in Cancer Cells. *Biomacromolecules* **2017**, *18* (8), 2594–2609.

(61) Saxena, S.; Jayakannan, M. Development of L-Amino-Acid-Based Hydroxyl Functionalized Biodegradable Amphiphilic Polyesters and Their Drug Delivery Capabilities to Cancer Cells. *Biomacromolecules* **2020**, *21* (1), 171–187.

(62) Saxena, S.; Jayakannan, M. Enzyme and PH Dual Responsive L-Amino Acid Based Biodegradable Polymer Nanocarrier for Multidrug Delivery to Cancer Cells. *J Polym Sci A Polym Chem* **2016**, *54* (20), 3279–3293.

(63) Saxena, S.; Jayakannan, M. Enzyme and PH Dual Responsive L-Amino Acid Based Biodegradable Polymer Nanocarrier for Multidrug Delivery to Cancer Cells. *J Polym Sci A Polym Chem* **2016**, *54* (20), 3279–3293.

(64) Khuddus, M.; Jayakannan, M. Melt Polycondensation Strategy for Amide-Functionalized L-Aspartic Acid Amphiphilic Polyester Nano-Assemblies and Enzyme-Responsive Drug Delivery in Cancer Cells. *Biomacromolecules* **2023**, *24* (6), 2643–2660.

(65) Joshi, D. C.; Saxena, S.; Jayakannan, M. Development of L-Lysine Based Biodegradable Polyurethanes and Their Dual-Responsive Amphiphilic Nanocarriers for Drug Delivery to Cancer Cells. *ACS Appl Polym Mater* **2019**, *1* (7), 1866–1880.

(66) Anantharaj, S.; Jayakannan, M. Polymers from Amino Acids: Development of Dual Ester-Urethane Melt Condensation Approach and Mechanistic Aspects. *Biomacromolecules* **2012**, *13* (8), 2446–2455.

(67) Anantharaj, S.; Jayakannan, M. Amyloid-Like Hierarchical Helical Fibrils and Conformational Reversibility in Functional Polyesters Based on L-Amino Acids. *Biomacromolecules* **2015**, *16* (3), 1009–1020.

(68) Anantharaj, S.; Jayakannan, M. Melt Polycondensation Approach for Reduction Degradable Helical Polyester Based on L-cystine. *J Polym Sci A Polym Chem* **2016**, *54* (18), 2864–2875.

(69) Aluri, R.; Jayakannan, M. Development of L-Tyrosine-Based Enzyme-Responsive Amphiphilic Poly(Ester-Urethane) Nanocarriers for Multiple Drug Delivery to Cancer Cells. *Biomacromolecules* **2017**, *18* (1), 189–200.

(70) Aluri, R.; Saxena, S.; Joshi, D. C.; Jayakannan, M. Multistimuli-Responsive Amphiphilic Poly(Ester-Urethane) Nanoassemblies Based on L-Tyrosine for Intracellular Drug Delivery to Cancer Cells. *Biomacromolecules* **2018**, *19* (6), 2166–2181.

Overall conclusion

The thesis titled *"L-Tyrosine Based Polymer Brushes for Drug Delivery In-vitro and In-vivo"* focuses on developing polymers derived from the renewable resource L-tyrosine as an alternative to petroleum-based polymers. These polymers offer exceptional structural tunability and biodegradability.

Chapter 1 This study presents the development of a novel class of biodegradable propargyl-functional poly(ester-urethane)s based on L-amino acids, synthesized via solvent-free melt polycondensation using L-tyrosine-derived monomers with phenolic propargyl and carboxylic ester urethane functionalities. High-molecular-weight poly(ester-urethane)s were produced through melt-transesterification with diols, followed by post-polymerization click reactions with PEG monomethyl ether azides to create amphiphilic polymers. These polymers self-assembled into brush rod-like nanoparticles (~250 ± 10 nm), demonstrating exceptional encapsulation of doxorubicin (DOX) and IR-780 dye. In vitro studies showed that enzymatic degradation of brush rods released drugs 90% faster at the intracellular level compared to spherical nanoparticles (65%), while remaining stable extracellularly. Endocytosis experiments confirmed that rod-like nanoparticles exhibited significantly higher uptake and faster degradation than their spherical counterparts. Cytotoxicity tests indicated that drug-loaded brush rods were highly effective against cancer cells, while their nascent forms were non-toxic. Confocal imaging and live-cell studies further validated enhanced cellular uptake and accelerated drug release from brush nano-rods compared to free DOX. In vivo biodistribution studies revealed improved circulation time and stability of brush nano-rods. This groundbreaking research highlights the untapped potential of L-amino acid-based PEGylated brush poly(ester-urethane)s for drug delivery, paving the way for innovative cancer therapies.

Chapter 2 A novel synthetic method was developed to create fully biobased poly(ester-urethane)s from two abundant natural resources, D-glucose and D-mannose. Through a multistep synthesis, glucose and mannose were selectively azidated at the anomeric position after protection of secondary hydroxyl groups as acetate linkages, yielding α- and β-isomeric sugars. Structural analysis using ^{1}H and ^{13}C NMR confirmed the formation of sugar azides. Amino acids were modified into ester urethane monomers, which underwent melt polymerization at 150°C to form rigid poly(ester-urethane)s, as evidenced by thermal analysis showing high glass transition temperatures. The resulting amino acid-sugar hybrid polymers were assembled into amphiphilic nanoparticles (~100 ± 10 nm) in aqueous solutions.

Enzymatic drug release studies showed 90% CPT release with enzymes and 25% without. Cytotoxicity tests in HEK-293, MCF-7, MDA-MB-264, and MIA PaCa-2 cell lines confirmed biocompatibility and efficient drug uptake. NIR imaging using ICG-green loaded polymers demonstrated better blood circulation stability for glucose-based polymers compared to mannose-based ones. This study marks the first example of fully natural-resource-derived polymers from sugars and amino acids, offering a sustainable alternative to petroleum-based materials with promising applications in drug delivery and imaging.

Chapter 3 A new class of L-tyrosine-based monomers was designed and polymerized via melt polycondensation to synthesize poly(ester-urethane)s, which were subsequently functionalized with PEG azide and CUM azide to create fluorescently tagged polymers. Structural characterization, including ^{1}H NMR and SEC, confirmed the polymer's composition and moderate molecular weight. The propargyl groups in the polymer enabled efficient clicking with PEG and CUM azides, resulting in PEG-functionalized polymers tagged with coumarin (CUM) and exhibiting thermal stability up to 300°C. Differential Scanning Calorimetry (DSC) revealed semi-crystalline properties, enhanced by PEG chains forming nucleation sites. Fluorescent emission studies determined the Critical Aggregation Concentration (CAC), and in aqueous environments, the polymers self-assembled into nano-assemblies. Short-chain PEG formed rod-like polymer brushes, while PEG-5000 yielded spherical brush nanoparticles, as confirmed by AFM and HR-TEM. Photophysical studies demonstrated Förster Resonance Energy Transfer (FRET) within the nanocavities, supporting their encapsulation capabilities for hydrophobic dyes. Biocompatibility assays showed the nanoparticles were non-toxic to normal and cancer cells, making them suitable drug delivery vehicles. FRET-based cellular studies confirmed polymer-drug interactions and real-time drug delivery, highlighting the potential of these fluorescently tagged polymer nanoparticles in biomedical applications.

Future direction

This thesis explores the development of functional poly(ester-urethane)s modified with PEG chains (PEG 350 to PEG 5000) to create PEGylated amphiphilic poly(ester-urethane)s. Future work could involve incorporating bifunctional PEG azides to form biodegradable crosslinked polymer brushes via click chemistry. Such brushes could enhance doxorubicin (DOX) encapsulation and support the design of polymer-based prodrugs for anticancer and antibacterial applications using amino acids as functional components. Chapter 2 Developed fully biodegradable polymer brushes based on sugars and amino acids using click chemistry. Future work could focus on targeted drug delivery via macrophages, evaluating enhanced drug encapsulation, and exploring the potential of these polymers for tumor-specific delivery. This approach is highly promising due to the complete biodegradability of the polymer, ensuring biocompatibility and safety for the body. Chapter 3 This work highlights CUM-tagged poly(ester-urethane)s, which can be utilized to synthesize photo-responsive polymer brushes. The CUM forms excimer coumarin, making the system suitable for targeted therapy. Unlike conventional monomers that exhibit monomeric emission, excimer-based fluorescent probes offer large Stokes shifts and long lifetimes, providing significant advantages for biological applications.

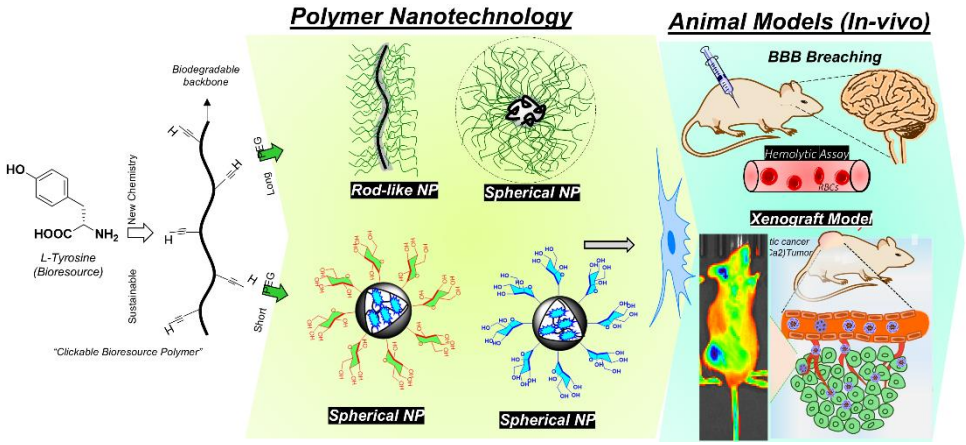

Figure 1 *Controlled architecture polymer brushes in specific sizes and shapes for tumor-targeted delivery"*

List of Publications

1. **Utreshwar Arjun Gavhane,** Dheeraj Joshi, and M. Jayakannan, Size- and Shape-Controlled Biodegradable Polymer Brushes Based on L-Amino Acid for Intracellular Drug Delivery and Deep-Tissue Penetration. *Biomacromolecules* **2024,** *25*, 3756-3774.

2. Mohammed Khuddus, **Utreshwar Arjun Gavhane**, and M. JayakannanStructural Engineering of L Aspartic Amphiphilic Polyesters for Enzyme Responsive Drug Delivery and Bioimaging in Cancer Cells. *ACS Polym. Au* **2024,** *4*, 5, 392-404.

3. Dheeraj Joshi, **Utreshwar Arjun Gavhane,** and M. Jayakannan, Melt Polycondensation Synthetic Strategy to Access Unexplored L-Amino acid and Sugar Polymers. *Biomacromolecules* **2024,** *25*, 11, 7311-7322.

4. Shibam Pal, **Utreshwar Arjun Gavhane** and S. K. Asha, Smart Biocompatible Polymer Photocrosslinker: Enzymatic Regulation of Dye Absorption and Release within Porous 3D Printed Framework Featuring Tunable Mechanical Properties, *ACS Appl. Mater. Interfaces* **2024,** *16,* 45, 62594-62605.

5. Ganesh Kamble, Dheeraj Joshi, **Utreshwar Arjun Gavhane** and S. K. Asha "Carbohydrate based Polyester and Amino acid polyester photocrosslinker and their Resin Formulation for 3D printing Applications" *Manuscript under revision manuscript asia.202401474 for Chemistry - An Asian Journal*

6. **Utreshwar Arjun Gavhane**, and Manickam Jayakannan, Design and Development of L-Tyrosine Sugar Hybrid Biodegradable Polymer Brushes for targeted Cancer Delivery" *Manuscript under Preparation*

7. **Utreshwar Arjun Gavhane**, and Manickam Jayakannan, "Development of CUM Fluorophore-Tagged Polymer Brushes for FRET-Based Theranostics in Cancer Cells" *Manuscript under Preparation*

RightsLink

Sign in/Register

ACS Publications
Most Trusted. Most Cited. Most Read.

Size- and Shape-controlled Biodegradable Polymer Brushes Based on l-Amino Acid for Intracellular Drug Delivery and Deep-Tissue Penetration

Author: Utreshwar Arjun Gavhane, Dheeraj Chandra Joshi, Manickam Jayakannan
Publication: Biomacromolecules
Publisher: American Chemical Society
Date: Jun 1, 2024

Copyright © 2024, American Chemical Society

PERMISSION/LICENSE IS GRANTED FOR YOUR ORDER AT NO CHARGE

This type of permission/license, instead of the standard Terms and Conditions, is sent to you because no fee is being charged for your order. Please note the following:

- Permission is granted for your request in both print and electronic formats, and translations.
- If figures and/or tables were requested, they may be adapted or used in part.
- Please print this page for your records and send a copy of it to your publisher/graduate school.
- Appropriate credit for the requested material should be given as follows: "Reprinted (adapted) with permission from {COMPLETE REFERENCE CITATION}. Copyright {YEAR} American Chemical Society." Insert appropriate information in place of the capitalized words.
- One-time permission is granted only for the use specified in your RightsLink request. No additional uses are granted (such as derivative works or other editions). For any uses, please submit a new request.

If credit is given to another source for the material you requested from RightsLink, permission must be obtained from that source.

BACK CLOSE WINDOW

© 2025 Copyright - All Rights Reserved | Copyright Clearance Center, Inc. | Privacy statement | Data Security and Privacy | For California Residents | Terms and ConditionsComments? We would like to hear from you. E-mail us at customercare@copyright.com

pubs.acs.org/Biomac Article

Size- and Shape-controlled Biodegradable Polymer Brushes Based on L-Amino Acid for Intracellular Drug Delivery and Deep-Tissue Penetration

Utreshwar Arjun Gavhane, Dheeraj Chandra Joshi, and Manickam Jayakannan*

Cite This: Biomacromolecules 2024, 25, 3756–3774 Read Online

ACCESS | Metrics & More | Article Recommendations | Supporting Information

Downloaded via IISER PUNE on July 24, 2024 at 07:22:36 (UTC).
See https://pubs.acs.org/sharingguidelines for options on how to legitimately share published articles.

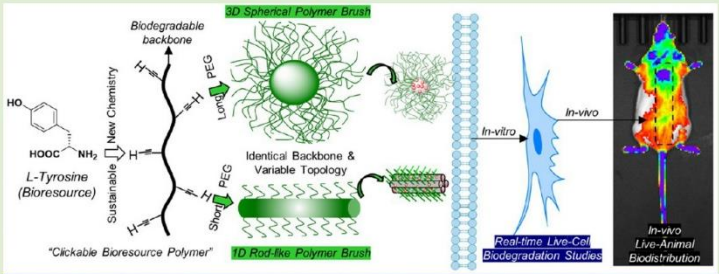

Size and Shape-controlled Biodegradable L-Amino acid Polymer Brushes: In-vitro and In-vivo

ABSTRACT: We report size- and shape-controlled polymer brushes based on L-amino acid bioresource and study the role of polymer topology on the enzymatic biodegradation and deep-tissue penetration under in vitro and in vivo. For this purpose, L-tyrosine-based propargyl-functionalized monomer is tailor-made and polymerized via solvent-free melt polycondensation strategy to yield hydrophobic and clickable biodegradable poly(ester-urethane)s. Postpolymerization click chemistry strategy is applied to make well-defined amphiphilic one-dimensional rodlike and three-dimensional spherical polymer brushes by merely varying the lengths of PEG-azides in the reaction. These core–shell polymer brushes are found to be nontoxic and nonhemolytic and capable of loading clinical anticancer drug doxorubicin and deep-tissue penetrable near-infrared biomarker IR-780. In vitro enzymatic drug-release kinetics and lysotracker-assisted real-time live-cell confocal bioimaging revealed that the rodlike polymer brush is superior than its spherical counterparts for faster cellular uptake and enzymatic biodegradation at the endolysosomal compartments to release DOX at the nucleus. Further, in vivo live-animal bioimaging by IVIS technique established that the IR-780-loaded rodlike polymer brush exhibited efficient deep-tissue penetration ability and emphasized the importance of polymer brush topology control for biological activity. Polymer brushes exhibit good stability in the blood plasma for more than 72 h, they predominately accumulate in the digestive organs like liver and kidney, and they are less toxic to heart and brain tissues. IVIS imaging of cryotome tissue slices of organs confirmed the deep-penetrating ability of the polymer brushes. The present investigation opens opportunity for bioderived and biodegradable polymer brushes as next-generation smart drug-delivery scaffolds.

■ INTRODUCTION

Polymer brushes are higher-order synthetic macromolecules of discrete nanocompartmentalization and provide unique opportunities to precisely control one- and three-dimensional shapes, subnanometer size objects and surfaces, and chemical functions, and they offer unlimited opportunity for application in material science and biomedical field.[1−4] Polymer brushes are typically synthesized by grafting-to and grafting-from strategies on the well-defined rigid polymer backbone with flexible side-chains for self-assembly in solution and solid state (in thin films).[5−7] Plug-and-play interfaces for guest–host interaction,[8] protein conjugates,[9] hybrid molecular brushes,[10] cross-linkable block copolymer brushes,[11] NIR probe tagged triblock micelles,[12] and bottlebrush adhesives[13] are some of the recent examples reported for multifaceted polymer brushes. Polymer brushes for biomedical field is typically achieved by incorporating hydrophilic–hydrophobic balance in combination with pH, redox, or thermal stimuli-responsiveness to impart on-demand delivery of cargoes at the intracellular compartments and tumor-specific environments.[14,15] Among many choices to introduce amphiphilicity in the polymer

Received: March 12, 2024
Revised: April 24, 2024
Accepted: April 24, 2024
Published: May 7, 2024

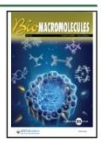

ACS Publications © 2024 American Chemical Society

https://doi.org/10.1021/acs.biomac.4c00341
Biomacromolecules 2024, 25, 3756–3774

ACS POLYMERS Au
AN OPEN ACCESS JOURNAL OF THE AMERICAN CHEMICAL SOCIETY

Open Access
This article is licensed under CC-BY-NC-ND 4.0

pubs.acs.org/polymerau
Article

Structural Engineering of L-Aspartic Amphiphilic Polyesters for Enzyme-Responsive Drug Delivery and Bioimaging in Cancer Cells

Published as part of ACS Polymers Au virtual special issue "Polymer Science and Engineering in India".

Mohammed Khuddus, Utreshwar Arjun Gavhane, and Manickam Jayakannan*

Cite This: *ACS Polym. Au* 2024, 4, 392−404
Read Online

ACCESS | Metrics & More | Article Recommendations | Supporting Information

ABSTRACT: Design and development of amphiphilic polyesters based on bioresources are very important to cater to the ever-growing need for biodegradable polymers in biomedical applications. Here, we report structural engineering of enzyme-responsive amphiphilic polyesters based on L-amino acid bioresources and study their drug delivery aspects in the cancer cell line. For this purpose, an L-aspartic acid-based polyester platform is chosen, and two noncovalent forces such as hydrogen bonding and side-chain hydrophobic interactions are introduced to study their effect on the aqueous self-assembly of nanoparticles. The synthetic strategy involves the development of L-aspartic acid-based dimethyl ester monomers with acetal and stearate side chains and subjecting them to solvent-free melt polycondensation reactions to produce side-chain-functionalized polyesters in the entire composition range. Postpolymerization acid catalyst deprotection of acetal yielded hydroxyl-functionalized polyesters. Amphiphilicity of the polymer is carefully fine-tuned by varying the composition of the stearate and hydroxyl units in the polymer chains to produce self-assembly in water. Various drugs such as camptothecin (CPT), curcumin (CUR), and doxorubicin (DOX) and biomarkers like 8-hydroxypyrene-1,3,6-trisulfonic acid trisodium salt (HPTS), rose bengal (RB), and Nile red (NR) are successfully encapsulated in the polymer nanoparticles. Cytotoxicity of biodegradable polymer nanoparticles is tested in normal and breast cancer cell lines. The polymer nanoparticles are found to be highly biocompatible and delivered the anticancer drugs in the intracellular compartments of the cells.

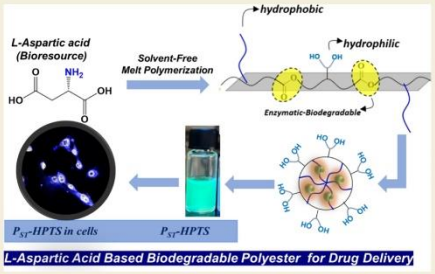

KEYWORDS: *amino acid, polyesters, melt polycondensation, polymer nanoparticles, drug delivery, biodegradable polymers*

Downloaded via IISER PUNE on January 16, 2025 at 03:57:59 (UTC).
See https://pubs.acs.org/sharingguidelines for options on how to legitimately share published articles.

INTRODUCTION

Polymers are emerging as indispensable components in biomedical applications, and they have become an integral part of drug delivery systems,[1−3] gene delivery vehicles,[4] tissue engineering scaffolds,[5,6] and antimicrobial agents.[7,8] Synthetic polymers gained significant importance because of their tunable properties, including biocompatibility, biodegradability, and versatility in molecular design, which made them highly attractive for addressing diverse biomedical challenges.[9−11] Among the myriad classes of polymers, biodegradable variants hold particular significance, offering controlled degradation that aligns with the dynamic needs of biological systems.[12−15] These polymers not only mitigate concerns related to long-term accumulation and toxicity but also facilitate the controlled release of therapeutic agents, thereby enhancing efficacy and minimizing adverse effects.[16−18] Within the domain of biodegradable polymers, those derived from natural resources hold immense promise; notably, the polymers synthesized from L-amino acids via ring-opening polymerization (ROP) have garnered considerable attention owing to their inherent biocompatibility and structural resemblance to biological macromolecules.[19−23] This includes the development of synthetic amphiphilic polypeptides mimicking the natural-protein-type self-assemblies under physiological conditions.[24] To address the limitation in the biodegradation aspects and broaden the scope of biomedical applications of L-amino acid bioresources, alternative non-peptide analogues such as poly(ester amides),[25−27] polycarbonates,[28] poly(ester urea urethanes),[29] poly(disulfide urethanes),[30] and poly(acetal urethanes)[31] have been explored. Our research has focused on the development of new classes of polyesters, polyurethanes, and poly(ester-urethanes) from L-amino acid bioresources.[32−42] These polymers have undergone

Received: February 25, 2024
Revised: July 10, 2024
Accepted: July 10, 2024
Published: July 17, 2024

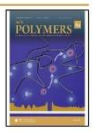

ACS Publications
© 2024 The Authors. Published by American Chemical Society

https://doi.org/10.1021/acspolymersau.4c00013
ACS Polym. Au 2024, 4, 392−404

ACS APPLIED MATERIALS & INTERFACES

www.acsami.org Research Article

Biocompatible PVAc-*g*-PLLA Acrylate Polymers for DLP 3D Printing with Tunable Mechanical Properties

Shibam Pal, Utreshwar Arjun Gavhane, and Asha S. K*

Cite This: *ACS Appl. Mater. Interfaces* 2024, 16, 62594−62605 Read Online

ACCESS | Metrics & More | Article Recommendations | Supporting Information

Downloaded via IISER PUNE on January 16, 2025 at 04:02:00 (UTC).
See https://pubs.acs.org/sharingguidelines for options on how to legitimately share published articles.

ABSTRACT: The technological advancement of Additive Manufacturing has enabled the fabrication of various customized artifacts and devices, which has prompted a huge demand for multimaterials that can cater to stringent mechanical, chemical, and other functional property requirements. Photocurable formulations that are widely used for Digital Light Processing (DLP)/Stereolithography (SLA) 3D printing applications are now expected to meet these new challenges of hard and soft or stretchable structural requirements in addition to good resolution in multiple scales. Here we present a biocompatible photocurable resin formulation with tunable mechanical properties that can produce hard or stretchable elastomeric 3D printed materials in a graded manner. Acrylate poly(lactic acid) (PLA) grafted polyvinyl acetate (PVAc) polymer was mixed with hydroxyl ethyl methacrylate (HEMA) and hydroxyl ethyl acrylate (HEA) as reactive diluents (50−70 wt %) in various compositions to form a series of photocurable resin formulations. Depending on the nature of the reactive diluent (HEMA or HEA) and their weight percentage, the mechanical properties of the 3D printed parts could be fine-tuned from hard (Tensile strength 20.6 ± 2 MPa, elongation 2 ± 1%) to soft (Tensile strength 1.1 ± 0.2 MPa, elongation 62 ± 8%) materials. The printed materials displayed remarkable dye absorption (95%), showing stimuli-responsive behavior for dye release (with respect to both pH and enzyme), while also demonstrating high cell viability (>90%) for mouse embryonic (WT-MEF) cells and degradability in PBS solution. These biobased 3D printing resins have the potential for a variety of applications, including tissue engineering, soft robotics, dye absorption, and elastomeric actuators.

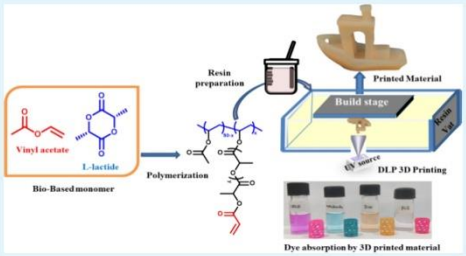

KEYWORDS: *graft polymer, photocurable resin formulation, 3D printing, digital light processing, biocompatible*

1. INTRODUCTION

Additive manufacturing (AM), also known as 3D printing technology, has grown in strength in recent years, opening up new possibilities for the on-demand production of complex 3D structures in fields as diverse as tissue engineering,[1−4] drug delivery,[5,6] medical device fabrication,[7,8] soft robotics,[9] dentistry,[10] and many others. Among the various 3D printing techniques like fused deposition modeling (FDM), direct ink writing (DIW), digital light processing (DLP), etc., light-based DLP 3D printing shows greater advantages in terms of precision, resolution, and layer unification compared to other 3D printing techniques.[11,12] Despite the rapid growth of AM technology, research on the development of suitable materials is still insufficient to expand the range of materials available for 3D printing.[13−15] Most of the photocurable resins commonly employed are either traditional epoxy resins or small-molecule acrylate-based resins readily accessible in the market. Their usage in creating biological implants is constrained since they are often neither biocompatible nor biodegradable.[16−18] In order to create biodegradable and biocompatible materials, AM technology makes considerable use of biobased polymers such as polylactic acid (PLA),[19−21] polycaprolactone (PCL),[22] polyglycolide (PGL),[23] and poly(propylene fumarate) (PPF).[24,25] For synthesizing biobased and degradable materials, PLA is the first choice due to its biodegradability and low environmental impact.[4,26,27]

Recently, our research group reported PLA-based polymeric cross-linkers in the form of acrylate-terminated linear and star PLA for DLP 3D printing.[21] Another synthetic approach to synthesizing polymeric cross-linkers is graft polymerization. To enhance the morphological, chemical, and physical characteristics of the entire polymer structure, polymer grafts are introduced as branches of one polymer component covalently attached to the main polymer backbone. The chemical composition and structure of graft copolymers can be fine-

Received: July 9, 2024
Revised: October 1, 2024
Accepted: October 16, 2024
Published: October 29, 2024

ACS Publications © 2024 American Chemical Society

pubs.acs.org/Biomac

Article

Melt Polycondensation Strategy to Access Unexplored L-Amino Acid and Sugar Copolymers

Dheeraj Chandra Joshi, Utreshwar Arjun Gavhane, and Manickam Jayakannan*

Cite This: *Biomacromolecules* 2024, 25, 7311−7322

Read Online

ACCESS | Metrics & More | Article Recommendations | Supporting Information

ABSTRACT: Biodegradable polymers from bioresources are highly in demand for the development of sustainable polymer platforms for commodity plastics and in the biomedical field. Here, an elegant one-pot synthetic strategy is developed, for the first time, to access unexplored hybrid polymers from two naturally abundant resources: carbohydrates (sugars) and L-amino acids. A bottleneck in the synthetic strategy is overcome by tailor-making D-mannitol-based six- and five-membered bicyclic acetalized diols, and their structures are confirmed by single-crystal X-ray diffraction and 2D NMR spectroscopy. L-Amino acids are converted into ester-urethane functional monomers, and they are polymerized with sugar-diols under solvent-free melt polycondensation to yield biodegradable poly(ester-urethane)s. Acid-catalyzed deprotection yielded amphiphilic polymers having exclusively alternating residues of sugar and L-amino acid in the polymer backbone. The polymer is self-assembled into 200 ± 10 nm sized nanoparticles that can encapsulate fluorescent dyes, are nontoxic to cells up to 250 μg/mL, and are readily endocytosed for lysosomal enzymatic biodegradation at the cellular level.

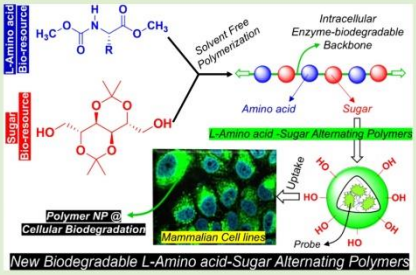

Downloaded via IISER PUNE on January 16, 2025 at 03:54:03 (UTC).
See https://pubs.acs.org/sharingguidelines for options on how to legitimately share published articles.

INTRODUCTION

The use of synthetic polymers based on bioresources is one of the most sought-after design strategies to overcome the nonbiodegradability of commodity plastics, minimize the plastic waste in the environment, contribute to circular economy, and cater to new technology in medical implants, tissue engineering, drug and gene delivery, etc.[1−6] Among the diverse polymer structures reported in the literature, aliphatic polyesters have unique advantages due to their inherent ability to undergo digestion via enzymatic biodegradation under physiological conditions.[7−13] Poly(L-lactide)s, poly(L-glycolide)s, poly(lactide-*co*-glycolide), and polycaprolactone are some of the most important commercial aliphatic polyesters that are currently explored as biodegradable polymer products and for diverse applications in the biomedical field.[14−16] In the last few decades, a sudden surge in attempts to replace or minimize existing petroleum-based nonbiodegradable polymer products in the market with bioresource-based sustainable polymer platforms has been distinctly observed.[17−25] Among the bioresources, both carbohydrates (sugars) and L-amino acids are largely abundant in nature, possess significantly high structural diversity, and are currently used as raw materials or intermediates in the chemical industry, biomedical formulations, cosmetic products, and so on.[25−30] In the polymer literature, sugar derivatives such as isosorbide, isoidide, isohexide, and acyclic carbohydrates such as D-mannitol, D-glucitol, and D-galactitol have been employed in polymer synthesis.[31−45] They are often used as copolymer constituents for value-addition in industrial polymers such as poly(alkylene terephthalate).[45−48] L-Amino acid bioresources are readily converted into N-carboxy anhydride cyclic monomers and subjected to ring-opening polymerization to produce high-molecular-weight polypeptides.[49−52] Unfortunately, these synthetic polypeptides do not melt (or flow); hence, they have exhibited limited success as thermoplastic engineering materials. Further, the existing protease-enzyme biomachinery in living organisms is highly selective to sequence-specific peptide-linkage cleavage, which further limits the biodegradation aspects of long-chain polypeptides under physiological conditions. It is astonishing to notice that there is no synthetic methodology available in the literature to polymerize sugar and L-amino acid bioresources together in a one-pot reaction. Hence, the development of a new polymerization process would enable researchers to access unexplored sugar and L-amino acid hybrid thermoplastic engineering materials, which would be a new class of entities for new biomedical and industrial applications. There are two main synthetic challenges to bringing sugars and amino acids together: (i) sugars require selective masking of secondary

Received: July 18, 2024
Revised: October 4, 2024
Accepted: October 7, 2024
Published: October 21, 2024

ACS Publications

© 2024 American Chemical Society

https://doi.org/10.1021/acs.biomac.4c00993
Biomacromolecules 2024, 25, 7311−7322

Indian Institute of Science Education and Research
(IISER – PUNE)

Dr. Homi Bhabha Road, Pashan, Pune 411 008.

Certificate

This is to certify that the project **"In Vivo Studies of Theranostic Block Copolymer Polymer Nanoparticles" (IISER_Pune/IAEC/2022_01/15)** from **Prof. M. Jayakannan** has been approved by the IAEC.

Authorized by	Name	Signature	Date
Chairman:	Dr. Nixon Abraham		04 Mar 2022
Member Secretary:	Dr. Suraj Ingle		04 Mar 2022
Main Nominee of CPCSEA:	Dr. Shital Suryavanshi	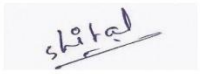	04 Mar 2022

Appendix

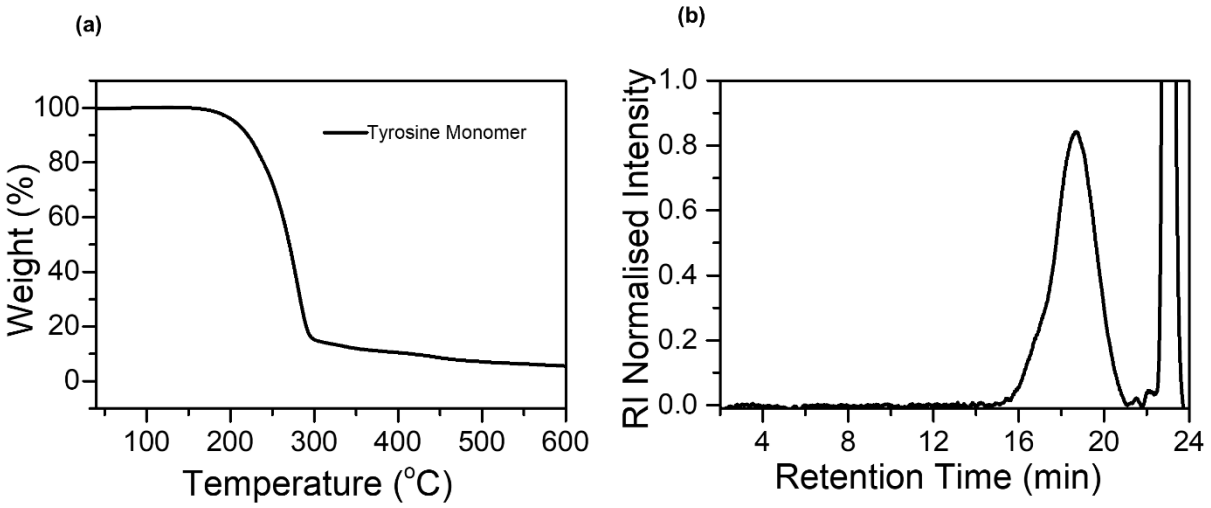

Appendix Figure S1 *(a) TGA thermograms of L-Tyrosine monomer performed at 10 °/min under N_2 atmosphere. (b) SEC profile of the P-Tyr polymer in THF as eluent at 25 °C.*

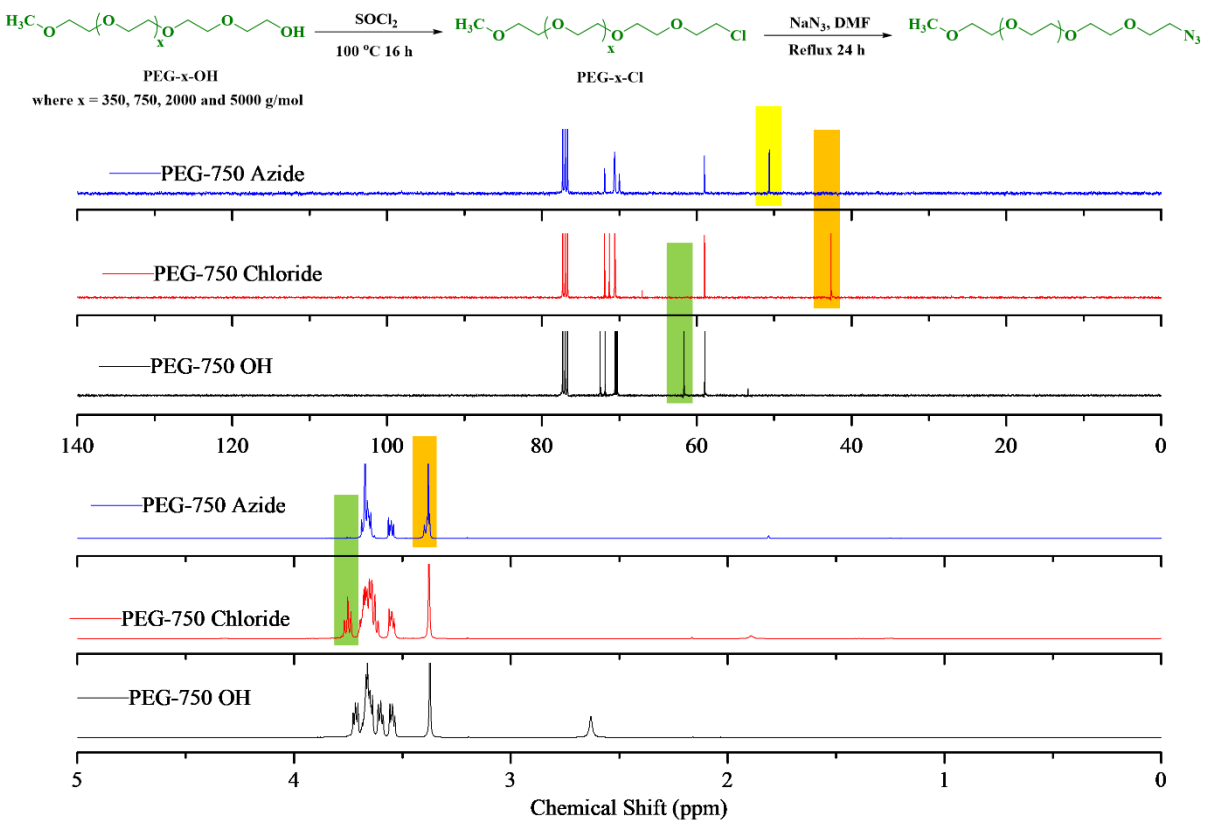

Appendix Figure S2 *^{1}H NMR spectra of PEG-750-OH to PEG-750 Azide, and ^{13}C PEG-750 OH, Azide, to PEG-750 Azide.*

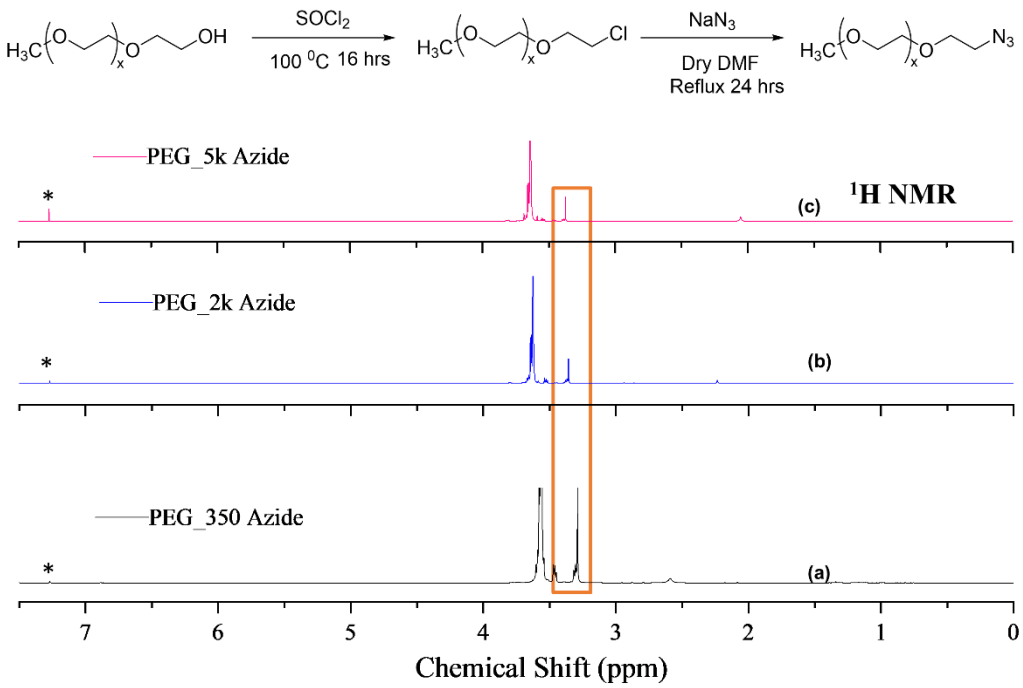

Appendix Figure S3 *^{1}H NMR spectra PEG Azides: (a) PEG-350 Azide, (b) PEG-750 Azide, (c) PEG-2000 Azide, and (d) PEG-5000 Azide. All the spectra were recorded in $CDCl_3$. The peaks corresponding to solvents are assigned by asterisks.*

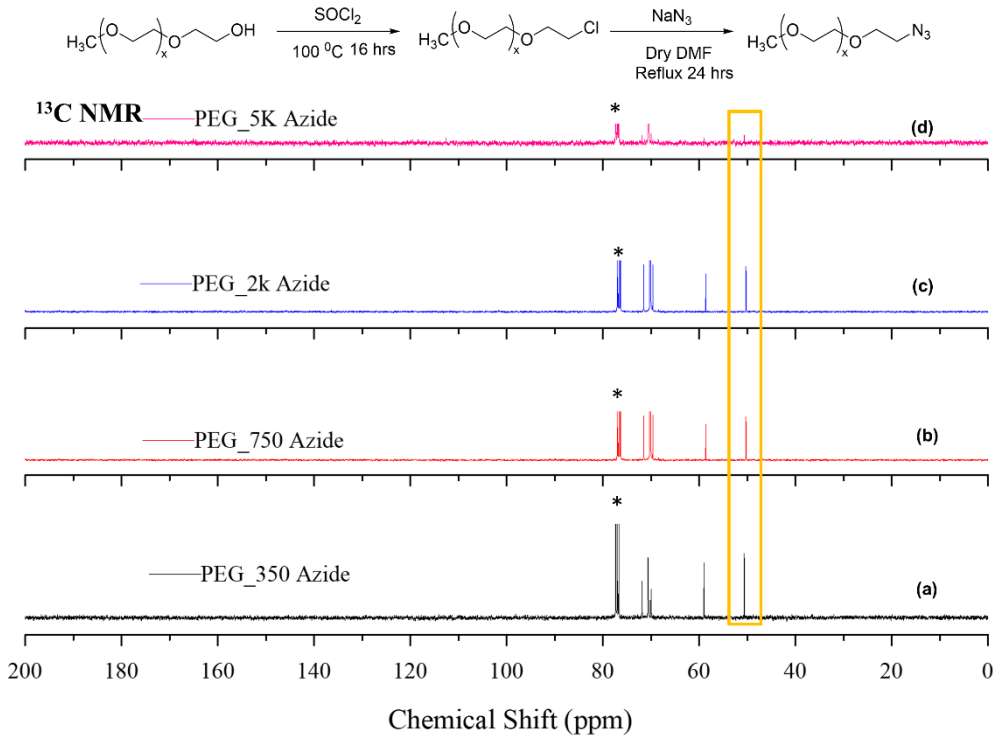

Appendix Figure S4 *^{13}C NMR spectra PEG Azides: (a) PEG-350 Azide, (b) PEG-750 Azide, (c) PEG-2000 Azide, and (d) PEG-5000 Azide. All the spectra were recorded in $CDCl_3$. The peaks corresponding to solvents are assigned by asterisks.*

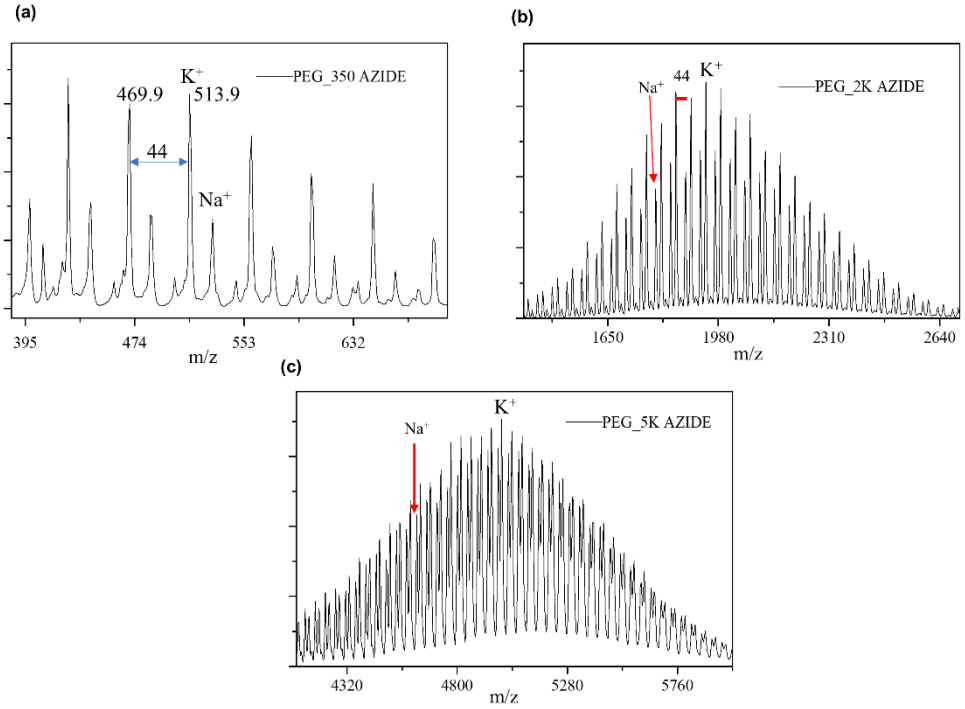

Appendix Figure S5 *MALDI TOF spectra of PEG-Azides: (a) PEG-350 Azide, (b) PEG-2000 Azide, and (c) PE-5000 Azide.*

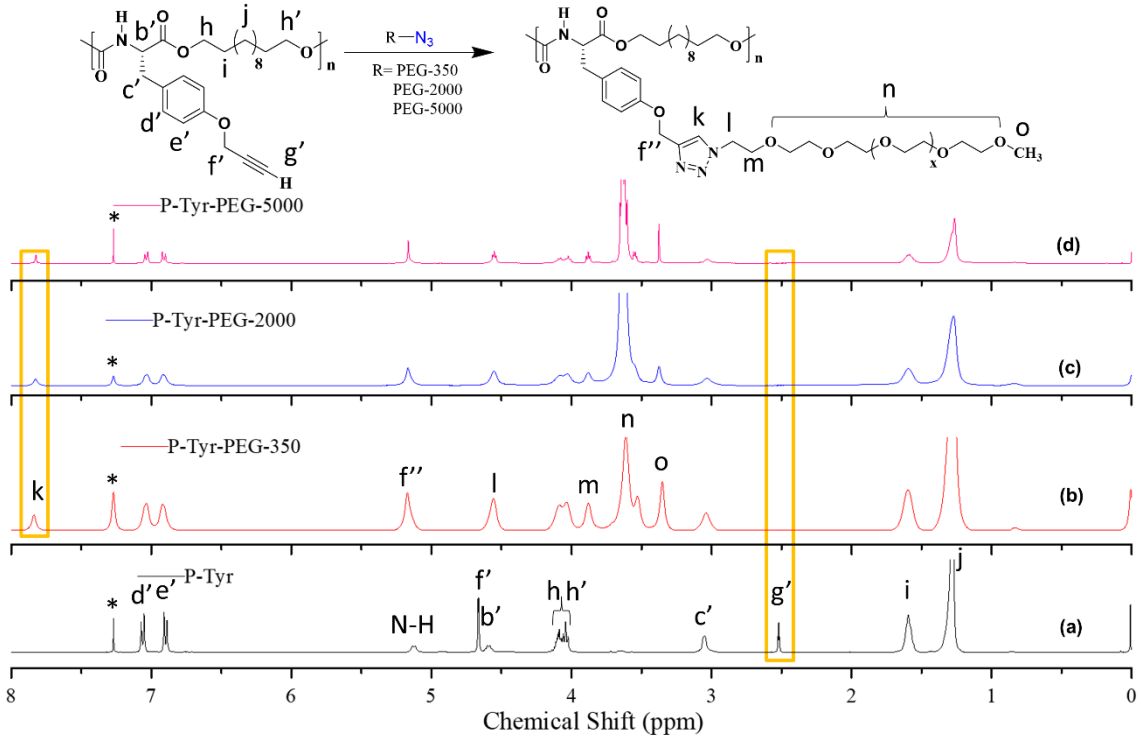

Appendix Figure S6 *^{1}H NMR spectra of clicked polymers: (a) P-Tyr, (b) P-Tyr-PEG-350, (c) P-Tyr-PEG-2000, and (d) P-Tyr-PEG-5000. All the spectra were recorded in $CDCl_3$. The peaks corresponding to solvents are assigned by asterisks.*

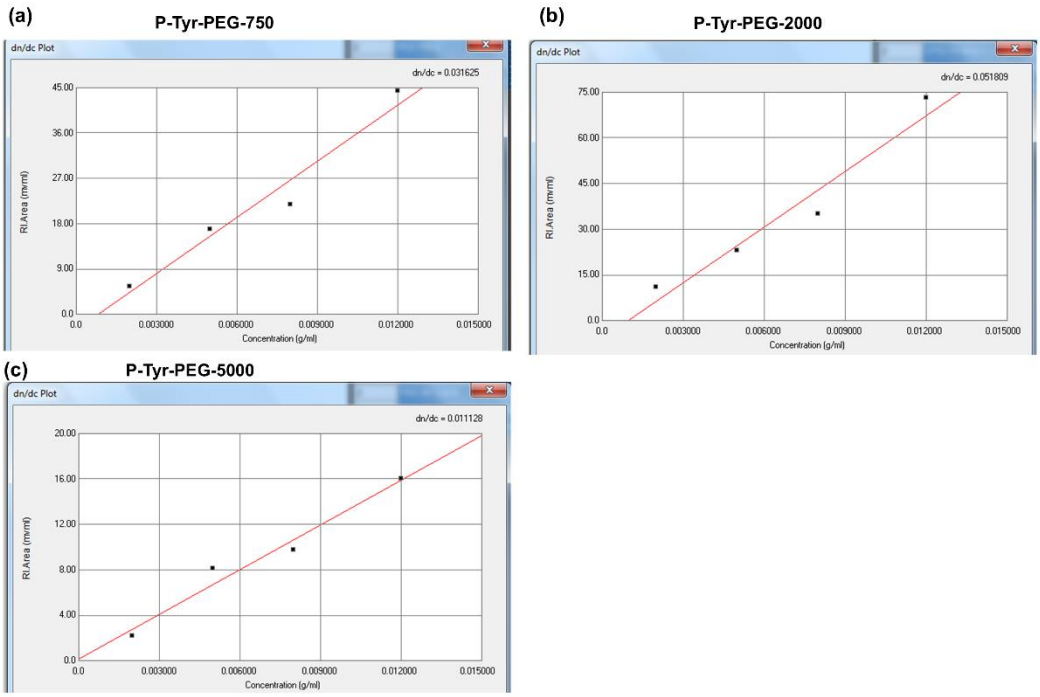

Appendix Figure S7 *The plots for the determination of dn/dc value of polymers Omnisec software, (a) P-Tyr-PEG-750, (b) P-Tyr-PEG-2000, and (c) P-Tyr-PEG-5000.*

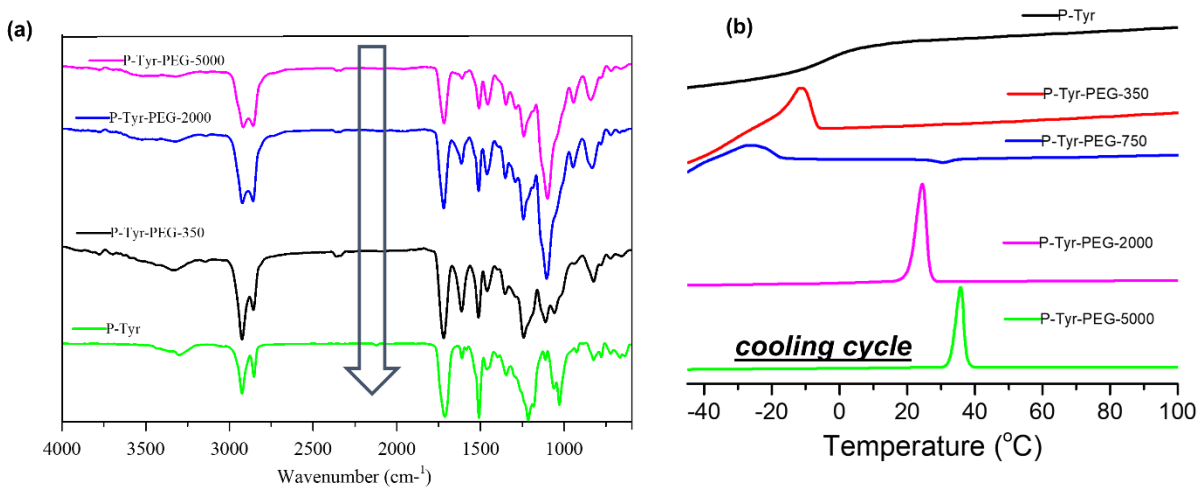

Appendix Figure S8 *(a) FT-IR spectra: (a) All the Clicked polymers. The peak corresponding to azide stretching frequency is vanished shown in Figure a by arrow. (b) profile of clicked Polymers Cooling cycle at 10 °/min under N_2 atmosphere, (c) Table containing the thermal stability of Polymers.*

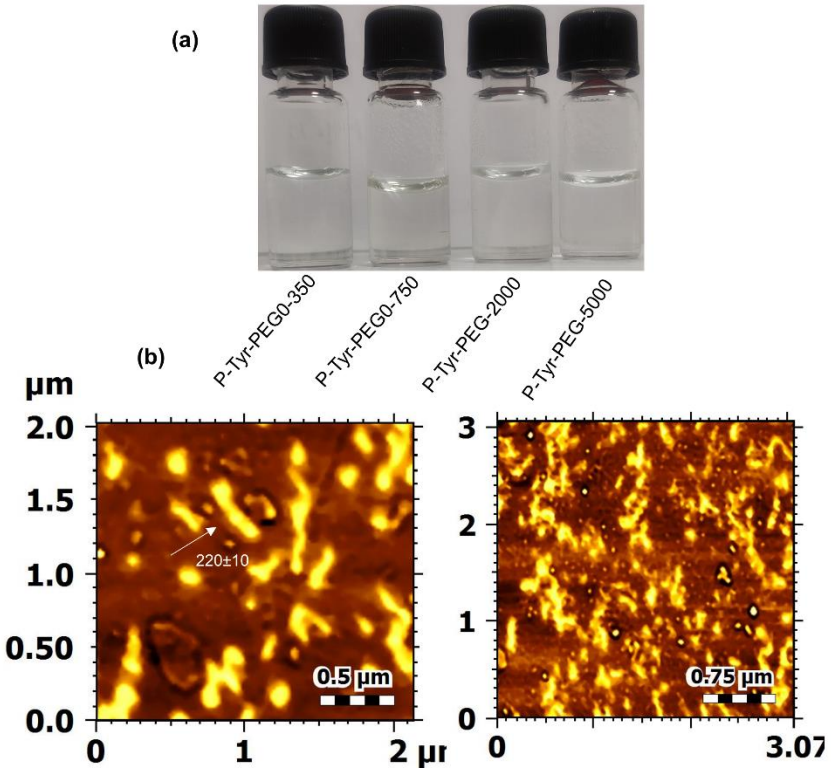

Appendix Figure S9 *(a) aqueous self-assemblies of polymers. (b) AFM images of P-Tyr-PEG-750 brush polymer.*

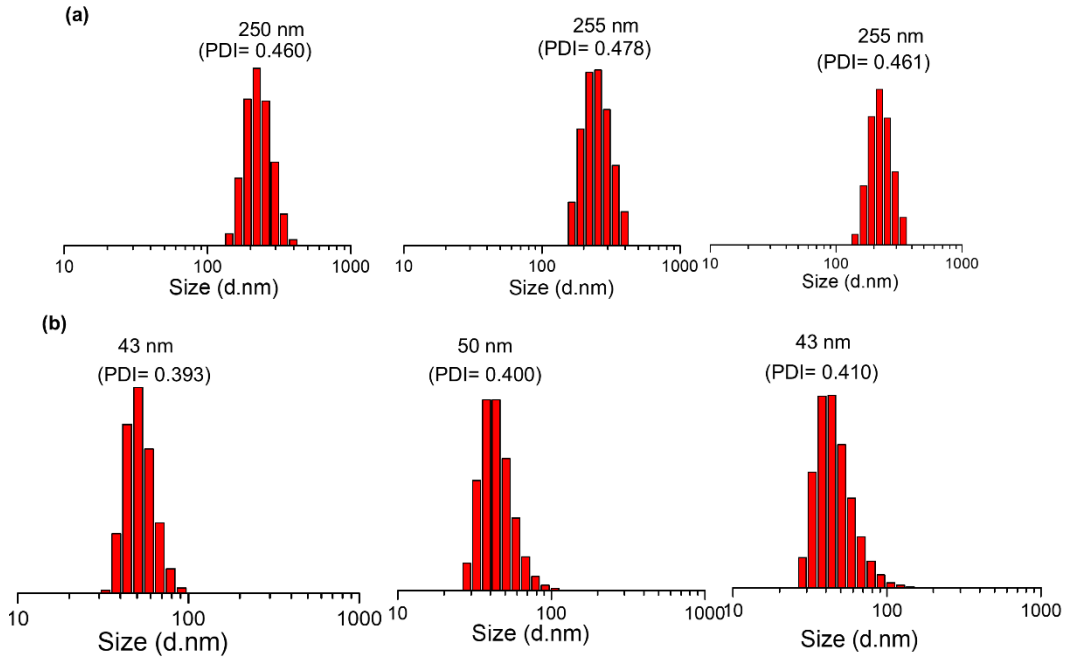

Appendix Figure S10 *DLS Histogram (a) P-Tyr-PEG-750-DOX, (b) P-Tyr-PEG-5000-DOX. Concentration = 0.1mg/ml*

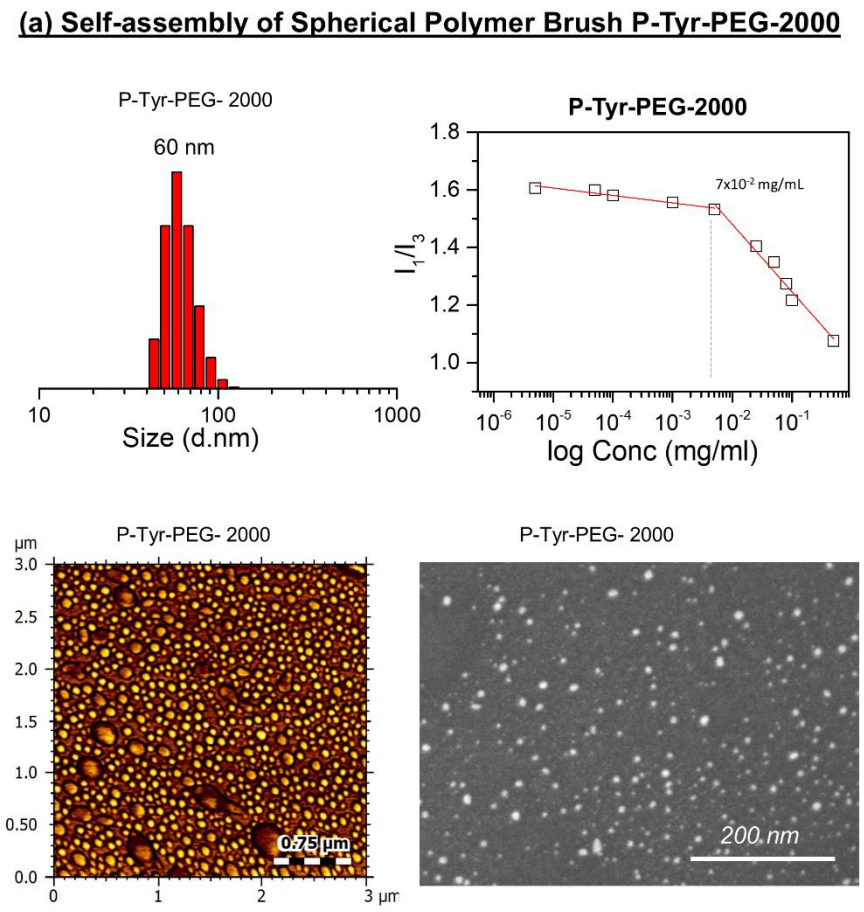

Appendix Figure S11 *(a) DLS histogram and Critical aggregation concentration (CAC) was determined by pyrene-probe. P-Tyr-PEG-2000 brush characterization by AFM, and FE-SEM images*

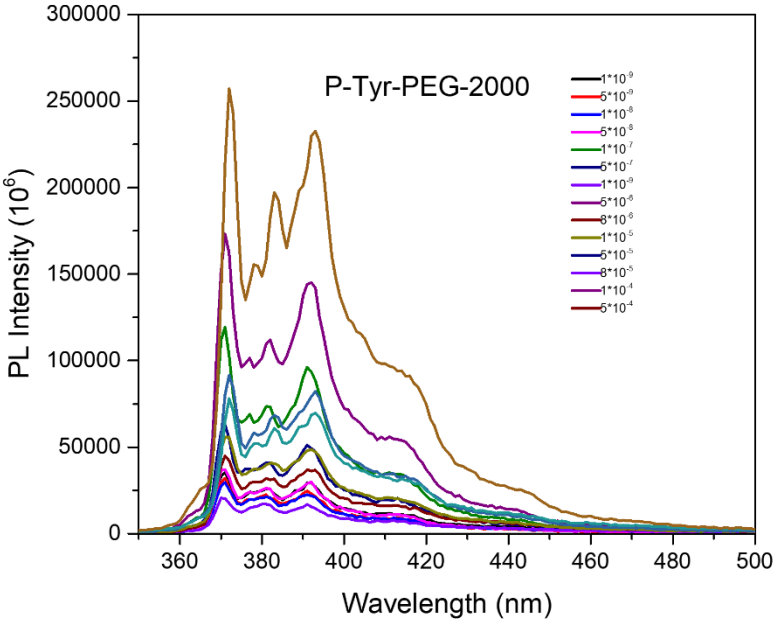

Appendix Figure S12 *Pyrene emission spectra for CMC determination. Pyrene chromophore was excited at λEx= 337 nm and emission was collected from 350-500 nm. (a) P-Tyr-PEG-750, (b) P-Tyr-PEG-2000.*

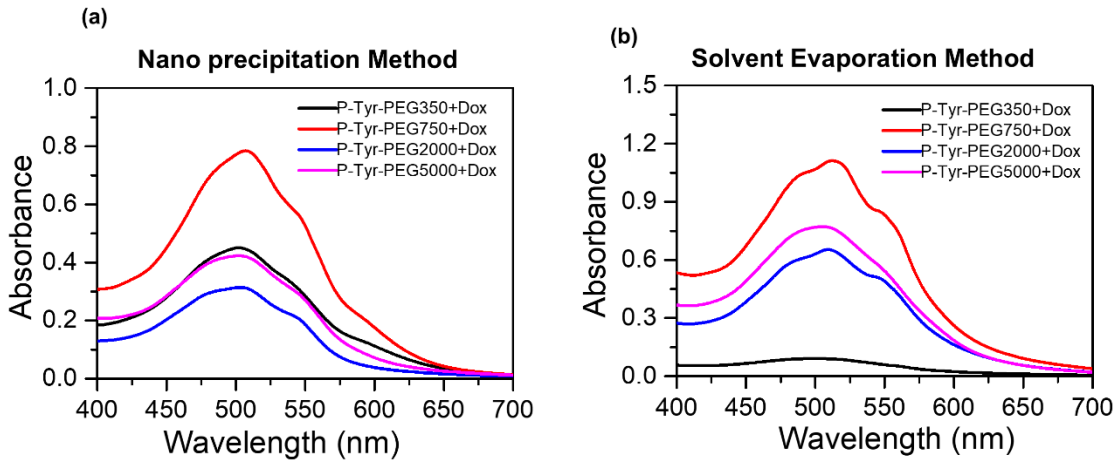

Appendix Figure S13 *Absorbance spectra of DOX loaded samples for different methods, (a) Nano precipitation method, and (b) Solvent evaporation method, sample name P-Tyr-PEG-350-DOX, of P-Tyr-PEG-750-DOX, P-Tyr-PEG-2000-DOX, and P-Tyr-PEG-5000-DOX.*

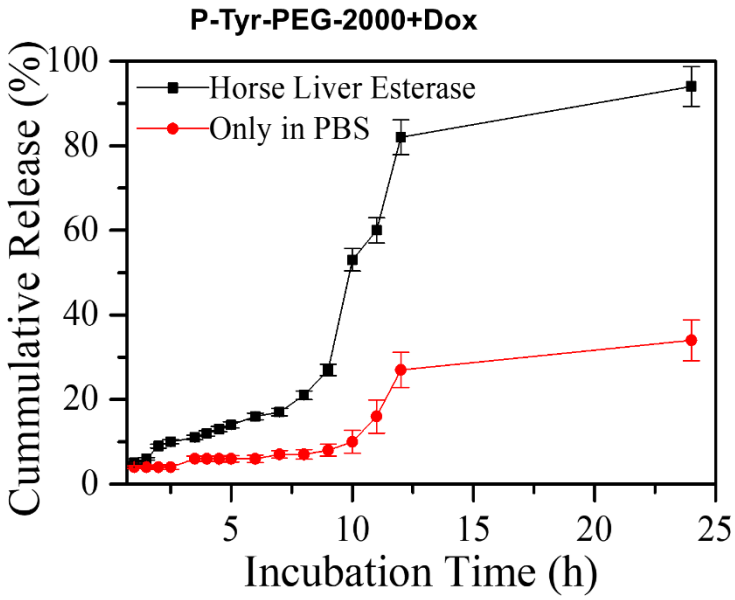

Appendix Figure S14 *Cumulative Drug release profile of P-Tyr-PEG-2000-DOX in the absence and in the presence of horse liver esterase enzyme at 37 ℃ and pH 7.4 in PBS.*

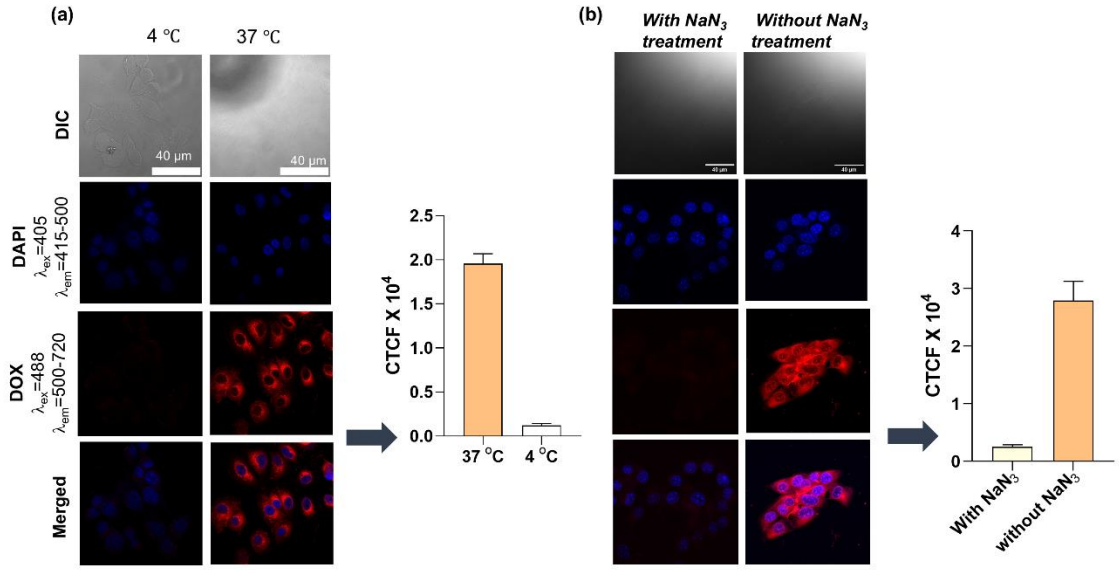

Appendix Figure S15 *(a) P-Tyr-PEG-2000-DOX Temperature-dependent cellular uptake studies in WT-MEF cell line. (b) Corresponding their CTCF values of P-Tyr-PEG-2000-DOX, at 37 ℃ and P-Tyr-PEG-2000-DOX at 4 ℃. (b) CLSM images of PTyr-PEG-2000+DOX sample incubated with cells that are pre-treated with NaN_3 at 37 ℃ (NaN_3 concentration = 6.5 µg/mL incubation 30 minute). A control experiment was carried out without NaN_3 at 37 ℃. CTCF plots estimated from the CLSM images of NaN_3 experiment.*

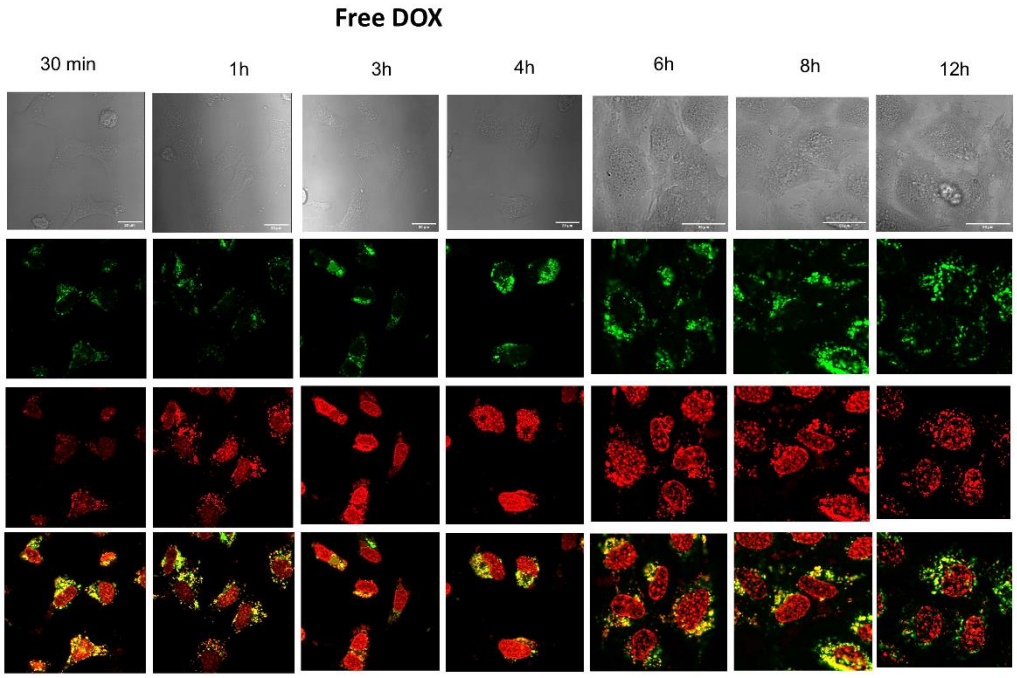

Appendix Figure S16 *Time dependent Live-cell imaging of free DOX at incubation time point 30 min, 1, 3, 4, 6, 8, and 12h in WET-MEF cell. Concentration of the DOX loaded sample were maintained as 5.0 μg/mL. The scale bar represents 40 μm in cell images.*

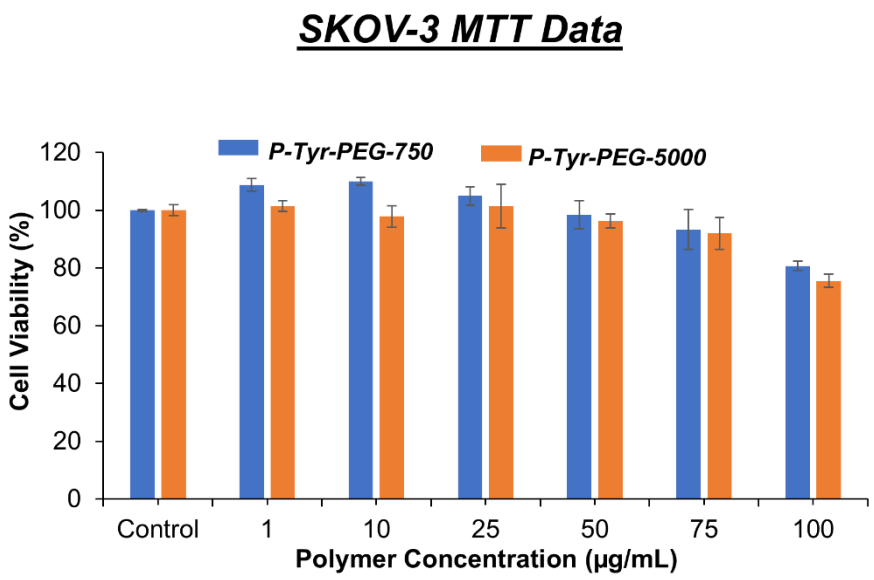

Appendix Figure S17 *Cytotoxicity of polymer alone P-Tyr-PEG-750, and P-Tyr-PEG-5000. nanoparticle in SKOV-3 cell line for 72 h incubation.*

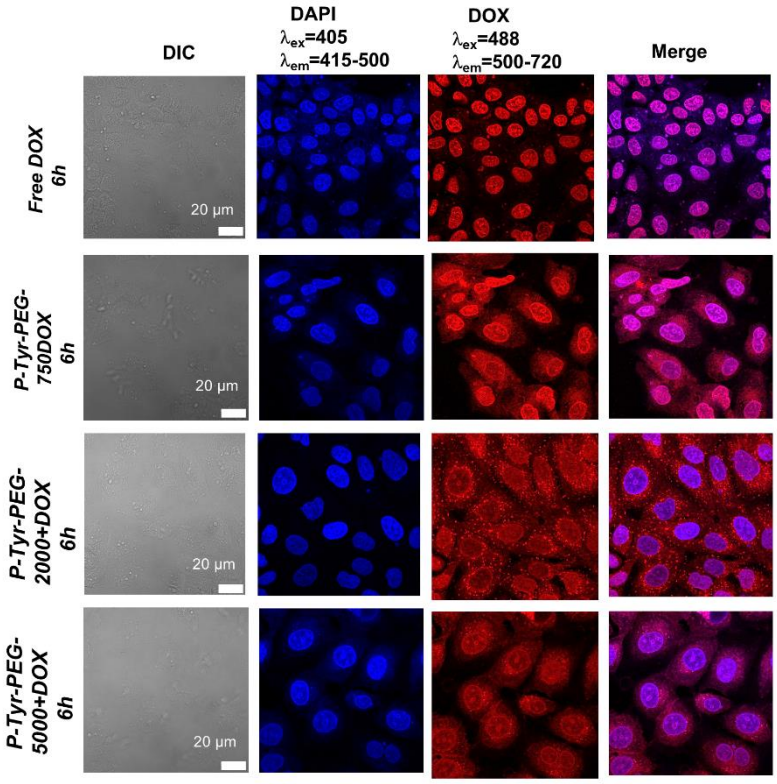

Appendix Figure S18 *Time-dependent cellular uptake fixed cell imaging in MCF-7 cell line. incubation time 6h.*

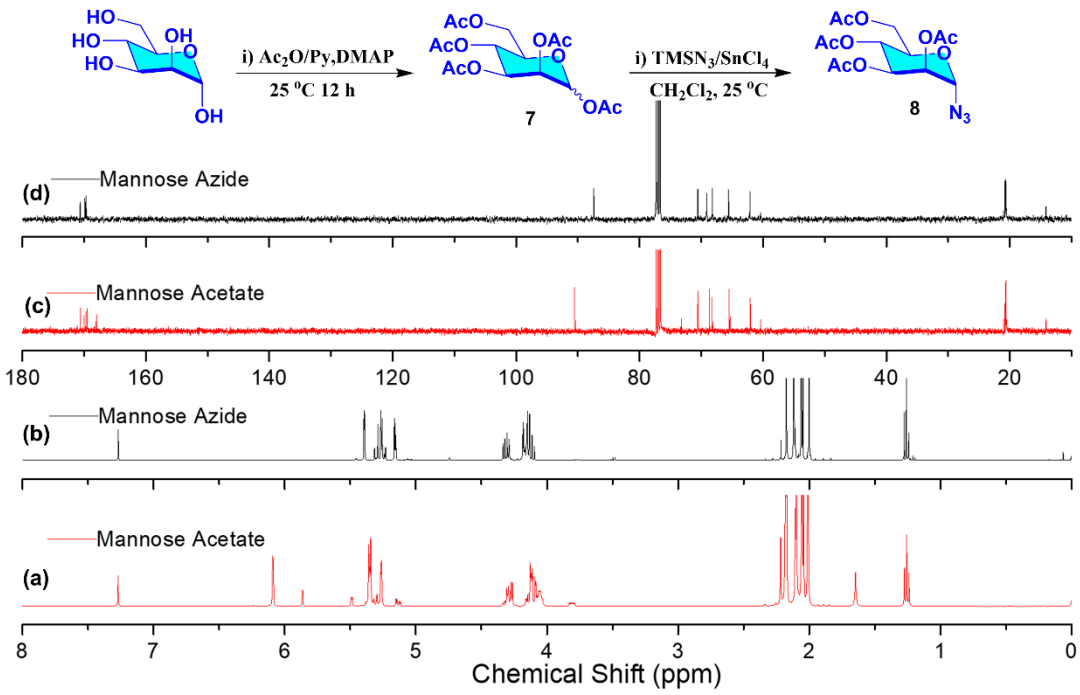

Appendix Figure S19 *(a) ^{1}H NMR of mannose Acetate, (b) ^{1}H NMR of mannose Acetate Azide, and (c) ^{13}C NMR of mannose Acetate and (d) ^{13}C NMR of mannose Acetate azide. All the spectra were recorded in the $CDCl_3$. The peaks corresponding to solvents are assigned by asterisks.*

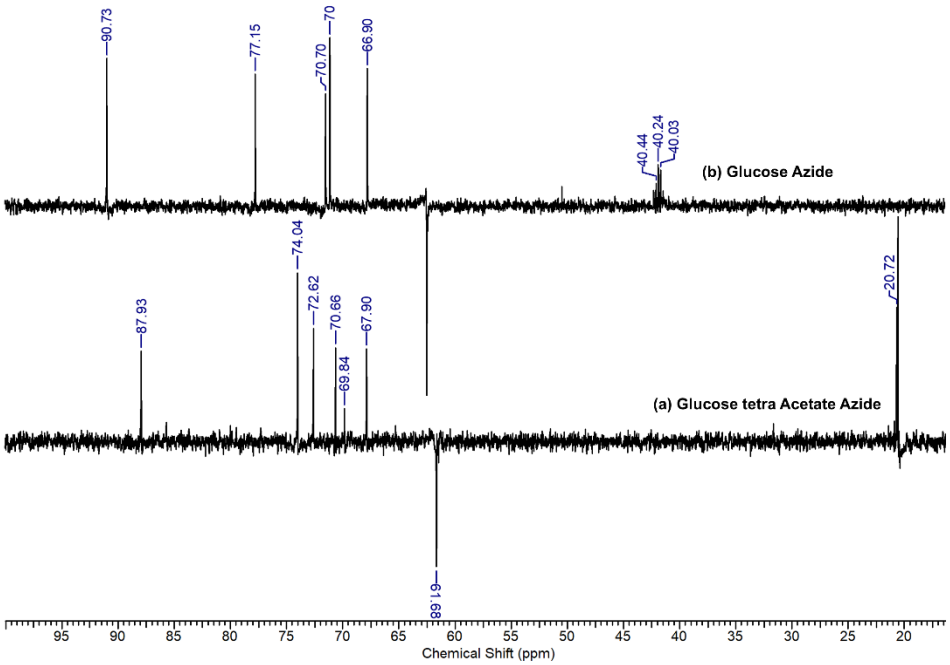

Appendix Figure S20 *(a) DEPT-135 NMR of glucose Acetate Azide, and (b) glucose Azide.*

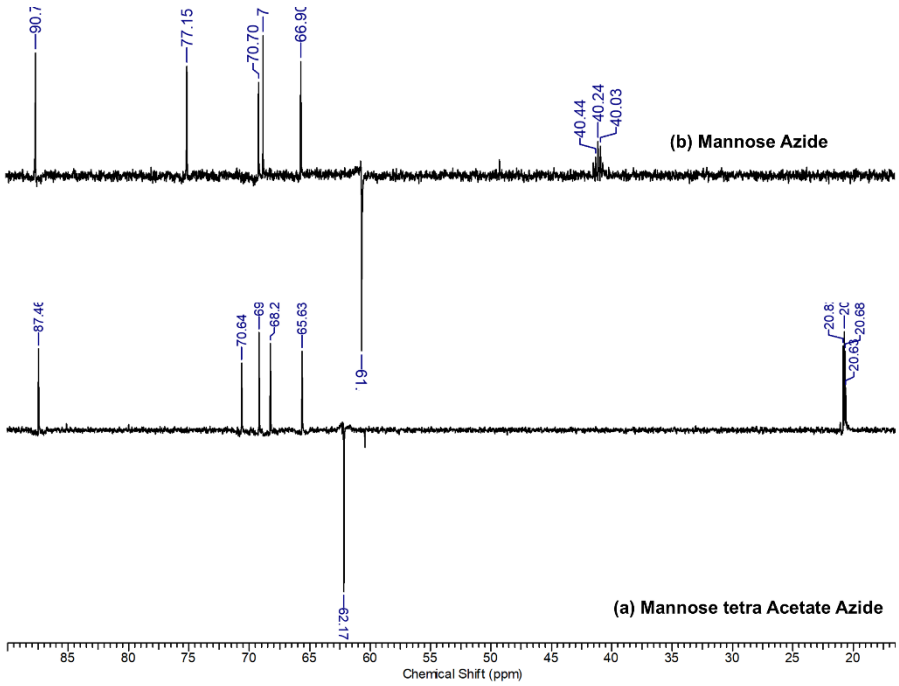

Appendix Figure S21 *(a) DEPT-135 NMR of mannose Acetate Azide, and (b) mannose Azide.*

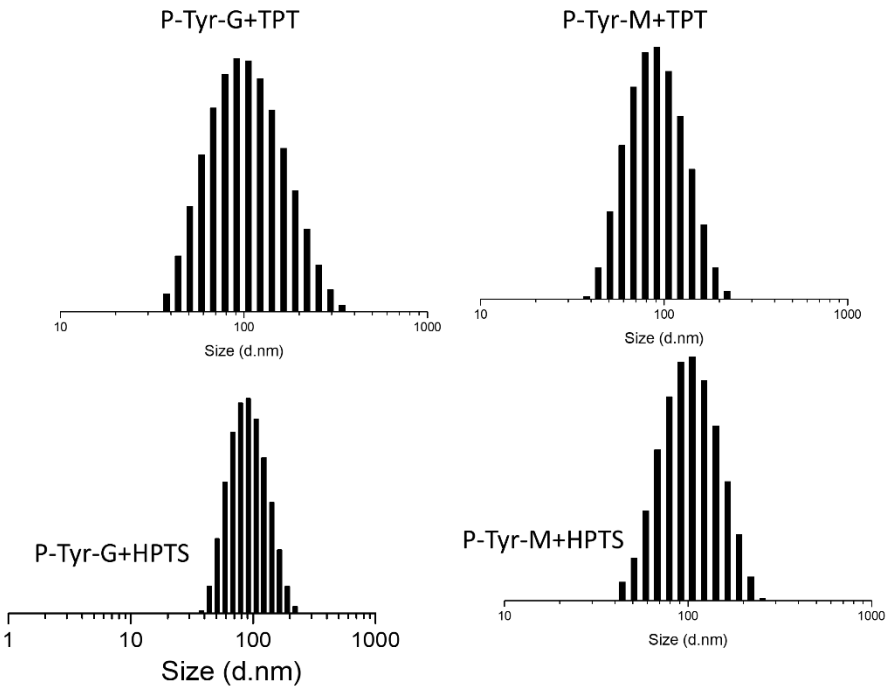

Appendix Figure S22 *DLS Histogram P-Tyr-G+TPT, P-Tyr-M+TPT, P-Tyr-G+HPTS, and P-Tyr-M+HPTS, Concentration = 0.1mg/ml*

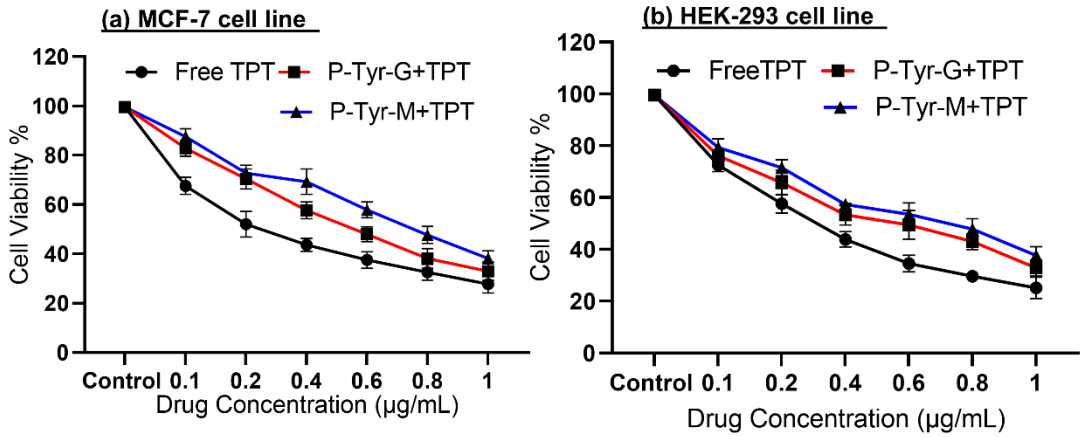

Appendix Figure S23 *(a) Plot showing the cytotoxicity of CPT loaded P-Tyr-G, and P-Tyr-M free TPT in breast cancer MCF-7 cell line. (b) Plot showing the cytotoxicity of TPT loaded P-Tyr-G, and P-Tyr-M free CPT in normal human kidney HEK-293 cell line*

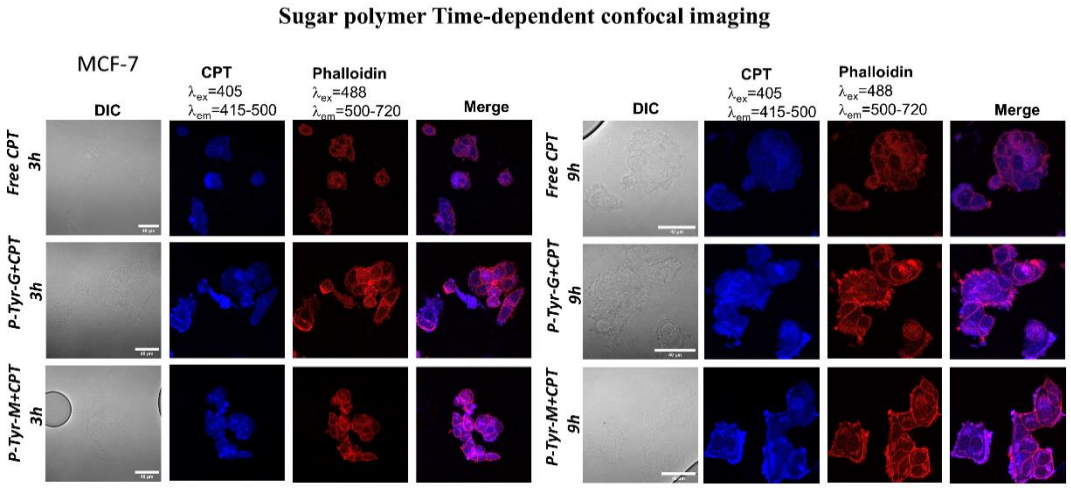

Figure S24 *Cellular uptake studies of fixed cell imaging in HEK-293 cell line and Cellular uptake studies of fixed cell imaging in MCF-7 cell line. The concentration of CPT was maintained as 5 µg/mL. The scale bar represents 40 µm in cell images.*

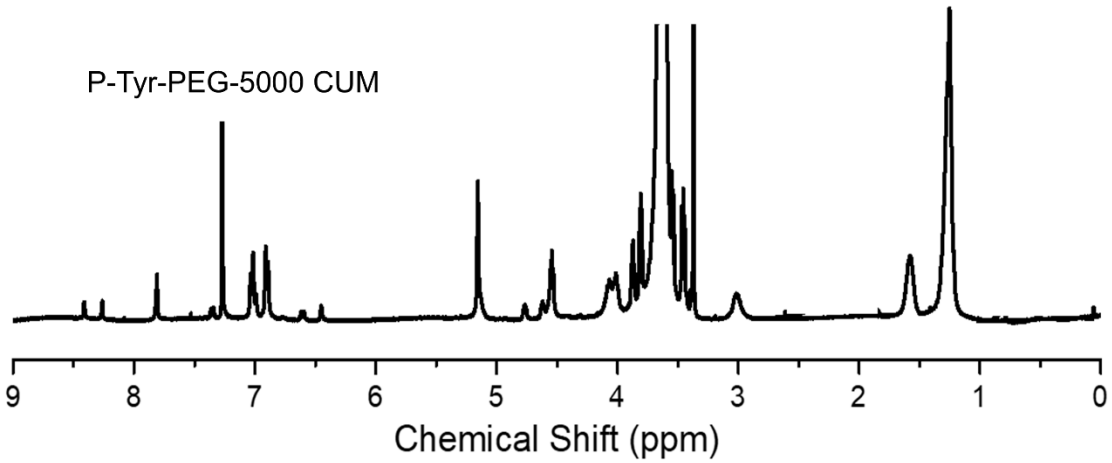

Appendix Figure S25 *^{1}H NMR of P-Tyr-PEG-5000-CUM recorded in CDCl3.*

Energy Transfer and FRET Distance

FRET is a distance dependent process and depends upon the intermolecular distance between donor and acceptor and the distance at which the FRET is 50% efficient is called Förster distance (R_0).[6] and determined by equation:

$$R_0 = [8.79 \times 10^{-5} (\kappa^2 \eta^{-4} Q_D J(\lambda))]^{1/6}$$

where κ^2 is the angle between the dipole moments of donor and acceptor, Q_D is the quantum yield of donor, η is refractive index of the medium and $J(\lambda)$, the overlap integral form the emission spectrum of donor with the absorption spectrum of acceptor is given as;6

$$J(\lambda) = \int F_D(\lambda) \varepsilon_A(\lambda) \lambda^4 \, d\lambda$$

where F_D is the corrected fluorescence intensity of donor and $\varepsilon_A(\lambda)$ is the molar extinction coefficient of the acceptor. The FRET efficiency can be determined from the equation:

$$E_{FRET} = (R_0^6) / [R_0^6 + R^6]$$

where R is the distance between donor and acceptor molecules. The parameter R_0 is also dependent on the $J(\lambda)$, the overlap integral of the emission spectrum of donor and absorption spectrum of acceptor. E_{FRET} is determined from the fluorescence life of donor molecule as follows:6 $E = 1-[\tau_{DA}/\tau_D]$

where τ_D is the average fluorescence lifetime of donor in absence of acceptor and τ_{DA} is the average fluorescence lifetime of donor in presence of acceptor. The values of $J(\lambda)$ and R_0 determined as above were computationally determined using the program as per the literature report.